

# Multiphoton Processes and Photocontrol of Biochemical Reaction Pathways

---

DISSERTATION  
ZUR ERLANGUNG DES DOKTORGRADES  
DER NATURWISSENSCHAFTEN



VORGELEGT BEIM FACHBEREICH  
BIOCHEMIE, CHEMIE UND PHARMAZIE  
DER JOHANN WOLFGANG GOETHE-UNIVERSITÄT  
IN FRANKFURT AM MAIN

VON

**MARVIN PHIL RONALD ASIDO**

AUS FRANKFURT AM MAIN

FRANKFURT AM MAIN 2022  
(D30)

Vom Fachbereich Biochemie, Chemie und Pharmazie der Johann Wolfgang  
Goethe-Universität als Dissertation angenommen.

Dekan: Prof. Dr. Clemens Glaubitz

1. Gutachter: Prof. Dr. Josef Wachtveitl

2. Gutachter: Prof. Dr. Alexander Heckel

Datum der Disputation: \_\_\_\_\_





# List of Publications and Conference Contributions

## Publications in the context of this work

Peer-reviewed publications as first or co-first author (indicated by †):

- (i) **Inactivation of competitive decay channels leads to enhanced coumarin photochemistry**  
R. Klimek †, M. Asido †, V. Hermanns, S. Junek, J. Wachtveitl and A. Heckel,  
Chem. Eur. J., **2022**, e202200647.
- (ii) **Ultrafast and Efficient Energy Transfer in a One- and Two-Photon Sensitized Rhodamine-BODIPY Dyad: A Perspective for Broadly Absorbing Photocages**  
M. Asido †, C. Hamerla †, R. Weber †, M. Horz †, M. S. Niraghatam, A. Heckel, I. Burghardt and J. Wachtveitl,  
Phys. Chem. Chem. Phys., **2022**, 24, 1795-1802.
- (iii) **Transient near-UV Absorption of the Light-Driven Sodium Pump *Krokinobacter eikastus* Rhodopsin 2: A Spectroscopic Marker for Retinal Configuration**  
M. Asido †, R. K. Kar †, C.N. Kriebel, M. Braun, C. Glaubitz, I. Schapiro and J. Wachtveitl,  
J. Phys. Chem. Lett., **2021**, 12, 6284-6291.
- (iv) **Time-resolved IR spectroscopy reveals mechanistic details of ion transport in the sodium pump *Krokinobacter eikastus* Rhodopsin 2**  
M. Asido, P. Eberhardt, C. N. Kriebel, M. Braun, C. Glaubitz and J. Wachtveitl,  
Phys. Chem. Chem. Phys., **2019**, 21, 4461-4471.

Other peer-reviewed publications:

- (v) **Probing the photointermediates of light-driven sodium ion pump KR2 by DNP-enhanced solid-state NMR**  
O. Jakdetchai, P. Eberhardt, M. Asido, J. Kaur, C. N. Kriebel, J. Mao, A. J. Leeder, L. J. Brown, R. C. D. Brown, J. Becker-Baldus, C. Bamann, J. Wachtveitl and C. Glaubitz,  
Sci. Adv., **2021**, eabf4213.

(not explicitly discussed in this thesis)

(vi) **Sensitizer-enhanced two-photon patterning of biomolecules in photoinstructive hydrogels**

H. Krüger, M. Asido, J. Wachtveitl, R. Tampé and R. Wieneke,  
Comm. Mat., 2022, 3.

## Conference Contributions

- **SFB 1507 Kick-off Symposium**  
Presentation: *The near-UV Region in Microbial Rhodopsins - A new Perspective for Optogenetic Research?*  
07.07.2022, Frankfurt am Main, Germany
- **IPTC Annual Symposium**  
Presentation: *From Fluorophores to Photocages*  
22.03.2022, Hirschegg, Austria
- **CLiC Summer School and Conference**  
Presentation: *A Perspective for Broadly Absorbing Photocages*  
13.09.2021, Niedernberg, Germany
- **Workshop on Photoreceptors**  
Presentation: *A Mechanistic Insight into the Ion Transport of the Light-driven Sodium Pump KR2*  
09.10.2019, Berlin, Germany
- **IPTC Annual Symposium**  
Presentation: *Ultrafast Deactivation Dynamics of a Channelrhodopsin-2 Variant*  
26.03.2019, Hirschegg, Austria
- **Biophysical Society 63<sup>rd</sup> Annual Meeting**  
Poster: *Time-resolved IR Spectroscopy Reveals Mechanistic Details of Ion Transport in the Sodium Pump Krokobacter Eikastus Rhodopsin 2*  
04.03.2019, Baltimore, USA
- **CLiC Summer Schools 2018, 2019, 2020**  
Presentations: Progress Reports

# Zusammenfassung

Eine Vielzahl an grundlegenden Fragestellungen im Bereich der modernen Lebenswissenschaften befasst sich mit der biochemischen Regulation in Organismen. Die Aufklärung dieser hochkomplexen Prozesse dient nicht nur dem besseren Verständnis der Prinzipien lebender Materie, sondern vor allem auch der Prävention, Diagnostik und Therapie im medizinischen Kontext. Vielerlei Krankheiten sind auf eine Fehlfunktion des Stoffwechsels zurückzuführen, die konventionell durch Verabreichung verschiedener Medikamente therapiert werden. Dieser Ansatz hat jedoch nicht selten zur Folge, dass der Organismus über die lokal beeinträchtigte Stelle hinaus mit Nebenwirkungen zu kämpfen hat. In diesem Zusammenhang ist eine zeitlich präzise, lokal beschränkte und minimal invasive Behandlungsmethode eine wünschenswerte Ergänzung. Diese Kriterien sollen mit dem Konzept der optischen Kontrolle realisiert werden. Mithilfe moderner Laser- und Bildgebungstechnologie kann je nach eingesetzter Wellenlänge im sogenannten phototherapeutischen Fenster eine optische Eindringtiefe von Mikrometern bis hin zu einigen Millimetern in biologischem Gewebe erreicht werden. Die hierbei eingesetzte Strahlung erzielt ihre maximale Wirkung im Bereich des Fokalvolumens, welches vor allem im Nahinfraroten Spektralbereich auf wenige Femtoliter reduziert werden kann. Eine noch bessere Genauigkeit kann unter Berücksichtigung von Mehrphotonen-Effekten wie zum Beispiel der Zwei-Photonen Absorption (2PA, engl. *two-photon absorption*), die sich auf den Bereich der höchsten Photonendichte beschränkt, erreicht werden. Zusammen mit der flexiblen Anpassung von Laserpuls-Sequenzen können hierbei nicht nur hoch-lokalisierte sondern auch zeitlich abgestimmte Aktivierungs- oder Deaktivierungsszenarien realisiert werden.

Die vorliegende Arbeit befasst sich mit verschiedenen Strategien zur Implementierung von optischer Kontrolle in biochemisch relevanten Systemen. Auf systemischer Ebene wurde einerseits die Licht-getriebene Natriumpumpe *Krokinobacter Eikastus* Rhodopsin 2 (KR2) vor dem Hintergrund optogenetischer Anwendungen untersucht, und andererseits die Optimierung der wichtigsten photochemischen Parameter von photolabilen Schutzgruppen (PPG, engl. *photolabile protecting group*) angestrebt. Von der technisch-photophysikalischen Seite wurde ein weiterer Fokus auf den Aktivierungs- und Deaktivierungsschritt gelegt. Hierbei wurden vor allem Mehrphotonen-Prozesse

## *Zusammenfassung*

betrachtet, die entweder durch simultane Absorption zweier Photonen zu einer spezifischen hoch-energetischen Anregung führen, oder durch sequentielle Absorption eine sukzessive Aktivierung und Deaktivierung eines Systems bewerkstelligen können.

Die in dieser Arbeit gesetzten Fragestellungen wurden im Rahmen der DFG finanzierten Graduiertenschule CLiC bearbeitet. Die Optimierung verschiedener PPGs wurde in enger Kollaboration mit dem Arbeitskreis von Prof. Dr. Alexander Heckel (Design und Synthese, Goethe Universität) und dem Arbeitskreis von Prof. Dr. Irene Burghardt (Computergestützte Photochemie, Goethe Universität) betrieben. Die Untersuchung mikrobieller Rhodopsine - hier KR2 - fußt auf einer lang anhaltenden Kollaboration mit dem Arbeitskreis von Prof. Dr. Clemens Glaubitz (NMR-Spektroskopie, Proteinbiochemie, Goethe Universität), der Nachwuchsgruppe von Prof. Dr. Igor Schapiro (Computergestützte Photochemie, Hebrew University of Jerusalem) und der Emeritus-Gruppe von Prof. Dr. Ernst Bamberg (Elektrophysiologie, MPI für Biophysik).

Der Wildtyp der Natriumpumpe KR2 ist nachgewiesenermaßen je nach Proteinumgebung in der Lage monovalente Kationen wie zum Beispiel Natriumionen, Lithiumionen oder Protonen vom intrazellulären in den extrazellulären Raum zu transportieren. Durch gezielte Mutationen einzelner Aminosäuren konnte KR2 sogar zu einer Kalium- oder Caesiumpumpe umfunktioniert werden. Diese Vielschichtigkeit und das Potenzial zur Anwendung als neuronales Werkzeug weckte großes Interesse im Bereich der Optogenetik. Bis zur Entdeckung von KR2 wurde die Existenz einer Kationenpumpe, mit Ausnahme der Protonenpumpe, aufgrund der elektrostatischen Umgebung im Inneren der mikrobiellen Rhodopsine nahezu ausgeschlossen. Hierbei stellen sich nun erneut Fragen bezüglich des Zusammenhangs zwischen der Struktur, der Funktion und den jeweiligen Pumpmechanismen. Die grundlegenden Unterschiede zwischen denen im Wildtyp gängigen (Natrium- oder Protonen-) Pumpmechanismen wurden mittels zeitaufgelöster IR- und UV/vis-Spektroskopie untersucht. Bei der Probenpräparation wurde darauf geachtet, dass eine kompetitive Kinetik zwischen beiden Pumpmechanismen ausgeschlossen werden konnte. Bereits auf den ersten Blick lassen sich grundlegend unterschiedliche Photozyklen nachweisen. Wohingegen die Photointermediate der Natriumpumpe nahezu sequentiell durchlaufen werden, zeichnen sich bei der Protonenpumpe mehrere kinetische Gleichgewichte ab. Diese Gleichgewichte äußern sich vor allem in den Ethenmoden des Chromophors, die im direkten Vergleich zu den korrespondierenden Absorptionsänderungen im UV/vis Bereich eine verlangsamte Relaxationskinetik aufweisen. Insbesondere im Bezug auf den Natriumtransport konnten, durch Zuweisung charakteristischer IR-Banden, wichtige funktionelle Gruppen wie die Aminosäure N112 oder die ECL1-Domäne identifiziert werden. Erstere ist - je nach Strukturreferenz - zu-



sammen mit S70 oder D251 direkt an der transienten Koordination des Natriumions während des O-Intermediates beteiligt. Der ECL1-Domäne hingegen wurde bis dahin lediglich eine stabilisierende Wirkung der Proteinstruktur, nicht jedoch ein direktes Einwirken in den Natriumtransport zugeschrieben.

Einen tieferen Einblick in die strukturellen Änderungen des Retinals und dessen Umgebung während der einzelnen Photointermediate ergaben Untersuchungen mittels NMR und optischer Spektroskopie, die zusammen mit dem Arbeitskreis Glaubitz durchgeführt wurden. Hier konnte aufgezeigt werden, dass der Chromophor im Vergleich zu anderen mikrobiellen Rhodopsinen in nahezu allen Phasen des Photozyklus stark verdrillt vorliegt. Dies resultiert vor allem aus der ausgeprägten Interaktion mit dem Gegenion D116, das eine direkte Wasserstoffbrücke mit der Schiff'schen Base des Retinals ausbildet. Darüber hinaus liefern diese Studien einen klaren Hinweis, dass im charakteristischen O-Intermediat das Retinal tatsächlich in der *all-trans* Konfiguration vorliegt. Dies konnte mit zeitaufgelösten Messungen im nahen UV-Bereich erhärtet werden. Die hierbei neu entdeckte Signatur erstreckt sich von wenigen hundert Femtosekunden bis hin zu einigen Millisekunden ohne dabei signifikante spektrale Änderungen zu durchlaufen. Diese Beobachtung ist vor allem vor dem Hintergrund der Photozyklusdynamik interessant, die für gewöhnlich durch starke spektrale Verschiebungen im UV/vis-Bereich geprägt ist. Einen tieferen Einblick in die Energetik des Chromophors konnte durch im Arbeitskreis Schapiro durchgeführte QM/MM-Rechnungen der K-, M- und O-Intermediate von KR2 gewonnen werden. Die ausbleibende spektrale Verschiebung im nahen UV-Bereich lässt sich mit sogenannten Übergangselektronendichten beschreiben, die hier eher auf eine Änderung des Bindungscharakters entlang des Retinalrückgrats hinweisen und größtenteils die Umgebung der Schiff'schen Base unbeeinflusst lässt. Dementsprechend sorgen elektrostatische Änderungen in der unmittelbaren Retinalumgebung, zum Beispiel induziert durch Wechselwirkungen mit dem Gegenion, für keine signifikante Anpassung der Übergangsenergie. Interessanterweise verschwindet die Oszillatorstärke dieses Übergangs für diejenige Struktur des O-Intermediats, welche ein *all-trans* Retinal enthält. Infolgedessen konnte die Signatur im nahen UV-Bereich als SBS (engl. *second bright state*) des 13-*cis* Retinals identifiziert werden.

In Anlehnung an die sogenannte Blaulicht-induzierte Deaktivierung (engl. *blue-light quenching effect*), wurde eine analoge Nutzbarkeit der SBS-Bande für die Deaktivierung des Photozyklus untersucht. Hierfür wurde KR2 aus einem photostationären Zustand mittels fs-Pulsen im nahen UV bestrahlt. Tatsächlich konnte hier eine Deaktivierungsdynamik festgestellt werden, die zu einer Regeneration des Dunkelzustandsspektrums

## Zusammenfassung

führt. Der zeitliche Verlauf der Deaktivierung ist dabei abhängig vom deaktivierten Intermediat, das je nach eingestellter Probenbedingung bevorzugt im photostationären Zustand akkumuliert wird. Obwohl - ausgehend vom M-Intermediat - sowohl ein Protonierungs- als auch ein Isomerisierungsschritt vollzogen werden muss, ist die Ausbildung des Dunkelzustandspektrums um mehr als eine Größenordnung schneller als bei der Deaktivierung des K-Intermediates. Dies kann zum einen an der stark ausgeprägten Wechselwirkung zwischen Gegenion und Schiffbase liegen, die eine schnelle Reprotonierung erleichtert, zum anderen aber auch an der starken Verdrillung des Retinals im K-Intermediat, welche eine Regenerierung der Dunkelzustandskonfiguration erschwert. Die hierbei aufgezeigten Ergebnisse bieten nicht nur interessante Ausgangspunkte für weitere mechanistische Untersuchungen dieser Deaktivierungsdynamik, sondern auch methodisch eine Perspektive für die Anwendung von Pulssequenzen für die gezielte Aktivierung und Deaktivierung der Pumpfunktion.

Die Untersuchungen an PPGs orientierten sich an den zwei wichtigsten Kenngrößen für die photoinduzierte Abspaltung: Der Fähigkeit der PPG Photonen einer bestimmten Wellenlänge zu absorbieren und der Effizienz der daraus resultierenden photochemischen Antwort. Im Hinblick auf den letzteren Aspekt wurde vor allem ein Augenmerk auf die kompetitiven Deaktivierungsprozesse gelegt. Hierbei wurde zugrunde gelegt, dass eine Reduzierung eben dieser Prozesse zu einer Steigerung der Abspaltungsausbeute führen müsste. Diese Hypothese wurde durch systematische Modifikationen an DEACM (engl. *(7-diethylaminocoumarin-4-yl)methyl*)-basierenden Modellsystemen und deren Auswirkung auf den angeregten Zustand derselbigen untersucht. Analoge Überlegungen gab es bereits im Bezug auf das Design fluoreszierender Moleküle, deren Fluoreszenzquantenausbeute durch gezielte Inaktivierung nicht-strahlender Deaktivierungspfade optimiert werden konnten. Ähnlicherweise wurde hier durch eine Fixierung der Aminogruppe mittels Zyklisierung, die Quantenausbeute der Abspaltung um das zwei- bis dreifache im Vergleich zur DEACM-Schutzgruppe erhöht. Eine weitere signifikante Verbesserung wurde durch zusätzliche Planarisierung der Struktur erreicht. Einen tieferen Einblick in die Dynamik des angeregten Zustands konnte durch zeitaufgelöste fs-Spektroskopie gewonnen werden. Die Anregung von Coumarin-basierenden Molekülen führt zu einem Gleichgewicht zwischen einem lokalen angeregten Zustand und einem Ladungstransferzustand. Letzterer ist ausschlaggebend für den Reaktionsweg, der zur Abspaltung der Abgangsgruppe führt, da - wie für Schutzgruppen üblich - hierfür eine Abschwächung der zu spaltenden C-C-Bindung nötig ist. Die Ladungsverschiebung selbst wird durch die unmittelbare Umgebung des Moleküls entweder stabilisiert oder destabilisiert. Hierbei spielen vor allem die Protizität und die Polarität des eingesetzten

Lösemittels eine Rolle. Diese Effekte wurden ebenfalls systematisch untersucht und eingeordnet. Mit der Inaktivierung nicht-strahlender Deaktivierungspfade, resultierend aus der strukturellen Optimierung, ging zwangsläufig auch eine signifikante Verbesserung der Fluoreszenzeigenschaften aller Modellsysteme einher. Fluoreszenz ist jedoch ein weiterer Prozess, der mit der photo-induzierten Abspaltung konkurriert. Interessanterweise zeigten alle untersuchten Verbindungen, die eine Abgangsgruppe enthalten und demnach effektiv als PPG fungieren, eine deutlich reduzierte Lebenszeit des angeregten Zustands auf. Einerseits lässt sich daraus schließen, dass ein signifikanter Anteil der Deaktivierung durch die tatsächliche photochemische Reaktion bedingt wird. Andererseits eröffnet sich hier auch die Möglichkeit für die optische Identifizierung von Edukt und Produkt zum Beispiel mittels Fluoreszenzlebensdauer-Mikroskopie. Konzeptionell hat die Refunktionalisierung von Fluorophoren hin zu PPGs auch den Vorteil, dass zusätzlich zur großen Vielfalt an dafür geeigneten Molekülklassen auch die Kosten und der Aufwand für die Synthese reduziert werden können.

Die große Bandbreite an Anwendungen von PPGs bedingt auch eine ebenso große Bandbreite an dafür geeigneten Verbindungen. Die Verwendbarkeit einer solchen Schutzgruppe ist jedoch oftmals auf nur einen relativ schmalen Bereich des sichtbaren Spektrums limitiert. Dementsprechend werden PPGs in den meisten Fällen auf das jeweilige Einsatzgebiet optimiert. Ein Ziel dieser Arbeit war demzufolge die spektrale Flexibilisierung solcher Schutzgruppen, die durch das Anbringen sekundärer Photonenantennen bewerkstelligt werden sollte. Als Modellsystem diente hierbei BODIPY (engl. *Boron-dipyromethene*) als Grundgerüst für die PPG und ein Rhodamin als Antenne. Letztere Molekülklasse zeichnet sich vor allem durch überdurchschnittlich hohe 2PA-Einfangsquerschnitte und einen langlebigen angeregten Zustand aus. Nach Anregung des Rhodamins wird die Energie in einem Zeitfenster von wenigen hundert Femtosekunden effizient an das BODIPY abgegeben und lokal eine photochemische Antwort hervorgerufen. Eine identische lichtinduzierte Dynamik ließ sich durch die direkte Bestrahlung von BODIPY feststellen. Die Dynamik dieses Prozesses wurde zum einen mittels zeitaufgelöster Spektroskopie nachvollzogen, und zum Anderen mit computer-gestützten Rechnungen untermauert. Insgesamt ist das Grundgerüst, bestehend aus BODIPY und Rhodamin, in der Lage einen großen Teil des sichtbaren Spektrums (500-680 nm) abzudecken. Unter Berücksichtigung der 2PA von Rhodamin kann dieser Bereich sogar in das Nahinfrarote erweitert werden, wodurch der Großteil des phototherapeutischen Fensters zugänglich gemacht wird. Im letzten Schritt wurde die photoinduzierte Abspaltung untersucht. Hierfür wurde PNA (engl. *p*-nitroaniline) als Abgangsgruppe gewählt. Die Abspaltung von PNA konnte zwar spektroskopisch nachvollzogen wer-

## *Zusammenfassung*

den, jedoch erwies sich eine quantitative Aussage über die Reaktionseffizienz aufgrund vieler überlappender Signaturen als schwierig. Dementsprechend sind hier noch weitere Optimierungsschritte nötig, die vor allem auf die Reaktionsausbeute selbst aber auch auf mögliche Strategien für eine vereinfachte Nachverfolgung der Reaktion abzielen. Die hierbei gefundenen strukturellen und spektroskopischen Kenngrößen, die vor allem einen effizienten Energietransfer garantieren, liefern hierfür einen vielversprechenden Ausgangspunkt.

# Contents

Zusammenfassung	iii
1 Introduction	1
2 Theoretical and Experimental Framework	5
2.1 Fundamentals of Optical Spectroscopy	5
2.1.1 Light and the Electromagnetic Spectrum	5
2.1.2 Interactions of Light with Matter	6
2.1.3 Molecular Relaxation Processes	11
2.1.4 Non-linear Optics	12
2.2 Experimental Techniques	16
2.2.1 Pump-probe Spectroscopy	16
2.2.2 Flash Photolysis	18
2.2.3 Ultrafast Transient Absorption Spectroscopy	22
2.2.4 Time-correlated Single Photon Counting	24
2.2.5 Two-photon Induced Fluorescence	25
2.2.6 Data Evaluation	27
2.3 Microbial Rhodopsins	29
2.3.1 Structural and Functional Features	30
2.3.2 The Primary Reaction	32
2.3.3 The Photocycle	34
2.4 Photolabile Protecting Groups	35
2.4.1 Coumarin-based PPGs	37
2.4.2 BODIPY-based PPGs	40
3 Aims and Scope	43
4 Research Projects	45
4.1 <i>Krokinobacter Eikastus</i> Rhodopsin 2	45
4.1.1 Introduction	45
4.1.2 A Closer Look into the Photocycle Mechanism	47
4.1.3 Expanding the View into the near-UV	53

## Contents

4.1.4	Implications for Optogenetic Applicability . . . . .	57
4.2	Optimization of Coumarin Photochemistry . . . . .	59
4.2.1	Introduction . . . . .	59
4.2.2	Photochemistry . . . . .	60
4.2.3	Generalized Model . . . . .	63
4.3	One- and Two-photon Sensitization of BODIPY-based PPGs . . . . .	64
4.3.1	Introduction . . . . .	64
4.3.2	Finding the right Antenna . . . . .	66
4.3.3	The Energy Transfer Process . . . . .	68
4.3.4	Applicability as PPG . . . . .	70
5	Concluding Remarks . . . . .	73
6	Publications . . . . .	77
6.1	Declaration of Author Contributions . . . . .	77
6.2	Klimek <i>et al.</i> , Chem. Eur. J., 2022 . . . . .	80
6.3	Asido <i>et al.</i> , Phys. Chem. Chem. Phys., 2022 . . . . .	89
6.4	Asido <i>et al.</i> , J. Phys. Chem. Lett., 2021 . . . . .	98
6.5	Asido <i>et al.</i> , Phys. Chem. Chem. Phys., 2019 . . . . .	107
6.6	Jakdetchai <i>et al.</i> , Sci. Adv., 2021 . . . . .	119
6.7	Krüger <i>et al.</i> , Comm. Mat., 2022 . . . . .	134
	Glossary of Terms and Abbreviations . . . . .	147
	List of Figures . . . . .	151
	List of Tables . . . . .	155
	Bibliography . . . . .	157
	Acknowledgements . . . . .	171
	Appendix . . . . .	174

# Introduction

By far one of the oldest but still not fully resolved scientific questions deals with the origin of life. Even though there have been many breakthroughs in coming closer to an answer, some aspects still remain vividly debated. In the current scientific community, however, it is widely accepted that life evolved around the formation of ribonucleic acid (RNA).<sup>[1-3]</sup> This *RNA world hypothesis* was first proposed by Alexander Rich in 1962<sup>[4]</sup> and the actual term was later coined by Walter Gilbert in 1986.<sup>[5]</sup> With the RNA in its different forms, the first basic processes like reproduction and chemical catalysis were introduced, which ultimately lead to the rise of the first single-cell organisms similar to the ones we know of today.<sup>[6]</sup>

During the first two billion years of biological evolution, the procaryotic organisms have developed the most fundamental biochemical processes for all life on earth. One of these processes is called photosynthesis,<sup>[7]</sup> which harnesses light from the sun to convert it into chemical energy. In the first stages of evolution, the photosynthetic reaction was reliant on H and H<sub>2</sub>S as electron and proton donors.<sup>[8]</sup> The most commonly known oxigenic photosynthesis, however, was developed later with the occurrence of cyanobacteria.<sup>[9]</sup> Almost all organic material on earth, and as a consequence also the major composition of the atmosphere, is the product of this natural process.

Fast forward to today, the vast majority of the visible world is now dominated by more complex multi-cellular organisms like plants and animals. Yet, an incredible amount of biochemical throughput in an ecosystem still comes from procaryotic or single-cell eukaryotic systems like algae or some fungi.<sup>[10]</sup> In the context of photosynthesis in plants or light-reception in animals, the evolutionary pathway originating from single-cell organisms is evident. Chloroplasts, which are colloquially called the powerhouse in plant cells, are considered to be the result of cyanobacterial endosymbiosis.<sup>[11,12]</sup> Vision in animals, for instance, is strongly reliant on (G-protein coupled) rhodopsins which are evolutionary related to rhodopsins found in microbial systems.<sup>[13]</sup>

With the revolutionary developments in physics from the theory of electrodynamics, to the theory of light up to the theory of quantum mechanics, many new scientific fields

## Chapter 1 Introduction

- most noteworthy the molecular sciences - have emerged over the years. This also led to a growing interdisciplinarity which blurred the boundaries between the domains of biology, chemistry and physics. In the same manner, this also drove technological advances like lasers and high-resolution microscopes which made the direct observation of structures and dynamics on the atomic scale possible. Ever since, our understanding of life and its underlying molecular mechanisms has risen tremendously.

In the context of life sciences, the regulation of biochemical processes is one of the key questions of fundamental and medical significance. On the one hand, such processes are at the heart of the basic principles of life on the molecular level, but even more importantly our understanding of the same is crucial to identify and treat malfunctions which lead to diseases. Conventionally, a treatment involves the supplementation of drugs, which directly interfere with a specific biochemical process. In many cases, however, critical malfunctions are just localized on smaller parts of the organism. Here it is desirable to find ways which allow a spatial and also temporal control of the treatment to minimize additional harm to the overall organism.

The concept of optical control has become one of the fastest growing drivers in the (bio-)molecular sciences of recent years.<sup>[14]</sup> By utilizing the properties of UV/vis and IR lasers, it is possible to achieve relatively high tissue penetration depths, localized irradiation in small volumes and variable irradiation durations. The development of photopharmacological strategies addresses the previously mentioned challenges by making drugs optically activatable. Common strategies involve the implementation of a photolabile protecting group (PPG), which irreversibly releases the biologically relevant compound after irradiation with light, or the implementation of a photoswitch to reversibly switch the activity of a drug “on” and “off”. Besides the evaluation of the complex biochemical functionality, a major effort in this field of research goes into the molecular design and the photochemical characterization and optimization of prospective systems.

A different approach is chosen in the relatively new field of optogenetics,<sup>[15-17]</sup> which focuses on the implementation of wildtype or modified photoreceptors (i.e. rhodopsins) into a non-native organism to manipulate cell activity. This methodology is different to photopharmacology, due to the inherent use of genetically encoded (and photosensitive) proteins which are directly expressed in the cells of interest allowing a very specific targeting of individual cells or cell compartments. For instance in neurons this is extensively done via microbial rhodopsins (mRhos) which enable the direct manipulation of the electrochemical potential across the cell membrane. In the earlier stages, this research mainly aimed at the controlled activation or deactivation of such neuronal



activity in order to map the overall neuronal circuitry and ultimately brain function. In the recent years, however, the focus started to shift towards the development of medical applications which might help to treat diseases by regenerating muscular or neuronal functionality.

In the course of this work, various aspects of photocontrol have been studied. This was done on the systemic level by taking a closer look into the photodynamics and photochemical properties of mRhos and PPGs. From a more methodological perspective, the possibilities for the activation or deactivation of such molecular systems - including multiphoton processes - were explored. In the first part of this dissertation, the theoretical framework of the experimental methodology and the investigated systems will be introduced. This is followed by the discussion of the individual research projects. The corresponding publications and an overview of the respective author contributions are found in the appendix.



# Theoretical and Experimental Framework

## 2.1 Fundamentals of Optical Spectroscopy

### 2.1.1 Light and the Electromagnetic Spectrum

The nature of light and its interactions with any form of matter has been a major field of interest for many generations of researchers. In the common language light is often referred to the visible portion of the electromagnetic (EM) spectrum, whereas in physical sciences it is synonymously used with any sort of EM radiation. In fact, the visible part - defined by the perception of the human eye - spans just a very small range of the overall EM spectrum (Fig. 2.1). In general, any electromagnetic wave (EMW) carries a certain amount of energy  $E$  and momentum  $p$  which are characterized by the wavelength  $\lambda$  or the frequency  $\nu$  of the oscillation

$$E = h\nu = \frac{hc}{\lambda} \quad (2.1)$$

$$p = \frac{h\nu}{c} = \frac{h}{\lambda} \quad (2.2)$$

The quantities defined above are connected by the speed of light  $c$  and the Planck constant  $h$  which are direct results of the Maxwell equations and quantum mechanical considerations. The rise of quantum mechanics in the early 20th century along with its concept of wave-particle duality did not just mean a complete paradigm shift in the domain of physics but it also resulted in the emergence of molecular sciences and their neighboring disciplines. The quantum nature of atoms and molecules manifests itself in the quantization of their intrinsic properties such as the electronic configuration or the vibrational and rotational states. The development of sophisticated spectroscopical methods was therefore a necessary means to investigate such quantum systems in more

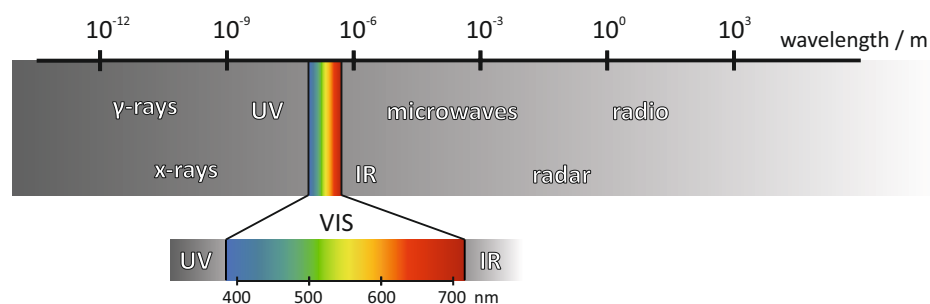


FIGURE 2.1: The electromagnetic spectrum and a zoom-in of the UV/vis part.

detail. Prominent examples are nuclear magnetic resonance (NMR), electron paramagnetic resonance (EPR) and optical spectroscopy. Even though there is a large variety of different techniques, the underlying principle - the interrogation of a system by EM radiation - remains the same. If one is also interested in the molecular dynamics of a system, several aspects have to be considered:

1. The type of molecular transition
2. The corresponding transition energies  $\Delta E$
3. The timescale of the transitions

Here it is important to understand that the temporal and the spectral resolution of a spectroscopic technique is inherently limited by the applied EM radiation due to the time-bandwidth product

$$\langle \tau \rangle \cdot \langle \nu \rangle \geq \text{constant} \quad (2.3)$$

with the uncertainties (or spread) of time  $\langle \tau \rangle$  and frequency  $\langle \nu \rangle$ . Further details on this relationship and their implications on time-resolved spectroscopy will be introduced in later sections.

### 2.1.2 Interactions of Light with Matter

When light hits a material there are several physical phenomena which can occur with the most prominent ones being diffraction, scattering and absorption. These effects are strongly dependent on the properties of the incident light and the molecular and structural composition of the material. Even though diffraction is at the heart of most

## 2.1 Fundamentals of Optical Spectroscopy

crystallographic techniques as well as many optical components used in modern spectroscopies, it is of lower importance on the atomistic or molecular level. Scattering and absorption effects on the other hand make up the majority of resonance or off-resonance molecular spectroscopy methodologies and shall therefore be introduced in more detail.

### Scattering

Light scattering usually leads to a change of trajectory with respect to the direction of incidence. The strength of this effect is mainly determined by the ratio of the wavelength  $\lambda$  to the size of the scattering centre  $D_p$ , following the relationship

$$\alpha = \frac{\pi D_p}{\lambda} \quad (2.4)$$

with the values  $\alpha \ll 1$  corresponding to Rayleigh scattering,<sup>[18]</sup>  $\alpha \approx 1$  to Mie scattering<sup>[19]</sup> and  $\alpha \gg 1$  to macroscopic (or geometric) scattering. Besides the change of direction of scattered light, and hence its momentum, the energy remains unchanged. In such a case the scattering process is referred to as elastic. The more complex, and spectroscopically more relevant case, occurs when in addition to the change of momentum a part of the photon energy is transferred to the molecule. This inelastic form of scattering is referred to as Raman effect<sup>[20]</sup> and it is the basis for all Raman spectroscopies. Here, one distinguishes between Stokes and anti-Stokes scattering, which corresponds to either a red- or blue-shift of the scattered light. The energetic difference comes from the population or depopulation of specific vibrational modes in the molecule. Such Raman-active modes require a change of polarizability with respect to the normal coordinate of the vibration.

### Absorption

The absorption of light by a molecule can be understood as the conversion of photon energy into molecular motion. For such a process to occur, several conditions have to be met which are determined by molecular symmetry and quantum mechanical considerations. The basic description of a molecule is given by the molecular orbital (MO) theory,<sup>[21,22]</sup> which defines the wavefunction  $\Psi_j$  of a MO as a  $c_{ij}$  weighted sum of its constituting atomic orbitals (AOs)  $\phi_i$

$$\Psi_j = \sum_{i=1}^n c_{ij} \phi_i \quad (2.5)$$

## Chapter 2 Theoretical and Experimental Framework

This linear combination of atomic orbitals (LCAO)<sup>[23]</sup> yields different kinds of MOs, such as bonding ( $\sigma$ ,  $\pi$ ), non-bonding (n) and anti-bonding ( $\sigma^*$ ,  $\pi^*$ ) depending on the symmetry and the spatial distribution of the electron densities of the AOs. The potential surface of an electronic state is given by the anharmonic Morse potential of the form

$$V(r) = D_e \left(1 - e^{-a(r-r_e)}\right)^2 \quad (2.6)$$

with the dissociation energy  $D_e$ , the equilibrium distance  $r_e$  and the anharmonicity constant  $a$ . The corresponding vibrational states  $E_v$  are then obtained by solving the Schrödinger equation

$$\left(-\frac{\hbar^2}{2m} \frac{\partial^2}{\partial r^2} + V(r)\right) \Psi(v) = E_v \Psi(v) \quad (2.7)$$

For a quantum mechanical treatment of photoabsorption, several aspects have to be considered. First, the absorbed photon has to match the energetic difference of the initial and final state (Bohr resonance condition). The rate of such a transition is derived from perturbation theory and results in the so-called first-order Fermi-Wentzel *golden rule*<sup>[24]</sup>

$$R_{i,f} = 2\pi g(\omega_{i,f}) |\alpha_{i,f}|^2 \quad (2.8)$$

Here, the transition rate is expressed as the product of the acting light source function  $g(\omega)$  at the transition frequency  $\omega_{i,f}$  and the square of the transition matrix element between the initial and the final state. By considering the actual wavefunctions of these states one can rewrite equation 2.8

$$R_{i,f} = \left(\frac{2\pi}{\hbar^2}\right) g(\omega_{i,f}) |\vec{E}_0 \cdot \langle \Psi_f | \hat{\mu} | \Psi_i \rangle|^2 \quad (2.9)$$

The introduced quantity  $\hat{\mu}$  is the dipole moment operator, which is given in the form

$$\hat{\mu} = \sum_n e r_n - \sum_m e Z_m r_m \quad (2.10)$$

with  $r_n$  and  $r_m$  being the coordinates of the electrons and the positive charges in the nuclei, respectively. The wavefunctions  $\Psi$  can be separated into their electronic, vibrational and spin contributions according to the Born-Oppenheimer (BO) approximation<sup>[25]</sup>

$$\Psi = \psi_e \chi_v \sigma_s \quad (2.11)$$

By considering a vibronic transition, thus a transition involving the change of the

## 2.1 Fundamentals of Optical Spectroscopy

electronic as well as the vibrational state, one can write the transition dipole moment

$$\vec{M}_{i,0 \rightarrow f,\nu} = \langle \psi_f \chi_\nu | \hat{\mu} | \psi_i \chi_0 \rangle \langle \sigma_f | \sigma_i \rangle \quad (2.12)$$

Due to the orthonormality of the spin wavefunctions, the first selection rule for a vibronic transition is obtained. The transition dipole moment is just non-zero if the multiplicity stays the same. Transitions which involve a change of multiplicity, e.g. singlet to triplet or vice versa, are forbidden in the framework of this approximation. The remaining integrals given in 2.12 can be reduced by separating the electron and nuclei contributions of the dipole moment operator

$$\vec{M}_{i,0 \rightarrow f,\nu} = e \langle \psi_f | \sum_n r_n | \psi_i \rangle \langle \chi_\nu | \chi_0 \rangle = \vec{M}_{e,i \rightarrow f} \langle \chi_\nu | \chi_0 \rangle \quad (2.13)$$

The expression  $\langle \chi_\nu | \chi_0 \rangle$  is the so-called Franck-Condon (FC) integral<sup>[26,27]</sup> (or FC factor in its squared form), which denotes the overlap of the vibrational wavefunctions in the initial and final electronic state. The sum of these vibronic transitions constitute an absorption band and are expressed as follows

$$\vec{M}_{i \rightarrow f} = \vec{M}_{e,i \rightarrow f} \sum_{\nu'} \langle \chi_\nu | \chi_0 \rangle \quad (2.14)$$

Here it is assumed that higher vibrational energy levels ( $\nu \geq 1$ ) in the initial electronic state are not significantly populated. The overall strength of such an absorption band is usually given by the oscillator strength  $f_{if}$ , which is proportional to the square of the transition dipole moment

$$f_{if} \propto |\vec{M}_{i \rightarrow f}|^2 \quad (2.15)$$

A similar analysis can be done for transitions which do not involve a change of the electronic state. Such vibrational transitions are the domain of infrared spectroscopy. In solution, the contributions of the rotational transitions are usually negligible, so that one can define the vibrational transition dipole moment

$$\vec{M}_{v,i \rightarrow f} = \langle \chi_f | \hat{\mu}_v | \chi_i \rangle \quad (2.16)$$

with the corresponding vibrational dipole moment operator  $\hat{\mu}_v$ , which can be approximated in a Taylor series expansion about the equilibrium bond length position

$$\hat{\mu}_v = \hat{\mu}_v(\vec{r}) = \mu(\vec{r}_e) + \sum_a \frac{\partial \mu}{\partial r_a} (r_a - r_e) + \dots \quad (2.17)$$

For small deviations from the equilibrium position  $r_e$  the higher order terms can be neglected, so that substitution of 2.17 into the integral given in 2.16 then yields

$$\vec{M}_{v,i \rightarrow f} = \langle \chi_f | \hat{\mu}_v | \chi_i \rangle = \mu(\vec{r}_e) \langle \chi_f | \chi_i \rangle + \sum_a \frac{\partial \mu}{\partial r_a} \langle \chi_f | (r_a - r_e) | \chi_i \rangle \quad (2.18)$$

The first term in 2.18 vanishes due to orthogonality of the vibrational wavefunctions, which indicates that a permanent dipole moment has no relevance for such a transition. In fact, for the overall  $\vec{M}_{v,i \rightarrow f}$  to be non-zero, a vibrational transition requires  $\mu$  to vary along the vibration of the specific mode. Such modes are also referred to as infrared (IR) active.

### The Beer-Lambert Law

In molecular absorption spectroscopy the sample is interrogated by application of EM radiation. The amount of residual light which is collected in the spectrometer then yields information about the sample composition. Even though the spectral domain of these techniques can vary from low-energetic radiowaves up to high-energetic X-rays, the underlying principles remain similar. Due to fundamental, as well as methodological limitations, absorption spectroscopy usually relies on the measurement of molecular ensembles. In practice, the absorbance  $A_i$  of a species is usually determined by the so-called Beer-Lambert law<sup>[28,29]</sup>

$$A_i = \epsilon_i(\nu) c_i d \quad (2.19)$$

with the molar extinction coefficient  $\epsilon_i(\nu)$  of a transition, the concentration  $c_i$  of the corresponding molecule and the thickness  $d$  of the sample at question. Whereas  $c_i$  and  $d$  can be adjusted by the experimantator, the intrinsic molecular information of an absorption band is contained in  $\epsilon_i(\nu)$ . By integrating the extinction coefficient over the spectral width of the absorption band, one can obtain the oscillator strength  $f$  given in the following relationship

$$f_i = \frac{4m_e c^2 \epsilon_0}{N_A e^2} \ln 10 \int_{\nu_1}^{\nu_2} \epsilon_i(\nu') d\nu' \quad (2.20)$$

It is important to be aware that 2.19 and 2.20 are just valid if molecules in a sample do not interfere with each other. Effects outside of this linear regime, such as strong



solvation effects, stacking or dimerization might lead to distortions of the absorption band, which complicates the spectral analysis.

### 2.1.3 Molecular Relaxation Processes

The absorption of a photon leads to the population of higher energetic states. In the domain of UV/vis spectroscopy, the photon energies correspond to vibronic transitions which are discussed in 2.1.2. The timescale of such a transition is determined - in simple terms - by the interaction time of the photon with the molecule and is on the order of a fraction of a femtosecond. The release of this excess energy is significantly slower and can range from hundreds of fs up to s and the corresponding decay pathways are usually summarized in a Jablonski diagram (Fig. 2.2).<sup>[30]</sup> One generally distinguishes between radiative, i.e. transitions which involve the emission of a photon, and nonradiative decays.

A vibronic transition from the electronic ground state (GS)  $S_0$  to the excited state (ES)  $S_N$  usually involves the population of vibrational modes  $v_n$  in that ES. The initial decay of these vibrational modes right after photoexcitation is often referred to as FC relaxation which occurs on the order of up to several hundred fs. If the excitation involves higher electronic states ( $N > 1$ ), then the system has to undergo further relaxation processes up to the point where the lowest electronic state is reached. This includes vibrational relaxation (VR) processes, which are the result of interactions between the excited molecule and its surrounding medium. The transition from a higher electronic state to a lower electronic state under conservation of multiplicity is called internal conversion (IC). Once the  $S_1$  state is populated, several processes can occur.

Firstly, the molecule can return into its GS by further collisions with its environment, leading to a full conversion of photonic energy into heat. Secondly, the electronic GS is repopulated by fluorescence under emission of a photon. And finally, the system can undergo a change of multiplicity leading to the population of a triplet state. Such intersystem crossings (ISCs) are generally forbidden by the selection rules. However, in a real molecule this is not strictly the case due to effects which are usually not considered in most approximate derivations. Such effects include spin-orbit couplings<sup>[31]</sup> which are prominent in molecules with heavy atoms. In the triplet state, the energy can be released by VR into the lowest excited triplet state configuration. From there the singlet GS can be repopulated either by another ISC or phosphorescence under the emission of a photon. Both radiative processes, namely fluorescence or phosphorescence, have to obey Kasha's rule<sup>[32]</sup> which is a direct result of the FC integrals for vibronic transitions from a higher

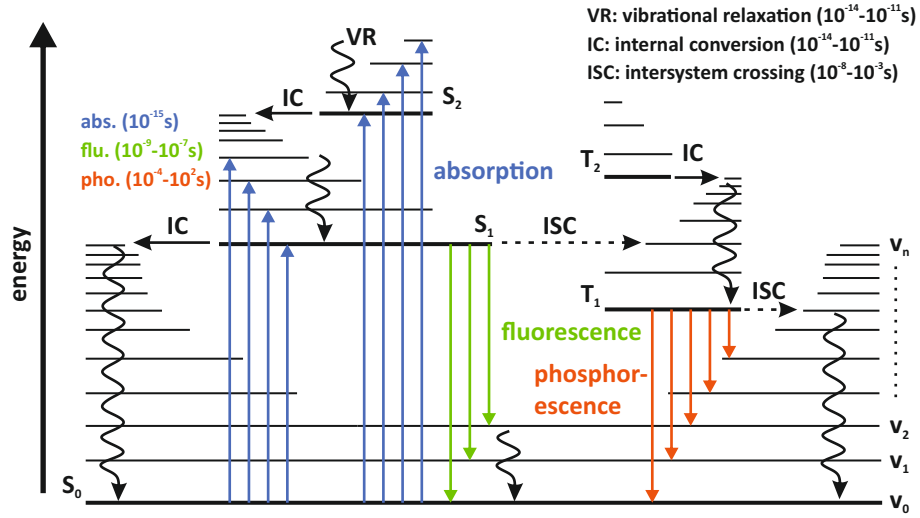


FIGURE 2.2: Jablonski diagram of the photochemical relaxation pathways. Processes involving absorption or emission of a photon are depicted in color. Non-radiative processes are depicted with black arrows: VR(curl), IC (solid) and ISC (dashed).

to a lower electronic state. It states that the probability for the emission of a photon from an ES is just significantly high, if the electron populates the lowest possible vibronic state of given multiplicity. The rates for such photochemical processes of molecules in solution usually follow a first-order law

$$N_{M,exc}(t) = N_{M,exc}(t=0)e^{-(\sum_i k_i)t} \quad (2.21)$$

with the population  $N_{M,exc}(t)$  of the molecule in the excited state, the starting excited state population and the rate constants  $k_i$  corresponding to the respective decay processes.

#### 2.1.4 Non-linear Optics

The temporal and spatial evolution of an electromagnetic wave is mathematically described by the Maxwell equations<sup>[33]</sup> and the thereby resulting linear and homogeneous wave equation of the form

$$\left(\nabla^2 - \frac{n^2}{c_0^2} \frac{\partial^2}{\partial t^2}\right)\psi(\vec{r}, t) = 0 \quad (2.22)$$

## 2.1 Fundamentals of Optical Spectroscopy

with the index of refraction  $n$  and the vacuum speed of light  $c_0$ . If an EMW travels through a medium, it induces an oscillatory response of bound charges in the material. Such oscillations, in turn, generate EMWs, which then propagate through the respective medium. This phenomenon can be expressed in terms of the electric displacement field  $\vec{D}$

$$\vec{D} = \epsilon_0 \vec{E} + \vec{P} \quad (2.23)$$

with  $\epsilon_0$  as the permittivity in free space,  $\vec{E}$  the electric field component of the initial EMW and the polarization  $\vec{P}$  which is induced by this electric field. The polarization is usually expressed in terms of a Taylor-series

$$\vec{P} = \epsilon_0 \sum_n \chi^n \vec{E}^n \quad (2.24)$$

$$\vec{P} = \epsilon_0 \cdot \left[ \chi^1 \vec{E}^1 + \chi^2 \vec{E}^2 + \chi^3 \vec{E}^3 + \dots \right] \quad (2.25)$$

where the tensor  $\chi^n$  is the  $n^{\text{th}}$ -order susceptibility of the medium. The high order terms in eq. 2.25 are responsible for a wide range of non-linear effects which are integral for advanced spectroscopic techniques. However, these effects only occur in the high intensity regime, which is commonly applied by short laser pulses. In order to demonstrate the aforementioned effects, one can consider a generalized EMW with two oscillating electric field components

$$\vec{E} = \vec{E}_1 + \vec{E}_2 \quad (2.26)$$

$$\vec{E} = \vec{E}_{01} \cdot \cos(\omega_1 t - \vec{k}_1 \vec{r}) + \vec{E}_{02} \cdot \cos(\omega_2 t - \vec{k}_2 \vec{r}) \quad (2.27)$$

with the respective frequencies  $\omega_{1,2}$  and wavevectors  $\vec{k}_{1,2}$ . After substitution of eq. 2.27 into the second order polarization term, one yields

$$\begin{aligned} \vec{P}^{(2)} = & \epsilon_0 \chi^{(2)} \vec{E}_{01}^2 \vec{E}_{02}^2 \\ & + \epsilon_0 \chi^{(2)} \left[ \vec{E}_{01}^2 \cos(2\omega_1 t - 2\vec{k}_1 \vec{r}) + \vec{E}_{02}^2 \cos(2\omega_2 t - 2\vec{k}_2 \vec{r}) \right] \\ & + \epsilon_0 \chi^{(2)} \left[ \vec{E}_{01} \vec{E}_{02} \cos((\omega_1 + \omega_2)t - (\vec{k}_1 + \vec{k}_2) \vec{r}) \right] \\ & + \epsilon_0 \chi^{(2)} \left[ \vec{E}_{01} \vec{E}_{02} \cos((\omega_1 - \omega_2)t - (\vec{k}_1 - \vec{k}_2) \vec{r}) \right] \end{aligned} \quad (2.28)$$

The cross-terms in equation 2.28 contain new frequencies as a result of frequency-mixing between the initially applied fields. The hereby introduced second harmonic generation (SHG), sum-frequency generation (SFG) and difference-frequency generation (DFG) are crucial processes for spectral tuning in time-resolved optical spectroscopies.

### Phase-matching

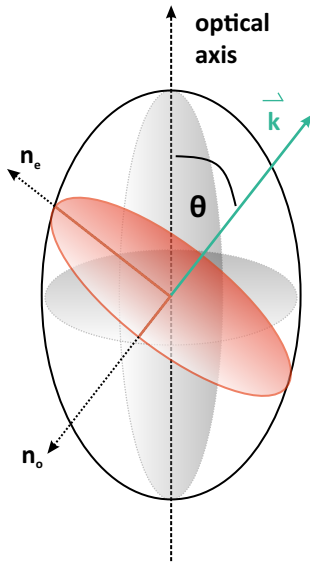


**FIGURE 2.3:** The index ellipsoid of a birefringent crystal. The relative orientation between the direction of incidence and the optical axis determine the elliptic surface of the  $n_e$  and  $n_o$  components.

For frequency-mixing processes to be efficient, the interacting pulses have to satisfy conservation of energy and momentum

$$\hbar\omega_3 = \hbar\omega_1 + \hbar\omega_2 + \Delta E \quad (2.29)$$

$$\vec{k}_3 = \vec{k}_1 + \vec{k}_2 + \Delta\vec{k} \quad (2.30)$$

Processes of this sort are also referred to as *parametric*. The energy loss  $\Delta E$  in eq. 2.29 is in general non-zero. Under the assumption that the complex amplitude of an EMW varies slowly compared to the periodic oscillations of the carrier wave, the wave equation 2.22 can be simplified to a first-order equation. This slowly varying envelope approximation (SVEA) results in  $\Delta E \rightarrow 0$ .<sup>[34]</sup> In practical terms, eq. 2.29 is simply met by choosing the right central frequencies  $\omega_1$  and  $\omega_2$  of the initial pulses to match the desired output frequency  $\omega_3$ .

The experimental challenge, however, lies in eq. 2.30. In an isotropic medium, dispersion leads to a phase mismatch  $\Delta\vec{k}$  between the respective pulses and consequently to destructive interference. This effect becomes significant at a material thickness which exceeds the coherence length of the generated pulse. To achieve phase matching, one needs to reside to anisotropic materials, such as birefringent crystals, which allow a precise tuning of the phase parameters. A uniaxial crystal is described by a main axis, which is referred to as extraordinary (e), and two ordinary (o) axes. A more rarely used biaxial crystal, in turn, consists of two e and one o axes. Once light enters such a material, its components will propagate along the e or o axis according to the polarization of their electric field. In

## 2.1 Fundamentals of Optical Spectroscopy

the case of a uniaxial crystal, the applied indices of refraction  $n_e$  and  $n_o$  are given by the index ellipsoid (Fig. 2.3) of the form

$$\frac{1}{n_e^2(\theta)} = \frac{\cos^2(\theta)}{n_o^2} + \frac{\sin^2(\theta)}{n_e^2} \quad (2.31)$$

with  $\theta$  being the angle between the optical axis of the crystal and  $\vec{k}$  of the incident beam. In the laboratory, the crystal has to be oriented in such a way, that the polarization of the interacting beams match the respective e or o axis. In the simple case of SHG one can find an optimal configuration which satisfies

$$n_o(\omega) = n_e(2\omega) \quad (2.32)$$

by additionally tilting the crystal, and therefore changing  $\theta$ . In time-resolved optical spectroscopy, one of the most commonly used materials is  $\beta$ -barium-borate (BBO) in its crystalline form, which is cut at appropriate angles for the specific phase matching range.

### Collinear Parametric Processes

In contrast to frequency-mixing, which combines two photons of low energy into one photon of higher energy, it is also possible to convert a high energy photon into two photons of lower energy. In laser spectroscopy, such a conversion process utilizes a high energy pump beam, which is then converted into lower energetic signal and idler beams. In principle, the amount of possible combinations for such signal and idler pairs is infinite. If the orientation of the non-linear crystal and the incident beams is appropriate, this continuum of generated frequencies, also called parametric fluorescence, can be seen behind the crystal. However, the resulting beams with frequency  $\omega_s$  and  $\omega_i$  are usually too weak and therefore require further amplification. Such optical parametric amplification (OPA) requires an input beam of frequency  $\omega_s$ , also referred to as seed, which is then amplified by the pump following the relationship

$$\omega_p = \omega_s + \omega_i \quad (2.33)$$

### Non-collinear Parametric Processes

Even though the utilization of non-linear crystals can compensate the mismatch of spectral phases, this is not the case for the group velocities of the individual pulses.

During OPA, pulses with different central frequencies  $\omega$  and temporal widths  $\Delta\tau$  are overlapped in the crystal. Dispersion inside the material leads to a group velocity mismatch (GVM) between the initially overlapped pulses which in turn causes the amplified signal to be temporally stretched. This becomes especially problematic in ultrafast applications, since short propagation distances already result in significant loss of temporal resolution. The established way to circumvent this issue is given by a non-collinear configuration of the incident beams. In such a non-collinear optical parametric amplification (NOPA), the angle between pump and seed pulses needs to be adjusted in such a way that the group velocity components of signal and idler are matched. This comes with the additional advantage that the resulting beams propagate at an angle, which simplifies the extraction of the signal beam in the optical setup. By making use of a spectrally broad supercontinuum (SC) as a seed pulse, the NOPA process enables spectral tuning of the generated signal pulse from the UV/vis up to the NIR.<sup>[35]</sup>

## 2.2 Experimental Techniques

As discussed in section 2.1.1 and 2.1.3, molecules can undergo complex dynamics on a timescale ranging from fs up to s.<sup>[36]</sup> Naturally, with increasing complexity of the molecule, the complexity of involved molecular processes increases as well. In terms of the actual experiment this requires a methodology, which does not just span the temporal range, but is also able to probe the relevant processes of the molecule at question. For optically active molecules, i.e. molecules which are able to absorb light, time-resolved optical spectroscopy is well suited. However, there is no spectroscopic technique which can probe the complete set of dynamics in a molecule simultaneously. Hence, in order to understand the photochemistry of a system, a large variety of methodology and instrumentation is necessary. In this section, a selection of spectroscopic techniques, which were integral to this work, will be introduced.

### 2.2.1 Pump-probe Spectroscopy

The most well established techniques in modern time-resolved optical spectroscopy are based on the pump-probe configuration. The basic principle of this method involves a laser source, which generates high intensity and temporally short pump pulses to initiate a photochemical reaction, and another light source which interrogates this process and serves as a probe.

## 2.2 Experimental Techniques

Here it is helpful to introduce the difference between continuous and stroboscopic probing (Fig. 2.4). The former one utilizes a continuous wave (cw) light source to constantly send light through the sample which is then collected by the detector. If the wavelength of the cw-beam corresponds to a transition in the molecule, it is possible to follow the dynamic changes of that specific transition. The information is then contained in the transient change of the difference absorption amplitudes. With the current state-of-the-art instrumentation it is possible to achieve temporal resolutions in the ns and ps timescale, with the bottleneck being the rise-time of the detection system. The spectral resolution on the other hand is determined by the spectral width  $\Delta\lambda$  of the probe light. A good resolution can be achieved by using quasi-monochromatic light, such as emitted by light-emitting diodes (LEDs), or by splitting white light into its spectral components prior to illumination of the sample.

The major disadvantage of cw-probing lies in the required time for data-acquisition. Complex dynamics, which usually stretch over a broad spectral range, make a recording of several dozens of transients at different probing wavelengths necessary. This problem is circumvented by broadband probing, which utilizes a spectral continuum in the form of a temporally short pulse. This technique is inherently stroboscopic, due to the delay between the pump and the probe pulses. The resulting data contains difference absorption spectra at specific delay times, which in sum can be used to reconstruct the transient dynamics of the system. In principle, the lower limit for the achievable temporal resolution is given by the temporal width  $\Delta\tau$  of the pump pulse. However, for experiments on the slower timescale it is mainly determined by the electronics, e.g. the flash lamp, the detection system and the synchronization of the individual components. Despite its simplicity, the actual implementation of the pump-probe technique in the laboratory setup can vary greatly depending on the temporal resolution of interest, the mode of probing and the complexity of the experiment.

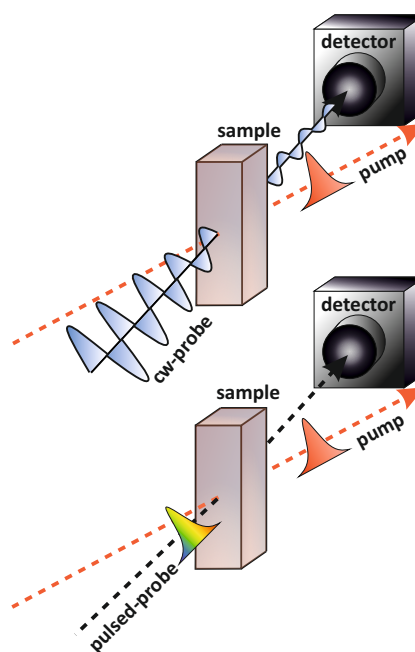


FIGURE 2.4: Schematic representation of cw- and stroboscopic probing in a pump-probe experiment.

### 2.2.2 Flash Photolysis

The flash photolysis (FP)<sup>[37]</sup> is one of the oldest time-resolved spectroscopic techniques, which was developed by Eigen, Norrish and Porter in 1949 and was later awarded the Nobel Prize in Chemistry in 1967. Initially, this term was coined for the general concept of pump-probe spectroscopy, however, these days the term is synonymously used with ns-pump-probe techniques by the majority of scientists in the spectroscopy community. The FP setup used in this work (Fig. 2.5) consists of three home-built modules, which allow measurements in the UV/vis and IR. They are fed with pump pulses generated by a coupled Neodymium-doped-yttrium aluminium garnet (Nd:YAG) laser (Spitlight 600, Innolas Laser GmbH, Germany) and optical parametric oscillator (OPO) system (preciScan, GWU Lasertechnik, Germany). The Nd:YAG is Q-switched with a Pockel's cell at a 10 Hz frequency. The 1064 nm fundamental of the Nd:YAG source is used for SHG with a 532 nm and third harmonic generation (THG) with a 355 nm output. These frequencies are mixed in the OPO to generate pump pulses covering the range of 412-2550 nm central wavelength with approximately 9-20 ns temporal width. UV pulses can be generated by using the SHG-module of the OPO, which allows an additional tuning in the range of 257-354 nm and 355-514 nm, respectively. The adjustment of the crystals and the corresponding phase-matching angles in the OPO are controlled by the commercial preciScan software. An optical shutter at the laser output is used to block unwanted pulses by default and to adjust the desired excitation sequence for the experiment. Before the pump beams are guided into the individual modules, they are resized and recollimated with a pair of lenses for each excitation pathway. Since the generation of the pump pulses is similar for all three modules, the next sections will primarily deal with the respective detection systems and their unique properties.

#### UV/vis Flash Photolysis

For measurements in the UV/vis, cw and broadband probing are implemented in the FP setup, which requires two sets of different probe light sources and their suitable detectors. To obtain cw light, a broadband beam generated by a mercury-xenon lamp (LC8, Hamamatsu, Japan) is guided through a monochromator (Photon Technologies International, USA) with interchangeable gratings of 300 nm or 500 nm blaze. The output wavelength can be manually adjusted with 0.5 nm precision via a screw on the outside of the casing. After passing the sample cuvette, the light passes a second monochromator to filter out straylight from the pump pulses before it finally enters the photomultiplier tube (PMT). This device converts light into an electrical signal which can be amplified by up to eight



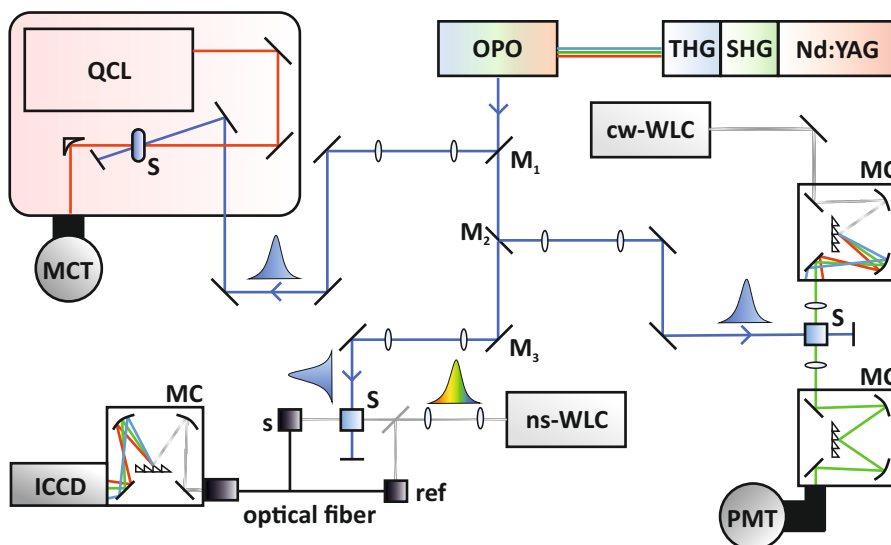


FIGURE 2.5: Schematic overview of the flash photolysis setup including cw- and pulsed UV/vis probing, as well as cw-probing in the IR. All three setups are fed with pump-pulses from the Nd:YAG and OPO configuration.

orders of magnitude. The thereby obtained transient electrical signal is then readout, recorded and saved with a digital oscilloscope (DPO 5204B, Tektronix, USA). The data acquisition is synchronized with the pump pulse sequence set by a digital pulse delay generator (PDG, Quantum Composers, USA). In contrast, the broadband probelight is generated by a xenon flashlamp (L7685, Hamamatsu, Japan) which yields pulses of a spectral width from 190 nm to 2000 nm and a temporal width of approximately 3  $\mu$ s. These spectrally broad pulses are detected with an intensified charge-coupled device (ICCD) camera (PI-MAX 3, Princeton Instruments, USA) after passing through the sample cuvette or the reference arm of the setup.

The most integral part of the intensifier in such an ICCD is composed of a photocathode, a microchannel plate and a phosphor screen.<sup>[38–40]</sup> The incident light is converted into photoelectrons, which are accelerated towards the microchannel plate by a controlled voltage ramp. These accelerated photoelectrons, in turn, produce a cascade of secondary electrons inside the microchannel plate leading to an amplification of the initial signal. The secondary electrons are caught by the phosphor screen and converted back into light, which is then guided towards the attached CCD array. Therefore, ICCDs are well suited for applications with low light intensities and very short exposure times due to the high gain capability and fast shutter operation.<sup>[41]</sup> The advanced electronics in

the broadband detection require a more sophisticated data acquisition software, which allows a precise synchronization of the pump pulse sequence, the gating of the ICCD and the variable delay of the probe pulses. Here a customized LabView program is used which works in tandem with the commercially available WinSpec package.

### Infrared Flash Photolysis

Complementary to the electronic transitions of a molecule, an even deeper understanding of molecular dynamics can be obtained by taking a look at its vibrational modes. Transitions of this nature are several orders of magnitude smaller than electronic transitions and therefore require a different instrumentation for their detection. However, the corresponding energy gaps come with inherent limitations in suitable light sources and detectors, making IR measurements much more delicate than their UV/vis counterpart. A modern alternative to the commonly used Fourier-transform (FT) IR spectrometers<sup>[42,43]</sup> was opened up with the invention of the quantum cascade laser (QCL) by Faist et al in 1994,<sup>[44]</sup> which can be used as a high intensity and stable IR light source for transient probing.

A QCL is a semiconductor laser which is based on intersubband transitions in an array of quantum wells and energy barriers. In contrast to conventional semiconductor lasers, which require specific mixtures of material for bandgap tuning,<sup>[45-49]</sup> the subband energies  $E_{\text{subband}}$  in a QCL are tuned mainly by the material thickness, allowing a continuum of possible emission energies in the IR. For the emission to occur, an electrical bias has to be applied to the material which promotes electrons from the valence to the conducting band. A transition of an electron from a higher energetic subband to a lower energetic subband in the conduction band leads to the emission of a photon with the energy  $\Delta E_{\text{subband}}$ . This process alone, however, does not guarantee a stable lasing output due to missing population inversion (PI). This PI is achieved by engineering the material in such a way, that the corresponding lower energetic subbands allow an electron to tunnel through the energetic barrier into a neighboring quantum well. In such a case, each quantum well is subsequently repopulated with a high energetic electron. The initially emitted photons are then able to start a cascade of stimulated emission along the quantum well lattice,<sup>[50]</sup> which leads in principle to quantum efficiencies greater than unity.

In practical terms, the actual composition of the QCL material is more complicated. The main components are condensed in the injector layer and the active region. The injector layer is crucial for maintaining a constant supply of high energetic electrons,

## 2.2 Experimental Techniques

whereas the active region is the place where the quantum cascade occurs. Together they form a periodic structure of alternating units. To achieve a stable output of coherent radiation, the gain medium needs to be placed in an optical cavity. In its simplest variant, the cavity is formed by the gain medium itself in a Fabry-Perot configuration, leading to high power outputs but a lack of tunability. More common are therefore external cavity configurations which allow the implementation of frequency-selective elements such as gratings.

The QCL system (MIRcat, Daylight Solutions, USA) used in this work is based on such a configuration. It comes with two interchangeable modules which cover a frequency range of  $930\text{-}1165\text{ cm}^{-1}$  and  $1510\text{-}1751\text{ cm}^{-1}$ , respectively. Due to the uneven output power profile of both modules, the actual output intensity has to be adjusted with filters and an automaticed iris. This becomes especially important for frequencies at the edges of the spectral window where the intensity drops are most significant. To detect the IR probing light, a mercury cadmium telluride (MCT) detector<sup>[51]</sup> is used. Like all semiconductive devices, its function is based on the separation of charges between the valence and the conductance band. The specific detection range of an MCT, given by the bandgap  $E_g$ , is determined by the ratio of CdTe and HgTe and the temperature of operation, following the relationship<sup>[52]</sup>

$$E_g(x, T_N) = E_g(x, T) - (T - T_N) \frac{\partial E_g}{\partial T} \quad (2.34)$$

with the normalization temperature  $T_N = 80\text{K}$  and common ratios of  $x = 0.2, 0.3, 0.4$  in the spectral range of  $3\text{-}14\text{ }\mu\text{m}$ . Advances in semiconductor growth techniques, such as liquid phase or vapour phase epitaxy,<sup>[53,54]</sup> made MCT detectors affordable and therefore the most widely used choice for IR detection. The actual photodiode chip of the MCT detector is comprised of several functional layers. On a supportive substrate (e.g. CdZnTe) a n-type layer (doped with In) and a p-type layer (doped with As) of HgCdTe are consecutively grown. This complex is usually coated with a passivation layer to ensure isolation and to avoid corrosion effects of the optically active region. IR radiation induces excitation of electrons in the n-type layer which leads to an electrical bias between the n-p-interface. This bias is transferred to a silicon based readout integrated circuit (ROID) via an indium bump contact on each pixel of the chip and then amplified. The performance of the detector system, including the photodiode chip and the pre-amplifier, is measured in the specific detectivity  $D^*$

$$D^* = \sqrt{\Delta f \cdot A} \frac{R}{S_N} \quad (2.35)$$

with the characteristic responsivity  $R$ , the spectral bandwidth  $\Delta f$ , the active area  $A$  and the noise spectral density  $S_N$ .  $D^*$  at given frequencies, together with the risetime  $\tau_{\text{rise}}$ , are the most important quantities for choosing a suitable detector for the respective experimental needs. The MCT device (KV104, Kolmar Tech., USA) chosen for the IR FP roughly matches the output profile of the QCL modules with an optimum in the range of  $950\text{-}1250\text{ cm}^{-1}$ . Similar to the inhomogeneity of the QCL power spectrum, the inhomogeneous specific detectivity at different frequencies has to be compensated by adjusting the output power of the IR beam to ensure comparable measurement conditions. Analogously to the cw UV/vis FP, the data acquisition and processing is done with an oscilloscope. The individual time traces are saved, reduced and can optionally be combined to yield a transient map of the photodynamics.

### 2.2.3 Ultrafast Transient Absorption Spectroscopy

The ultrafast transient absorption (fs-TA) spectrometer relies on the stroboscopic pump-probe principle. The temporal resolution of this technique is mainly limited by the pulse width  $\Delta\tau$  of the pump pulses, which requires the utilization of a fs laser source. The laser system used in this work is built around a  $\text{Ti}^{3+}$ -doped sapphire (Ti:Sa) based regenerative amplifier (MXR-CPA-iSeries, Clark-MXR Inc., USA). This multilayered system is comprised of a seed-pulse generation unit, the pump-pulse generation unit and the actual amplifier. The seed-pulses are generated by a cw diode laser which pumps a modelocked erbium fiber oscillator. This leads to the generation of pulses with a temporal width of 130 fs and a central wavelength of 1550 nm at a repetition rate of 1 kHz. Subsequently these pulses are converted to 775 nm via SHG, then temporally stretched and guided into the Ti:Sa crystal in the amplifier. Here they are overlapped with the pump-pulses, produced by a Nd:YAG laser, to achieve amplification of several orders of magnitude. In the last step the pulses are compressed again to yield high-intensity ultrashort pulses. The principle of amplifying a temporally stretched (i.e. chirped) pulse, followed by its recompression is referred to as chirped pulse amplification (CPA) - a technique firstly introduced by Strickland and Mourou,<sup>[55]</sup> for which they were awarded the Nobel Prize in Physics in 2018.

The fundamental beam of 775 nm central wavelength is guided to the experimental setup (Fig. 2.6) where it is initially split into two separate branches. Each branch makes use of non-linear optical processes (see 2.1.4) to convert the fundamental into pump and probe pulses, respectively. The latter are generated by focussing the fundamental beam into a transparent (non-linear) medium. This results in the so-called supercontinuum

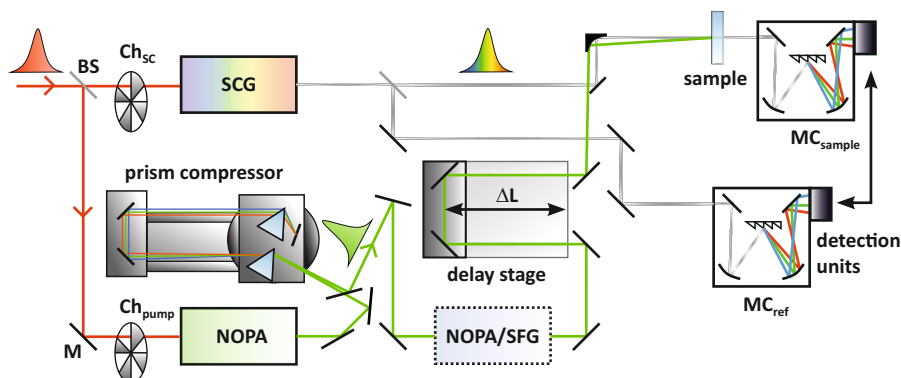


FIGURE 2.6: Schematic overview of the ultrafast TA setup. In addition to a two-staged NOPA for pump-pulse generation, it is also possible to produce UV-pulses via SFG.

generation (SCG), which describes a strong spectral broadening of an initially narrow-bandwidth pulse. The SCG is a complex process, which involves several non-linear effects such as self-phase modulation (SPM), self-focussing and group velocity dispersion (GVD). The characteristics and quality of the SC are determined by the material of choice, its thickness and the stability of the pump source. Typical materials used in UV/vis spectroscopies are sapphire and  $\text{CaF}_2$  crystals, which cover the spectral range from the near-UV up to the near-IR. The generated probe pulses are then split and guided through a sample and reference branch, where they are collected in the respective spectrographs. Here they are decomposed into their spectral components and recorded by a multipixelated photodiode array.

The pump pulses, in turn, undergo several steps before they are suitable for the actual experiment. Besides the non-linear optical (NLO) processes such as SHG, NOPA and SFG (see 2.1.4), an adjustment of the temporal characteristics is of significant importance. This is done with a prism compressor, which applies an additional (negative) chirp to the pulse to compensate GVD over the optical pathlength of the setup. The pump beam is aligned over an optical delay stage and spatially overlapped with the probe beam inside the sample cuvette. Unlike the ns-FP, the temporal delay between pump and probe pulses on the ultrafast timescale can not be adjusted electronically. In the fs-TA spectrometer one therefore relies on the pathlength  $L$  each pulse has to travel. The temporal delay is then determined by the difference in pathlength  $\Delta L$  between the pump and the probe arm of the setup. The time-zero position, in other words the position at which both pulses exactly overlap temporally in the sample, is dependent on the

characteristics of the pulses and the optical elements they have to pass through. Once this position is defined, the actual delay sequence for the measurement is set relative to this position. The amount of incremental steps and their spacing determine the size and the temporal range of the transient dataset. For each delay position a spectrum of the unexcited and the excited sample is recorded. This requires a specific sequence of pump and probe pulses, which is determined by the frequency of the choppers in the respective beam path.

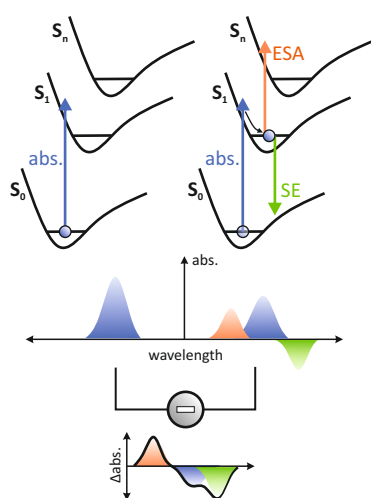


FIGURE 2.7: Origin of the  $\Delta\text{abs.}$  spectra in a fs-TA experiment.

In contrast to the simple GS spectrum, the ES opens up additional processes like excited state absorption (ESA), photoproduct absorption (PPA) and stimulated emission (SE) (Fig. 2.7). The resulting difference absorption spectra can vary in complexity depending on the sample at question. Positive difference signals are usually assigned to ESA or PPA, whereas negative signals arise from SE and ground state bleach (GSB). The latter is the consequence of a reduced GS population due to the excitation. Each spectrum is recorded for a specified number of times, statistically filtered and averaged to reduce shot-to-shot fluctuations. The filter needs to be set in such a way that a certain minimal threshold value for usable single-shot scans is reached. A complete transient scan has to be repeated several times to improve the overall data quality.

## 2.2.4 Time-correlated Single Photon Counting

Measurements of radiative processes on the ps to ns timescale can be done by time-correlated single photon counting (TCSPC). In this method, an ES population is induced by a pulsed laser source or a pulsed LED with sufficiently short pulse widths. The radiative decay, namely the fluorescence, of the system is then recorded by counting the individual emission events in a single photon detector. This results in a histogram of photon counts at specific delay times with respect to the photoexcitation. The kinetics follow an exponential decay function which is consistent with the rate equation given in 2.21. However, the temporal trace is convoluted with the instrument response function (IRF) of the excitation pulses. Therefore, the analysis must include a deconvolution in

order to obtain the underlying kinetics of the fluorophore at question, following the relationship<sup>[56]</sup>

$$I(t) = \int_{-\infty}^t IRF(t') \sum_i^n A_i e^{-\frac{t-t'}{\tau_i}} dt' \quad (2.36)$$

This is done with the commercially available FluoFit software package (FluoFit Pro 4.6, PicoQuant GmbH, Germany). On the hardware side, the experimental setup used in this work is comprised of an interchangeable excitation pathway, which can either be fed by a 80 MHz Ti:Sa laser system (Tsunami, Spectra Physics, USA) or a selection of pulsed LEDs (PicoQuant GmbH, Germany), as well as a detection unit based on a PMT (PicoQuant GmbH, Germany) and a fast counter card (TimeHarp Single PCIe, PicoQuant GmbH, Germany). Due to the statistical nature of such measurements, a significant amount of emission events have to be counted. This requires on the one hand large repetition rates of the excitation source to ensure a reasonable time frame of the measurement, and on the other hand a moderate excitation energy to omit pile-up effects. Due to molecular rotational effects, which become relevant on the nanosecond timescale, the excitation and the emission light have to be set at the magic angle configuration.

### 2.2.5 Two-photon Induced Fluorescence

So far just the case of a one-photon absorption (1PA) has been discussed. However, given a sufficiently high photon flux, a non-linear two-photon absorption (2PA) from an electronic GS  $S_0$  to a higher energetic state  $S_N$  is possible. Similar to the extinction coefficient in 1PA, the ability of a molecule to undergo 2PA is quantified by its 2PA cross section  $\sigma_{2P}$  which is given in units of GM [ $1GM \triangleq 10^{-50} cm^4 s / (photon \cdot molecule)$ ] named after Maria Goeppert-Mayer.<sup>[57]</sup> The total absorbance of a sample in a nonlinear excitation regime is then given by the differential equation

$$-\frac{dI}{dz} = \alpha I + \beta I^2 \quad (2.37)$$

Here, the linear term describes the commonly known Beer-Lambert law and the second order term describes 2PA. The 2P coefficient  $\beta$  is a function of wavelength (or frequency) and is related to  $\sigma_{2P}$  by

$$\beta(\omega) = \frac{N}{E_{ph}} \sigma_{2P} \quad (2.38)$$

with the volume density of the molecules  $N$  and the energy of the excitation photons

$E_{ph}$ . 2PA can either occur by the absorption of two photons of the same (degenerate case) or different (generate case) energy. In both cases the combined excitation energy must be resonant to the energetic gap of the transition. From here on, however, the more commonly used degenerate case shall be considered. Similar to 1PA, the possibility for 2PA is determined by the selection rules which result from the quantum mechanical treatment of the involved transition states and their corresponding wave equations.

Under aspects of molecular symmetry one can deduce that in centrosymmetric molecules, a 2PA involves conservation of parity so that transitions of the form  $u \rightarrow u$  or  $g \rightarrow g$  are allowed. Conversely, 1PA is allowed for transitions with a change of parity, e.g.  $u \rightarrow g$  or vice versa. This mutual exclusiveness does not exist for molecules without a center of inversion. The above mentioned aspects demand specific conditions for a 2PA experiment.<sup>[58,59]</sup> Significant 2PA can just be observed at sufficiently high photon densities and ultrafast interaction times. This condition is practically met in the focal volume of a tightly focussed femtosecond laser beam. The very small amplitudes of 2P effects relative to the high intensity excitation sources make transmission experiments non-trivial.<sup>[60-62]</sup>

A work-around for this problem, at least for fluorescent molecules, is the indirect measurement of 2PA via fluorescence detection. This so-called two-photon induced fluorescence (2PIF) technique uses a confocal geometry for the excitation in a small sample volume as well as the collection of the emitted photons (Fig. 2.8). The excitation system used in this work is based on a 80 MHz Ti:Sa laser (Tsunami, SPectra Physics, USA) which is pumped by a neodymium-doped-yttrium vanadate (Nd:YVO<sub>4</sub>) cw-source (Millenia, Spectra Physics, USA). In order to scan the 2P response of a large variety of molecules, the excitation source needs to be tunable on a broad spectral range. The tunability of this system covers the NIR range from 690 nm to 1080 nm with its optimum at 730-930 nm. To keep the emitted pulses sufficiently short, the beam is guided through a prism compressor. Both, spectral and temporal, profiles of the pulses are checked with a camera (BP209, Thorlabs, USA) and an auto correlator (pulseCheck, APE, Germany). This is necessary to ensure a Gaussian beam profile which simplifies data evaluation. The emitted photons are guided to an internally cooled spectrograph (SpectraPro 300i, Acton Research, Germany) with an integrated CCD-camera (Roper Scientific, Germany). The remaining excitation beam is filtered by a set of dichroic mirrors and band-pass filters to avoid artefacts of over saturation of the detector. The data acquisition itself is done with the WinSpec software package. This allows the recording of several subsequent fluorescence spectra, which can be averaged to optimize the signal-to-noise ratio.

To obtain the 2PA cross section  $\sigma_{2P}$ , the following equation is used<sup>[63,64]</sup>



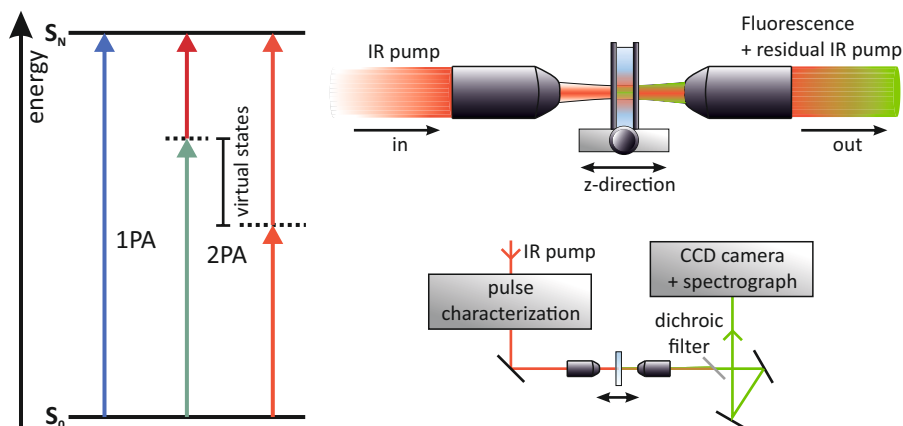


FIGURE 2.8: Energy diagram showcasing the generate and degenerate 2PA cases. Schematic overview of the 2PIF setup and a closed-in view on the focal volume. The remaining IR pump beam has to be filtered with a dichroic filter in order to get a clean fluorescence signal.

$$\phi_{fl,s}\sigma_{2P,s} = \frac{\langle I \rangle_{fl,s} c_r n_r}{\langle I \rangle_{fl,r} c_s n_s} \phi_{fl,r}\sigma_{2P,r} \quad (2.39)$$

with the fluorescence quantum yield  $\phi_{fl}$ , the 2PA cross section  $\sigma_{2P}$ , the integrated fluorescence intensity  $\langle I \rangle_{fl}$ , the concentration of the molecule  $c$  and the refractive index  $n$  of the solvent. The indices  $s$  (sample) and  $r$  (reference) emphasize that 2PIF relies on a reference compound. The obtained values are therefore not just dependent on the experimental setup but also on the quality and reproducibility of reported data. Therefore, the reference and the sample have to be carefully measured with identical excitation conditions, e.g. beam profile and laser intensity. A common, however not generally justified approximation, lies in the assumption that the fluorescence response after 1PA and 2PA are similar.<sup>[59,63,64]</sup> In that case the fluorescence quantum yield  $\phi_{fl}$  can be obtained by a simple 1P fluorescence measurement.

### 2.2.6 Data Evaluation

One of the main objectives in time-resolved spectroscopy lies in the extraction of kinetic information of a molecular system (Fig. 2.9). As introduced in section 2.1.3, the photochemical deactivation after the initial photoabsorption event is described by an exponential behaviour. However, in a spectrally broad and complex dataset such as obtained by flash photolysis or fs-TA measurements, the individual spectral changes over a

large temporal range can not be treated independently. Instead it is necessary to subject such data to a *global* analysis approach.<sup>[65,66]</sup> Here one distinguishes roughly between model-dependent and model-independent methodologies. As the names suggest, in the former one a set of mathematical functions is used to describe a very specific reaction mechanism, whereas the latter one works without any prior assumptions about the mechanistic details. The most commonly used model-dependent approach is given by global lifetime analysis (GLA),<sup>[65]</sup> which uses a discrete sum of  $n$  exponential functions

$$S(t, \lambda_{exc}, \lambda_i) = \sum_{j=1}^n A_j(\lambda_{exc}, \lambda_i) e^{-\frac{t}{\tau_j}} \quad (2.40)$$

The resulting fit yields the characteristic lifetimes  $\tau_j$  of the decay function and associates them with the amplitudes  $A_j$  of each trace. These so-called decay-associated spectra (DAS) are then used as a simple representation of the spectrally resolved kinetics of the system. It is important to stress that the obtained lifetimes - along with their amplitudes - do not automatically correspond to a mechanistic model. The actual kinetic modeling is rather complicated and generally requires knowledge about additional parameters, such as spectral properties, in order to reduce the amount of possible solutions. One possibility to move away from this model-based approach is given in the lifetime density analysis (LDA),<sup>[66,67]</sup> which has gained more popularity in recent years. Even though this method still relies on exponential functions, it describes the overall kinetics as a continuous distribution of lifetimes

$$S(t, \lambda_{exc}, \lambda_i) = \int_0^{\infty} \Phi(\tau, \lambda_{exc}, \lambda_i) e^{-\frac{t}{\tau}} d\tau \quad (2.41)$$

The spectral information is now contained in the distribution function  $\Phi(\tau)$  and is, similarly to GLA, linked to the individual decay components. To make a numerical solution of this integral possible, it has to be transformed into a discrete sum of  $n$  components (with  $n > 50$ ). The result is then represented in a lifetime density map (LDM) which delivers a compact overview of the underlying kinetics. Both methods, GLA and LDA, are part of the analysis software package OPTIMUS<sup>[66]</sup> which was developed in-house and is therefore the analysis toolkit of choice in this work. As introduced in section 2.2.3, experimental data is usually convoluted with the IRF which requires a deconvolution routine in addition to the actual data fitting procedure, so that equation 2.41 is reformulated to

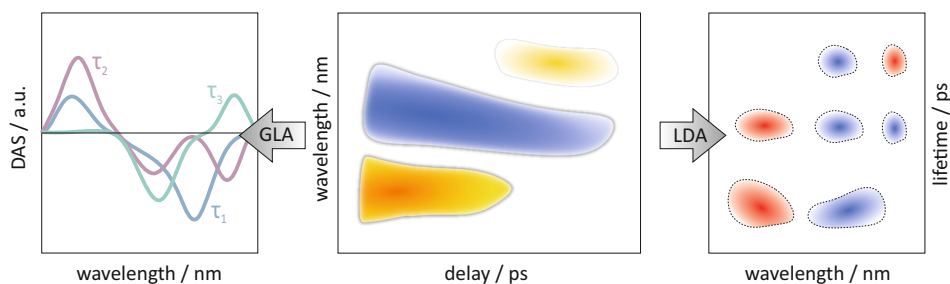


FIGURE 2.9: Schematic representation of time-resolved data evaluation. The dataset (middle) can either be evaluated by GLA or LDA. The former one yields DAS, whereas the latter one yields LDMs. Both strategies are implemented in the OPTIMUS package.<sup>[66]</sup>

$$S(t, \lambda_{exc}, \lambda_i) = \sum_{j=1}^n A_j(\tau, \lambda_{exc}, \lambda_i) e^{-\frac{t}{\tau_j}} \otimes IRF(t) \quad (2.42)$$

Even though equation 2.42 is the basis for both, GLA and LDA, the respective analysis differs in the implemented algorithm to find the pre-exponential factors. The details of these algorithms can be found in the OPTIMUS documentation and the corresponding original publication.<sup>[66]</sup>

## 2.3 Microbial Rhodopsins

Rhodopsins constitute the largest family of light-sensitive proteins and are found amongst all domains of life. In animals they are coupled to G-proteins,<sup>[68]</sup> which in turn regulate signal transduction processes for phototaxis or vision.<sup>[69,70]</sup> However, in microorganisms - such as algae or bacteria - they are mainly responsible for the conversion of light into an electric signal or chemical energy by either passive or active ion conductance across a biological membrane. They are often divided into four different groups: cation or anion channels, proton pumps, chloride ion pumps and sodium ion pumps (Fig. 2.10). A precise classification therefore involves the mode of action (active or passive) and the actual cellular function (signaling or generation of ion gradients).<sup>[71,72]</sup> Ever since the extraction of the proton pump Bacteriorhodopsin (BR)<sup>[73]</sup> from *Halobacterium salinarium* in 1971, a large number of additional mRhos have been discovered and characterized. Prominent examples for mRhos - besides BR - are the proton pump Protonrhodopsin (PR),<sup>[74]</sup> the chloride pump Halorhodopsin (HR),<sup>[75,76]</sup> the sodium pump *Krokinobacter eikastus* rhodopsin 2 (KR2)<sup>[77]</sup> and the ion channel Channelrhodopsin-2

(ChR2).<sup>[78]</sup> Research on mRhos is subdivided into two major sections. On the one hand

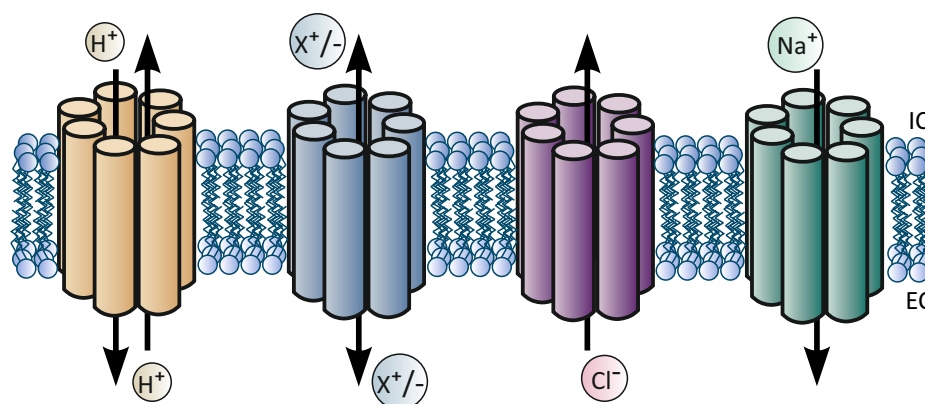


FIGURE 2.10: Schematic representation of the four MRh types: Proton pumps, cation or anion channels, chloride pumps and sodium pumps.

there is the fundamental research on the evolutionary, functional, structural and mechanistic aspects of these families of photoreceptors.<sup>[71,72]</sup>

On the other hand there is the new field of optogenetics,<sup>[15-17]</sup> which has emerged after the discovery of the light-gated ion channel ChR2. In essence, the main objective of optogenetic research is the implementation of mRhos into non-native membranes to specifically manipulate a cell's electrochemical equilibrium by application of light. This is especially interesting in the context of neurobiology, where a change of membrane potential leads to a neuronal response. Due to the nature of these large fields of research a close collaborative effort of many disciplines ranging from the molecular description, over the biochemical implementation up to the cellular readout strategy is necessary.

In this work, the main focus is put on the photophysical aspects of light reception as well as the mechanistic response of the protein. In order to lay the ground work for the discussion of the experimental results, the next sections will introduce some of the fundamental structural and mechanistic features of mRhos.

### 2.3.1 Structural and Functional Features

Rhodopsins are made of two building blocks: the protein scaffold - which is referred to as opsin - and the retinal chromophore.<sup>[71]</sup> The opsin itself consists of seven  $\alpha$ -transmembrane helices (TMHs) which are connected via intracellular (ic) and extracellular (ec) loops (Fig. 2.11). The chromophore is bound to the opsin via a Schiff base

(SB) linkage<sup>[79]</sup> between the amino group of a lysine residue in helix G (or 7) and the aldehyde group of the retinal. Depending on the type of rhodopsin, either *all-trans* retinal (type I) or *11-cis* retinal (type II) are bound.<sup>[71]</sup> Both kinds of chromophores originate from the oxidative cleavage of  $\beta$ -carotene<sup>[80]</sup> or can be interconverted from retinol (or vitamin A).<sup>[81]</sup> Even though type I and type II rhodopsins seem to be similar at first sight, they differ largely in terms of their genetic sequence as well as their function. In the scope of this work, however, just type I rhodopsins - which make up all mRhos - will be discussed. All mRhos have in common that - upon irradiation with light - charges are translocated from one side of the protein to the other. The determination of the exact translocation pathway as well as the underlying mechanisms is still one of the major objectives in rhodopsin research.

However, several structural motifs have been identified which turn out to be crucial for the overall functionality of the respective mRho. The most obvious feature is the chromophore. In the dark state of the mRho, the retinal is found in the *all-trans* configuration with a protonated Schiff base.<sup>[71]</sup> Upon absorption of a photon, the chromophore undergoes an isomerization to the *13-cis* configuration (Fig. 2.12). In the subsequent steps the protein undergoes several changes, which typically involve protonation steps including the deprotonation and reprotonation of the retinal Schiff base (RSB). This requires very specific amino acids which function as a proton acceptor (PA) or proton donor (PD).<sup>[71,82,83]</sup> In BR, this functional unit is formed by D85, T89 and D96.<sup>[82]</sup> This DTD motif on helix C is highly conserved in other archaeal  $H^+$ -pumping rhodopsins. In analogy to BR, similar functional motifs have been identified such as DTE or DTX for bacterial  $H^+$ -pumps (e.g. PR), TSA for archaeal  $Cl^-$ -pumps (e.g. HR), NTQ for bacterial  $Cl^-$ -pumps (e.g. CIR) and NDQ for bacterial  $Na^+$ -pumps (e.g. KR2).<sup>[71,83,84]</sup> In addition to the aforementioned protonation steps, the charged amino acid residues play a major role in the dynamic balancing of the electrostatic environment in the hydrophobic protein interior.<sup>[85,86]</sup> This is often assisted by a tight network of protein-bound water molecules,<sup>[87,88]</sup> which - in many cases - interconnect the ec and the ic side of the protein. In the same context it is worth mentioning that

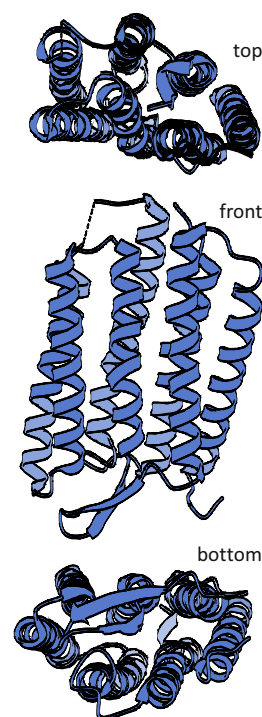


FIGURE 2.11: Reduced structure of BR from the side, top and bottom view.

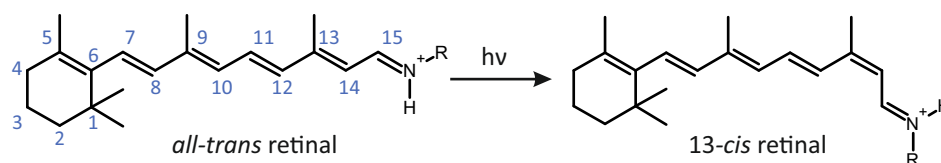


FIGURE 2.12: Isomerization of *all-trans* into 13-*cis* retinal upon absorption of a photon.

bulky and aromatic amino acids, such as tyrosines and tryptophans are similarly well conserved in the retinal binding pocket. Especially the BR motif W86, W182 and Y185 is strongly tied to the electrostatic stabilization of the direct chromophore proximity.<sup>[85,86,89]</sup> Importantly, the strong interaction of charged residues with the retinal itself - either directly or via hydrogen bonding - also determine its photophysical characteristics such as the absorption maximum<sup>[90-92]</sup> and the isomerization quantum yield.<sup>[93,94]</sup> The charge distribution also dictates which ions are able to pass the interior and the vectoriality of the ion translocation. In fact, mutagenic studies have shown that the replacement of just a few specific amino acids already leads to a change or a complete loss of protein function.<sup>[71]</sup> A closer look into such structural details is therefore highly important for finding an appropriate mechanism.

### 2.3.2 The Primary Reaction

The functionality of mRhos is closely tied to their ability to absorb light of a defined wavelength. The event of photoabsorption by the chromophore leads to a population of its excited state.<sup>[95,96]</sup> This HOMO→LUMO-transition is accompanied by a charge transfer from the  $\beta$ -ionone ring towards the RSB, leaving the former moiety positively charged compared to the RSB part.<sup>[89]</sup> Several studies in the last two decades have found that the sudden change of charge distribution in this primary event is in fact crucial to prepare the protein for the subsequent translocation processes.<sup>[89,97-101]</sup>

From here, different energetic pathways are possible which are determined by the topology of the corresponding ES potential surfaces (Fig. 2.13).<sup>[93,95,96]</sup> As already mentioned in the previous section, the photophysical properties of the chromophore are strongly influenced by its direct environment. In terms of potential surfaces these effects can then be understood as a modulation of the energetic barriers along a reaction coordinate. From our current understanding, the mechanism of a functioning mRho must involve the isomerization from *all-trans* to 13-*cis* retinal. However, the isomerization quantum yield  $\phi_{iso}$  is found to be 30-70% depending on the system.<sup>[96,102-104]</sup> This

implies that a substantial amount of initially absorbed energy is actually dissipated in non-reactive pathways. The existence of such reactive pathways (RPs) and non-reactive pathways (NRPs) have been shown spectroscopically on a large variety of mRhops. This is usually expressed in a fast lifetime on the timescale of a few hundred fs, and slower lifetimes which can reach up to the ps range.<sup>[105–111]</sup> In this sense, the fast lifetime corresponds to the transition from the ES to the isomerized GS photoproduct via a conical intersection (CI), whereas the slower lifetime components reflect the NRP of retinal back to its initial GS configuration. Mechanistically these results remain ambiguous and highly debated, which is reflected in two opposing models (and their variants) for the primary dynamics: The excited state branching (ESB) and the ground state heterogeneity (GSH) model.<sup>[93,95,105,112–118]</sup> It is important to note that a thorough assessment of the viability (i.e. strengths and weaknesses) of both models is out of scope of this work, however some key aspects will be briefly introduced.

As the name suggests, the ESB model postulates that parts of the ES population are branched off at specific points on the ES potential surface. The initial branching into the NRP and RP must occur right after photoabsorption - namely in the FC regime - due to the very fast isomerization time of retinal.<sup>[108,115,119]</sup> However,  $\phi_{iso}$  is not solely dictated by the population of the RP.<sup>[112,120,121]</sup> In fact, an additional branching of the ES population at the CI between the  $S_1$  and  $S_0$  states is required to account for this inconsistency. The ratio of the non-isomerized and isomerized retinal products is then mainly influenced by a variable barrier,<sup>[116]</sup> which is the result of the coupling between the  $S_1$  and  $S_2$  states. The coupling of these states is in turn modulated by changes of the electrostatic environment of the chromophore.<sup>[122]</sup>

In contrast, the GSH model is based on the view that the ES dynamics is predetermined by the GS configuration of the retinal and its close surroundings. Differences in the GS configuration therefore result in heterogeneous subpopulations, which will undergo different pathways once they are excited by a photon. This model is usually supported by the fact, that mRhops such as PR,<sup>[108,113,123]</sup> BR<sup>[96,113,124,125]</sup> and KR2<sup>[102,113,126]</sup> show a

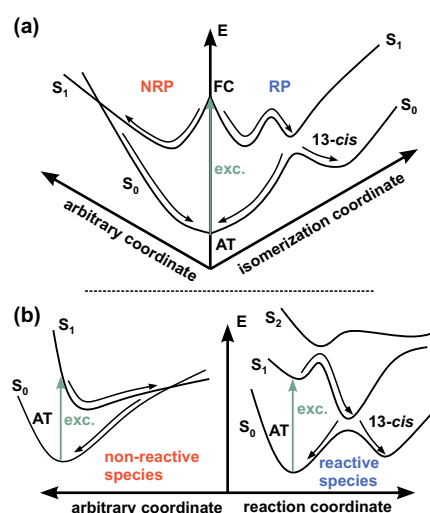
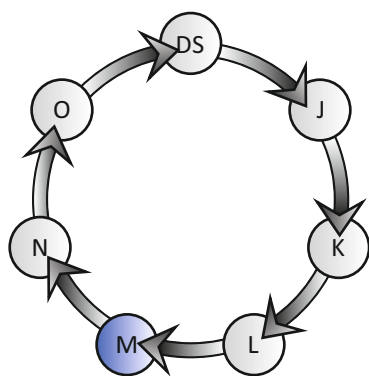


FIGURE 2.13: Schematic representation of the ESB (a) and GSH (b) models.

strong pH-dependence in terms of ES dynamics. Here, it is suggested that  $\phi_{iso}$  is mainly modulated by hydrogen bonding<sup>[113]</sup> between the chromophore and neighboring amino acids (i.e. the counter-ion) or water molecules. Subpopulations without such a hydrogen bond would in turn undergo the NRP. Even though the GSH model is fairly simple and reasonable, it still comes with a few inconsistencies. A major critique is rooted in the fact, that the lifetime distribution of the ES decay seems to be temperature independent.<sup>[127]</sup> It is therefore important to keep in mind that each model excels at describing certain aspects of the primary dynamics in mRhos, but they still come with a set of flaws.

### 2.3.3 The Photocycle

The overall functional mechanism from the photoabsorption, over the actual translocation of a charge up to the regeneration of the initial dark state involves several structural changes in the protein which span a broad timescale from fs up to s.<sup>[71]</sup> Due to the cyclic nature of this process, one generally refers to the collective description of all these steps as a photocycle (Fig. 2.14). Historically, the individual intermediates in a mRho photocycle have been defined and named after the prototypic mechanism found in BR.<sup>[71]</sup> Even though mRhos differ slightly in terms of structure and function, the generalized model based on BR still holds very well in many cases.



**FIGURE 2.14:** Generalized photocycle scheme with the crucial M-intermediate highlighted in blue.

In total there are six distinct intermediates which differ in their structural configuration and as a result also in their spectral properties.<sup>[82,128–131]</sup> As already discussed in the previous section, the initial photoabsorption leads to either a NRP or RP. Populations which undergo the RP can then end up with an isomerized - but still strongly twisted - 13-*cis* retinal.<sup>[95,96,132]</sup> This vibrationally hot GS photoproduct is populated in a few hundred fs and is referred to as the J-intermediate (J). With the cooling process on the ps timescale the thermally stable K-intermediate (K) is formed. After a structural change in the retinal binding pocket, the SB proton is prepared to be transferred to the PA.<sup>[133]</sup>

This stage is usually ascribed to the L-intermediate (L). Once the proton is transferred, and hence the RSB becomes deprotonated, the M-intermediate (M) is formed.<sup>[86,134]</sup> This intermediate now contains a 13-*cis* retinal and



## 2.4 Photolabile Protecting Groups

**TABLE 2.1:** Highlighted photocycle characteristics in BR. The prefixes d (deprotonated) and p (protonated) in the RSB, PD and PA columns indicate proton movements along the respective transitions.

intermediate	retinal configuration	RSB	PD	PA	misc.
DS	AT	p	p	d	-
J	13-cis	p	p	d	hot GS
K	13-cis	p	p	d	-
L	13-cis	p	p	d	contact pRSB and dPA
M	13-cis	d	p	p	-
N	13-cis	p	d	d	-
O	AT	p	p	d	-

a deprotonated RSB, which leads to a major spectral blue-shift of the chromophore absorption. In proton-pumps, M is also considered electrogenic due to the net-movement of charge.<sup>[71,135]</sup> In a subsequent step the RSB is then reprotonated by the PD, leading to the formation of the N-intermediate (N).<sup>[136-139]</sup> The thermal reisomerization to *all-trans* takes place in the last step forming the O-intermediate (O). Further adjustment in the protein then leads to the final regeneration of the initial dark state. The kinetics involved in the photocycle are strongly dependent on the protein conditions such as pH-value, salt concentrations, oligomerization state, temperature and even the medium of reconstitution. A quick way to identify an intermediate is given by UV/vis spectroscopy. On the downside, this methodology is blind to many structural nuances since it is most sensitive to the changes of the chromophore itself. For a more complete picture it is therefore required to involve (time-resolved) vibrational spectroscopy, NMR or X-ray crystallography.

## 2.4 Photolabile Protecting Groups

The introduction of a protecting group (PG) into a molecule is an established strategy in organic synthesis which allows the modulation of chemoselectivity.<sup>[140]</sup> The basic concept involves an alteration of a functional group so that a specific chemical reaction is prevented. In an additional step the functionality of the molecule must then be restored.<sup>[140-142]</sup> Conventionally the deprotection is done chemically by a single or several successive reactions with added reactants.<sup>[143]</sup> On large scales this turns out to

be very costly due to the comparably low yields of the additional reaction steps relative to the amount of required material. From a synthesis perspective it is therefore often desired to find alternative reaction routes which make the utilization of PGs obsolete.

On the small scale, however, PGs open up interesting applications in the domain of biochemistry. By and large such applications evolve around the activation or deactivation of specific receptors, which are involved in major biochemical responses.<sup>[144,145]</sup> The microscopic or sub-microscopic scale, as well as the enormous chemical complexity of such systems like whole cells or smaller organelles, require a delicate way to achieve deprotection of the PG. The most promising strategy is given by the application of light, which allows high spectral selectivity, temporal and spatial resolution and non-invasiveness. PGs of this sort are then referred to as PPGs or photocages.<sup>[146–148]</sup> In fact, this expression was already coined in one of the very first publications on PPGs by Barltrop and Schofield,<sup>[149]</sup> who proposed a way to liberate glycine after irradiation with UV light. Another outstanding application - which has still a significant impact on the scientific profile at Goethe University Frankfurt - was proposed by Engels and Schlaeger.<sup>[150]</sup> They used an *ortho*-nitrobenzyl (oNB) scaffold to protect adenosine cyclic 3',5'-phosphate (cAMP), which plays an important role in the regulation of various cellular processes. Their molecular design did not just add an additional degree of control, but it was also crucial to overcome low cell permeability of cAMP in its native form.

The design and further development of new PPGs is stimulated from different directions. On the one hand there is a broad spectrum of applications in biochemistry, pharmacology and medicine which all come with different requirements for a meaningful use.<sup>[144,145,151–154]</sup> On the other hand there is the fundamental research, which mainly focusses on the photochemistry of such molecular systems.<sup>[148]</sup> Especially the latter field has been growing very fast in the recent years due to the large improvements of computational methodologies, which significantly facilitate overall design strategies.<sup>[155–157]</sup> The mechanistic details of a photocleavage (or uncaging) vary from system to system but there are some general steps which need to be followed.

Generally, the absorption of a photon must lead to a change of electronic configuration so that the bond, which is meant to be cleaved, is either weakened or chemically more accessible.<sup>[148,158]</sup> Such an intermediate state must then be temporally stabilized, for example by the solvent, in order for the actual chemical reaction to occur. Finally, both photoproducts - the remaining PPG scaffold and the liberated molecule - must be stable enough to prevent a backreaction. The overall efficiency of the uncaging reaction is mainly determined by the ability of the molecule to absorb light of specific wavelengths,

the competing relaxation pathways<sup>[159]</sup> from the excited state, the solvent interactions and the leaving group (LG) itself.<sup>[148]</sup> These factors are often not independent from each other, which makes a rational design rather complicated. In terms of the final application, however, several properties are of larger importance than others. For example, high uncaging quantum yields  $\phi_u$  are often desired, but a high light-sensitivity could also limit the use of a PPG in situations where ambient light is inevitable. Likewise, large substituents for an increased solubility in a specific medium could hamper the photochemistry due to additional vibrational decay channels. Therefore it is crucial to adjust the design of PPGs by prioritizing individual characteristics for the specific application.

In the domain of biology - which is the most prominent field of application - the most important aspects include: non-toxicity, water-solubility and absorption in the so-called phototherapeutic window (300-800 nm) paired with a sufficient efficiency in that wavelength range.<sup>[148,160]</sup> The latter aspect is usually defined by the absorption of deoxyribonucleic acids (DNAs), RNAs and proteins in the near-UV and the resonance of water in the near-IR. This implicitly includes the principle of spectral selectivity,<sup>[161,162]</sup> which demands a well separated spectral window of operation in order to limit any side effects upon initiation of the photocleavage. In order to minimize tissue damage, a red-shifted absorption is often preferred as long as the uncaging efficiency remains sufficiently high. This also led to the search of two-photon activatable PPGs which are meant to address this issue.<sup>[151,163-166]</sup>

### 2.4.1 Coumarin-based PPGs

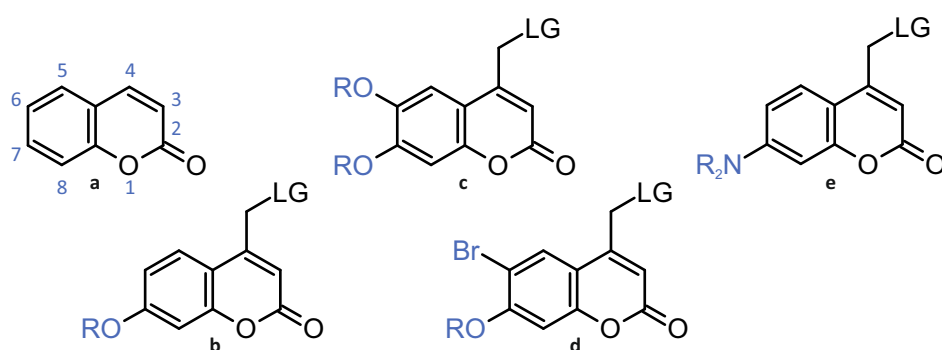


**FIGURE 2.15:** The basic structure of coumarin (a) and its PPG-variants based on the 7-alkoxy- (b), 6,7-dialkoxy- (c), 6-bromo-7-alkoxy- (d) and 7-dialkyl-amino-substituted coumarins (e).

Coumarin and its derivatives are among the most commonly used photochemically active molecules. Common applications include laser dyes,<sup>[167,168]</sup> fluorophores for imag-

ing and sensitizers in larger molecular constructs. The conversion of a coumarin scaffold into a PPG was first reported in 1984 by Givens and Matuszewski, who used a (7-methoxycoumarin-4-yl)methyl (MCM) derivative to protect diethylphosphate.<sup>[169]</sup> Ever since, other derivatives with a large range of modifications have been designed and reported. They can be roughly categorized into four groups consisting of 7-alkoxy-, 6,7-dialkoxy-, 6-bromo-7-alkoxy- and 7-dialkyl-amino-substituted coumarins (Fig. 2.15). The substituents at given positions are crucial for the performance of the overall compound in terms of solubility, permeability, spectral properties and ES dynamics. The effects of a large variety of site-specific modifications on such coumarin compounds are well studied and have been reported in numerable original publications and reviews.<sup>[148,159,170–172]</sup> Considering the potential use in biological systems, (7-diethylaminocoumarin-4-yl)methyl (DEACM) and its variants have become model compounds of choice. Besides the relatively large red-shift towards 370-410 nm - depending on the substituents - DEACM-based PPGs also have an increased uncaging quantum yield (QY).

### Photochemistry and Uncaging Mechanism

Since parts of this work deal with the systematic characterization of 7-dialkyl-amino-substituted coumarins, the general photochemistry of these compounds shall be explained on the simple example of DEACM. Like all coumarins, DEACM absorbs most dominantly in the UV. The main absorption band is attributed to a  $\pi \rightarrow \pi^*$ -transition which corresponds to a transition from HOMO to LUMO ( $S_0 \rightarrow S_2$ ). The energetically close  $n \rightarrow \pi^*$ -transition is characterized by HOMO-2  $\rightarrow$  LUMO and HOMO-2  $\rightarrow$  LUMO+2 transitions ( $S_0 \rightarrow S_1$ ), which do not exhibit significant oscillator strengths and are therefore spectrally dark.<sup>[173]</sup>

The spectral position and the shape of the main band is strongly dependent on the solvent and the attached substituents.<sup>[174]</sup> This is rationalized in the electronic configuration of the corresponding HOMO and LUMO orbitals, which in general facilitate an intramolecular charge transfer (ICT) from the benzylic to the pyranone moiety.<sup>[173,175]</sup> The ICT character of this sort is stabilized by polar solvents. Likewise, an additional enhancement of this effect is achieved with strong push-pull systems, consisting of an electron-donating and an electron-withdrawing substituent at position C7 and C3, respectively.<sup>[148]</sup> Besides a simple ICT, an additional twisted intramolecular charge transfer (TICT)<sup>[176]</sup> was postulated and reported for DEACM and its derivatives.<sup>[177,178]</sup> In such a TICT-state, the dialkyl-amino-substituent at the C7 position undergoes a twisting to form a pyramidal configuration, which further stabilizes the charge transfer (CT)

character. As a result of nearly four decades of research, a large number of publications

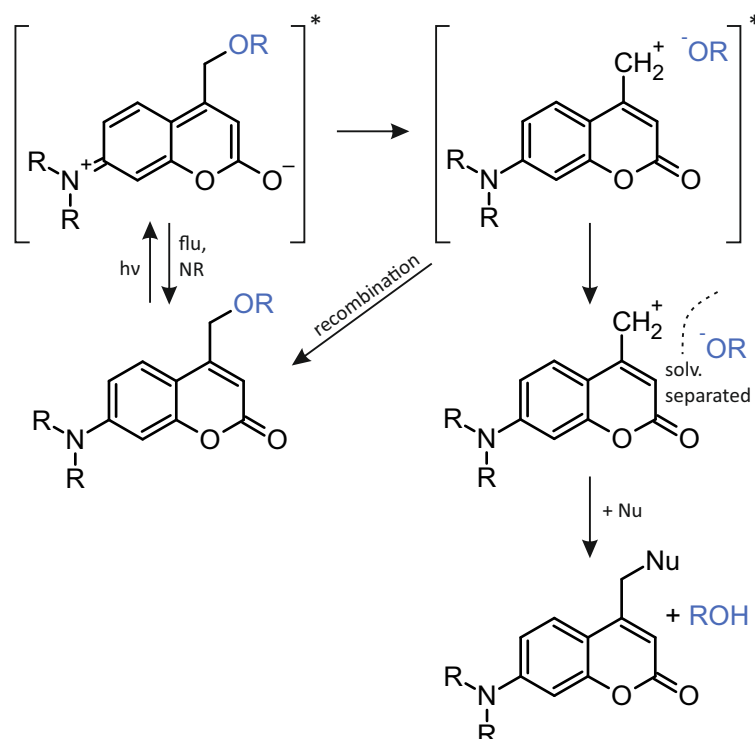


**FIGURE 2.16:** Reaction pathways pathways of DEACM after photoabsorption. The photochemical cleavage occurs via a TIP, which needs to be stabilized by the solvent.

on the uncaging mechanism of coumarin based PPGs have been published.<sup>[171,174,179,180]</sup> Even though slight differences might arise depending on the LG or the attached linker, it is accepted that the uncaging mechanism (Fig. 2.16) involves the formation of a tight ion pair (TIP) between the coumarinylmethyl cation and the LG conjugate base.<sup>[179]</sup>

The initial excitation of the coumarin leads to the population of a locally ES which is in equilibrium with the ICT state mentioned previously. Depending on the local environment of the molecule, e.g. solvent, this ICT state is either stabilized or deactivated via non-radiative or radiative processes.<sup>[159,173,174]</sup> In the ICT state, the bond between the benzylic carbon and the LG can be heterolytically cleaved which results in the aforementioned TIP. This TIP needs to be sufficiently stabilized by the solvent in order to prevent a recombination process which would yield the initial educt. If the coumarinylmethyl cation is stabilized it can be attacked by a nucleophile to form the inactivated PG, making it inaccessible for the LG. This mechanism is facilitated by strong electron-donating groups on the benzylic moiety and LGs with a low  $pK_a$  value, which

help to stabilize the cation and the anion, respectively. The overall efficiency of this process is also determined by the availability of the nucleophile. Practically solvents like water or alcohols can take that role, so that the kinetics is usually not limited by the amount of nucleophiles. At the same time, the solvent has a major influence on the excited state dynamics of the coumarin<sup>[159,181,182]</sup> which can also lead to a decrease of uncaging efficiency. This is one of the reasons why the optimization of the uncaging reaction still remains non-trivial.

## 2.4.2 BODIPY-based PPGs

Boron-dipyrromethene (BODIPY) and its derivatives are strongly fluorescent dyes which are structurally related to porphyrins. They were first described by Treibs and Kreuzer in 1968,<sup>[183]</sup> however the unsubstituted core structure itself has just been isolated in 2009.<sup>[184–186]</sup> The high extinction coefficient ( $> 80000 M^{-1} cm^{-1}$ ), high fluorescence QY ( $> 0.5$ ), narrow absorption and fluorescence bands and the rich derivative chemistry has made BODIPY a popular scaffold for a wide range of applications such as laser dyes, fluorescence labels in imaging and sensor systems.<sup>[187–190]</sup>

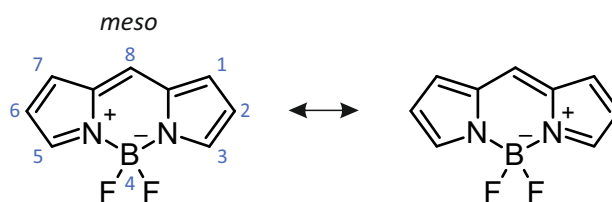


FIGURE 2.17: Mesomeric structures of the BODIPY scaffold.

The GS structure of the unsubstituted BODIPY consists of two mesomeric forms (Fig. 2.17), which is the reason why position 8 is often referred to as *meso*. This position turns out to be chemically easily accessible, despite the rather stable structure of the core.<sup>[148,191,192]</sup> Therefore, the first successful attempts to functionalize BODIPYs into a PPG utilized the *meso* position to attach a LG.<sup>[191–195]</sup> The results opened up the possibility to move further away from the UV into the visible range of the spectrum. This is especially crucial for applications in biological tissue, due to the reduced phototoxicity and deeper tissue penetration depth. Even though there is a large variety of vis-absorbing molecules, their functionalization into a PPG is challenging due to the non-trivial structure-reactivity relationship.<sup>[148]</sup> The computation of photophysical properties is often not enough to make a meaningful prediction on the uncaging behavior of a compound. In contrast,

the simple synthesis of BODIPY and its derivatives helped to circumvent this issue in part by accumulating large amounts of experimental datasets via laborious screening. Certainly, this is also reflected in the high number of original publications and reviews on these compounds in the recent decades.<sup>[192]</sup>

### Photochemistry and Uncaging Mechanism

Most of the aforementioned properties of BODIPY compounds are based on the rigidity of the core structure which is strongly stabilized by the BF<sub>2</sub>-group. However, significant tuning of the photophysical properties, solubility and overall chemical functionality is possible by substitution at positions 1-8.<sup>[191,196]</sup> The most prominent derivatives contain heavy atoms at position 2 or 6, which results in a significantly higher population of triplet states due to spin-orbit coupling. Positions 1,3,5 and 7 are usually substituted to increase solubility in specific solvents or to change the spectral properties. For example, the attachment of large aromatic systems can lead to a significant bathochromic shift of the main absorption band. From a photophysical perspective, this band is usually attributed to a HOMO → LUMO transition ( $S_0 \rightarrow S_1$ ) with significant electron density in the LUMO at the *meso* position.<sup>[191,197]</sup> The energetic gap of the transition is therefore strongly influenced by the electron-withdrawing or electron-donating character of the substituent at this position.

The electronic shift is also crucial for the photocleavage of common *meso*-substituted PPGs. If a LG is attached, the uncaging mechanism (Fig. 2.18) involves - similarly to DEACM - the formation of a carbocation.<sup>[191,194-197]</sup> The additional charge at the *meso* position facilitates heterolytic cleavage of the LG and stabilizes the formed carbocation. The underlying photochemical pathways, however, are not yet fully resolved. In principle

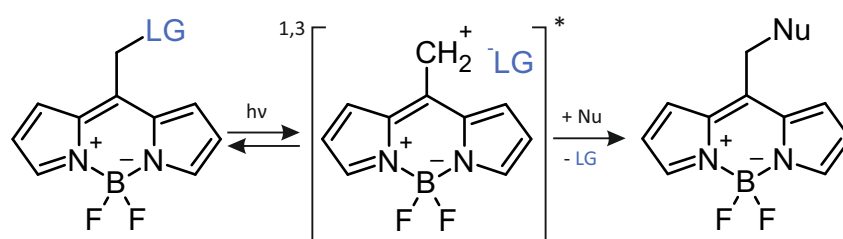


**FIGURE 2.18:** Uncaging mechanism of BODIPY-based PPGs. The mechanism involves the formation of a carbocation, which is stabilized by the solvent. Both, singlet and triplet, mechanisms have been reported.

## Chapter 2 Theoretical and Experimental Framework

both, singlet and triplet, ES mechanisms are possible and have been reported.<sup>[191,192]</sup> The efficiency of the uncaging reaction varies quite strongly depending on the derivative and its corresponding substituents. Besides the influence of the LG itself, the most significant increases in  $\phi_u$  are observed for compounds with high triplet formation rates. This observations can be rationalized either by the spin-forbidden recombination of the TIP or simply by the increased lifetime of the ES itself. A further enhancement is achieved in an oxygen-free environment. The strong triplet reactivity renders the legitimate question whether BODIPYs are generally suited as PPGs in a biological application. This might not be a big problem in reduced systems with well-defined experimental conditions, however even more so in more complex systems like a whole cell.



## Aims and Scope

The research in this work was done under the umbrella of the graduate school Complex Light Control (CLiC), which is funded by the Deutsche Forschungsgemeinschaft (DFG). The research focus of this consortium is set around light as a means to initiate and drive a chemical output. This requires the development of such optical control methodology on the one hand, but on the other hand also the design, synthesis and implementation of specific compounds and more complex systems which are photochemically addressable. This broad spectrum of expertises is also reflected in many of the individual projects of CLiC – some of which will be discussed in the framework of this thesis.

In the context of this work, different approaches/strategies for optical control have been studied with a focus on mRhos and PPGs. Whereas mRhos are often evolutionary optimized in terms of their photophysical properties and functionality in their native environment, PPGs are designed for a specific application in any (biochemical) system. The utilization of these compounds as optical tools, in turn, requires different technical strategies for the implementation and functionalization of the same.

The light-driven sodium pump KR2 and its variants sparked large interest in the scientific community, due to their ability to pump several kinds of monovalent positive charges ( $H^+$ ,  $Na^+$ ,  $K^+$  and  $Cs^+$ ) across a biological membrane. The assessment of the structure-function relationships of the involved pumping mechanisms is therefore crucial to develop optimized optogenetic tools of this sort. Here, time-resolved UV/vis and IR spectroscopy is used to follow the photo-induced protein dynamics from the initial absorption in the chromophore up to the protein response. Besides this photochemical characterization, a major effort is put in the development of optical control schemes, which are needed for a temporally precise activation and deactivation of the photocycle dynamics. The projects related to mRhos are embedded in the long-standing collaborations between the Wachtveitl group (Goethe University), the Glaubitz group (Goethe University), the Schapiro group (Hebrew University of Jerusalem) and the former Bamberg group (MPI for Biophysics).

In the field of PPGs, the focus is put on two main aspects: the optimization of the

### *Chapter 3 Aims and Scope*

uncaging QY and the spectral accessibility. The optimization of the photochemistry in coumarin-based compounds is addressed in a bottom-up approach, using DEACM as a simple base structure which is consecutively modified. Here, the main goal lies in the identification of structural features, which are integral for the photochemical performance of the desired PPG.

In the previous iteration of CLiC, Dr. Christopher Hammer (Wachtveitl group), Dr. Andreas Jakob (Heckel group) and Dr. Konstantin Falahati (Burghardt group) worked on a coumarin-based molecular dyad with the main focus on two-photon sensitization of the PPG. Even though the overall functionality of this dyad was demonstrated, some photochemical aspects were not yet ideal. The project in this work expands on this conceptual framework in terms of the structural design as well as the spectral properties of such molecular systems. To allow a flexible use in the phototherapeutic window, both, 1PA and 2PA cases are considered. Such broadly addressable dyads, in turn, require a shift from coumarins to more red-absorbing compounds like BODIPY and rhodamines. The individual constituents are then chosen in such a way, that the ET properties from the photosensitizer (Rho) to the PPG scaffold (BPY) are optimized. Again, all phases from the design, over the photochemical characterization up to the actual finalization and implementation of the sensitized PPG are done in tight collaboration with the Heckel and Burghardt group.

## Research Projects

In this chapter, the major aspects of the conducted experiments and their results will be discussed for each research topic. The first part of the respective project section will briefly introduce the framework of the research and the rationale behind the investigation. Overall, there are three major projects which will be discussed. Section 4.1 deals with the mechanistic and photophysical description of the light-driven sodium pump KR2 and its applicability as an optogenetic tool. Section 4.2 is centered around the systematic optimization of coumarin photochemistry in terms of photocleavage and suitable spectroscopic readout strategies. The project discussed in section 4.3 expands on the concept of photosensitization of PPGs which is shown for a BODIPY-rhodamine dyad system. All projects are highly collaborative and therefore involve a broad spectrum of methodologies and expertise. The main focus of the discussion will be set around the spectroscopic contributions of this work, however it will be contextualized in the overarching framework whenever it is due. For a detailed look into the experimental conditions or the complete datasets of the individual research topics, the respective publications are attached in the appendix of this thesis.

### 4.1 *Krokinobacter Eikastus* Rhodopsin 2

#### 4.1.1 Introduction

The light-driven sodium pump KR2 was discovered in 2013<sup>[77]</sup> and is the first example of its kind. Like every mRho, it consists of the opsin unit and the retinal chromophore. A distinct structural feature is given in the antiparallel  $\beta$ -sheet of the ECL1-domain,<sup>[198,199]</sup> which is differently oriented in comparison to the one found in BR. Some studies have proposed its involvement in the Na<sup>+</sup> binding and transport mechanism, whereas others mainly ascribe its significance in terms of thermal stabilization.<sup>[198]</sup> The mechanistically most important features are found in the retinal binding pocket (RBP). In contrast to BR, KR2 does not contain a PD/PA-pair but an aspartic acid counterion at position

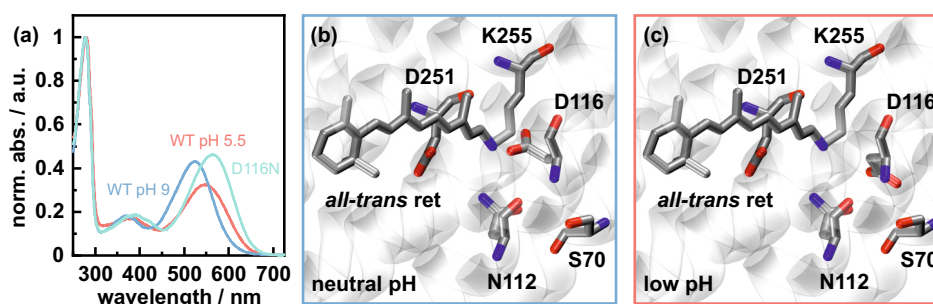


FIGURE 4.1: Absorption spectra of KR2 at different conditions (a). Close-up view on the RBP at neutral (b) and acidic (c) pH conditions.

116.<sup>[198,199]</sup> Together with N112 and Q123 it forms the so-called NDQ-motif<sup>[200,201]</sup> which is characteristic for light-driven sodium pumps. In the dark state (DS) of KR2, the counterion D116 forms two rotamers depending on its protonation state. The protonated rotamer is slightly turned away from the RSB, leading to a reduced electrostatic interaction (Fig. 4.1c). In contrast, the deprotonated rotamer is able to form a strong hydrogen bond with the RSB proton (Fig. 4.1b).<sup>[198–200]</sup> This interaction leads to major shifts in the dark state absorption which range from 525 nm to 560 nm (Fig. 4.1a). In close proximity to the counterion, the amino acids S70, N112 and D251 are located. They are suggested to be crucial for transient ion-binding. However, it is not yet clear whether such a site is formed between S70 and N112 (site a)<sup>[202]</sup> or N112 and D251 (site b).<sup>[203,204]</sup>

KR2 has gained large popularity due to its ability to transport  $\text{Na}^+$ -ions, which has not been expected so far mainly due to structural and electrostatic reasons.<sup>[77,205]</sup> Moreover, it has also been demonstrated that it is able to transport smaller monovalent cations ( $\text{H}^+$  or  $\text{Li}^+$ ) in the wildtype (WT) or even larger ones ( $\text{K}^+$ <sup>[198,199]</sup> or  $\text{Cs}^+$ )<sup>[206]</sup> in specific mutants. This automatically raised questions about the distinct transport mechanisms, especially in the range of conditions where  $\text{Na}^+$ - and  $\text{H}^+$ -transport seem to compete.<sup>[207]</sup>

By the time of the first experiments related to this work, structural as well as mechanistic data were scarce. Even though models for the photocycle in KR2 have been reported from early on,<sup>[77,198,199,208,209]</sup> many details were not clear. This includes - among others - the involvement of specific amino acids in the ion-translocation, the configurational changes of the retinal and the dynamical changes of the electrostatic environment in the RBP. It was therefore crucial to take a closer look into these important mechanistic aspects, to not just get a deeper understanding in terms of the ion-translocation in KR2 specifically, but also in terms of ion-translocation in mRhos as a whole.

In the first set of studies (section 4.1.2, refs. iv and v), time-resolved spectroscopy in the

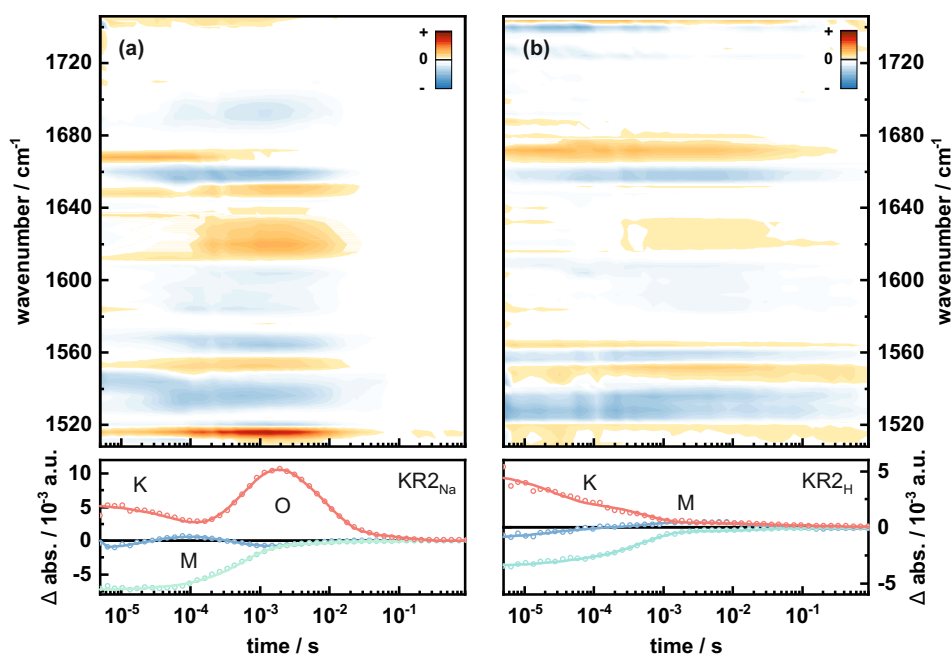


FIGURE 4.2: Overview of the IR dataset for KR2<sub>Na</sub> and KR2<sub>H</sub>. The UV/vis data is given in the lower panels to simplify the temporal correlation of the signals.

IR and the UV/vis, as well as structure-focussed techniques like NMR (in collaboration with the group of Prof. Clemens Glaubitz) were applied. During these investigations we also came across an additional - and to that date unreported - spectral signature in the near-UV, which was the starting point for a thorough look into this spectral region (section 4.1.3, ref. iii). It turned out that this near-UV signature spans from the fs up to the ms timescale and indeed corresponds to a blue-shifted transition of the *13-cis* retinal in KR2. The experimental findings are supported by quantum mechanical calculations (in collaboration with the group of Dr. Igor Schapiro). Apart from the photophysical characterization, a first set of photocontrol experiments were conducted which are the basis for a future implementation in optogenetic applications (section 4.1.4).

#### 4.1.2 A Closer Look into the Photocycle Mechanism

The studies discussed here are mainly focused on the structural and mechanistic insights of the KR2 photocycle. This is achieved by IR spectroscopy on the  $\mu$ s to s timescale, which is supported by UV/vis measurements in order to correlate the vibrational changes with the photocycle kinetics of the chromophore. The sheer size of mRhos - and therefore

large amount of vibrationally active modes - results in rather complicated IR spectra (Fig. 4.2), which generally make an analysis difficult. However, there are spectral regions which are characteristic for specific changes in a protein. The data recorded spans from  $950\text{-}1050\text{ cm}^{-1}$  and  $1500\text{-}1750\text{ cm}^{-1}$ , which is the full range of the QCL setup used in this work. The former range mainly covers the so-called hydrogen out-of-plane (HOOP) modes, whereas the latter covers the amide I and amide II bands, the ethylenic chain of the retinal, the RSB and site specific changes of amino acid residues.<sup>[210,211]</sup>

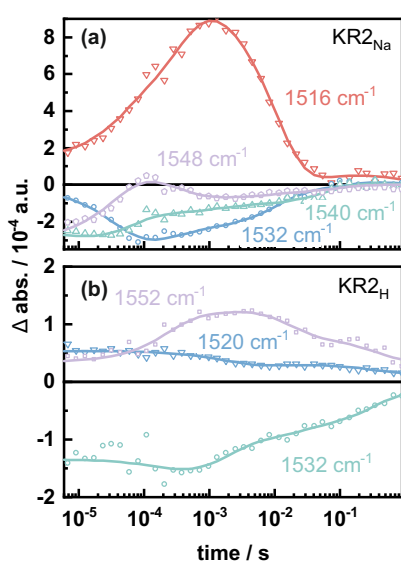


FIGURE 4.3: Transients representing the ethylenic stretch modes of the chromophore.

Due to the ability of KR2 to transport either  $\text{Na}^+$  or  $\text{H}^+$ , the first objective was to determine mechanistic similarities as well as differences of both pumping modes. To achieve this without a mixed kinetics due to competing pumping mechanisms, two samples were prepared which were adjusted to 100 mM NaCl at pD 8.3 ( $\text{Na}^+$ -pumping,  $\text{KR2}_{\text{Na}}$ ) and 0 mM NaCl at pD 6 ( $\text{H}^+$ -pumping,  $\text{KR2}_{\text{H}}$ ). Besides the obvious lack of salt in  $\text{KR2}_{\text{H}}$ , the pD-value had to be reduced to guarantee a sufficient amount of protons for the actual transport. Instead of using a dried film to perform the IR measurements, the samples were kept solvated in a  $\text{D}_2\text{O}$ -buffer. The supplementary UV/vis data was then recorded with the identical sample to simplify the correlation of the time-resolved traces (Fig. 4.2). Further information on the sample preparation and experimental procedure is given in the original publication.<sup>[212]</sup>

In order to get a first estimation of the photocycle kinetics it is useful to start with the chromophore. Here it is possible to directly correlate the lifetimes obtained in the UV/vis measurements with the bands of the retinal ethylenic stretch modes (Fig. 4.3). In  $\text{KR2}_{\text{Na}}$ , both, the spectral shifts as well as the lifetimes of the individual intermediates, match those of the UV/vis experiment quite well. Large spectral changes during the formation of the M-intermediate or the O-intermediate are reflected by corresponding up- and downshifts in the wavenumber of the ethylenic stretch mode, following the commonly used empiric rule.<sup>[213,214]</sup> It is therefore possible to assign the bands at (+)  $1532\text{ cm}^{-1}$  to K, (+)  $1548\text{ cm}^{-1}$  to M, (+)  $1516\text{ cm}^{-1}$  to O and (-)  $1540\text{ cm}^{-1}$  to the dark state. In  $\text{KR2}_{\text{H}}$ , however, this becomes more complicated. Here,

#### 4.1 *Krokinobacter Eikastus* Rhodopsin 2

the most prominent decays occur on the  $\mu\text{s}$  to  $\text{ms}$  scale whereas the small residual decay components span up to 100  $\text{ms}$ . In contrast to  $\text{KR2}_{\text{Na}}$ , the ethylenic stretch modes in  $\text{KR2}_{\text{H}}$  clearly remain populated up to several hundred  $\text{ms}$ , indicating a prolonged reorganization of the chromophore which is not reflected in the UV/vis data. It is also noteworthy, that the ethylenic stretch modes are temporally overlapping in  $\text{KR2}_{\text{H}}$ , which hints at a - at least partial - tendency to form kinetic equilibria.

More pronounced spectral differences between the two pumping modes are found in the window ranging from  $1600\text{ cm}^{-1}$  to  $1700\text{ cm}^{-1}$ . Here, the most dominant feature is given by the triple signature consisting of bands at (+)  $1652$ , (-)  $1660$  and (+)  $1668\text{ cm}^{-1}$  which are characteristic amide I vibrational modes (Fig. 4.4). In  $\text{KR2}_{\text{Na}}$ , the mode at  $1668\text{ cm}^{-1}$  is mainly populated during the K-intermediate and shows a rapid decrease of amplitude during the formation of the M-intermediate. Simultaneously, the mode at  $1652\text{ cm}^{-1}$  is populated until it peaks in amplitude with the formation of the O-intermediate. This behaviour is not seen in  $\text{KR2}_{\text{H}}$ , where the blue-shifted band at  $1668\text{ cm}^{-1}$  decays multi-exponentially and in parallel with the band at  $1652\text{ cm}^{-1}$ . This result strongly underlines major - and highly ordered - structural changes of the protein backbone during the  $\text{KR2}_{\text{Na}}$ -photocycle. This is not surprising since several steps are required for the successful ion-translocation, including the removal of the ion hydration shell,<sup>[215]</sup> the transient shielding of the ion-charge inside the protein<sup>[205]</sup> and the coordination of the ion after passing the RSB.<sup>[202,203]</sup> It is suggested, that these steps are in large parts mediated by the internal water network<sup>[202,203,209,216,217]</sup> similar to other mRhos.

Interestingly, an additional feature is exclusively found in  $\text{KR2}_{\text{Na}}$  at (-)  $1692\text{ cm}^{-1}$  (Fig. 4.5). This band is spectrally well isolated, extraordinarily broad and temporally aligned with the formation of the O-intermediate. Since it is not found in  $\text{KR2}_{\text{H}}$ , it is very likely that a sodium related interaction might be the cause of the intense absorption changes. In this context, there are two reasonable explanations for the origin of this signal. For one it could result from the  $\text{C}=\text{O}$  stretch mode of asparagine, which is usually observed in the

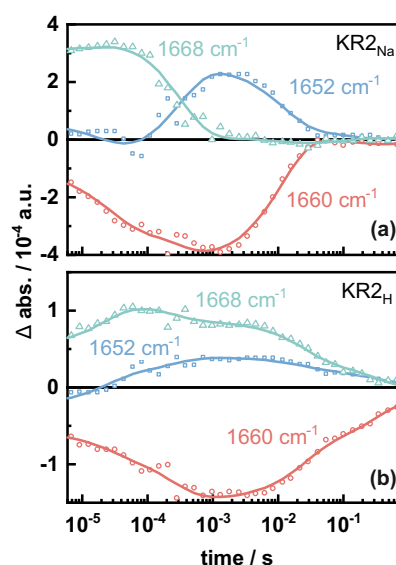


FIGURE 4.4: Transients representing changes of the amide I band.

range of 1648-1704  $\text{cm}^{-1}$  in several proteins.<sup>[210,211]</sup> In fact, a similar signature has been reported for the D96N mutant in BR.<sup>[218]</sup> In the case of KR2 the most obvious candidate is N112. As mentioned before, N112 is assumed to play a crucial role in the stabilization of the D116 counterion during the formation of the M-state and the actual coordination of  $\text{Na}^+$  during the O-intermediate. Both processes involve the rearrangement of hydrogen bonds with N112, which could be reflected in the bi-exponential nature of its decay. However, the intensity as well as the spectral width are not typical for changes of one individual amino acid.

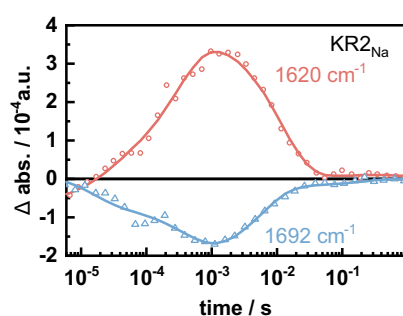


FIGURE 4.5: Possible marker bands for changes in the ECL1-domain.

A second explanation could therefore be given by a closer look into the spectral composition of amide I bands. In general, the amide I band contains contributions from random coils,  $\alpha$ -helices and  $\beta$ -sheets, which are spectrally overlapping but in terms of their peak position are still sufficiently distinguishable.<sup>[211,219,220]</sup> Interestingly, the  $\beta$ -sheet structure is characterized by a splitted band with a high-frequency (low intensity) peak around 1680-1690  $\text{cm}^{-1}$  and a low-frequency (high intensity) peak around 1620-1630  $\text{cm}^{-1}$ .<sup>[211,221-225]</sup> The ratio of the peak amplitudes is influenced by the relative orientation and consequently the coupling of the individual sheets.<sup>[224,225]</sup> In antiparallel structures, the high-frequency contribution is usually larger compared to the parallelly structured counterpart due to a more favorable orientation of the contributing dipole moments.<sup>[225]</sup> This in turn means, that variations in orientation also result in intensity changes of the high-frequency part of the  $\beta$ -sheet band. For KR2, which just contains one antiparallel  $\beta$ -sheet in the ECL1-domain, this implies that the antiparallel orientation is disturbed resulting in a bleaching of the band at 1692  $\text{cm}^{-1}$ . This is substantiated by the observation that positive bands around 1620-1640  $\text{cm}^{-1}$  emerge at a similar timescale, which could at least partially stem from the low-frequency  $\beta$ -sheet band or even an increase of random coil contribution.

Due to the general complexity of IR signals it is reasonable to assume that both mechanisms - the structural change in the backbone as well as interactions with N112 - contribute to the overall signature. Nonetheless, this result suggests that a significant change of this structural feature occurs during the KR2<sub>Na</sub>-photocycle, which reopens questions about the involvement of the ECL1-domain in the  $\text{Na}^+$ -translocation. A more



general mechanistic concept in mRhops involves the concerted protonation reactions of the RSB and - in the case of KR2 - the counterion D116. In that context it is useful to focus on modes which are directly affected by such protonation changes. For the protonated RSB, such modes involve the C=N stretching ( $\sim 1635\text{ cm}^{-1}$ ) and the C=N-H bending ( $1350\text{-}1400\text{ cm}^{-1}$ ) mode, whereas the deprotonated RSB just exhibits a redshifted C=N stretching ( $\sim 1620\text{ cm}^{-1}$ ) mode. For the protonated carboxyl group of D116 this includes the O-H stretching ( $3500\text{ cm}^{-1}$ ), the C=O stretching ( $1700\text{-}1780\text{ cm}^{-1}$ ) and the O-H bending ( $1200\text{-}1300\text{ cm}^{-1}$ ), as well as the symmetric ( $1300\text{-}1420\text{ cm}^{-1}$ ) and antisymmetric ( $1550\text{-}1610\text{ cm}^{-1}$ ) stretching mode of the deprotonated carboxylate, respectively.<sup>[211]</sup> However, not all of the aforementioned modes are suitable for an unambiguous assignment, due to significant overlap with other spectral signatures. This becomes even more complicated by considering the limitations in the experimental probing window.

Therefore, a major emphasis is given on the well isolated C=O stretching band at (+)  $1744\text{ cm}^{-1}$  which is found for both KR2<sub>Na</sub> and KR2<sub>H</sub>. In the case of KR2<sub>Na</sub>, the signal amplitude significantly increases with the formation of M and almost completely vanishes with the formation of O, which fits the protonation and deprotonation steps of D116. Complementary, the band at  $1636\text{ cm}^{-1}$  - representative for the protonated RSB - shows a major decay component on a similar timescale.

In contrast, KR2<sub>H</sub> turns out to be more complicated (Fig. 4.6). As already mentioned, the photocycle is not just significantly slowed at lower pD-values but also its photointermediates are more difficult to disentangle due to more pronounced equilibria. Moreover, the D116 counterion is initially protonated and differently rotated compared to higher pD values which in turn complicates the deprotonation mechanism of the RSB.<sup>[198]</sup> These aspects are well reflected in the transient behaviour of the (+)  $1744\text{ cm}^{-1}$  band, which is not as sharply rising and decaying as in the KR2<sub>Na</sub> case. Surprisingly, in addition to this positive band, a slightly red-shifted bleaching band at  $1740\text{ cm}^{-1}$  is observed in KR2<sub>H</sub>. It is possible that the altered resting configuration around D116 and the RSB, which involves an additional interaction with N112, causes a strong downshift of the dark state absorption of this specific mode. This signal is particularly interesting, because it almost perfectly mirrors the kinetics of its

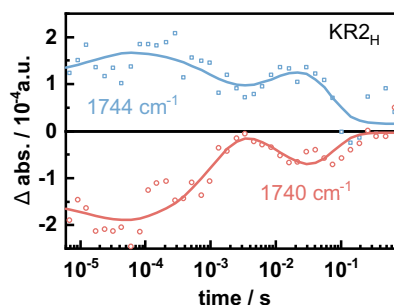


FIGURE 4.6: Transients representing changes of the D116 protonation state in KR2<sub>H</sub>.

positive counterpart at  $1744\text{ cm}^{-1}$ . This implies that the D116 counterion remains in a dynamic equilibrium between two different structural configurations which is reflected in the amplitude modulations of both IR bands. In analogy to  $\text{KR2}_{\text{Na}}$ , the most dominant signal rise of  $1744\text{ cm}^{-1}$  can be attributed to the formation of M, which is delayed by more than one order of magnitude in  $\text{KR2}_{\text{H}}$ . Again, the corresponding mode of the protonated RSB at  $1632\text{ cm}^{-1}$  decays on a similar timescale.

The last step of the photocycle, which is mainly driven by the thermal reversion of the retinal chromophore, can not be fully resolved in the IR region of  $1500\text{-}1750\text{ cm}^{-1}$ . In the simplest case, one has to probe the C–C stretch modes which can be found at  $1150\text{-}1250\text{ cm}^{-1}$ .<sup>[226]</sup> Here, the  $\text{C}_{14}\text{-C}_{15}$  mode in particular is a good indicator for the isomerization state of retinal. Unfortunately, this spectral region is not accessible by the setup used in this work. In a collaborative study with the Glaubitz lab, in particular Dr. Orawan Jakdetchai, a major focus of the research effort was put into the characterization of the structural changes of the chromophore during the KR2 photocycle in its sodium pumping mode. The main technique applied here is based on cryo dynamic nuclear polarization (DNP)-enhanced solid-state NMR, which allows a trapping and recording of NMR spectra for the successive photointermediates with an excellent resolution and sensitivity. Complementary cryo-trapping experiments in the UV/vis, which are necessary for the assignment of the intermediates, were done by Dr. Peter Eberhardt from the Wachtveitl lab.

This was supported on the IR spectroscopy side by looking closer into the dynamic changes in the HOOP mode region, which is indicative for the twisting motions of the retinal chain. In brief, the NMR data reveals that retinal in KR2 is already significantly twisted in its dark state compared to other mRhos like BR. After isomerization and the subsequent formation of K, the chromophore relaxes slightly but becomes strongly twisted again with the formation of L due to a tight interaction with the counterion D116. In this state the deprotonation step leading to M is prepared, which is also underlined by the strong deshielding effect of the RSB nitrogen. M itself could not be resolved with this technique, most likely due to insufficient population of this state. In O, however, the retinal is found to be back in its *all-trans* configuration, yet the dark state configuration of the ethylenic chain is not fully reinstated with major distortions at  $\text{C}_{13}$ ,  $\text{C}_{20}$  and the RSB itself. A similar result has also been obtained by x-ray crystallography of the isolated O-intermediate,<sup>[202]</sup> albeit with an additional emphasis on the out-of-plane configuration of the  $\text{C}_{14}\text{-C}_{15}$  bond. These structural findings are underlined by IR resonances found in the HOOP region of KR2. It is important to stress that the evaluation of the individual bands is non-trivial due to the large amount of overlapping signals and

possible couplings. A definitive assignment is therefore just possible with sophisticated isotope labeling and H/D-exchange of specific groups. Still it is possible to gain a deeper insight by direct comparison with common signatures found in the literature for similar mRhos such as BR or PR.

In the case of KR2, six distinct bands in the range of 955-1040  $\text{cm}^{-1}$  are found (Fig. 4.7), with the higher frequency modes stemming mostly from methyl in-plane bending and the lower frequency modes stemming from coupled (or decoupled)  $\text{C}_{15}, \text{N}$ -HOOP vibrations.<sup>[227]</sup> In contrast to BR, the low frequency band at (+) 960  $\text{cm}^{-1}$  is already populated at the sub- $\mu\text{s}$  timescale. This band is usually the result of the coupling between the  $\text{N}$ -HOOP of the RSB and the  $\text{C}_{15}$ -HOOP of retinal due to hydrogen bonding with protein-bound water molecules in later photointermediates. In KR2, however, a similar interaction is maintained with the counterion D116 during most phases of the photocycle, which is in line with the chemical shifts found in the NMR data. Hence, the main decay of this mode occurs with the deprotonation step of the RSB during transition from K/L to M. The band around 980  $\text{cm}^{-1}$  is assigned to the  $\text{C}_{15}$ -HOOP itself. In contrast to the lower frequency mode, the (+) 980  $\text{cm}^{-1}$  band shows its major decay during the formation of O which is indicative for the reisomerization step. Complementary to these signals, the bleaching band at 1012  $\text{cm}^{-1}$  originates from the methyl in-plane bending modes of  $\text{C}_9$  and  $\text{C}_{13}$ , underlining major distortions of the ethylenic chain at the center of the chromophore. Similar to the observations in the NMR, the IR signals in the HOOP-region point towards an incomplete regeneration of the retinal DS configuration in O. This is reflected in residual amplitudes which decay during the very last steps of the KR2 photocycle.

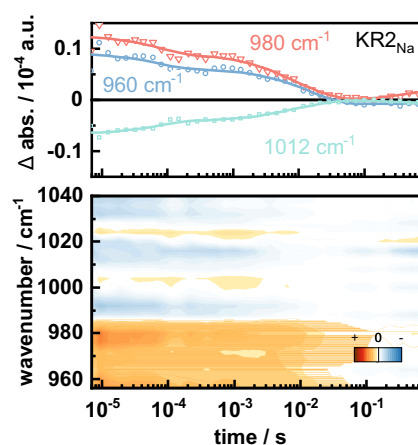


FIGURE 4.7: The HOOP-mode region in  $\text{KR2}_{\text{Na}}$ .

### 4.1.3 Expanding the View into the near-UV

The absorption spectrum of most mRhos can be sub-divided into three regions (from low-energetic to high-energetic): The main absorption band of retinal, a blue-shifted band originating from either a deprotonated RSB species or unbound chromophore

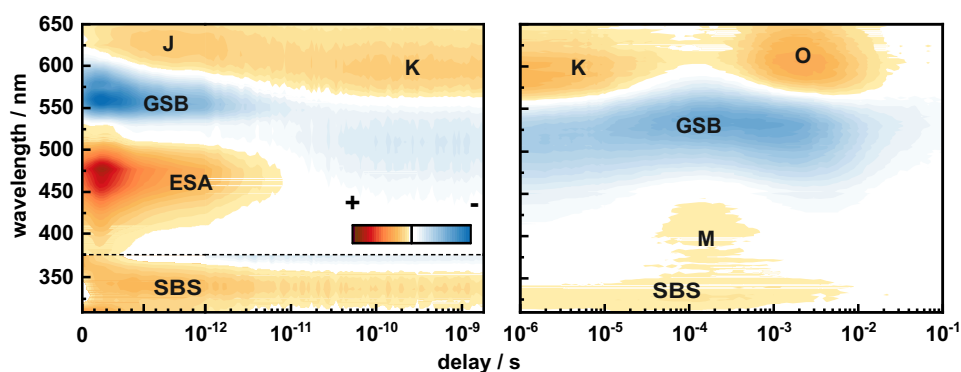


FIGURE 4.8: Complete representation of the transient absorption measurements ranging from fs to s. The near-UV region of the fs-measurements is scaled by a factor of 5 to account for the smaller signal amplitude in this spectral region.

and the protein band mainly stemming from the absorption of tryptophane or tyrosine residues.<sup>[228–232]</sup> In the long history of mRho research, the major focus has been put - with a few exceptions - on the main absorption band of retinal and its changes during the photocycle. The spectral range covered in these kind of measurements usually spans from 350 nm to 750 nm. In this work, additional effort was put into extending the probing range in the near-UV down to 300 nm. This is especially non-trivial in fs-TA, where additional challenges due to optical chirp occur. The measurements discussed in this section are performed on the KR2 WT at pH 9 and 5.5, as well as the counterion mutant D116N at pH 9. Here, mainly the interaction between the RSB and the counterion and its effects on the photochemical properties of KR2 are investigated. Prior to this study, several photocycle models based on optical spectroscopy have already been proposed. Therefore, this discussion will be centered around the new insights which are obtained through the near-UV region. In this spectral range, an additional absorption signature is found for all three sample preparations.

At first glance, it is particularly interesting that the signal is build up in the fs range and is maintained over more than ten temporal orders of magnitude leading up to the ms range (Fig. 4.8). In the course of that time, the spectral position does not change which is surprising considering the major electrostatic changes around the chromophore. A direct comparison of the near-UV signal and the red-shifted absorption which represents the formation of J, hints at a similar dynamic behaviour of both spectral signatures on the ultrafast timescale (Fig. 4.9). On the slower end of the temporal range it becomes somewhat more complicated due to a spectral overlap with the M-intermediate. The ac-

tual spectral width of M becomes obvious in the WT measurement at pH 5.5. In contrast to commonly reported spectral data, M seems to span down to 300 nm. At this point, however, it is not clear whether this broad spectrum represents one singular M state or in fact two subpopulations of M as proposed for several other mRhops. In contrast, a complete omission of M is achieved in the D116N mutant due to its inability to deprotonate the RSB. Here, it is clear that the near-UV band decays with the regeneration of the KR2 parent state. A more detailed view on the kinetics for the individual measurement conditions is obtained by the LDA. Whereas the near-UV band decays with the last photocycle intermediate in both, the WT at pH 5.5 and the D116N mutant, it shows a different behaviour for the WT at pH 9. In the latter case, the spectral component centered around 330 nm decays with a slight delay to the decay of M but still before the maximum population of O. Considering that the reisomerization from 13-*cis* to *all-trans* most likely - as discussed in section 4.1.2 - already occurs during the formation of O, the hereby obtained results suggest that the near-UV band is tightly correlated with the isomerization state of retinal.

To understand the nature of the near-UV transition, additional quantum mechanics/molecular mechanics (QM/MM) calculations were performed by Dr. Rajiv Kar of the Schapiro group. The calculations are based on the reported structures for the parent state of KR2 and the photointermediates K, M and O. Even though there are several structures available for the KR2 parent state, structural data on the individual photointermediates have been more difficult to come by. Therefore, the majority of the QM/MM calculations relied on the structures published by Skopintsev *et al.*,<sup>[203]</sup> which were obtained using time-resolved X-ray crystallography. Merely for O, in addition to the Skopintsev structure (A), another crystal structure (B) has been reported by Kovalev *et al.*<sup>[202]</sup> The O structures in both publications differ in the retinal isomerization state and the proposed sodium binding site. Consequently those differences turned out to be an excellent starting point to test the experimental observations obtained in the time-resolved spectroscopic data against the theoretical model. For a detailed depiction of the computational setup it is advised to refer to the supporting material of the original publication.

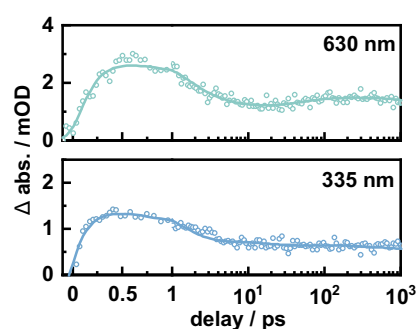
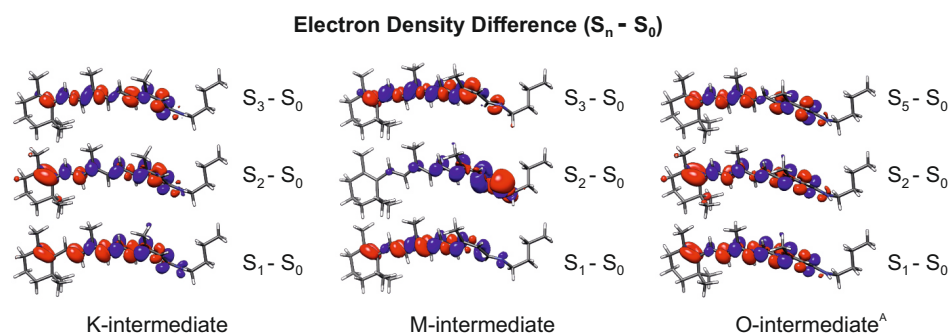


FIGURE 4.9: Transients of the red-shifted absorption corresponding to J (upper panel) and the near-UV band (lower panel).

In brief, the QM/MM calculations were set up in such a way, that the QM region includes the site of interest consisting of the retinal and the amino acid side chains of K255, N112, D116 and D251, as well as the sodium ion in O. The remaining protein was then defined as the MM region under treatment of the AMBER ff14SB force field. As a result, electron density differences and their corresponding excitation energies for the optical transitions in each photointermediate have been obtained. The quality of the chosen parameters and the validity of the methodology has been controlled by direct comparison of the  $S_0 \rightarrow S_1$  transitions with the empiric data, which indeed align - despite a methodological energy offset - quite well. To find the transition which constitutes the near-UV signature, a closer look at the higher order transitions is necessary. Here, the  $S_0 \rightarrow S_3$  transition for K and M, and the  $S_0 \rightarrow S_5$  transition for O are of major interest. The transition energies (Tab. 4.1) found for these transitions match the observed signature in the margins of methodological error. Moreover, there is no major energetic shift in between the intermediates which is in line with the constant spectral positioning in the time-resolved data. This can be rationalized by the electron density differences (Fig.



**FIGURE 4.10:** Electron density differences of the K-, M- and O-intermediate in KR2. The higher order transitions correspond to the SBS. In the case of the O-intermediate, calculations on structure A are shown.

4.10). In contrast to the  $S_0 \rightarrow S_1$  transition, which is dominated by a major shift of positive charge from the RSB to the  $\beta$ -ionone ring, the higher order  $S_0 \rightarrow S_{3,5}$  transition rather reflects a change of bonding character along the ethylenic chain. Consequently in the latter case, the RSB region is mostly unaffected by changes of the electrostatic surrounding. Even for the O-intermediate, no significant change of the  $S_0 \rightarrow S_5$  transition energy is found in neither of the two reported structures (A and B) despite the additional positive charge due to the transient binding of the sodium ion. Yet, the outstanding difference lies in the oscillator strengths of their respective transitions. Whereas structure

#### 4.1 *Krokinobacter Eikastus Rhodopsin 2*

A (containing 13-*cis* retinal) shows an increase of oscillator strength compared to the earlier photointermediates in that transition, the oscillator strength of a similar transition in structure B (containing *all-trans* retinal) vanishes almost completely (Tab. 4.1). The latter result is in line with the experimental observation that the near-UV band decays in between the decay of M and the rise of O. This in turn implies that the same signature is a second bright state (SBS) of the 13-*cis* retinal in KR2, and hence a spectroscopic marker for the isomerization state. Together with the previously discussed NMR and IR data, as well as structure B itself, there are now strong arguments speaking for a reisomerized retinal in the O-intermediate. One of the remaining questions is rooted in the discrepancy of both structural and spectroscopic data of different sources. The retinal configuration in O has been object of major discussions in the community. One reasonable explanation could simply be the sample itself. Most reported structures and their spectroscopic characterization are based on monomers. However, from our current understanding, KR2 forms pentamers in its native environment and functionality. Such pentamers have indeed been used to resolve structure B and to perform the experiments in this work. The mechanistic details and consequences of the oligomerization in mRhos are not fully understood yet, but significant effects ranging up to the retinal binding pocket have been reported already.<sup>[233]</sup> Therefore, it is far from impossible that different oligomers undergo slightly altered photocycles.

**TABLE 4.1:** Transition energies and oscillator strengths of the SBS transition for the individual photointermediates in KR2. The O-state was calculated with 13-*cis* and *all-trans* retinal.

SBS	parent state		K		M		O (13- <i>cis</i> ) <sup>A</sup>		O ( <i>all-trans</i> ) <sup>B</sup>	
	f	E / eV	f	E / eV	f	E / eV	f	E / eV	f	E / eV
	0.32	4.42	0.27	4.33	0.16	4.51	0.42	4.19	0.07	4.15

#### 4.1.4 Implications for Optogenetic Applicability

The spectral position as well as the temporal length of the SBS in KR2 lead to the question whether or not this signature could be utilized for more advanced experiments. The concept of optical control plays a major role in mRho research and its tightly connected field of optogenetics. One of the most prominent and widely used optical effects in this field is based on the so-called blue-light quenching (BLQ),<sup>[234–236]</sup> which was originally proposed for BR. Hereby the photocycle of a mRho is cut short by applying blue light on the blue-shifted M-intermediate. Even though this effect has been shown several decades

ago, a mechanistic description based on spectroscopic data was just offered relatively recently by Eckert *et al.*<sup>[237]</sup> The experiments performed in this publication offered a conceptual blueprint for similar experiments in the near-UV. In brief, the sample is continuously illuminated with cw radiation to pump the photocycle. Depending on the conditions of the protein (i.e. pH or salt concentration) a kinetic equilibrium of the individual photointermediates is formed. This photostationary state (PSS) is then the basis for the actual quenching process, which is initiated with a fs pulse. To isolate the pure quenching dynamics, a second control measurement on the identical sample is performed. Here, the sample is not illuminated with cw irradiation but still pumped with fs pulses. By subtracting both time-resolved datasets it is possible to eliminate potential contributions of the ordinary photocycle dynamics. The near-UV quenching experiments were performed on the KR2 WT at pH 5.5 and pH 9. The PSS was generated and maintained with a 565 nm LED, resulting in difference spectra with three pronounced bands at (+) 330 nm, (-) 520-550 nm and (+) 610 nm. The quenching was then initiated by fs pulses of 330 nm central wavelength.

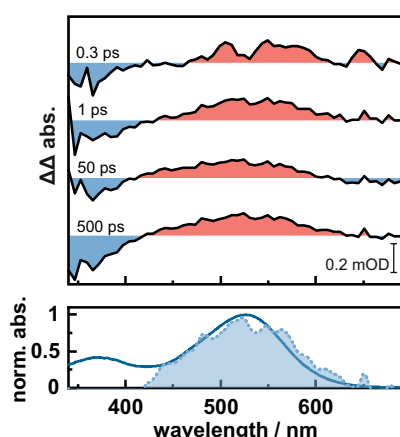


FIGURE 4.11: Double difference spectra at different time delays for the KR2 WT at pH 9. The photoproduct band resembles the absorption of the parent state.

The double difference spectra (Fig. 4.11) obtained by these measurements clearly show that the absorption of the respective parent states is regenerated over the course of several hundred fs (pH 9) or 50 ps (pH 5.5). The discrepancies in the temporal behaviour are a result of different starting conditions in the PSS. Whereas the main quenched state at pH 9 is the blue-shifted M-intermediate, it is the K-intermediate at pH 5.5, which can be deduced from the additional bleaching bands in the time-resolved data. Albeit in both cases a 13-*cis* to *all-trans* isomerization is required, an additional reprotonation step of the RSB has to occur from M. Surprisingly, the recovery of the parent state spectrum is by two orders of magnitude faster at the higher pH value. In accordance with the data discussed previously, this result stresses that a close interaction between the

RSB and the counterion is maintained at all times during the photocycle,<sup>[238]</sup> which probably leads to a fast response to changes of the retinal configuration. In contrast to M, however, the retinal is significantly more twisted in the early stages of the photocycle



## 4.2 Optimization of Coumarin Photochemistry

which could hamper the near-UV-induced reversion. Still, to obtain a deeper insight into the quenching mechanism, further experiments in the IR are needed. The results demonstrated here can be seen as a proof of principle, which needs to be subjected to further optimization of the experimental as well as sample parameters. If the SBS turns out to be a generalized feature in mRhos, the major advantage of near-UV quenching - as opposed to BLQ - would lie in the specific targeting of different photointermediates with just one spectral signature. Its spectral position in between the dominant absorption bands of mRhos allows a continuous or pulsed illumination at the corresponding wavelength with a reduced risk of inducing unwanted secondary dynamics.

## 4.2 Optimization of Coumarin Photochemistry

### 4.2.1 Introduction

The demand for optically controllable systems in many branches of the life sciences has risen tremendously in the recent decade. In contrast to most photoreceptors, which are evolutionary optimized for their light-triggered functionality, the key challenge for the design of photochemical compounds lies in finding a reasonable balance between functionality and efficiency. When it comes to PPGs, two photophysical properties are of major importance: the excitation wavelength and the uncaging QY. The latter is a measure of how efficiently the energy of the absorbed photons is used for the actual release of the LG. Considering the bandwidth of available PPGs with QYs ranging from fractions of a percent up to the double digits, questions about the driving determinants of these differences occur.

One way to approach this problem is to take a look at the pathway of the *excess* energy which does not end up in the uncaging reaction. Possible deactivation pathways of this kind usually involve radiationless decays through interactions with the solvent, structural reorganization or even relaxation under emission of a photon either from the singlet (fluorescence) or triplet state (phosphorescence). These processes do not just compete with each other but also with the desired photochemical reaction, which - in the case of uncaging - often occurs on a timescale of several hundred ps up to ns.

The main objective of this project was therefore centered around finding ways to keep the photon energy in the molecular system so that the uncaging process becomes more favorable. The hereby used strategy involved not just the identification but also the suppression of possible competitive deactivation pathways. Conceptually, this has been done on many fluorophores to optimize the emission QY. Building on previous

work in this regard as well as the in-house expertise on several PPG-classes, the model-systems of choice are based on coumarin compounds. Specifically the DEACM-based fluorophore ATTO 390 was chosen as a precursor, which was functionalized into a PPG and systematically modified (Fig. 4.12). The additional six-membered ring in the ATTO 390 compounds leads to a significant loss of rotational degrees of freedom at the nitrogen atom which in turn suppresses the formation of a TICT state. This rigidity was enhanced even further by introducing a double bond at the 6-position of the ring. To test the effects of hydrogen bonding, the hydrogen atom at the nitrogen has been replaced by an ethyl group. The LG of choice was serotonin, which plays a crucial role in the signal transduction pathway in the central nervous system. It was attached to the PPG via a carbamate linkage. Overall, this resulted in four pairs of newly designed test compounds, which were compared to DEACM and DEACM-serotonin as reference in terms of photochemical performance (Fig. 4.12 and 4.13). The design of these compounds and the optimization of the involved synthesis strategies was done by Robin Klimek (group of Prof. Alexander Heckel). Furthermore all compounds discussed here are labeled identically to the original publication (ref. i) to simplify cross-referencing. In section 4.2.2 the main focus is put on the solvent-dependent photochemical characterization and the implications on the uncaging process. The results are then contextualized and summarized in an overall photochemical model in section 4.2.3.

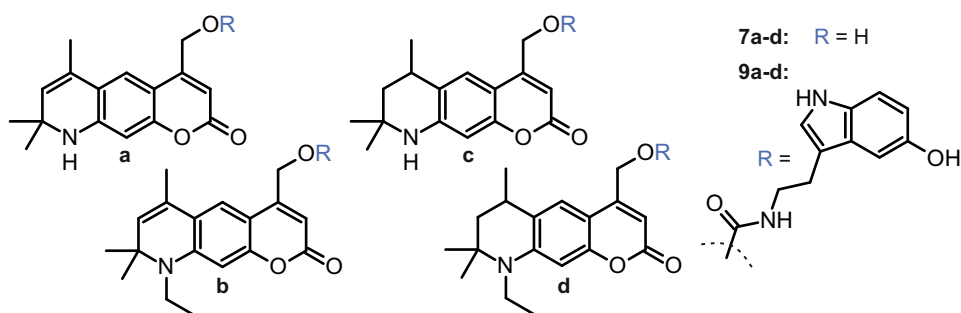


FIGURE 4.12: Overview of the ATTO-derived compounds without (7a-d) and with a serotonin LG (9a-d).

## 4.2.2 Photochemistry

As introduced in section 2.4.1, coumarins undergo an ICT from the benzylic to the pyranone moiety upon photoabsorption.<sup>[175]</sup> This ICT leads to a strong interaction with the surrounding solvent, which in turn influences the overall ES dynamics.<sup>[173,174]</sup> To

## 4.2 Optimization of Coumarin Photochemistry

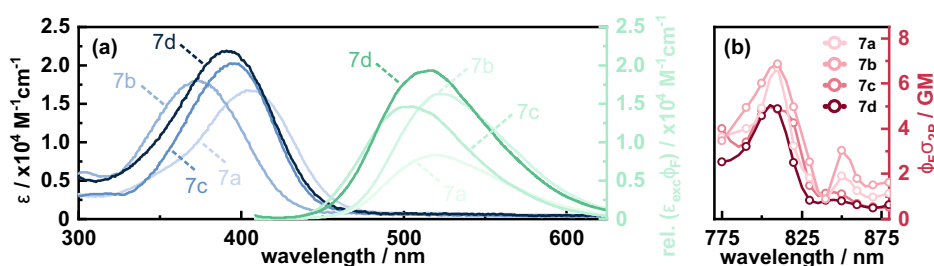


FIGURE 4.13: The corresponding absorption and fluorescence spectra (a) and 2P action cross sections (b) of compounds 7a-d in PBS.

account for these effects, most of the experiments were performed in several solvents with varying polarity and proticity namely toluene, DMSO, MeOH and phosphate-buffered saline (PBS). Indeed, the solvent effects on the respective compounds are already clearly visible in the corresponding steady state absorption and fluorescence spectra. The Stokes' shifts are most dominant in polar and protic solvents, underlining a more pronounced stabilization of the CT state in these conditions.

Compared to the DEACM reference, all compounds furthermore exhibit a strong fluorescence similar to the structurally close ATTO 390 fluorophore. This result is not surprising due to the inactivated TICT pathway as a result of the implementation of the 6-membered ring. Surprisingly, in protic solvents the additional double bond in 7a and 7b does not affect the fluorescence QY as much as the substitution of the hydrogen by an ethyl group in 7b and 7d, which implies that the fluorescence is quenched by hydrogen bonding at the nitrogen proton. This also needs to be considered in the evaluation of the 2P action cross sections  $\phi_F \sigma_{2P}$ , which are determined by 2PIF. Even though the  $\phi_F \sigma_{2P}$  of 7a-7d are relatively close in the range of 5-7 GM, the highest values are found for 7a and 7b. Here it is noteworthy that the  $\phi_F$  of 7a is 0.5, whereas it is 0.9 for 7b, demonstrating that the actual 2PA strength could be shrouded by other parameters related to the experiment of choice. An overview of the most relevant steady state characteristics of 7a-7d can be found in the original publication.

The ES dynamics of 7a-7d have been investigated in a similar manner. To simplify the discussion, the general features will be introduced on the example of 7a in MeOH (Fig. 4.14a). With the population of the ES right after photoexcitation, a broad ESA<sub>S</sub> around 620-730 nm as well as a SE<sub>1</sub> in the range of 430-550 nm - being consistent with the steady state fluorescence - occurs. Temporally delayed, a second absorption signal ESA<sub>ICT</sub> is formed in the blue end of the spectrum. This signature becomes more pronounced on the 1-50 ps timescale, which is accompanied by a decrease of the ESA<sub>S</sub> band and a

strong red-shift from SE<sub>1</sub> into SE<sub>2</sub>. This dynamic shift is the consequence of solvent reorganization due to the formed CT state. The ICT character is less stabilized in toluene (Fig. 4.14b) and DMSO, which is reflected in significantly smaller dynamic Stokes' shifts of the SE. Instead, an additional absorption ESA<sub>T</sub> around 600 nm is formed at 100 ps. This signature can be attributed to the formation of a triplet state, which is seemingly facilitated in an aprotic environment. Albeit the stabilizing factor of solvent polarity is easily extractable from the data, the effects of solvent proticity are more complicated.

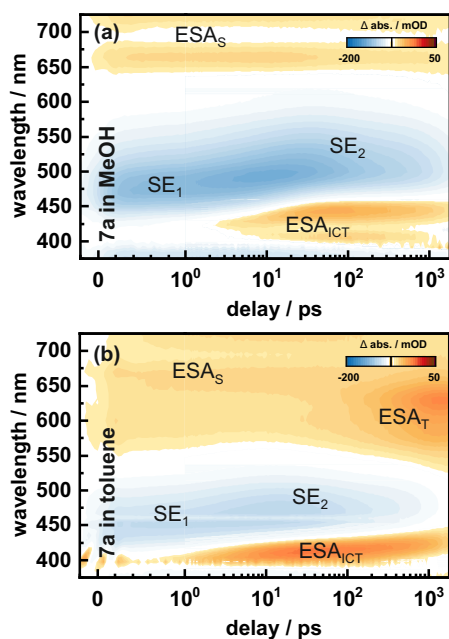


FIGURE 4.14: Excited state dynamics of 7a in MeOH (a) and toluene (b).

depending on the mole fraction of the mixture with a maximum effect at a 1:2 ratio (DMSO:water).<sup>[240]</sup> The DMSO content in the used solvent mixture is significantly smaller, however in the local environment of the coumarin compounds it is most likely increased. This locally nonideal mixing behaviour results in a change of the overall solvent polarity, proticity and viscosity and hence in a hampered stabilization of the ICT.

The dominance of this phenomenon is even reflected in the uncaging experiments of the respective compounds 9a-9d, which were performed by Volker Hermanns of the Heckel group. In the initial high-performance liquid chromatography (HPLC) measurements of 9a-9d in a PBS/DMSO mixture, no appreciable increase of the uncaging QY  $\phi_u$

In general there are three possible sites for hydrogen bonding in coumarin compounds.<sup>[239]</sup> Hydrogen bonds with the carbonyl oxygen or the nitrogen-bound proton usually stabilize the CT state, whereas a hydrogen bond with the lone-pair of nitrogen leads to the stabilization of a GS-like configuration. All these effects have to be considered for a thorough explanation of the dynamic behaviour in the ES of coumarins. Interestingly, in the PBS/DMSO (9:1) mixture, which was necessary due to low solubility in pure PBS, the aforementioned reasoning seems to break down. Even though the solvent mixture contains highly polar and protic groups, the formation of the CT state is significantly less pronounced as seen in the corresponding ESA<sub>ICT</sub> (Fig. 4.15). An explanation for this effect is given by the inter-solvent interactions. It is known that DMSO and water form highly ordered clusters

## 4.2 Optimization of Coumarin Photochemistry

TABLE 4.2: Uncaging QYs of compounds 9a-9d and the DEACM-Ser reference in PBS/MeOH.

	DEACM-Ser	9a	9b	9c	9d
$\phi_u$	0.0056	0.0256	0.0297	0.0163	0.0096
$\phi_u \epsilon / \text{M}^{-1} \text{cm}^{-1}$	50	504	617	173	184

compared to the DEACM-serotonin reference was obtained.

Here, two aspects of the inter-solvent interactions between DMSO and water come into play: the reduced stabilization of the CT state and the coordination of DMSO molecules in the direct vicinity of the reactive site. It was shown in previous work<sup>[173,174]</sup> that the redistribution of electron density facilitates the elongation of the C–C bond, which needs to be cleaved in the uncaging process. Yet, the DMSO/water clusters prevent such a stabilization. At the same time the water molecules, which are needed for a nucleophilic attack to form the photoproduct, are shielded by the tight DMSO network around the PPG. In contrast, after substitution of DMSO with MeOH as a co-solvent in the PBS mixture, compounds 9a-9d all show a significant increase in  $\phi_u$  relative to the reference (table 4.2). Compounds 9a and 9b, which contain an additional double bond at the 6-position, are even 5-6 times more efficient. This result confirms the initial hypothesis of this work that an inactivation of competing decay channels results in an enhanced photochemical output.

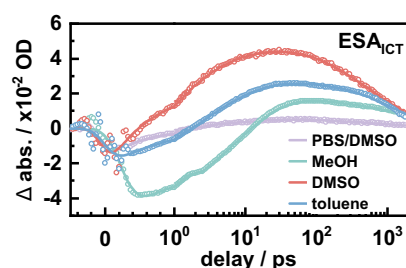


FIGURE 4.15: Solvent dependent transients of  $\text{ESA}_{\text{ICT}}$  in 7a.

### 4.2.3 Generalized Model

Based on the systematic investigation on key structural features as well as the influence of solvent polarity and proticity, it is possible to formulate a minimalistic model for the photochemistry of coumarins (Fig. 4.16). Initially after photoexcitation, the locally excited state (LE) is populated which is in equilibrium with the CT state. The redistribution of charge alongside the molecule leads to a subsequent reorganization of the surrounding solvent. Polar solvents and hydrogen bonds with either the nitrogen-bound proton or the carbonyl oxygen induce a further stabilization of the CT state, which is reflected in a strong Stokes' shift as indicated in the steady state and time-resolved data.

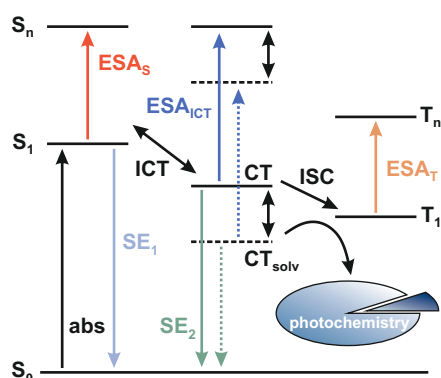


FIGURE 4.16: Schematic representation of the ES pathways in ATTO-based compounds.

In contrast, nonpolar solvents and hydrogen bonding with the lone-pair of nitrogen rather stabilize a GS-like configuration. The lacking stabilization of the CT state - such as shown in toluene - ultimately results in the formation of a triplet state via ISC on the hundreds of ps timescale. The uncaging reaction, however, just occurs with a reasonable QY if the CT is stabilized sufficiently. This is explained by two aspects. First, the increased density of negative charge at the pyranone moiety leads to a pre-weakening of the cleavable C–C bond and in turn to a stabilization of the prospective carbocation. Second, the photochemical reaction - in this case uncaging - happens on the

timescale of hundreds of ps or even ns, which requires the reactive system to be long-lived enough. Even though the primary goal was centered around the structural optimization of coumarin-based PPGs, the results clearly underline that similar care has to be taken in terms of the molecular environment. The solvent does not just partake in the uncaging reaction but it also plays a crucial role in the modulation of the ES pathways. This complicates the analysis and prediction of the involved photochemistry to a major degree, due to the dynamic nature of the solvent (re-)arrangement, which is often overlooked in common characterization protocols.

## 4.3 One- and Two-photon Sensitization of BODIPY-based PPGs

### 4.3.1 Introduction

When it comes to the optimization of PPGs, in addition to the improvement of the uncaging QY, which was the main focus of the study in section 4.2, it is also crucial to work on the molecules ability to actually collect photons of very specific wavelengths. Here, the concept of photo-sensitization comes into play, which allows a targeted modification of the spectral properties in a molecule. In the simplest case this is done directly at the basic structure of question by systematically adding functional groups, which for example extend the  $\pi$ -electron system or significantly change the oscillator strength of a wanted transition. An alternative way is given by combining the functional

### 4.3 One- and Two-photon Sensitization of BODIPY-based PPGs

molecule with one (or several) chromophores which then act as photon-antennas (or photo-sensitizers).

To make this work, the major requirement - besides the necessity to collect photons - lies in the ability to transfer the acquired photon energy to the functional site. Consequently, in addition to selecting a sufficiently suitable sensitizer it is also necessary to find an appropriate way of linking the molecular systems together. This comes with the challenge to match the photophysical properties of all constituents on the one side, while also guaranteeing an optimal structural arrangement, so that the energy transfer (ET) process can occur as efficient as possible. The structural design is mainly dependent on the nature of the ET process, which could for example come in the form of Förster-resonance energy transfer (FRET) over larger distances or a CT in electronically coupled systems. The study on such molecular systems has been an integral part of the scientific profile in several research groups of the CLiC consortium.

Projects of this sort include the modulation of fluorescence in photoswitchable BODIPY-DTE dyads<sup>[241]</sup> or the 2PA-sensitization of a DEACM-PPG.<sup>[165]</sup> In the latter case, ATTO 390 was used as the photosensitizer. It was shown that excitation of the sensitizer indeed leads to the release of the LG from the DEACM-PPG. The energy flow from ATTO 390 to DEACM, however, was mediated by  $\pi$ -stacking of the aromatic systems which was mainly supported by intramolecular hydrogen bonding at the linker itself. Still, this proof-of-principle was the starting point for the project discussed in the following. Here, several conceptual changes and improvements were considered. First, the excitation range was moved towards the red end of the visible spectrum due to a prospective use in the phototherapeutic window. This also includes the implementation of an inherently strong 2P-absorber as an antenna. Second, a major focus was put on the actual ET which was required to be fast and efficient without leading to any side-reactions or structural changes (i.e.  $\pi$ -stacking).

All these aspects should result in a spectrally broadly addressable molecular-dyad, which could be functionalized as a PPG. Ultimately, a rhodamine-BODIPY dyad was designed as the base compound and tested as the PPG with p-nitroaniline (PNA) as the LG (ref. ii). In the course of this project, several iterative adjustments on the molecular design and spectral properties have been done, requiring a tight collaborative network of synthesis, theoretical modeling and spectroscopic characterization. Rebekka Weber (group of Prof. Alexander Heckel) was responsible for the structural design and the corresponding synthesis strategy. On the theory side this project was driven by Carsten Hamerla, Maximiliane Horz and Dr. Madhava S. Niraghatam (group of Prof. Irene Burghardt). In the next sections, critical results of this iterative process ranging from

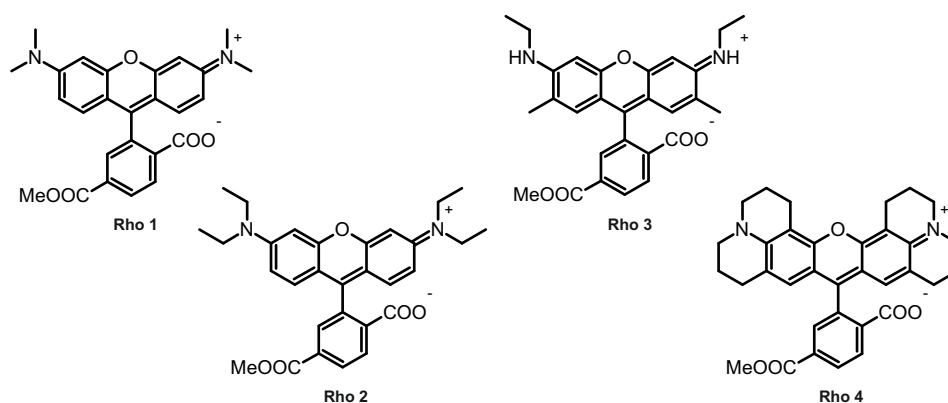


FIGURE 4.17: Chemical structures of Rho 1-4.

the selection of a suitable sensitizer (section 4.3.2), over the characterization of the ET (section 4.3.3) up to the actual tests on the uncaging properties (section 4.3.4), will be given.

### 4.3.2 Finding the right Antenna

The first part of the project dealt with the identification of suitable photosensitizers which meet the requirements explained above, including a relatively red-shifted absorption maximum, high 2PA cross sections and suitable fluorescence properties. The latter requirement is especially important for the ET to the actual PPG. With this reasoning the main focus was set on rhodamine compounds, which are known to be excellent fluorophores with a high tunability.<sup>[242,243]</sup> Even though rhodamines 1-4 (Fig. 4.17) share the same core structure, their spectroscopic properties vary by large margins.

Whereas the structurally very close Rho 1 and Rho 2 are quite similar in terms of

TABLE 4.3: Photophysical properties of the tested antenna compounds Rho 1-4 in MeOH.

	$\lambda_{abs}$ nm	$\epsilon_{max}$ $M^{-1}cm^{-1}$	$\lambda_{em}$ nm	$\phi_F$	$\tau_F$ ps	$\sigma_{2P}\phi_F$ GM
<b>Rho 1</b>	542	86500	571	0.41	2.66	30-80
<b>Rho 2</b>	549	67000	578	0.47	2.25	30-80
<b>Rho 3</b>	519	69800	548	0.91	4.16	15-30
<b>Rho 4</b>	572	117000	597	0.84	4.96	60-110



### 4.3 One- and Two-photon Sensitization of BODIPY-based PPGs

absorption and fluorescence, Rho 3 and Rho 4 are significantly blue- or red-shifted, respectively. They furthermore exhibit roughly double the fluorescence QY of Rho 1 and Rho 2. This is also reflected in the ES lifetimes obtained by fs-TA and TCSPC. The reason for this stabilized ES in Rho 3 and Rho 4 lies in the steric barrier which decreases the rotational degrees of freedom of the benzoic acid moiety and therefore the rate of energy loss to the solvent.

The structural features of rhodamines also contribute to their generally strong 2PA response. Due to molecular symmetry, the absorption of two photons leads to a transition from the HOMO-1 (symmetric) to the LUMO (symmetric), which corresponds energetically to  $S_0 \rightarrow S_2$  and is strictly 1PA-forbidden.<sup>[244]</sup> In turn this also poses some experimental and conceptual problems since all time-resolved measurements are based on 1PA. For instance, the energetically weaker  $S_0 \rightarrow S_1$  transition must not necessarily lead to the same photochemical pathway as the 2PA case. In the particular case of rhodamines, this means that two requirements have to be met. First, the population of  $S_2$  is followed by a very fast crossing to  $S_1$ . Second, this crossing must then lead to similar photodynamics as if  $S_1$  was populated directly. One attempt to at least partially test this was given by excitation of the even higher energetic  $S_0 \rightarrow S_3$  transition, which indeed yielded similar spectral changes and corresponding lifetimes as the  $S_0 \rightarrow S_1$  case. Consequently, the population of  $S_1$  from  $S_3$  must occur significantly faster than the temporal resolution of the experiment (<200 fs).

Finally, the 2P action cross-sections were obtained by 2PIF in the range of 780-880 nm. Here, some drastic differences are observed in the direct comparison of the compounds. Again, Rho 1 and Rho 2 share similar values ranging from 30 to 80 GM. However, Rho 3 has a comparably weak action cross section which is lower than 30 GM over the whole spectral probing range. In contrast, Rho 4 exceeds with values of more than 80 GM over almost the whole spectrum. Considering all of the measured photophysical quantities (Fig. 4.3), Rho 4 clearly stands out as the superior photosensitizer. The spectral properties

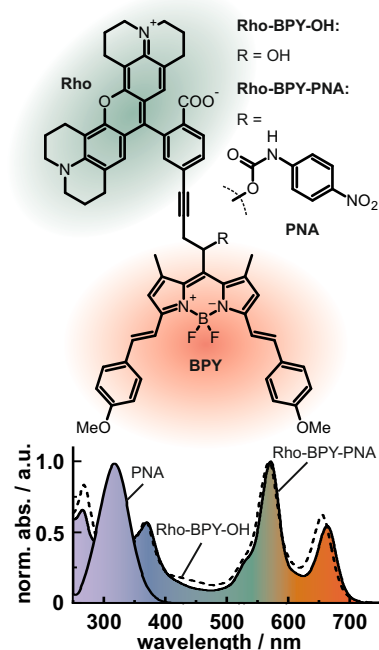


FIGURE 4.18: Chemical structure of the dyad system with and without LG and the corresponding absorption spectra.

of the rhodamine antenna also dictate the requirements for the actual acceptor molecule and prospective PPG. The hereby chosen BODIPY base structure therefore needed some structural modifications to match its absorption spectrum with the fluorescence of Rho 4. The extension of the  $\pi$ -electron system was achieved by the attachment of a styryl-group at position 3 and 5 of BODIPY, respectively, which shifts the absorption maximum to 660 nm. Rho 4 and the modified BODIPY were then coupled through an alkyne-linkage forming Rho-BPY-OH (Fig. 4.18).

### 4.3.3 The Energy Transfer Process

The dynamics right after photoexcitation were followed by fs-TA experiments on the individual compounds Rho and BPY, as well as the Rho-BPY-OH dyad itself. Hereby, fs-pulses of 560 nm and 660 nm central wavelength were used to account for the respective absorption maxima of the molecules at question. As expected, the dynamics of Rho and BPY are mainly characterized by a long-lived ES which starts to decay in the hundreds of ps up to ns timescale.

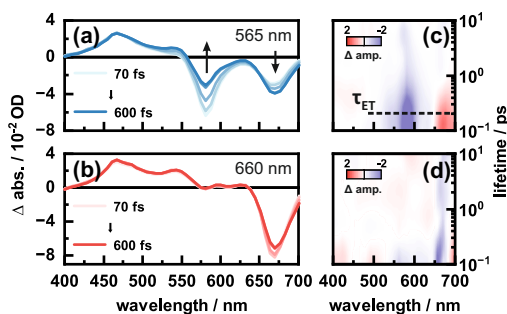


FIGURE 4.19: Photodynamics of the first 600 fs after excitation of Rho-BPY-OH with 565 nm (a) or 660 nm (b) pulses and their respective lifetime densities (c) and (d).

The more interesting cases are given by excitation of the Rho-BPY-OH dyad (Fig. 4.19). Here, the activation of the BPY moiety with 660 nm pulses (Fig.4.19b) leads to similar dynamics as seen in the isolated BPY compound, albeit with a reduced ES lifetime. This implies that in the dyad the Rho part is not influenced by the local excitation of BPY, yet the relaxation process is slightly accelerated. This looks different after excitation of the photosensitizer (Fig.4.19a), which leads to a clearly mixed dynamics with features of both, the Rho and BPY ES. The most dominant spectral signatures are given by the two bleaching signals  $GSB_{Rho}$  and  $GSB_{BPY}$  (Fig. 4.20a), which correspond to the absorption maxima of Rho and BPY, respectively.

### 4.3 One- and Two-photon Sensitization of BODIPY-based PPGs

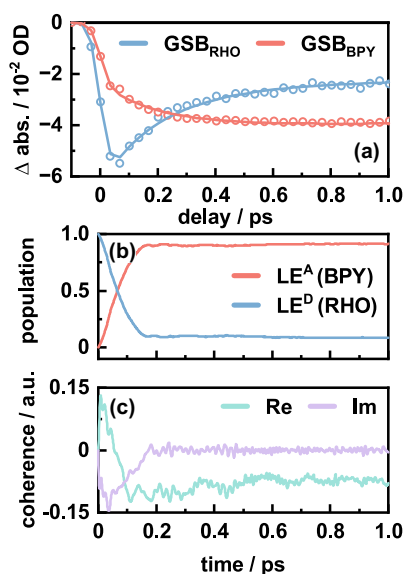


FIGURE 4.20:  $\text{GSB}_{\text{Rho}}$  and  $\text{GSB}_{\text{BPy}}$  representing the ET process (a). Corresponding LE populations (b) and coherence lifetimes (c).

The kinetic analysis via LDA, reveals that the ES population is transferred from the Rho moiety to the BPy part of the molecule in the course of less than 600 fs. This becomes even more obvious by comparing the temporal traces of  $\text{GSB}_{\text{Rho}}$  and  $\text{GSB}_{\text{BPy}}$  directly. Whereas,  $\text{GSB}_{\text{Rho}}$  decreases down to 50% of its initial value,  $\text{GSB}_{\text{BPy}}$  reaches more than 90% of its overall maximum value on a similar timescale. The obtained experimental result speaks for an efficient ET which is relatively fast compared to similar molecular dyads. To learn more about the energetic and mechanistic details of this process, the system was subjected to electronic structure calculations based on time-dependent density functional theory (TD-DFT) as well as a thorough quantum dynamics (QD) analysis based on multi-layer multiconfiguration time-dependent Hartree (ML-MCTDH).

The ES analysis of the Rho-BPy-OH dyad shows three 1PA bright states ( $S_1$ ,  $S_2$  and  $S_3$ ) with significant oscillator strengths and one additional dark state  $S_4$ . Both,  $S_1$  and  $S_3$ , are localized on the BPy moiety, whereas  $S_2$  and the dark  $S_4$  correspond to local ES of Rho. In fact, the  $S_4$  is exclusively populated by 2PA due to molecular symmetry of the HOMO-3 $\rightarrow$ LUMO+1 transition. With the knowledge about the energetic landscape of the system, a more detailed look was put into the QD computation which focussed mainly on the ET process. In the framework of this analysis, two diabatic LEs of the donor (Rho) and acceptor (BPy) part of the dyad have been modeled. Details on the exact model, the included vibrational modes, the coupling constants and the energetic offsets can be found in the supplementary information of the original publication (ref. ii).

The central result is best represented in the time-evolving diabatic populations of  $\text{LE}^{\text{A}}$  and  $\text{LE}^{\text{D}}$  and their corresponding coherences. The initial population of  $\text{LE}^{\text{D}}$  decreases whilst  $\text{LE}^{\text{A}}$  becomes populated in the course of approximately 200 fs (Fig. 4.20b). Similarly, the imaginary part of the coherence decays to zero, whereas the real part levels off at a constant value, which is explained by the formation of a weighted population equilibrium between  $\text{LE}^{\text{D}}$  and  $\text{LE}^{\text{A}}$  (Fig. 4.20c).

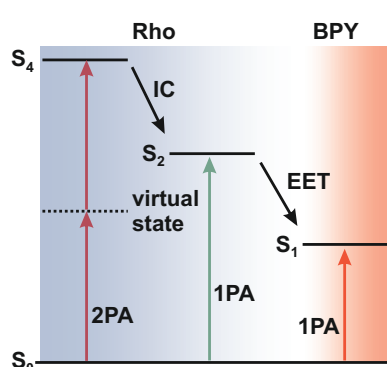


FIGURE 4.21: Energy diagram representing crucial pathways after 1PA or 2PA.

the  $S_2$  is directly populated via 1PA at Rho. This stresses again that the hereby proposed dyad can indeed act as a broadly absorbing system with an efficient and fast ET pathway.

The QD computations and the experimental data fit quite nicely, even though the former yields slightly faster ET times. One of the reasons for this mismatch could be due to the omission of explicit solvent effects in the theoretical model. Still, putting the obtained experimental and computational results together one can come up with a complete description of the photodynamics in Rho-BPY-OH (Fig. 4.21). Excitation of the dyad via 2PA leads to the population of the localized  $S_4$  which becomes depopulated by an ultrafast IC to the localized  $S_2$ . From here, the system undergoes an ET from the Rho moiety to the localized  $S_1$  of BPY. A similar scenario occurs when

#### 4.3.4 Applicability as PPG

The functionality of the dyad was tested by attaching the commonly used PNA as the LG. Besides its small size, which reduces the potential risk of significant changes in the photochemistry of the compound, another advantage of PNA normally lies in the spectral shift as a result of the uncaging process.<sup>[195]</sup> The uncaging experiments were performed under constant cw irradiation with LEDs of 565 nm and 660 nm central wavelength over the course of 100 min.

The first observation is the similarity of the time-resolved spectral changes in both irradiation cases. The dynamics is mostly dominated by the bleaching of the BPY absorption in the near-UV and the vis. Strikingly, the absorption change of the corresponding bands is almost 3-fold as strong by excitation of the Rho part of the molecule. Yet, this again speaks for the ability of Rho to collect photons (high  $\epsilon$ ) and transfer the energy efficiently. It also stresses that both excitation wavelengths lead to the same photochemical output. Unfortunately, the near-UV band also overlaps with the expected read-out signal of the liberated PNA. Here, only a small spectral shoulder around 280-300 nm can be identified, which is most likely the result of the blue-shift of the PNA absorption (Fig. 4.22a and b) or the difference in the UV contribution of both, Rho-BPY-OH and Rho-BPY-PNA. To test this, a similar irradiation experiment was done on the initial Rho-BPY-OH dyad, which does not contain a LG.

### 4.3 One- and Two-photon Sensitization of BODIPY-based PPGs

The corresponding difference spectra differ in terms of spectral shape and their spectral shifts. The shape indicates that there is a significant overlap between the reactant and the product absorption. In fact, the spectral changes hint at a cleavage of the styryl-groups at BPY, which is reflected in the blue-shift of the BPY absorption bands around 360 nm and 660 nm due to a reduction of the  $\pi$ -system. In addition, in contrast to Rho-BPY-PNA, no spectral shift is observed in the near-UV (Fig. 4.22). This at least qualitatively demonstrates that PNA is cleaved as a result of the irradiation. However, a quantitative assessment of the uncaging kinetics or an estimate of the uncaging QY is difficult to obtain for this compound. Here it is important to note that a change of the LG or an improvement of the uncaging QY of the BPY scaffold might lead to a better photochemical performance, but it would also require a change of the overall structure. It is not necessarily guaranteed that the ET characteristics found for Rho-BPY-OH or Rho-BPY-PNA would apply to such an altered compound. Consequently, TD-DFT and QD calculations on several rhodamines and BODIPYs (some of which have already been screened in the framework of this project) are crucial to determine important structural features and to predict similar functionalities.

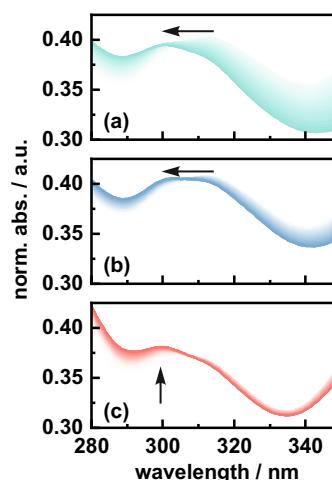


FIGURE 4.22: Spectral changes in the region of the PNA absorption after illumination of Rho-BPY-PNA with (a) 565 nm or (b) 660 nm. No shift is observed in Rho-BPY-OH after illumination with 565 nm light (c).



## Concluding Remarks

Overall, this work has explored different approaches of optical control in a biochemically relevant context. This has been done on the molecular level, either in the form of a photoreceptor (here KR2) or in the form of more flexibly usable PPGs, but also in terms of the more technical and photophysical aspects of the activation or deactivation of such molecular systems. Even though the main focus of this written work lies on the spectroscopic results, all projects discussed here have been strongly collaborative, involving a broad range of different techniques. This reflects the interdisciplinary nature of many of the currently driving questions in photochemical research, which are – in many cases - ultimately targeted at medical or pharmaceutical advances.

First, the light-driven sodium pump KR2 was investigated which became popular due to its possible application as an optogenetic tool. In a comparative study of KR2s sodium and proton pumping mode, it was possible to identify important mechanistic principles for the proteins functionality as a sodium pump. This includes the direct involvement of specific structural features such as N112 and/or the ECL1-domain in the ion-translocation pathway, as well as the tight interplay between the retinal chromophore and its counterion D116. At the same time this IR study offered one of the first mechanistic insights into the proton pumping photocycle in KR2, which was significantly less explored. In collaboration with the Glaubitz lab, a closer look was put into the structural changes of the chromophore and its surrounding during the different photointermediates via DNP-enhanced ssNMR and optical spectroscopy. Here, time-resolved IR measurements in the HOOP-mode region helped to follow the dynamic changes of the chromophore configuration and twisting. It was shown that retinal is in fact reisomerized to its *all-trans* configuration in the O-intermediate, but remains noticeably more twisted compared to its DS configuration. This was further substantiated by the results obtained in the near-UV region, which is often omitted in the characterization of mRhos. The newly found signature turned out to be a SBS of the *13-cis* configuration of the retinal chromophore, which vanishes with the formation of O in KR2. Besides the obvious utilization as a spectral marker, the SBS transition was also explored

## Chapter 5 Concluding Remarks

in terms of its applicability for optical control experiments. Similarly to the BLQ-effect, it was possible to regenerate the KR2 parent state by application of fs near-UV pulses to a PSS. By varying the sample conditions it was possible to specifically target K (pH 5) or M (pH 9), which furthermore allowed a differentiation of the quenching dynamics from different starting points. These results alongside the hereby proposed experimental concept can be used as a basis for more advanced multiphoton excitation schemes in the context of optogenetics.

In contrast to the rather large and complex photoreceptors, PPGs – amongst others - offer a more delicate way to specifically target and control biochemical reactions. In this context, two characteristics are of major importance: The ability of the PPG to absorb photons of specific wavelengths and the efficiency of the desired photochemical response. The latter aspect has been investigated under the working hypothesis that the reduction of competing deactivation channels in PPGs leads to a higher uncaging QY. This has been tested on DEACM-based model compounds, which were systematically modified in order to pinpoint different ES pathways. By simply adding an additional six-membered ring – now being more similar to ATTO fluorophores – the uncaging QY was increased by 2- to 3-fold compared to DEACM. This could even be more improved (up to a factor of 5-6) by further planarization of the system with an extra double bond at the C6 position. The excitation of the coumarin moiety leads to a LE which is in equilibrium with the CT state. Depending on the local environment, most importantly determined by the solvent proticity and polarity, the CT state or a more GS-like configuration is stabilized. The electronic redistribution in this CT state also leads to a pre-weakening of the cleavable C-C bond, which is a prerequisite for the uncaging reaction. It was furthermore demonstrated that the additional decay channel due to the uncaging reaction leads to a more than 2-fold decrease of the ES lifetime in the functionalized PPG. This could be potentially used as a photophysical readout for the uncaging reaction by spectroscopic or – with the addition of spatial resolution – by microscopic means as in fluorescence lifetime imaging microscopy.

The wide range of applications for PPGs leads to the design of a similarly wide array of different PPG classes with different spectral properties. This optimization for very specific conditions comes at the cost of flexibility, which might be necessary when data needs to be collected by different techniques. This problem was tackled by designing a spectrally broadly addressable molecular dyad based on a Rho photosensitizer and BPY as prospective PPG. The Rho antenna was chosen under consideration of sufficient 2PA cross sections, optimal ES characteristics and structural suitability for the attachment to BPY. Indeed, the ET between the Rho and BPY moieties turned out to be extraordinarily



fast and highly efficient. It was shown – in tandem with computational analysis - that the excitation of Rho by either 1PA or 2PA end up in the same photochemical pathway as a direct 1P excitation of the BPY, which allows the utilization of an overall spectral range from 500-900 nm. The uncaging reaction itself was qualitatively verified, but a quantitative assessment remains difficult due to spectral overlap of the corresponding signals in the UV. Certainly, a further improvement of the uncaging properties as well as the spectral readout strategy needs to be the main focus for the further development. Here, the spectroscopic and computational results offer a useful blueprint for the determination of crucial functional sites and possible modifications.



# Publications

The supplementary information of each publication is electronically available at the respective publisher websites and are not included in this written thesis.

## 6.1 Declaration of Author Contributions

Peer-reviewed publications as first or co-first author (indicated by <sup>†</sup>):

(i) **Inactivation of competitive decay channels leads to enhanced coumarin photochemistry**

R. Klimek <sup>†</sup>, M. Asido<sup>†</sup>, V. Hermanns, S. Junek, J. Wachtveitl and A. Heckel,  
Chem. Eur. J., **2022**, e202200647.

- Two-Photon characterization, time-resolved spectroscopic measurements (TCSPC, fs-TA) on all compounds of interest, evaluation of the experimental data, formulation of a photochemical model, interpretation of the overall results (together with all co-authors and PIs)
- Writing of the spectroscopic part of the manuscript, providing figures (spectroscopy part)

(ii) **Ultrafast and Efficient Energy Transfer in a One- and Two-Photon Sensitized Rhodamine-BODIPY Dyad: A Perspective for Broadly Absorbing Photocages**

M. Asido<sup>†</sup>, C. Hamerla<sup>†</sup>, R. Weber<sup>†</sup>, M. Horz<sup>†</sup>, M. S. Niraghatam, A. Heckel, I. Burghardt and J. Wachtveitl,  
Phys. Chem. Chem. Phys., **2022**, 24, 1795-1802.

- Steady-state and time-resolved spectroscopic measurements (TCSPC, fs-TA) on all compounds of interest, evaluation of the experimental data, interpretation of the overall results (together with all co-authors and PIs)

## Chapter 6 Publications

- Writing of the manuscript and coordination of the writing process, providing figures (spectroscopy part, TOC)
- (iii) **Transient near-UV Absorption of the Light-Driven Sodium Pump *Krokinobacter eikastus* Rhodopsin 2: A Spectroscopic Marker for Retinal Configuration**  
M. Asido<sup>†</sup>, R. K. Kar<sup>†</sup>, C.N. Kriebel, M. Braun, C. Glaubitz, I. Schapiro and J. Wachtveitl, *J. Phys. Chem. Lett.*, **2021**, 12, 6284-6291.
- Steady-State and time-resolved spectroscopic measurements (ns-FP, fs-TA) on KR2 in different conditions, near-UV quenching experiments, evaluation of the experimental data, interpretation of the overall results (together with all co-authors and PIs)
  - Writing of the manuscript and coordination of the writing process, providing figures (spectroscopy part, TOC)
- (iv) **Time-resolved IR spectroscopy reveals mechanistic details of ion transport in the sodium pump *Krokinobacter eikastus* Rhodopsin 2**  
M. Asido, P. Eberhardt, C. N. Kriebel, M. Braun, C. Glaubitz and J. Wachtveitl, *Phys. Chem. Chem. Phys.*, **2019**, 21, 4461-4471.
- Steady-state and time-resolved spectroscopic measurements (IR and UV/vis ns-FP) on KR2 in different conditions, evaluation of the experimental data, band assignment, interpretation of the overall results (together with all co-authors and PIs)
  - Writing of the manuscript and coordination of the writing process, providing figures (spectroscopy part, TOC)

Other peer-reviewed publications:

- (v) **Probing the photointermediates of light-driven sodium ion pump KR2 by DNP-enhanced solid-state NMR**  
O. Jakdetchai, P. Eberhardt, M. Asido, J. Kaur, C. N. Kriebel, J. Mao, A. J. Leeder, L. J. Brown, R. C. D. Brown, J. Becker-Baldus, C. Bamann, J. Wachtveitl and C. Glaubitz, *Sci. Adv.*, **2021**, eabf4213.
- Time-resolved IR measurements in the HOOP-region, evaluation of the IR data, band assignment, interpretation of the overall results (together with all co-authors and PIs)

## 6.1 Declaration of Author Contributions

- Writing the IR spectroscopy part of the manuscript, providing figures (IR spectroscopy part)

(not explicitly discussed in this thesis)

### (vi) **Sensitizer-enhanced two-photon patterning of biomolecules in photoinstructive hydrogels**

H. Krüger, M. Asido, J. Wachtveitl, R. Tampé and R. Wieneke,  
Comm. Mat., **2022**, 3.

- Two-Photon characterization of the sensitizer, fluorescence measurements (quantum yield determination), evaluation of the spectroscopic data
- Writing of the spectroscopy parts of the manuscript, providing figures (spectroscopy part)

## 6.2 Klimek *et al.*, Chem. Eur. J., 2022

### **Inactivation of competitive decay channels leads to enhanced coumarin photochemistry**

R. Klimek<sup>†</sup>, M. Asido<sup>†</sup>, V. Hermanns, S. Junek, J. Wachtveitl and A. Heckel,  
Chem. Eur. J., **2022**, e202200647.

# Inactivation of Competitive Decay Channels Leads to Enhanced Coumarin Photochemistry

Special  
Collection

Robin Klimek<sup>+</sup>,<sup>[a]</sup> Marvin Asido<sup>+</sup>,<sup>[b]</sup> Volker Hermanns,<sup>[a]</sup> Stephan Junek,<sup>[c]</sup> Josef Wachtveitl,<sup>\*,[b]</sup> and Alexander Heckel<sup>\*,[a]</sup>

**Abstract:** In the development of photolabile protecting groups, it is of high interest to selectively modify photochemical properties with structural changes as simple as possible. In this work, knowledge of fluorophore optimization was adopted and used to design new coumarin-based photocages. Photolysis efficiency was selectively modulated by inactivating competitive decay channels, such as twisted intramolecular charge transfer (TICT) or hydrogen-bonding, and the photolytic release of the neurotransmitter serotonin

was demonstrated. Structural modifications inspired by the fluorophore ATTO 390 led to a significant increase in the uncaging cross section that can be further improved by the simple addition of a double bond. Ultrafast transient absorption spectroscopy gave insights into the underlying solvent-dependent photophysical dynamics. The chromophores presented here are excellently suited as new photocages in the visible wavelength range due to their simple synthesis and their superior photochemical properties.

## Introduction

In recent years, the use of light has gained enormous interest in the life sciences. An increasing number of research groups focusses on the use of photolabile protective groups (so-called “photocages”) to regulate biological processes.<sup>[1–5]</sup> Aside from the application, however, also the development of new photocages is of high interest.<sup>[6,7]</sup> In order to be able to use light for targeted regulation, the photo-physical and -chemical properties of protecting groups have to match the requirements of the biological context. Here, especially two parameters are of crucial importance. The first is the excitation wavelength, preferably in the red range of the visible light spectrum and the second is the uncaging efficiency of the respective photocage. Regarding the first parameter, many studies have been

published that focused on shifting the extinction maximum to longer wavelengths.<sup>[8,9]</sup>

Taking the coumarin photocage as an example, popular methods were the extension of the  $\pi$ -system, or the addition of donor and acceptor substituents (see Figure 1a).<sup>[10–13]</sup> Also with other photolabile protecting groups, for example BODIPY,<sup>[14,15]</sup> fluorenyl,<sup>[16,17]</sup> or nitrobenzyl<sup>[18,19]</sup> a considerable red-shift was achieved with similar approaches. Nevertheless, the improvement of the second parameter, the uncaging efficiency, has not

[a] R. Klimek,<sup>+</sup> V. Hermanns, Prof. Dr. A. Heckel  
Institute for Organic Chemistry and Chemical Biology  
Goethe University Frankfurt  
Max-von-Laue Str. 9, 60438 Frankfurt (Germany)  
E-mail: heckel@uni-frankfurt.de

[b] M. Asido,<sup>+</sup> Prof. Dr. J. Wachtveitl  
Institute of Physical and Theoretical Chemistry  
Goethe University Frankfurt  
Max-von-Laue Str. 9, 60438 Frankfurt (Germany)  
E-mail: wweitl@theochem.uni-frankfurt.de

[c] Dr. S. Junek  
Max Planck Institute for Brain Research  
Max-von-Laue Str. 4, 60438 Frankfurt (Germany)

[<sup>+</sup>] These authors contributed equally to this work.

Supporting information for this article is available on the WWW under <https://doi.org/10.1002/chem.202200647>

This manuscript is part of an Indo-German special collection.

© 2022 The Authors. Chemistry - A European Journal published by Wiley-VCH GmbH. This is an open access article under the terms of the Creative Commons Attribution License, which permits use, distribution and reproduction in any medium, provided the original work is properly cited.

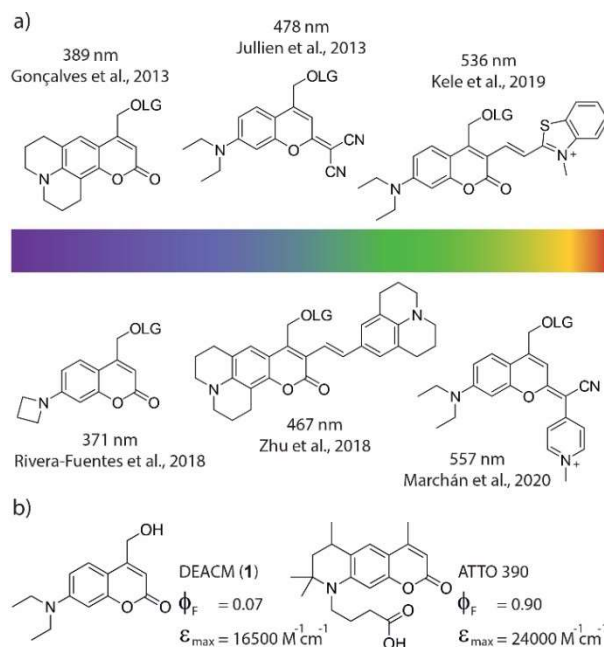


**Figure 1.** a) Selection of prominent coumarin based photocages in recent years and their reported absorption maxima. LG = leaving group. b) Structures and photophysical properties of DEACM 1 and ATTO 390.<sup>[29]</sup>

been studied as systematically in the recent literature. Still, this is highly important, because if the applied light can be used more efficiently, side effects such as cell damage can be reduced.

Efficient photolysis means that the chromophore must have both a high extinction coefficient ( $\epsilon$ ) and a good uncaging quantum yield ( $\phi_u$ ). To increase the uncaging efficiency of a photocage, it is important to understand what other processes compete with the photolytic cleavage of a leaving group. A molecule in the excited state can release its energy through a variety of pathways (see Jablonski diagram, Figure 2a). In the fast range, there are rotations, vibrations, and isomerization around single atoms or bonds. Also, internal conversion (heat loss to the solvent)<sup>[20]</sup> or hydrogen-bonding<sup>[21]</sup> can lead to relaxation to the ground state.<sup>[22]</sup> If the excited state lives long enough (e.g. nanoseconds) and does not decay in any of the faster channels, the molecule can also release the energy via luminescence,<sup>[23]</sup> or a directed bond cleavage.

To date, there is only little information on how to rationally optimize the uncaging quantum yield of photocages. However, there are many advanced studies that have successfully optimized the performance of fluorophores.<sup>[24–26]</sup> Extinction coefficients and absorbance maxima have been modified. Unwanted photoreactions (e.g. photobleaching) and the amount of deactivation processes that happen earlier than fluorescence have been reduced. In many cases also the water solubility has been improved. Therefore, a possible strategy to develop new photocages with improved photolysis can be to use an optimized fluorophore with one major decay channel as a guide – an analogy that has recently also been followed by *Rivera-Fuentes et al.*<sup>[27]</sup> – and divert the excited state population into an uncaging reaction pathway.

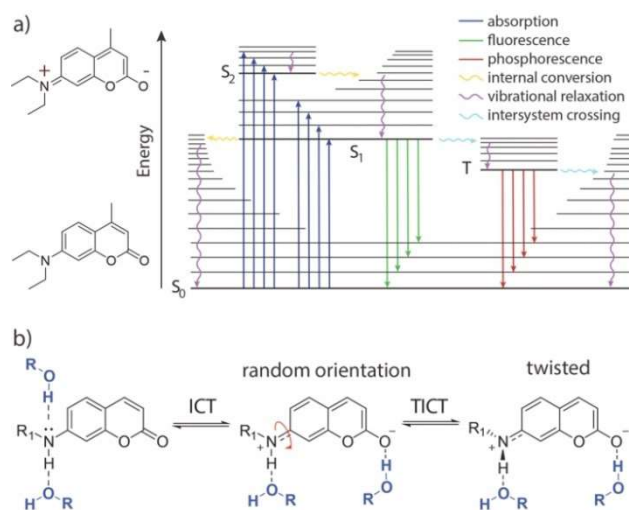


**Figure 2.** a) Jablonski diagram showing relevant transitions of coumarin chromophores when excited with light.  $S_0$ : ground state,  $S_1$ : first electronically excited singlet state,  $S_2$ : second electronically excited singlet state, T: triplet state. b) General model for twisted intramolecular charge transfer (TICT) in coumarin dyes. In addition, possible hydrogen-bonding sites are shown, that can affect non-radiative decay.

In this study, we explored this idea using ATTO 390<sup>[28,29]</sup> as an example, which has a fluorescence quantum yield of more than 90% in aqueous solution. Here, we show how to improve the uncaging cross section ( $\epsilon\phi_u$ ) of new ATTO 390-based photocages by up to one order of magnitude compared to literature known DEACM (1) (Figure 1b), applying principles from fluorophore optimization. Using ultrafast transient absorption spectroscopy, we gain insight into the fundamental photo-physical processes that are critical both for fluorescence as well as for photolytic cleavage of a leaving group. Overall, we demonstrate that understanding excited state decay channels in fluorophores can be helpful for developing new photocages.

## Results and Discussion

In coumarin fluorophores substituted like the one shown in Figure 2b, it is known that the molecule can adopt an intramolecular charge transfer (ICT) state.<sup>[30–32]</sup> After excitation, a rotation around the C–N bond at the donor moiety can occur. Thereby, repulsive interactions are minimized and charge separation is stabilized. The resulting twisted intramolecular charge transfer (TICT) state can release its energy to the medium non-radiatively.<sup>[33,34]</sup> In addition, as indicated in Figure 2b, it is possible that coumarins release their energy to the environment via hydrogen bonding.<sup>[21,35–37]</sup> However, a restricted rotation around the C–N bond is known to suppress the TICT and therefore increase fluorescence.<sup>[38]</sup> This can be observed, for example, with ATTO 390, in which the exocyclic nitrogen atom is fixed by a six-membered ring. Therefore, ATTO 390 shows a high fluorescence quantum yield in comparison to freely rotating coumarins like DEACM (1).

Guided by this principle, we synthesized four new coumarin photocages **7a–d** (see Figure 3) which have a structure similar to ATTO 390. In all four compounds, the rotation around the C–N bond is restricted by a six-membered ring. Compounds **7a** and **7b** were additionally equipped with a double bond at the 6-position, which should make the framework even more rigid and the rotation more confined (see Figure 3b). By using this double bond, we hoped to limit non-radiative energy release on short time scales. The coumarin photocage should be even less capable of forming a TICT. However, derivatives **7b** and **7d** also featured an additional ethyl group on the nitrogen atom at the 7-position. This exhibits an electron donating character compared to the proton in **7a** and **7c** and should thus enhance the charge transfer character formation originating from the nitrogen that is necessary for uncaging. The absence of a hydrogen-atom can also prevent possible non-radiative decay upon hydrogen-bonding with protic solvents<sup>[34–37,39]</sup> and eliminates a potentially photoacidic site.<sup>[40,41]</sup>

The synthesis of compounds **7a–d** started from commercially available *m*-aminophenol **2** (see Figure 3a). In the first step, the hydroxy group of **2** was protected with *tert*-butyldimethylsilyl (TBDMS) in a quantitative yield. The resulting compound **3** was reacted with acetone under  $\text{Yb}^{3+}$  catalysis to quinoline **4a** in a Doebner-Miller type reaction.<sup>[42]</sup> Starting from **4a**, compound **4b** was obtained via alkylation with iodoethane



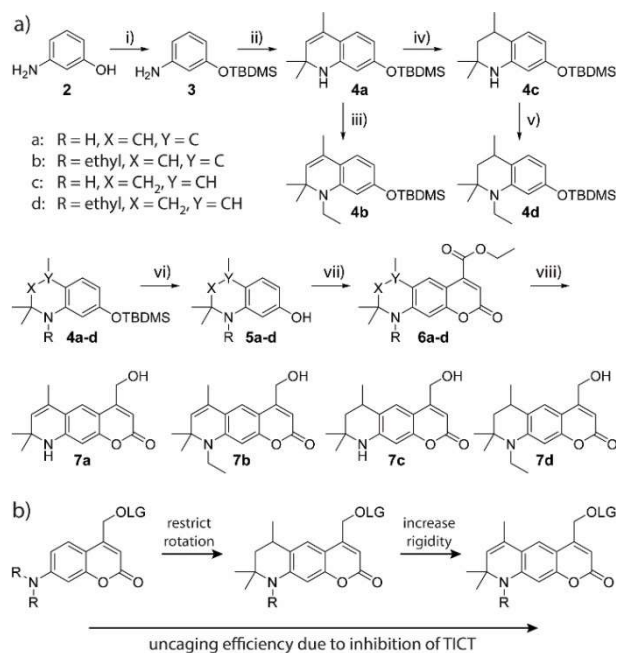


**Figure 3.** a) Synthesis of compounds **7a–d**. i) TBDMS–Cl, imidazole, DCM, quant. ii) Yb(OTf)<sub>3</sub>, acetone, 77%. iii) iodoethane, Cs<sub>2</sub>CO<sub>3</sub>, MeCN, 78%. iv) Pd/C, H<sub>2</sub>, MeOH, 98%. v) iodoethane, Cs<sub>2</sub>CO<sub>3</sub>, MeCN, 83%. vi) TBAF, AcOH, THF, 89–94%. vii) sodium diethyl oxalacetate, EtOH, 31–47%. viii) NaBH<sub>4</sub>, MeOH, 37–62%. TBDMS = tert-butyldimethylsilyl. b) Evolution of new coumarin-photocages with improved uncaging efficiency due to inhibition of intramolecular twisting. LG: leaving group, R: H/ethyl, TICT: twisted intramolecular charge transfer.

and Cs<sub>2</sub>CO<sub>3</sub> under microwave irradiation and **4c** was isolated after selective hydration with H<sub>2</sub>, Pd/C under atmospheric pressure in excellent yields. Hydration needed to be performed before the silyl protecting group was removed. Otherwise, we observed cleavage of the C–N bond at 7-position with H<sub>2</sub>, Pd even at very short reaction times. The reduced compound **4c** was also alkylated with iodoethane to get **4d**. The TBDMS-groups of **4a–d** were removed with tetrabutylammonium fluoride (TBAF) and glacial acetic acid in 89–94% yields to give alcohols **5a–d**. Pechmann-condensation based on a procedure of Begoyan et al.<sup>[43]</sup> resulted in coumarin esters **6a–d**. During the reaction, several side products occurred that were hard to separate from the main product by column chromatography. Recrystallization further removed impurities but also resulted in poorer yields. Therefore, we decided to use compounds **6a–d** for further reactions after single column chromatography with minor impurities. After the reduction of the respective esters with NaBH<sub>4</sub>, the alcohols **7a–d** were isolated in good yields and purities.

To evaluate the photophysical properties of compounds **7a–d**, one-photon (1P) absorption and fluorescence spectra were recorded in different solvents (see Figure 4 and Table 1). We compared the data to the most commonly used coumarin photocage DEACM (**1**) and ATTO 390 as reference compounds. In PBS (phosphate-buffered saline), compounds **7a–d** showed higher extinction coefficients in their absorption maxima ( $\epsilon_{\text{max}}$ ) than DEACM (**1**). Compared to ATTO 390 the  $\epsilon_{\text{max}}$  of **7a–d** were

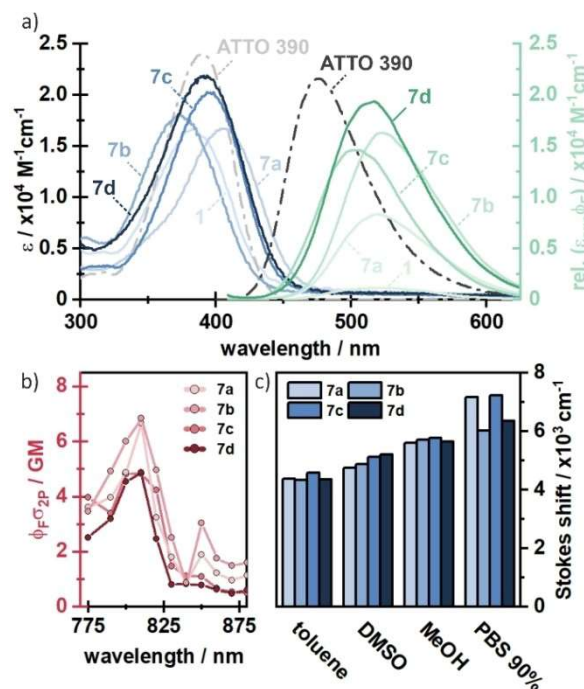


**Figure 4.** a) Steady-state absorption and fluorescence spectra of compounds **7a–d** in PBS. Spectra of ATTO 390 (taken from ATTO-tec<sup>[29]</sup>) and compound **1** are added for comparison. b) Two-photon absorption spectra of compounds **7a–d**. c) Stokes shifts in different solvents with different polarity.

**Table 1.** Photophysical properties of compounds **1**, ATTO 390<sup>[29]</sup> and **7a–d**.

	$\epsilon_{\text{max}}$ (PBS) [ $\text{M}^{-1} \text{ cm}^{-1}$ ]	$\lambda_{\text{abs}}$ (PBS) [nm]	$\lambda_{\text{em}}$ (PBS) [nm]	$\phi_{\text{F}}$ (PBS)	$\phi_{\text{F}}$ (DMSO)
<b>1</b>	16500	385	520	0.07	0.74
ATTO 390	24000	390	476	0.90	–
<b>7a</b>	16700	383	528	0.50	0.51
<b>7b</b>	18100	405	536	0.90	0.51
<b>7c</b>	20300	373	511	0.72	0.89
<b>7d</b>	21500	394	526	0.95	0.92

slightly smaller. Compound **7d**, which has the most similar structure to ATTO 390 has also the lowest difference in the extinction coefficient. In general, an increased extinction coefficient compared to DEACM (**1**) is already a promising start towards the desired increase of the uncaging cross section  $\epsilon\phi_{\text{U}}$ . The absorption maxima themselves ( $\lambda_{\text{max}}$ ) were located between 373 nm and 405 nm. Thus, they were in the same range as the absorption maxima of DEACM and ATTO 390. The strongest shift was observed for compound **7b**, which had a 20 nm bathochromic wavelength shift relative to DEACM. Nevertheless, a minimal blue shift of 13 nm could also be observed for compound **7c**. In comparison, the data indicated that the compounds with the additional ethyl group showed a more red-shifted absorption spectrum. Compound **7d** ( $\lambda_{\text{max}} = 394 \text{ nm}$ ) absorbs most similarly to ATTO 390 ( $\lambda_{\text{max}} = 390 \text{ nm}$ ), what again can be rationalized with their very similar structure. The additional double bond in compound **7b** ( $\lambda_{\text{max}} = 405 \text{ nm}$ ) further increases the absorption wavelength. This red-shifting

effect of the double bond can also be observed when comparing compounds **7c** ( $\lambda_{\text{max}}=373$  nm) and **7a** ( $\lambda_{\text{max}}=383$  nm).

To evaluate whether our new coumarin compounds can also be excited with NIR light, we measured two photon absorption spectra of compounds **7a–d**. Here, we observe a two-photon absorption of 5–7 GM at 800–810 nm for all measured compounds (Figure 4b), which is in the same range as ATTO 390 (13 GM).<sup>[44]</sup> This 2P-transition is energetically equivalent to the main absorption maxima found at around 380–410 nm (Figure 4a), indicating that the proposed compounds can be one- or two-photon activated. This measurement shows that excitation is also possible in the so-called phototherapeutic window (650–950 nm), in which light has a particularly high penetration depth into biological tissue.<sup>[45]</sup>

To get a first impression of how the newly synthesized chromophores release their excitation energy, we measured fluorescence quantum yields (see Table 1). Since fluorescence and uncaging occur on approximately the same time scale, this parameter may provide a first indication of successful inactivation of faster decay channels. Additionally, comparing polar solvents (such as PBS) to less polar ones (such as DMSO) may indicate whether TICT is involved. For medium polar solvents like DMSO, it is known that coumarin charge separation is only stabilized to a limited extent, resulting in a high  $\phi_F$ , independent of their flexibility.<sup>[46]</sup> It is also possible that rotation around the C–N bond is hindered in solvents with relatively high viscosity, such as DMSO.<sup>[47]</sup>

In aqueous solution, however, the amine substituent can rotate freely if it is not fixed by a six-membered ring, since water is less viscous. This is in agreement with the measured high  $\phi_F$  for compounds **7a–d** and DEACM (**1**) in DMSO, ranging between 51% and 95%. When DMSO was replaced by PBS, the  $\phi_F$  of DEACM (**1**) was reduced from 74% to 7% whereas fluorescence of **7a–d** remained on a high level. This reduction in fluorescence suggests that rotation around the C–N bond in DEACM is possible in less viscous PBS, but it is inhibited in all newly synthesized derivatives **7a–d**. In turn, this points towards a TICT state in DEACM, which is hindered in compounds **7a–d**. The fluorescence quantum yields further show that the two compounds with the ethyl group **7b** and **7d** emit best in PBS. This can be explained by the fact that the ethyl group can stabilize the charge separation more effectively over a longer period of time. A similar quantum yield in PBS (90%) is shown by ATTO 390 itself, which also carries an alkyl group at the nitrogen atom.

To investigate the effect of stabilization of charge separation in more detail, we also studied the Stokes shifts in different polar solvents (see Figure 4c). Again, the polarity of the solvent is expected to have a strong influence on the emission wavelength. We observed that all compounds **7a–d** showed already large Stokes shifts in unpolar solvents (4334–4583  $\text{cm}^{-1}$  in toluene). When the polarity of the solvent was increased, an overall rise in the Stokes shifts was observed. The largest Stokes shifts were measured in PBS buffer (6035–7240  $\text{cm}^{-1}$ ), supporting that there is charge transfer in all molecules which is stabilized by the solvent to different degrees.

To gain an even deeper insight into the photophysical dynamics of the newly synthesized compounds, we employed ultrafast UV/vis transient absorption spectroscopy in different solvents. Here, the general spectral features of these compounds shall be explained exemplarily in the case of compound **7a** in MeOH (see Figure 5a). The photoexcitation from the ground state leads to a broad excited state absorption ( $\text{ESA}_S$ ) signature, which spans from 620 nm up to more than 730 nm. Simultaneously, the stimulated emission ( $\text{SE}_1$ ) from  $S_1$  to  $S_0$  can be found in the range of 430–550 nm, which is consistent with the steady state fluorescence spectra. After about 300–500 fs, an additional absorption signal ( $\text{ESA}_{\text{ICT}}$ ) appears at approximately 400 nm and 430 nm. The amplitude of the 430 nm component rises further on the 1–50 ps timescale, which is accompanied by a decrease of the  $\text{ESA}_S$  band and a strong red-shift of the stimulated emission by 40 nm forming  $\text{SE}_2$  (Figure 5a and 5c). The latter effect is related to the excited state intramolecular charge transfer (ICT) from the nitrogen of the amine group to the oxygen of the carbonyl group, which is further stabilised by the solvent response on the ps timescale.

In contrast to compound **7a**, it can be observed that in compound **7b** (Figure S1b, Supporting Information) the blue component of the  $\text{ESA}_{\text{ICT}}$  feature at around 400 nm is mainly populated, which means that the excited state is more stabilized in **7b** relative to **7a**. The less pronounced stabilization of the excited state in **7a** most likely results from a hydrogen

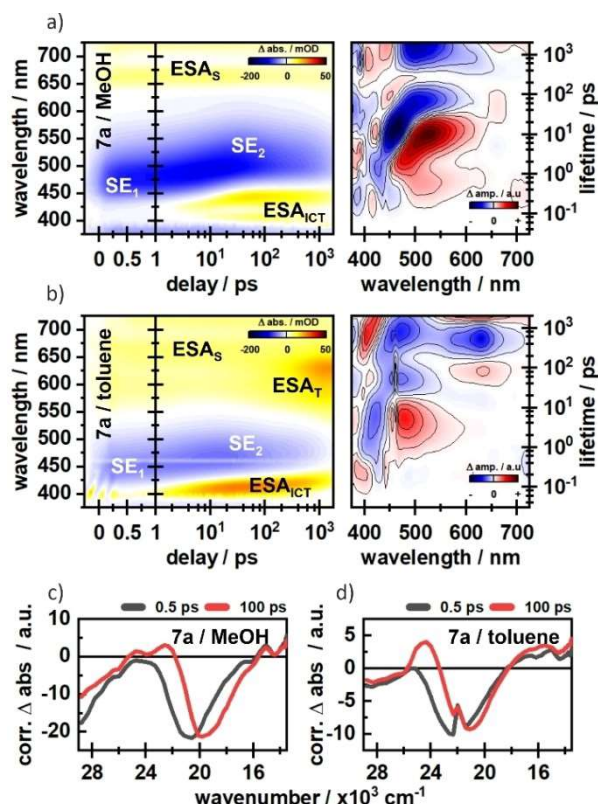


Figure 5. Transient absorption spectra of compound **7a** in MeOH (a) and toluene (b). Time slices at 0.5 ps and 100 ps underline the dynamic Stokes shifts in c) MeOH and d) toluene.

bond at the nitrogen, which is formed in addition to the stabilizing hydrogen bond at the carbonyl group.<sup>[27]</sup> In toluene, compound **7a** shows a miniscule dynamic Stokes-shift of the SE band (Figure 5b and 5d). However, the  $ESA_{ICT}$  is still formed, indicating a population of an ICT state, which is less stabilised by the surrounding solvent. Instead, an additional absorption ( $ESA_T$ ) around 600 nm is formed on the 100 ps timescale, which we tentatively assign to triplet formation. A similar  $ESA_T$  signature is found for **7a** in DMSO (Figure S1c, Supporting Information), which is also aprotic but significantly more polar. Therefore, the excited state dynamics are not just strongly influenced by the solvent polarity, but also by the solvent proticity and the general accessibility of hydrogen bonding interactions. Besides the obvious stabilization of the excited state in polar solvents, the effect of solvent proticity is more complicated, since there are different sites for hydrogen bonding. Whereas hydrogen bonds with the carbonyl oxygen or the nitrogen-bound proton are reported to have a stabilising effect on the excited state, a hydrogen bond with the lone-pair of nitrogen has the opposite effect.<sup>[35–37]</sup> The reduction of energy in the ICT state due to these effects leads to a favourable ICT-population. In contrast, the population of the triplet state is seemingly facilitated in the case of missing hydrogen bonding.<sup>[48–50]</sup> Further details on the solvent effects as well as cross-comparisons between the compounds are given in the Supporting Information of this article. The transient absorption measurements demonstrated that all four new compounds form an ICT state. The ethyl group in compound **7b** seems to further stabilize the charge separation in comparison to compound **7a** as can be seen in the significantly increased  $ESA_{ICT}$  amplitudes (Figure S1, Supporting Information). However, this effect is not seen in the direct comparison of compounds **7d** and **7c** (see Figure S2, Supporting Information), which lack the additional double bond.

But even more interesting to us was, whether the added rigidity of the new compounds would also lead to improved photolysis. Therefore, we attached serotonin as a biologically active leaving group (see Figure 6). Serotonin is an important

neurotransmitter that plays a crucial role in signal transduction in the central nervous system.<sup>[51]</sup> The synthesis started by reacting compounds **7a–d** with carbonyldiimidazole (CDI) under microwave irradiation resulting in **8a–d**. To generate the final photolabile protected serotonin-derivatives **9a–d**, compounds **8a–d** were reacted with 5-hydroxytryptamine hydrochloride. The same procedure was used to synthesize DEACM-protected serotonin **11**, starting from DEACM (**1**) as a reference.

After preparation we performed first photolysis tests in PBS/DMSO (9:1). We added this small amount of DMSO because the photocages were only moderately soluble in pure PBS. To make the photolysis results comparable, the quantum yields for compounds **9a–d** and **11** were determined at 405 nm using a fulgide derivative as actinometer.<sup>[52]</sup> The decrease of starting materials was monitored by HPLC with the addition of an internal standard. After the experiments, we were surprised that the uncaging quantum yields for compounds **9a–d** and **11** differed only minimally from each other. This contradicted all assumptions from previous literature and the earlier determined fluorescence behaviour of the compounds. The fluorescence experiments indicated that competitive relaxation pathways in compounds **7a–d** were blocked which in turn leads to an increased fluorescence quantum yield compared to DEACM. Since fluorescence and uncaging occur on the same time scale, the uncaging quantum yield of compounds **9a–d** should also be enhanced in direct comparison to reference compound **11**.

To investigate this unexpected outcome in more detail, we performed ultrafast transient absorption spectroscopy in PBS/DMSO (9:1). Interestingly, in this solvent, the amplitudes of the difference signals are significantly reduced (Figure S1b and f, S2b and f). This becomes most obvious in the  $ESA_{ICT}$  band, which is the dominant feature in all measurements. In contrast to the other tested solvents, the  $ESA_{ICT}$  does not show a major rise in amplitude on the 10–100 ps timescale in PBS/DMSO (Figure S3), implying a less pronounced population of the CT state. However, it was shown in recent work<sup>[53]</sup> that the charge separation is crucial in order to facilitate elongation of the C–C bond, which is cleaved in the subsequent uncaging process. Additionally, the solvent response due to the ultrafast change in dipole moment is somewhat more complicated in PBS/DMSO mixtures. It is reported that DMSO and H<sub>2</sub>O form strong hydrogen bond clusters even at small amounts of DMSO.<sup>[54,55]</sup> For simple coumarin-based compounds this means that the solvent reorganization in the excited state is mostly driven by DMSO, which “drags” H<sub>2</sub>O along through their H-bond network.<sup>[56]</sup> It is therefore possible that DMSO at the photochemically relevant site suppresses photocleavage in a PBS/DMSO mixture due to the less pronounced CT character and a possible shielding from H<sub>2</sub>O. The latter aspect is especially relevant since water molecules (or other nucleophiles) are needed to capture the carbo-cation which is formed during uncaging.<sup>[57]</sup>

Therefore, we substituted PBS/DMSO with PBS/MeOH (1:1) in further experiments, because MeOH and H<sub>2</sub>O do not interact as strongly, and MeOH itself can serve as a nucleophile to trap the exocyclic carbocation in the coumarin scaffold formed

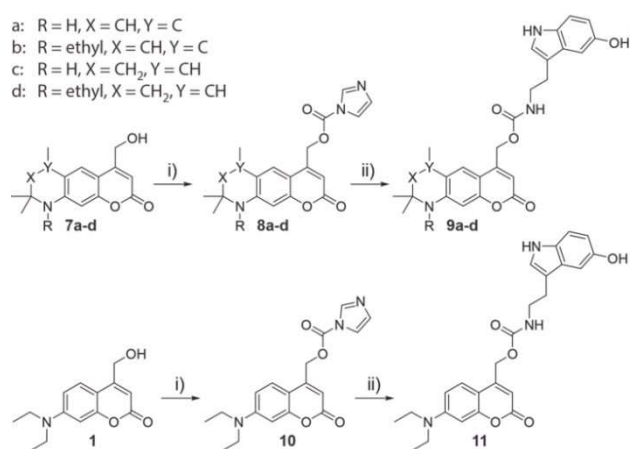


**Figure 6.** Synthesis of compounds **9a–d** and **11**. i) CDI, DCM, 79–89%. ii) 5-Hydroxytryptamine hydrochloride, Et<sub>3</sub>N, DMF, 56–77%.

during uncaging. After changing the solvent, we were now able to see clear differences in uncaging quantum yield between the newly synthesized compounds **9a–d** and the reference DEACM derivative **11**. The photolysis results are shown in Table 2. An exemplary photolysis curve of compound **9b** is shown in Figure 7, the remaining curves are shown in Figures S6–S10. Our experiments show, that the uncaging quantum yield ( $\phi_u$ ) was already significantly increased by the ring closure in **9c** and **9d**. While **11** releases serotonin with a  $\phi_u$  of 0.56%, it is increased by a factor of 2–3 in compounds **9c** (0.96%) and **9d** (1.63%). This already shows the positive effect of the restricted rotation. If an additional double bond is now introduced, a further increase in the uncaging quantum yield can be observed. Compound **9a** releases serotonin with a quantum yield of 2.56% and **9b** even with 2.97%. As expected, this increase in quantum yield clearly indicates that the additional restricted rotation suppresses competitive decay channels. Therefore, a more than fivefold increase in uncaging quantum yield was observed for **9b** compared to **11**. The improvement of the photochemical properties becomes even more obvious if the extinction coefficient  $\epsilon$  at the excitation wavelength is included in order to study the uncaging cross section ( $\phi_u \epsilon$ ). It can be seen in Table 2, that solely adding a six-membered ring

**Table 2.** Photophysical and photochemical properties of compounds **9a–d** and reference DEACM **11** at 405 nm used for uncaging experiments in PBS/MeOH (1:1).

	$\phi_u$ (405 nm) (PBS/MeOH)	$\epsilon$ (405 nm) (PBS/MeOH) [ $M^{-1} \text{ cm}^{-1}$ ]	$\phi_u \epsilon$ (405 nm) (PBS/MeOH) [ $M^{-1} \text{ cm}^{-1}$ ]
<b>11</b>	0.0056	9097	50
<b>9a</b>	0.0256	19666	504
<b>9b</b>	0.0297	20788	617
<b>9c</b>	0.0163	10606	173
<b>9d</b>	0.0096	19268	184

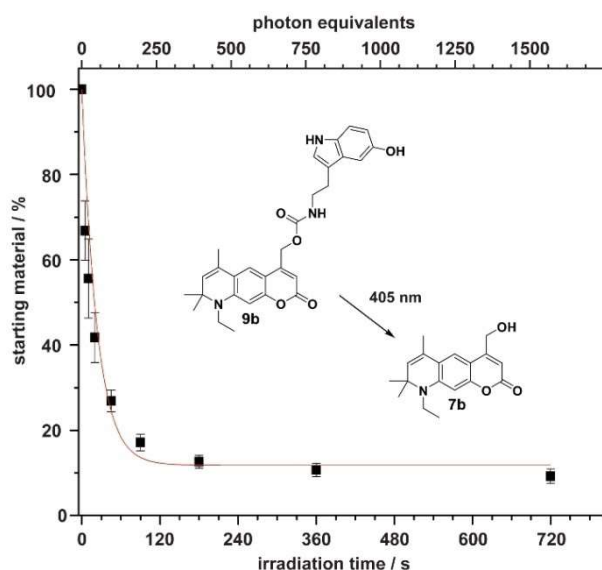


**Figure 7.** Exemplary photolysis curve of compound **9b** in PBS/MeOH (1:1). Photolysis product **7b** was identified via mass spectrometry.

leads to an increase by a factor of 3–4 compared to DEACM. When the double bond is additionally introduced, the uncaging cross section at 405 nm raises by one order of magnitude. While **11** photolyzes with  $50 \text{ L mol}^{-1} \text{ cm}^{-1}$  at 405 nm, the best compound **9b** shows  $617 \text{ L mol}^{-1} \text{ cm}^{-1}$ . Compound **9d**, on the other hand, which has a similar structure as **9b** only without a double bond, has a cross section of  $184 \text{ L mol}^{-1} \text{ cm}^{-1}$ . At this point, it is clear that the simple introduction of a double bond can lead to a more than threefold increase in photolysis efficiency.

In the last step, we wanted to investigate whether uncaging as an additional excitation pathway can also be observed using ultrafast UV/vis pump-probe transient absorption spectroscopy. For this purpose, we sought to compare the derivatives with leaving group (**9a–d**) with those previously measured without leaving group (**7a–d**, see Figure 5). The measurements of **9a–d** revealed very similar photophysical signatures compared to **7a–d**. All compounds show the characteristic solvent- and time-dependent ESA and Stokes shifts on the picosecond timescale. More interestingly, we observed that the excited state (ES) decay of **9a–d** is shifted towards earlier times compared to **7a–d**, which can be seen in the lifetime density distribution of the respective measurements (Figures 8a and 8b, and Figure S5). To validate this temporal shift we performed time correlated single photon counting (TCSPC) measurements in PBS/MeOH (1:1) (Figure 8c). These experiments showed a very clear difference in the fluorescence lifetimes of **7a–d** and **9a–d**. While the fluorescence lifetimes of **7a–d** are found to be between 4.6 and 5.4 ns, the fluorescent states of **9a–d** are depopulated between 2 and 2.6 ns (Table S1), being consistent with the lifetimes found in the TA-experiments (Figure S5). This more than 2-fold reduction of radiative decay lifetimes is most likely due to added possibility to undergo photocleavage, which is competing with fluorescence. An overview of the proposed energy pathways is given in Figure 8d.

## Conclusion

In this work, we show a systematic investigation of uncaging efficiency of coumarin photolabile protecting groups. Guided by the principles of fluorophore optimization, we wanted to reduce competitive decay channels on new ATTO 390-based photocages. To improve the photolysis, in a first step, the rotation around the electron donor on the coumarin scaffold was prevented using a simple six-membered ring (compounds **7c** and **7d**). This already increased the uncaging efficiency by a factor of 3–4 compared to DEACM (**1**). However, the simple introduction of an additional double bond on that six-membered ring had an even stronger effect. Again, the efficiency of light-induced release of serotonin was increased by a factor of 2–3 (compounds **6a** and **6b**). This is the first time that such a minimal change to the coumarin backbone has resulted in a significant improvement in photolysis efficiency. We used ultrafast transient absorption spectroscopy to investigate the underlying photophysical dynamics. The newly synthesized photocages showed strong solvent dependencies

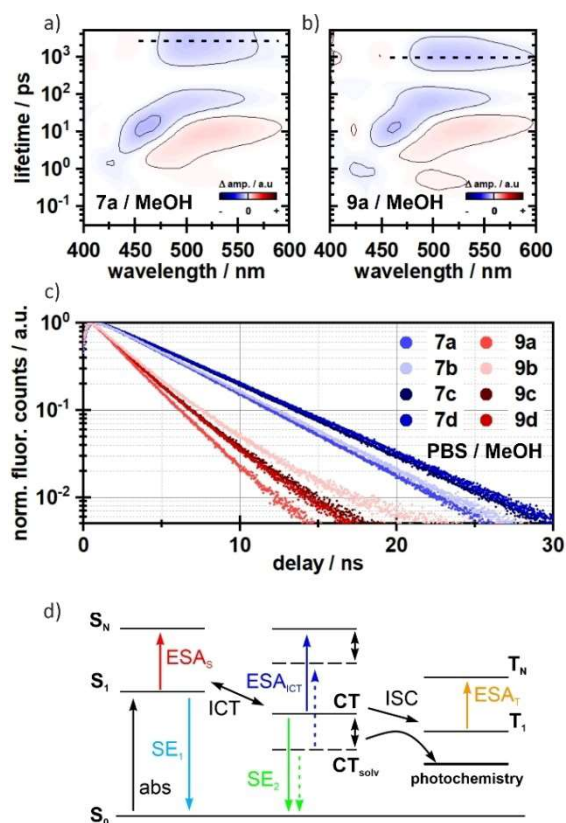


**Figure 8.** Lifetime density analysis of **7a** (a) and **9a** (b) measured in MeOH. The ES decay is faster in compound **9a** (indicated as dashed lines), whereas the dynamics on the fs- to ps-timescale do not differ. A similar pattern is seen in the TCSPC measurements (c). The fluorescence lifetimes of compounds **9a–d** are roughly 2-fold faster. The corresponding lifetime components are given in the Supporting Information. d) Schematic representation of possible energy pathways. After excitation, an equilibrium between the locally excited state  $S_1$  and the CT state is formed. The CT state is further stabilized by the solvent (indicated by double-sided arrows), which increases the population of the CT state. Without this stabilization an additional channel for triplet formation becomes relevant, which then competes with the actual photochemistry.

in their fluorescence and uncaging properties. It became clear that the charge-transfer state in coumarin chromophores is not just well stabilized by polar solvents, but also essential for photolysis. The new photocages described here are easy to synthesize and, due to their photophysical properties, can be used for both one-photon applications using blue light and in the phototherapeutic window (700–900 nm) using two-photon excitation. In summary, we think that the development of photolabile protecting groups can indeed very well profit from what has already been learned in the optimization of fluorophores. This can be a good guiding principle for future development.

## Experimental Section

**Chemical synthesis:** All reactions were performed under an argon atmosphere unless otherwise specified. Solvents and reagents were purchased from commercial sources. DEACM **1** was synthesized according to literature.<sup>[56]</sup> Synthetic procedures of new compounds

and their characterization are provided in the Supporting Information. Microwave reactions were performed in a *Biotage Initiator* system. NMR spectra of new compounds were recorded on (250 MHz, 300 MHz, 400 MHz, 500 MHz and 600 MHz) *Bruker* instruments. MALDI HRMS spectra were recorded on a *ThermoScientific MALDI LTQ Orbitrap XL* instrument.

**Ultrafast TA-spectroscopy:** The time-resolved transient absorption measurements were performed using a home-built pump-probe setup. A Ti:Sa chirped pulse regenerative amplifier (MXR-CPA-iSeries, Clark-MXR Inc., USA) with a central output wavelength of 775 nm, a 1 kHz repetition rate, and a pulse width of 150 fs was used as the fs-laser source. The fundamental was split for pump and probe pulse generation. Pump pulses at a central wavelength of 388 nm were generated in a second harmonic generation (SHG). The temporal FWHM of the final pump pulses was determined to be ~120–130 fs. The excitation energy was set to 90 nJ/pulse at the sample position. The supercontinuum for the probe pulses was generated by focusing the fundamental in a constantly moving  $\text{CaF}_2$  window of 5 mm thickness, leading to stable white light in the range of 375–740 nm. The white light was then split and guided through the sample and the reference arm of the detection setup. Each arm makes use of a spectrograph (Multimode, AMKO, Germany), which is equipped with two gratings (300 nm/500 nm blaze, 600/1200 grooves per mm), a photodiode array (S8865-64, Hamamatsu Photonics, Japan) and a corresponding driver circuit (C9118, Hamamatsu Photonics, Japan). The signals were digitized by a 16 bits data acquisition card (NI-PCI-6110, National Instruments, USA). The pump and probe pulses were set to the magic angle configuration at 54.7° to account for anisotropic effects. The sample-compartment was constantly moved to minimize sample degradation.

**Fluorescence lifetimes:** The fluorescence decays of the compounds **7a–d** and **9a–d** were determined by the time-correlated single photon counting (TCSPC) technique. Our home-built TCSPC setup is composed of a single-photon detection photomultiplier tube (PMA-C 182 M, PicoQuant, Germany) and a PCIe card (TimeHarp 260 PICO Single, PicoQuant) for sub-ns data processing. Pulsed orthogonal excitation of the samples was achieved by a pulsed LED (PLS360, PicoQuant) with a peak wavelength of 360 nm and a FWHM < 800 ps. Deconvolution with the IRF and multi-exponential fitting of the temporal traces was performed with FluoFit Pro 4.6 (PicoQuant) based on the following equation<sup>[59]</sup>

$$I(t) = \int_{-\infty}^t \text{IRF}(t') \sum_{i=1}^n A_i e^{-\frac{t-t'}{\tau_i}} dt'$$

The samples were measured in 4 × 10 mm quartz glass cuvettes with an OD of ~0.1 on 10 mm optical pathlength.

**Determination of quantum yields:** Three stock solutions of each compound **9a–d** and **11** were prepared by diluting approx. 1.0 mg in MeOH/PBS (1:1). For photolysis 50 μL were taken and irradiated at nine different irradiation times ( $t=0$  s, 5 s, 10 s, 20 s, 45 s, 90 s, 180 s, 360 s, 720 s) with a 405 nm LED (*Thorlabs*), resulting in 27 differently irradiated solutions for each compound. The photon flux for the setup was determined with a fulgide-derivative – as described in literature.<sup>[52]</sup> The photolysis was analyzed via RP-HPLC (*Agilent 1200*) as the ratio of the peak areas of starting material and uridine as internal standard – as described in literature.<sup>[16]</sup>

## Acknowledgements

We gratefully acknowledge funding of the Deutsche Forschungsgemeinschaft (DFG) through the research training group “CLiC” (GRK 1986, Complex Light-Control) and the CRC902 “Molecular principles of RNA-based regulation”. Open Access funding enabled and organized by Projekt DEAL.

## Conflict of Interest

The authors declare no conflict of interest.

## Data Availability Statement

The data that support the findings of this study are available in the supplementary material of this article.

**Keywords:** ATTO 390 · coumarin · fluorophore · photocage · TICT

- [1] N. Ankenbruck, T. Courtney, Y. Naro, A. Deiters, *Angew. Chem. Int. Ed.* **2018**, *57*, 2768–2798; *Angew. Chem.* **2018**, *130*, 2816–2848.
- [2] B. Bort, T. Gallavardin, D. Ogden, P. I. Dalko, *Angew. Chem. Int. Ed.* **2013**, *52*, 4526–4537; *Angew. Chem.* **2013**, *125*, 4622–4634.
- [3] W. Szymański, J. M. Beierle, H. A. V. Kistemaker, W. A. Velema, B. L. Feringa, *Chem. Rev.* **2013**, *113*, 6114–6178.
- [4] V. M. Lechner, M. Nappi, P. J. Deneny, S. Folliet, J. C. K. Chu, M. J. Gaunt, *Chem. Rev.* **2022**, *122*, 1752–1829.
- [5] C. Briek, F. Rohrbach, A. Gottschalk, G. Mayer, A. Heckel, *Angew. Chem. Int. Ed.* **2012**, *51*, 8446–8476; *Angew. Chem.* **2012**, *124*, 8572–8604.
- [6] P. Klán, T. Šolomek, C. G. Bochet, A. Blanc, R. Givens, M. Rubina, V. Popik, A. Kostikov, J. Wirz, *Chem. Rev.* **2013**, *113*, 119–191.
- [7] R. Weinstein, T. Slanina, D. Kand, P. Klán, *Chem. Rev.* **2020**, *120*, 13135–13272.
- [8] L. Josa-Culleré, A. Llebaria, *ChemPhotoChem* **2021**, *5*, 298–316.
- [9] P. Štacko, T. Šolomek, *Chimia* **2021**, *75*, 873–881.
- [10] L. Fournier, I. Aujard, T. Le Saux, S. Maurin, S. Beaupierre, J. B. Baudin, L. Jullien, *Chem. Eur. J.* **2013**, *19*, 17494–17507.
- [11] Q. Lin, L. Yang, Z. Wang, Y. Hua, D. Zhang, B. Bao, C. Bao, X. Gong, L. Zhu, *Angew. Chem. Int. Ed.* **2018**, *57*, 3722–3726; *Angew. Chem.* **2018**, *130*, 3784–3788.
- [12] M. Bojtár, A. Kormos, K. Kis-Petik, M. Keller Mayer, P. Kele, *Org. Lett.* **2019**, *21*, 9410–9414.
- [13] M. López-Corrales, A. Rovira, A. Gandioso, M. Bosch, S. Nonell, V. Marchán, *Chem. Eur. J.* **2020**, *26*, 16222–16227.
- [14] P. Shrestha, K. C. Dissanayake, E. J. Gehrmann, C. S. Wijesooriya, A. Mukhopadhyay, E. A. Smith, A. H. Winter, *J. Am. Chem. Soc.* **2020**, *142*, 15505–15512.
- [15] T. Slanina, P. Shrestha, E. Palao, D. Kand, J. A. Peterson, A. S. Dutton, N. Rubinstein, R. Weinstein, A. H. Winter, P. Klán, *J. Am. Chem. Soc.* **2017**, *139*, 15168–15175.
- [16] M. Reinfelds, J. von Cosel, K. Falahati, C. Hamerla, T. Slanina, I. Burghardt, A. Heckel, *Chem. Eur. J.* **2018**, *24*, 13026–13035.
- [17] V. Hermanns, M. Scheurer, N. F. Kersten, C. Abdellaoui, J. Wachtveitl, A. Dreuw, A. Heckel, *Chem. Eur. J.* **2021**, *27*, 14121–14127.
- [18] Y. Becker, E. Unger, M. A. H. Fichte, D. A. Gacek, A. Dreuw, J. Wachtveitl, P. J. Walla, A. Heckel, *Chem. Sci.* **2018**, *9*, 2797–2802.
- [19] Y. Becker, S. Roth, M. Scheurer, A. Jakob, D. A. Gacek, P. J. Walla, A. Dreuw, J. Wachtveitl, A. Heckel, *Chem. Eur. J.* **2021**, *27*, 2212–2218.
- [20] C. Reichardt, *Chem. Rev.* **1994**, *94*, 2319–2358.
- [21] G. J. Zhao, K. L. Han, *Acc. Chem. Res.* **2012**, *45*, 404–413.
- [22] C. A. Hoelzel, H. Hu, C. H. Wolstenholme, B. A. Karim, K. T. Munson, K. H. Jung, H. Zhang, Y. Liu, H. P. Yennawar, J. B. Asbury, X. Li, X. Zhang, *Angew. Chem. Int. Ed.* **2020**, *132*, 4815–4822.
- [23] L. B. McGown, K. Nithipahkom, *Appl. Spectrosc. Rev.* **2000**, *35*, 353–393.
- [24] J. B. Grimm, A. K. Muthusamy, Y. Liang, T. A. Brown, W. C. Lemon, R. Patel, R. Lu, J. J. Macklin, P. J. Keller, N. Ji, L. D. Lavis, *Nat. Methods* **2017**, *14*, 987–994.
- [25] J. B. Grimm, L. D. Lavis, *Nat. Methods* **2022**, *19*, 149–158.
- [26] M. V. Sednev, V. N. Belov, S. W. Hell, *Methods Appl. Fluoresc.* **2015**, *3*, 042004.
- [27] G. Bassolino, C. Nançoz, Z. Thiel, E. Bois, E. Vauthey, P. Rivera-Fuentes, *Chem. Sci.* **2018**, *9*, 387–391.
- [28] D. Luo, C. Kuang, X. Liu, G. Wang, *Opt. Laser Technol.* **2013**, *45*, 723–725.
- [29] “ATTO-TEC GmbH – ATTO 390,” can be found under [https://www.atto-tec.com/product\\_info.php?info=p1\\_atto-390.html](https://www.atto-tec.com/product_info.php?info=p1_atto-390.html).
- [30] T. Debnath, H. N. Ghosh, *ChemistrySelect* **2020**, *5*, 9461–9476.
- [31] D. Cao, Z. Liu, P. Verwilst, S. Koo, P. Jangjili, J. S. Kim, W. Lin, *Chem. Rev.* **2019**, *119*, 10403–10519.
- [32] J. V. Jun, D. M. Chenoweth, E. J. Petersson, *Org. Biomol. Chem.* **2020**, *18*, 5747–5763.
- [33] A. Barik, M. Kumbhakar, S. Nath, H. Pal, *Chem. Phys.* **2005**, *315*, 277–285.
- [34] G. Jones, W. R. Jackson, C. Y. Choi, W. R. Bergmark, *J. Phys. Chem.* **1985**, *89*, 294–300.
- [35] Y. Liu, J. Ding, R. Liu, D. Shi, J. Sun, *J. Photochem. Photobiol. A* **2009**, *201*, 203–207.
- [36] N. P. Wells, M. J. McGrath, J. I. Siepmann, D. F. Underwood, D. A. Blank, *J. Phys. Chem. A* **2008**, *112*, 2511–2514.
- [37] P. Zhou, P. Song, J. Liu, K. Han, G. He, *Phys. Chem. Chem. Phys.* **2009**, *11*, 9440–9449.
- [38] C. Wang, W. Chi, Q. Qiao, D. Tan, Z. Xu, X. Liu, *Chem. Soc. Rev.* **2021**, *50*, 12656–12678.
- [39] T. López Arbeloa, F. López Arbeloa, M. J. Tapia Estévez, I. López Arbeloa, *J. Lumin.* **1994**, *59*, 369–375.
- [40] T. Halbritter, C. Kaiser, J. Wachtveitl, A. Heckel, *J. Org. Chem.* **2017**, *82*, 8040–8047.
- [41] C. Kaiser, T. Halbritter, A. Heckel, J. Wachtveitl, *Chem. Eur. J.* **2021**, *27*, 9160–9173.
- [42] S. A. Yamashkin, E. A. Oreshkina, *Chem. Heterocycl. Compd.* **2006**, *42*, 701–718.
- [43] V. V. Begoyan, L. J. Weseliński, S. Xia, J. Fedie, S. Kannan, A. Ferrier, S. Rao, M. Tanasova, *Chem. Commun.* **2018**, *54*, 3855–3858.
- [44] C. A. Hammer, K. Falahati, A. Jakob, R. Klimek, I. Burghardt, A. Heckel, J. Wachtveitl, *J. Phys. Chem. Lett.* **2018**, *9*, 1448–1453.
- [45] A. M. Smith, M. C. Mancini, S. Nie, *Nat. Nanotechnol.* **2009**, *4*, 710–711.
- [46] R. Misra, S. P. Bhattacharyya, in *Intramol. Charg. Transf.*, Wiley-VCH Verlag GmbH & Co. KGaA, Weinheim, Germany, **2018**, pp. 115–148.
- [47] D. Liese, G. Haberhauer, *Isr. J. Chem.* **2018**, *58*, 813–826.
- [48] G. J. Zhao, K. L. Han, *J. Phys. Chem. A* **2007**, *111*, 9218–9223.
- [49] G. J. Zhao, K. L. Han, *J. Phys. Chem. A* **2009**, *113*, 14329–14335.
- [50] L. Biczók, T. Bérces, T. Yatsuhashi, H. Tachibana, H. Inoue, *Phys. Chem. Chem. Phys.* **2001**, *3*, 980–985.
- [51] R. L. Carhart-Harris, D. J. Nutt, *J. Psychopharmacol.* **2017**, *31*, 1091–1120.
- [52] M. Reinfelds, V. Hermanns, T. Halbritter, J. Wachtveitl, M. Braun, T. Slanina, A. Heckel, *ChemPhotoChem* **2019**, *3*, 441–449.
- [53] C. Hamerla, C. Neumann, K. Falahati, J. Von Cosel, L. J. G. W. Van Wilderen, M. S. Niraghatam, D. Kern-Michler, N. Mielke, M. Reinfelds, A. Rodrigues-Correia, A. Heckel, J. Bredenbeck, I. Burghardt, *Phys. Chem. Chem. Phys.* **2020**, *22*, 13418–13430.
- [54] A. K. Soper, A. Luzar, *J. Phys. Chem.* **1996**, *100*, 1357–1367.
- [55] I. I. Vaisman, M. L. Berkowitz, *J. Am. Chem. Soc.* **1992**, *114*, 7889–7896.
- [56] L. R. Martins, A. Tamashiro, D. Laria, M. S. Skaf, *J. Chem. Phys.* **2003**, *118*, 5955–5963.
- [57] T. Eckardt, V. Hagen, B. Schade, R. Schmidt, C. Schweitzer, J. Bendig, *J. Org. Chem.* **2002**, *67*, 703–710.
- [58] T. Weinrich, M. Gränz, C. Grünwald, T. F. Prisner, M. W. Göbel, *Eur. J. Org. Chem.* **2017**, *2017*, 491–496.
- [59] J. Enderlein, R. Erdmann, *Opt. Commun.* **1997**, *134*, 371–378.

Manuscript received: February 28, 2022

Accepted manuscript online: April 14, 2022

Version of record online: May 12, 2022

### 6.3 Asido *et al.*, *Phys. Chem. Chem. Phys.*, 2022

#### **Ultrafast and Efficient Energy Transfer in a One- and Two-Photon Sensitized Rhodamine-BODIPY Dyad: A Perspective for Broadly Absorbing Photocages**

M. Asido<sup>†</sup>, C. Hamerla<sup>†</sup>, R. Weber<sup>†</sup>, M. Horz<sup>†</sup>, M. S. Niraghatam, A. Heckel, I. Burghardt and J. Wachtveitl,  
*Phys. Chem. Chem. Phys.*, **2022**, 24, 1795-1802.


 Cite this: *Phys. Chem. Chem. Phys.*,  
2022, 24, 1795

# Ultrafast and efficient energy transfer in a one- and two-photon sensitized rhodamine-BODIPY dyad: a perspective for broadly absorbing photocages†

 Marvin Asido,<sup>‡</sup> Carsten Hamerla,<sup>‡</sup> Rebekka Weber,<sup>‡</sup> Maximiliane Horz,<sup>‡</sup> Madhava Shyam Niraghatam,<sup>a</sup> Alexander Heckel,<sup>‡</sup> Irene Burghardt<sup>‡</sup> and Josef Wachtveitl<sup>‡</sup>

In view of the demand for photoactivatable probes that operate in the visible (VIS) to near infrared (NIR) region of the spectrum, we designed a bichromophoric system based on a rhodamine fluorophore and a BODIPY photocage. Two-photon excited fluorescence (TPEF) measurements and quantum chemical calculations reveal excellent two-photon properties of the employed rhodamine derivative. Excitation of the rhodamine unit *via* a one- or two-photon process leads to excitation energy transfer (EET) onto the BODIPY part, which is followed by the liberation of the leaving group. Ultrafast transient absorption spectroscopy provides evidence for a highly efficient EET dynamics on a sub-500 femtosecond scale. Complementary quantum dynamical calculations using the multi-layer multiconfiguration time-dependent Hartree (ML-MCTDH) approach highlight the quantum coherent character of the EET transfer. Photorelease of *p*-nitroaniline (PNA) was investigated by UV/vis absorption spectroscopy by either excitation of the rhodamine or the BODIPY moiety. Even though a quantitative assessment of the PNA yield could not be achieved for this particular BODIPY cage, the present study provides a design principle for a class of photocages that can be broadly activated between 500 and 900 nm.

 Received 3rd October 2021,  
Accepted 17th December 2021

DOI: 10.1039/d1cp04528h

rsc.li/pccp

## Introduction

The possibility to control chemical processes with light paved the way for numerous innovations in biological and medical science ranging from high resolution imaging techniques<sup>1</sup> to photodynamic therapy<sup>2–4</sup> and drug release.<sup>5,6</sup> Such applications favor excitation light of the so called “phototherapeutic window” (600–1000 nm) which provides less phototoxicity and deep tissue penetration due to little light scattering and competitive absorption.<sup>7</sup> Photolabile Protecting Groups (PPGs) that

operate in this area are rare and mainly include BODIPY-, xanthene- or cyanine-derived structures.<sup>8,9</sup> However, while demonstrating strong absorption, these compounds often lack efficient photorelease quantum yields.

Alternatively, photoactivation in the NIR region can be realized by two-photon absorption (2PA).<sup>10,11</sup> The tight spatial focus of 2PA (due to the quadratic dependence on the intensity of the incident light) offers a particular advantage for photorelease reactions in a physiological context since biological signaling molecules can be liberated with very high precision.<sup>12,13</sup> Unfortunately, most of the established PPGs show only little 2P response.<sup>14</sup> Efforts have been made to convert these compounds into better 2P absorbers by structural modifications, which resulted in the development of a number of 2P activatable photocages including *ortho*-nitrobenzyl,<sup>15,16</sup> coumarinyl,<sup>17,18</sup> nitroindolinyl<sup>19,20</sup> or quinoline<sup>21,22</sup> based chromophores. However, improvement of the 2P cross section  $\sigma_{2P}$  by such structural alterations often has an adverse effect on the photorelease quantum yield  $\Phi_{rel}$ .<sup>23</sup> Therefore high 2P action cross sections  $\delta_u$  (with  $\delta_u$  being the product of  $\sigma_{2P}$  and  $\Phi_{rel}$ )<sup>24</sup> are difficult to achieve. The idea to separate the absorption process from the uncaging process was realized by the development of cooperative dyads based on photoinduced electron

<sup>a</sup> Institute of Physical and Theoretical Chemistry, Goethe University Frankfurt, Max-von-Laue Straße 7, 60438 Frankfurt am Main, Germany.

E-mail: burghardt@chemie.uni-frankfurt.de, wweitl@theochem.uni-frankfurt.de

<sup>b</sup> Institute of Organic Chemistry and Chemical Biology, Goethe University Frankfurt, Max-von-Laue Straße 7, 60438 Frankfurt am Main, Germany

E-mail: heckel@uni-frankfurt.de

† Electronic supplementary information (ESI) available: General procedures; chemical synthesis; experimental details; steady-state absorption/fluorescence experiments; two-photon excitation fluorescence (TPEF) experiments of rhodamine compounds using rhodamine 6G as reference; fluorescence lifetimes of rhodamine compounds; ultrafast transient absorption measurements; electronic structure calculations; excited state analysis; electronic coupling analysis; NMR- & mass spectra of new compounds. See DOI: 10.1039/d1cp04528h

‡ These authors contributed equally.



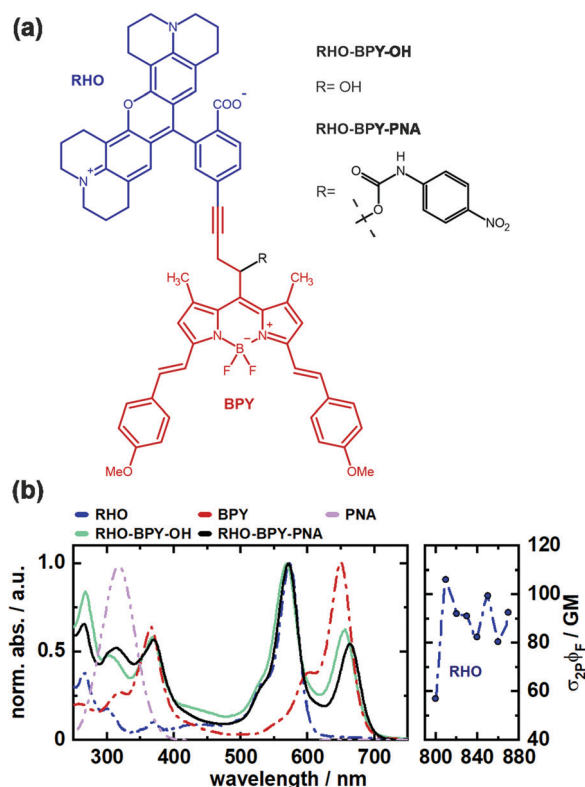


Fig. 1 (a) Molecular structure of RHO-BPY-OH and RHO-BPY-PNA with rhodamine part (RHO) labeled blue and BODIPY part (BPY) labeled red. (b) Corresponding 1P absorption spectra of RHO-BPY-OH and RHO-BPY-PNA, as well as their corresponding individual constituents (left) and 2P absorption cross section of RHO (right) in MeOH.

transfer (PET),<sup>25</sup> fluorescence resonance energy transfer (FRET)<sup>26</sup> or triplet-triplet energy transfer (TT-ET).<sup>27</sup> In 2013 the Blanchard-Desce group introduced a FRET-based tandem system for enhanced two-photon uncaging which was further optimized to reach record two-photon action cross section of estimated 20 GM at 710 nm.<sup>28</sup> In 2018 we presented a related system with special focus put on the electronic interactions between the coactive chromophores.<sup>29</sup>

In this work we investigate the excitation energy transfer (EET) dynamics in a one- and two-photon sensitive uncaging system based on covalently linked rhodamine (RHO) and BODIPY (BPY) chromophores (Fig. 1a). Rhodamine was chosen as 2P donor molecule since this class of fluorophores features high stability and brightness as well as outstanding 2PA properties.<sup>30,31</sup> In our experiments, the conformationally rigid X-type rhodamine showed superior 2PA response between 810 and 870 nm compared to other alkylated rhodamines (Fig. S3, ESI†). A styryl-substituted BODIPY photocage with red-shifted absorption served as suitable EET acceptor. The two chromophores were connected *via* a rigid alkyne linker to prevent electronic interactions due to  $\pi$ -stacking. This dyad system undergoes an ultrafast EET on the sub-500 fs scale with high efficiency, which was shown by ultrafast transient absorption spectroscopy. Given that the transfer dynamics falls into a

non-Förster regime, high-dimensional quantum dynamical calculations were carried out which are in agreement with the observed time scale and provide an interpretation of the quantum coherent EET step.

To test the suitability of the dyad for an application as a PPG, *p*-nitroaniline (PNA) was inserted as model leaving group. Details of the synthesis of the depicted compounds can be found in the ESI.†

The absorption spectra of both, RHO-BPY-OH as well as RHO-BPY-PNA, reflect well the main bands of their individual constituents (Fig. 1b), which absorb from 500–600 nm (RHO) and 570–700 nm (BPY). In the UV region below 400 nm the spectral components are more overlapping. For both dyads the bands at around 250 nm can be attributed to a higher order transition of RHO, whereas the bands at 380 nm mostly originate from BPY. In contrast to RHO-BPY-OH, the dyad with an attached leaving group (PNA) has a broader and slightly red-shifted absorption around 300–320 nm. The spectrum of the sensitizer (RHO) extends into the NIR region by considering 2PA effects. With 2P action cross sections ( $\sigma_{2P}\Phi_F$ ) of 80–110 GM in the range of 810–870 nm, RHO shows excellent 2PA abilities similar to the values of other rhodamines found in the literature.<sup>32–35</sup> Such high GM values for rhodamines are usually explained by the corresponding  $S_0$ – $S_2$  transition, which is 1P forbidden due to its symmetry, and in turn strongly 2P active.<sup>36,37</sup>

## Results and discussion

### Time-resolved spectroscopy

In order to investigate the ultrafast dynamics of all compounds we employed UV/vis transient absorption spectroscopy. In the initial experiment on RHO-BPY-OH we used pump pulses with a central wavelength of 560 nm to account for an excitation of RHO. The bleaching of the RHO ground state ( $GSB_1$ ) is reflected in the negative signal around 550–620 nm (Fig. 2a). Correspondingly, the excited state of RHO becomes populated, which leads to an excited state absorption ( $ESA_1$ ) with a central wavelength of 470 nm. The rise of these signals is faster than the temporal resolution of this experiment, which is around 75 fs.

The decay, however, begins to occur on the 200–500 fs timescale, as can be seen in the lifetime density analysis (LDA) of the dataset. Simultaneously one can observe the rise of an additional bleaching signal ( $GSB_2$ ) centered at 670 nm, which corresponds to the BPY ground state absorption. This is easily visualized by comparing the transients at 575 nm and 670 nm (Fig. 2c). The bleaching signal at 575 nm decreases to 50% of its initial value in the first 300 fs after photoexcitation. On the same timescale  $GSB_2$  reaches more than 90% of its maximum value. Hence we assume an efficient EET from RHO to BPY, which then levels off once an equilibrium with the locally excited RHO is formed.

In the same manner we can identify a delayed excited state absorption at 525 nm ( $ESA_2$ ) with a similar rise time as  $GSB_2$ ,

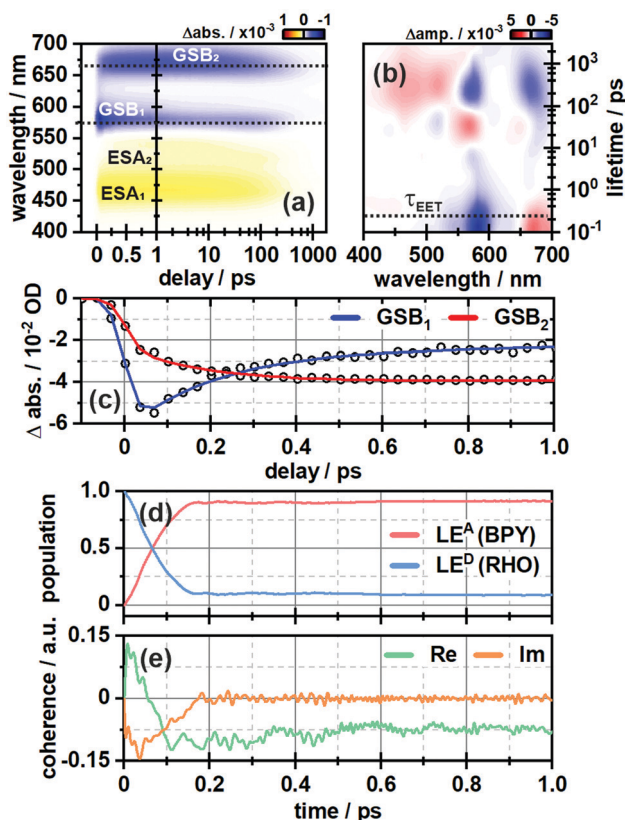


Fig. 2 (a) Ultrafast transient absorption dataset of RHO-BPY-OH (in MeOH) and (b) its corresponding lifetime density analysis. The time of energy transfer  $\tau_{\text{EET}}$  is highlighted by the dashed line. (c) Transients of  $\text{GSB}_1$  and  $\text{GSB}_2$ , which are indicative for the EET from RHO to BPY. (d) Population of the locally excited states at the BODIPY ( $\text{LE}^{\text{A}}$ ) and the rhodamine moiety ( $\text{LE}^{\text{D}}$ ) as a function of time derived from quantum dynamical calculations. (e) Corresponding coherences according to eqn (3).

which indicates an excited state absorption of BPY. Unlike  $\text{GSB}_1$ ,  $\text{ESA}_1$  does not show a corresponding decay component. This can be explained by comparing the excited state dynamics of the isolated RHO and BPY, respectively (Fig. S5, ESI<sup>†</sup>). Whereas the ESA of RHO is centered around 470 nm (Fig. S5a, ESI<sup>†</sup>), BPY has a rather broad ESA with two main bands at 470 nm and 570 nm (Fig. S5c, ESI<sup>†</sup>). Therefore, the  $\text{ESA}_1$  band of RHO-BPY-OH is actually a superposition of the RHO and BPY excited state absorptions.  $\text{ESA}_2$  can then be considered as the residual shoulder of the BPY band at 570 nm, which partly overlaps with the  $\text{GSB}_1$  signal.

In order to determine the possibility of electronic coupling, we also excited RHO-BPY-OH with 655 nm pulses, which should mainly target the BPY part of the molecule. Indeed, in this case the photophysics of RHO-BPY-OH is dominated by the ultrafast dynamics of BPY (Fig. S6, ESI<sup>†</sup>). However, one can also observe an additional bleaching component of RHO at 575 nm, which occurs on the 10–100 ps timescale. This could stem from a slight spectral overlap of the RHO absorption and the excitation pulses. On the earlier timescale, this band overlaps with (and is compensated by) the red shoulder of the BPY excited state

absorption, which is also apparent in the corresponding LDM (Fig. S6b, ESI<sup>†</sup>).

### Computational analysis

To interpret the spectroscopic finding of an ultrafast energy transfer from the donor fragment RHO to the acceptor fragment BPY, electronic structure calculations and a quantum dynamical analysis were performed for the considered dyad. Time-dependent density functional theory (TD-DFT) was employed to study the low-lying singlet excitations of the dyad. For the quantum-dynamical calculations, the multi-layer multi-configuration time-dependent Hartree (ML-MCTDH) method<sup>38–40</sup> was employed, based upon a linear vibronic coupling (LVC) Hamiltonian for two electronic states and 266 vibrational modes. Due to the ultrafast transfer dynamics, conventional FRET rates are not expected to give reliable results.

All electronic structure calculations were performed using DFT and TD-DFT as implemented in the Gaussian16 package.<sup>41</sup>

The ground state geometry was optimized using the B3LYP functional<sup>42,43</sup> and 6-31G\* basis.<sup>44</sup> Other functionals yielded implausible ground state geometries where the carboxylate group of the respective rhodamine fragment formed a lactone type ring with the  $\pi$ -system, leading to a loss of planarity, as discussed in the Fig. S8 (ESI<sup>†</sup>). The minimum geometry based on B3LYP was confirmed using the Hessian. Solvent effects (here, methanol) were accounted for by the Polarizable Continuum Model (PCM).<sup>45,46</sup>

Excited state calculations were performed by means of TD-DFT with the long-range corrected CAM-B3LYP functional<sup>47</sup> and 6-31G\* basis set. Quadratic response calculations using the same functional were carried out with the DALTON program package.<sup>48</sup> As detailed in the Table S2 (ESI<sup>†</sup>), benchmark calculations with other functional and basis set combinations were performed, from which we concluded that CAM-B3LYP/6-31G\* yields the most accurate description of the system with respect to state energies and two-photon absorption properties as compared to the experimental findings. This functional was also employed in ref. 49, where 2PA spectra of rhodamine 6G were computed.<sup>49</sup>

The excited state analysis of the RHO-BPY-OH dyad (Table 1) shows three spectroscopic (one-photon) bright states with excitation energies of 2.14 eV (579 nm), 2.86 eV (434 nm) and 3.43 eV (362 nm) followed by a dark state at 3.51 eV (354 nm). The first bright excited state ( $S_1$ ), is localized on the acceptor BPY fragment whereas the  $S_2$  state is localized on the donor RHO fragment. The  $S_3$  state is another BPY centered state while the subsequent dark state ( $S_4$ ), at 3.51 eV is again localized at the RHO fragment. The latter state ( $S_4$ ), is the two-photon active state as further explained below. These four excited states  $S_1$ ,  $S_2$ ,  $S_3$  and  $S_4$  are illustrated in Fig. 3a.

For the quadratic response calculations, a smaller model system was used; *i.e.*, a slightly adapted dyad (referred to as “model” system (M) in the following, see ESI<sup>†</sup> Table S3) consisting of a dimethyl substituted Rho1 moiety and a BPY1 fragment without the *ortho*-methoxyphenyl substituent linked

**Table 1** Excited state energies, oscillator strengths and two-photon cross-sections for the four relevant states of RHO-BPY-OH and the model system Rho1-BPY1-OH, respectively, using the CAM-B3LYP functional and 6-31G\* basis

System		RHO-BPY-OH	Rho1-BPY1-OH (M)
S <sub>1</sub>	Excitation Energy [eV]	2.1413	2.8611
	Oscillator strength f	1.1307	0.5711
S <sub>2</sub>	Excitation Energy [eV]	2.8624	3.0616
	Oscillator strength f	1.0555	0.9615
S <sub>3</sub>	Excitation Energy [eV]	3.4293	3.5648
	Oscillator strength f	1.6060	0.3422
S <sub>4</sub>	Excitation Energy [eV]	3.5065	3.7837
	Oscillator strength f	0.0788	0.0559
	$\sigma_{2P}$ [GM]		5.1

through an acetylene bond. The excited state analysis of the model system turns out to be very similar to the original RHO-BPY system and exhibits the same orbital transitions contributing to the respective states (Fig. S11 and S12, ESI†). The S<sub>1</sub><sup>M</sup> state

is a bright state at 2.86 eV (433 nm) localized on the BPY1 moiety, the S<sub>2</sub><sup>M</sup> state is another bright state at 3.06 eV (405 nm) localized on the Rho1 fragment and the subsequent state, the S<sub>3</sub><sup>M</sup> state, is a dark state at 3.56 eV (348 nm), also localized on the Rho1 fragment.

The quadratic response calculation shows that the S<sub>3</sub><sup>M</sup> state has the highest two-photon absorption cross-section. That is, the S<sub>3</sub><sup>M</sup> state has a two-photon cross section  $\sigma_{2P}$  of 175 GM, whereas the S<sub>1</sub><sup>M</sup> and the S<sub>2</sub><sup>M</sup> states have two-photon cross-sections of 3 GM and 28 GM, respectively. The S<sub>3</sub><sup>M</sup> state exhibits the same orbital transitions as the S<sub>4</sub> state of RHO-BPY-OH and is, hence, considered the equivalent state in the model system. We therefore conclude that the S<sub>4</sub> state of RHO-BPY-OH is the two-photon active state.

From the assignments above, the following picture of the photochemical process results: following excitation by a two-photon pulse the molecule is first directly excited to the S<sub>4</sub> state in the case of RHO-BPY-OH (or the S<sub>3</sub><sup>M</sup> state in case of the model system Rho1-BPY1-OH). This is followed by internal conversion (IC) to the S<sub>2</sub>/S<sub>2</sub><sup>M</sup> state within the RHO/Rho1 fragment, and

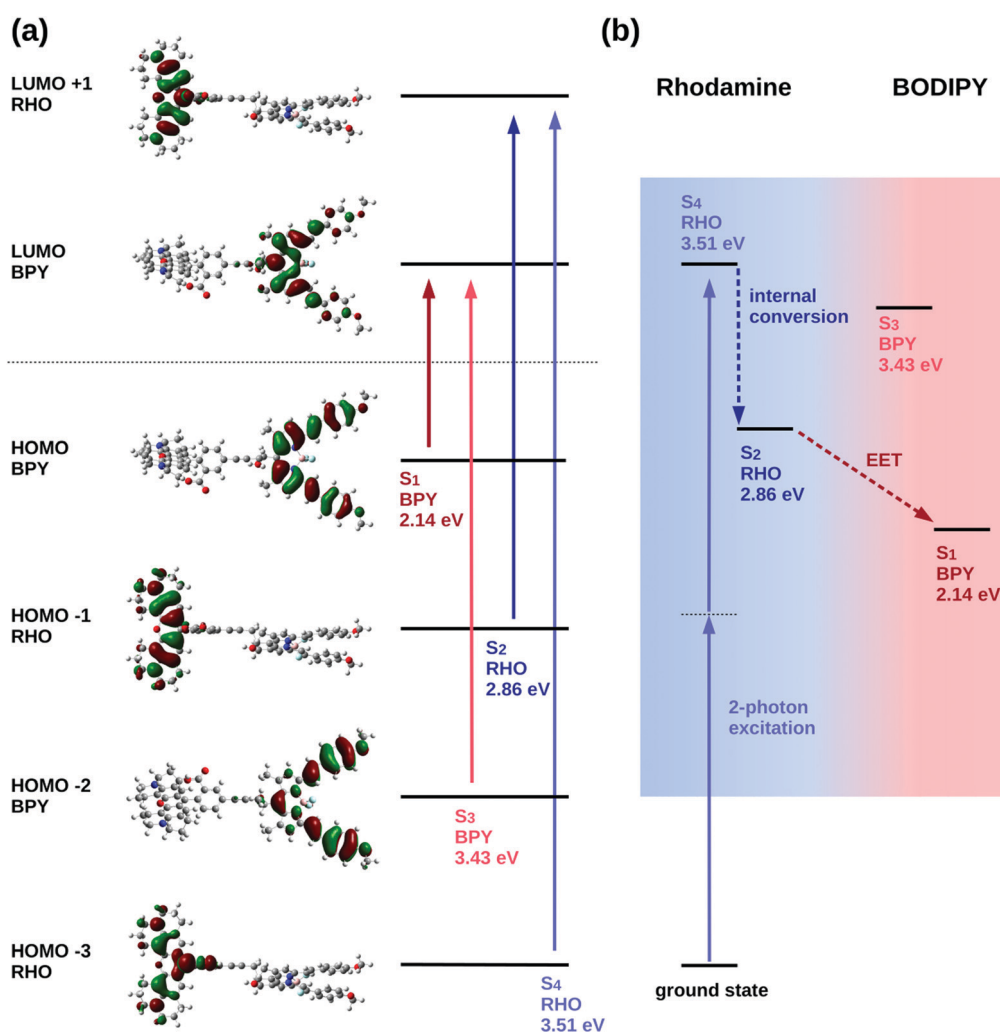


**Fig. 3** (a) Frontier molecular orbitals involved in the excited electronic states of interest in RHO-BPY-OH. (b) Schematic illustration of the processes triggered by two-photon excitation of RHO-BPY-OH.

subsequently the energy is transferred *via* EET to the  $S_1/S_1^M$  state on the BPY/BPY1 fragment. A scheme representing these steps following the initial two-photon excitation is shown in Fig. 3b. The next higher state involving a transition on the BPY fragment is the  $S_3$  state of RHO-BPY-OH, also shown in Fig. 3. This state features a negligible admixture of transitions on the RHO fragment, such that there is no indication that the  $S_3$  state is involved in the IC step. Indeed, the IC can be understood as an intramolecular process within the RHO fragment, involving the  $S_4 \rightarrow S_2$  transition. In the following we assume that the IC and EET steps are sequential, but a more detailed analysis would allow for temporal overlap of these steps.

In the quantum dynamical analysis, we focus on the EET step, assuming that the preceding IC happens within tens of femtoseconds. Here, too, we refer to the smaller model system permitting to include the full set of  $N = 266$  vibrational modes; details are given in the ESI† (Sec. Excited state analysis of Rho1-BPY1-OH). An LVC model was parameterized based upon the electronic structure calculations complemented by excited state gradients. The LVC Hamiltonian reads as follows, using mass- and frequency weighted coordinates

$$\hat{H} = \sum_{i=1}^N \left( \frac{\omega_i}{2} (\hat{q}_i^2 + \hat{p}_i^2) + \sum_j \kappa_{i,j} \hat{q}_i |\text{LE}^j\rangle \langle \text{LE}^j| \right) + j_{\text{DA}} (|\text{LE}^A\rangle \langle \text{LE}^D| + |\text{LE}^D\rangle \langle \text{LE}^A|) + \Delta E \quad (1)$$

with  $\hat{q}_i$  being the position operator, the momentum operator  $\hat{p}_i = -i\hbar \frac{\partial}{\partial q_i}$ , the vibronic couplings  $\kappa_{i,j}$ , Coulombic EET coupling  $j_{\text{DA}}$  and the electronic offset  $\Delta E$ .

The Hamiltonian encompasses two diabatic electronic states, which here correspond to locally excited states (denoted  $\text{LE}^A$  and  $\text{LE}^D$ ). These locally excited (diabatic) states correspond to a very good approximation to the adiabatic  $S_1^M$  and  $S_2^M$  state of the Rho1-BPY1 model dyad obtained by the above electronic structure calculations. Furthermore, the Hamiltonian includes  $N = 266$  normal modes, among which  $N_A = 117$  modes are localized on the BPY1 (acceptor) fragment and  $N_D = 149$  modes are localized on the Rho1 (donor) fragment, respectively. The vibronic coupling constants  $\{\kappa_{i,j}\}$  are computed by projecting the gradient of the two relevant excited states at the Franck-Condon geometry onto the ground state normal modes. For this purpose, the CAM-B3LYP method had to be consistently used for the ground state geometry optimization and the excited state gradient calculation; thus, a constraint was introduced in order to match the CAM-B3LYP optimized geometry with the B3LYP reference geometry (see Fig. S14, ESI†). The normal-mode frequencies  $\{\omega_i\}$  were obtained by normal mode analysis for the donor and acceptor fragment respectively. Analysis of the spectral densities (that can be computed from the vibronic couplings, see ESI† eqn (S9)) shows, that the normal modes are localized either on the Rho1 or BPY1 fragment and only couple to one of the locally excited states  $\text{LE}^A$  or  $\text{LE}^D$  respectively. The electronic coupling  $j_{\text{DA}}$  (0.024 eV) was determined using a transition density cube (TDC) procedure,<sup>50</sup>

implemented in an in-house code as detailed in the ESI.† The coupling derives from the respective transition densities as follows<sup>51</sup>

$$j_{\text{DA}} = \iint \rho_{\text{D}}^{\text{el}}(\vec{r}_{\text{d}}) \frac{1}{|\vec{r}_{\text{d}} - \vec{r}_{\text{a}}|} \rho_{\text{A}}^{\text{el}}(\vec{r}_{\text{a}}) d\vec{r}_{\text{d}} d\vec{r}_{\text{a}} \quad (2)$$

with the transition densities  $\rho_{\text{D}}^{\text{el}}(\vec{r}_{\text{d}}) = \Psi_{\text{D}_g}(\vec{r}_{\text{d}}) \Psi_{\text{D}_e}^*(\vec{r}_{\text{d}})$  and  $\rho_{\text{A}}^{\text{el}}(\vec{r}_{\text{a}}) = \Psi_{\text{A}_g}(\vec{r}_{\text{a}}) \Psi_{\text{A}_e}^*(\vec{r}_{\text{a}})$ , where  $\Psi_{\text{D}_g}$ ,  $\Psi_{\text{D}_e}$ ,  $\Psi_{\text{A}_g}$  and  $\Psi_{\text{A}_e}$  are the donor and acceptor ground (g) and excited state (e) wavefunctions and  $\vec{r}_{\text{d}}$  and  $\vec{r}_{\text{a}}$  are the electron coordinates on the donor and acceptor fragment. The energy difference between the two relevant electronic states  $\Delta E$  (0.25 eV) was taken from the experimental absorption spectrum.

Fig. 2d shows the time-evolving diabatic populations of the two relevant states  $\text{LE}^A$  and  $\text{LE}^D$  and Fig. 2e depicts the time-evolving diabatic electronic coherence  $\rho_{\text{DA}}(t)$ . The latter was obtained by taking the trace over the electronic and vibrational degrees of freedom of the density operator  $\hat{\rho}(t) = |\Psi(t)\rangle \langle \Psi(t)|$  of the full electronic-vibrational system.

$$\rho_{\text{DA}}(t) = \text{Tr}\{|\text{LE}^A\rangle \langle \text{LE}^D| \hat{\rho}(t)\} \quad (3)$$

From the quantum dynamical analysis, an initial decay to the  $\text{LE}^A$  state mainly “localized” on the acceptor fragment BPY1, is found on a time scale of 200 fs. Although a bit faster than the experiment this is in good agreement with the time-resolved spectroscopic measurements where the energy transfer occurs on a 300 fs timescale (Fig. 2a–c). The coherence decays on a similar time scale; more precisely, the transient state-to-state population flux (corresponding to the imaginary part of the coherence), decays to zero, while the persistent real part indicates that the system tends towards a coherent superposition involving a non-zero admixture of the  $\text{LE}^D$  state ( $P_{\text{D}} \sim 0.1$ ) to the mainly populated  $\text{LE}^A$  state ( $P_{\text{A}} \sim 0.9$ ). The equilibrated donor population is possibly underestimated as compared with experiment, one of the reasons being that solvent effects were not explicitly included.

### Analysis of photocleavage

In order to investigate the proposed system in terms of photocleavage, we performed illumination experiments with high-power LEDs of 565 nm and 660 nm central wavelength, respectively. Irradiation of RHO-BPY-PNA with 565 nm light (Fig. 4a–c) results in a strong photobleaching at 300–400 nm and 580–700 nm, which correspond to the absorption bands of the BPY scaffold (see Fig. 1b). In contrast, the main absorption band of RHO at around 560 nm remains mostly intact. At the blue end of the spectrum, a new absorption feature at 300 nm arises. This difference band could indeed originate from liberated PNA, which is expected to absorb at 250–380 nm (Fig. 1b) and/or a blue shift due to the formation of a stable (leaving group free) photoproduct (Fig. 4b). The latter argument can be rationalized by the red-shifted absorption of RHO-BPY-PNA compared to the leaving group free reference compound RHO-BPY-OH in the spectral range of 280–350 nm (Fig. 1b).

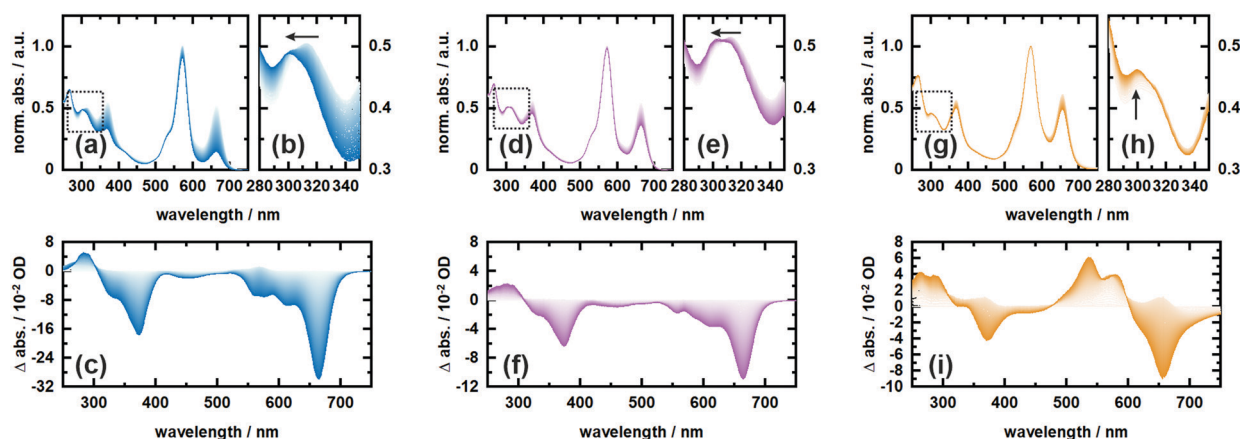


Fig. 4 Irradiation experiments of RHO-BPY-PNA (in MeOH) with 565 nm light (a–c) and 660 nm light (d–f), as well as irradiation of RHO-BPY-OH (in MeOH) with 565 nm light (g–i). (a), (d) and (g) depict the respective normalized spectra with a closer zoom in (b), (e) and (h) as indicated by the dashed boxes. (c), (f) and (i) show the respective difference spectra referenced to the initial dark measurement. The spectra were recorded in 30 s intervals in a total timeframe of 6000 s.

Strikingly, the illumination of the same sample with 660 nm light (Fig. 4d–f) leads to the same difference spectrum, albeit with a significantly weaker amplitude compared to the 565 nm illumination. On the one hand this underlines that direct excitation of either the RHO or BPY scaffold leads to the same photochemistry. On the other hand it further underlines the remarkable ability of RHO to collect photons due to its high extinction coefficient, as well as its very efficient energy transfer to BPY, which is reflected in the almost 3-fold signal amplitude upon excitation with 565 nm light. Unfortunately, the direct observation, and therefore a quantitative assessment, of PNA photorelease is challenging due to the strong spectral overlap of the PNA absorption with the relatively strong BPY band in the UV.

Therefore, we also irradiated RHO-BPY-OH with 565 nm light (Fig. 4g–i) as a control to substantiate our observation of photocleavage. The resulting difference spectrum (Fig. 4i) clearly differs from Fig. 4c and f. The two bleaching bands centered at 360 nm and 660 nm, which are again mainly due to BPY contributions, are each accompanied by a rise of a blue shifted absorption at 250–300 nm and 500–600 nm, respectively. Unlike RHO-BPY-PNA (Fig. 4b and e), no spectral blue-shift of the band around 300 nm is observed (Fig. 4h). The shapes of the difference bands in Fig. 4i also indicate a significant spectral overlap between reactant and product, which further underlines a different photochemistry compared to the illumination of RHO-BPY-PNA. Here, we assume that the excitation energy is mainly funneled into the cleavage or a disruption of the conjugation of the styryl-residues, which consequently leads to an intact but blue shifted BPY scaffold due to its reduced  $\pi$ -electron system. This is in contrast to results reported by Peterson *et al.*,<sup>52</sup> which show such a cleavage of a styryl residue only as a result of actual cargo release. However, they investigated a BODIPY system with a different leaving group and no additional rhodamine attached, which makes a direct comparison difficult.

## Conclusions

In conclusion, we developed a cooperative dyad based on a rhodamine fluorophore and a BODIPY photocage for one- or two-photon induced uncaging between 500 and 900 nm. This broad spectral window could be advantageous for applications and studies, which demand the usage of different excitation sources. The utilized X-rhodamine derivative displays high two-photon action cross sections ( $\sigma_{2P}\Phi_F$ ) of around 100 GM between 810 and 870 nm, covering parts of the phototherapeutic window. Investigation of the energy transfer from rhodamine to BODIPY by ultrafast transient absorption spectroscopy and quantum dynamics simulations revealed a very fast and efficient EET on the sub-500 fs timescale. Photolysis experiments were performed at 565 and 660 nm using *p*-nitroaniline as a leaving group. It can be deduced from the UV/vis spectra that PNA is released upon illumination. However, the quantification of the uncaging reaction remained challenging due to overlapping bands in the spectrum. Moreover, the employed BODIPY derivative is known for low uncaging quantum yields and photodecomposition, which can partly be compensated by the large extinction coefficient of rhodamine. Future work will therefore focus on identifying variants of the BODIPY moiety which improve its uncaging properties.

## Conflicts of interest

The authors declare no competing financial interest.

## Acknowledgements

We thank Jan von Cosel and Konstantin Falahati for providing the in-house implementation used to compute the electronic TDC coupling and Francesco Di Maiolo for useful discussions and help with preparing the figures. We gratefully acknowledge funding of the Deutsche Forschungsgemeinschaft (DFG)

through the research training group “CLiC” (GRK 1986, Complex Light-Control).

## Notes and references

- W. Denk, J. H. Strickler and W. W. Webb, *Science*, 1990, **248**, 73–76.
- J. D. Bhawalkar, N. D. Kumar, C.-F. Zhao and P. N. Prasad, *J. Clin. Laser Med. Surg.*, 1997, **15**, 201–204.
- P. Majumdar, R. Nomula and J. Zhao, *J. Mater. Chem. C*, 2014, **2**, 5982–5997.
- A. M. Durantini, L. E. Greene, R. Lincoln, S. R. Martínez and G. Cosa, *J. Am. Chem. Soc.*, 2016, **138**, 1215–1225.
- M. Matsuzaki, G. C. R. Ellis-Davies, T. Nemoto, Y. Miyashita, M. Iino and H. Kasai, *Nat. Neurosci.*, 2001, **4**, 1086–1092.
- I. Elamri, C. Abdellaoui, J. K. Bains, K. F. Hohmann, S. L. Gande, E. Stirnal, J. Wachtveitl and H. Schwalbe, *J. Am. Chem. Soc.*, 2021, **143**, 10596–10603.
- C. Morville, J. Chaud, F. Bolze and A. Specht, *J. Inclusion Phenom. Macrocyclic Chem.*, 2021, **101**, 291–304.
- R. Weinstain, T. Slanina, D. Kand and P. Klán, *Chem. Rev.*, 2020, **120**, 13135–13272.
- L. Josa-Culleré and A. Llebaria, *ChemPhotoChem*, 2021, **5**, 298–316.
- W. Denk, *Proc. Natl. Acad. Sci. U. S. A.*, 1994, **91**, 6629–6633.
- P. Lipp and E. Niggli, *J. Physiol.*, 1998, **508**, 801–809.
- G. C. R. Ellis-Davies, *Front. Synaptic Neurosci.*, 2019, **10**, 1–13.
- G. C. R. Ellis-Davies, *Acc. Chem. Res.*, 2020, **53**, 1593–1604.
- T. Furuta, S. S. H. Wang, J. L. Dantzker, T. M. Dore, W. J. Bybee, E. M. Callaway, W. Denk and R. Y. Tsien, *Proc. Natl. Acad. Sci. U. S. A.*, 1999, **96**, 1193–1200.
- A. Momotake, N. Lindegger, E. Niggli, R. J. Barsotti and G. C. R. Ellis-Davies, *Nat. Methods*, 2006, **3**, 35–40.
- Y. Becker, S. Roth, M. Scheurer, A. Jakob, D. A. Gacek, P. J. Walla, A. Dreuw, J. Wachtveitl and A. Heckel, *Chem. – Eur. J.*, 2021, **27**, 2212–2218.
- J. P. Olson, H. B. Kwon, K. T. Takasaki, C. Q. Chiu, M. J. Higley, B. L. Sabatini and G. C. R. Ellis-Davies, *J. Am. Chem. Soc.*, 2013, **135**, 5954–5957.
- M. Bojtár, A. Kormos, K. Kis-Petik, M. Kellermayer and P. Kele, *Org. Lett.*, 2019, **21**, 9410–9414.
- J. Morrison, P. Wan, J. E. T. Corrie and G. Papageorgiou, *Photochem. Photobiol. Sci.*, 2002, **1**, 960–969.
- G. C. R. Ellis-Davies, M. Matsuzaki, M. Paukert, H. Kasai and D. E. Bergles, *J. Neurosci.*, 2007, **27**, 6601–6604.
- Y. Zhu, C. M. Pavlos, J. P. Toscano and T. M. Dore, *J. Am. Chem. Soc.*, 2006, **128**, 4267–4276.
- C. Tran, T. Gallavardin, M. Petit, R. Slimi, H. Dhimane, M. Blanchard-Desce, F. C. Acher, D. Ogden and P. I. Dalko, *Org. Lett.*, 2015, **17**, 402–405.
- I. Aujard, C. Benbrahim, M. Gouget, O. Ruel, J. B. Baudin, P. Neveu and L. Jullien, *Chem. – Eur. J.*, 2006, **12**, 6865–6879.
- M. Abe, Y. Chitose, S. Jakkampudi, P. T. T. Thuy, Q. Lin, B. T. Van, A. Yamada, R. Oyama, M. Sasaki and C. Katan, *Adv. Synth. Catal.*, 2017, **49**, 3337–3346.
- K. A. Korzycka, P. M. Bennett, E. J. Cueto-Diaz, G. Wicks, M. Drobizhev, M. Blanchard-Desce, A. Rebane and H. L. Anderson, *Chem. Sci.*, 2015, **6**, 2419–2426.
- S. Picard, E. J. Cueto-Diaz, E. Genin, G. Clermont, F. Acher, D. Ogden and M. Blanchard-Desce, *Chem. Commun.*, 2013, **49**, 10805–10807.
- G. Papageorgiou, M. Lukeman, P. Wan and J. E. T. Corrie, *Photochem. Photobiol. Sci.*, 2004, **3**, 366–373.
- E. Cueto Diaz, S. Picard, M. Klausen, V. Hugues, P. Pagano, E. Genin and M. Blanchard-Desce, *Chem. – Eur. J.*, 2016, **22**, 10848–10859.
- C. A. Hammer, K. Falahati, A. Jakob, R. Klimek, I. Burghardt, A. Heckel and J. Wachtveitl, *J. Phys. Chem. Lett.*, 2018, **9**, 1448–1453.
- M. Beija, C. A. M. Afonso and J. M. G. Martinho, *Chem. Soc. Rev.*, 2009, **38**, 2410–2433.
- A. Nag and D. Goswami, *J. Photochem. Photobiol., A*, 2009, **206**, 188–197.
- C. Xu and W. W. Webb, *J. Opt. Soc. Am. B*, 1996, **13**, 481.
- C. Xu, R. M. Williams, W. Zipfel and W. W. Webb, *Bioimaging*, 1996, **4**, 198–207.
- M. A. Albota, C. Xu and W. W. Webb, *Appl. Opt.*, 1998, **37**, 7352–7356.
- D. A. Oulianov, I. V. Tomov, A. S. Dvornikov and P. M. Rentzepis, *Opt. Commun.*, 2001, **191**, 235–243.
- C. B. Milojevich, D. W. Silverstein, L. Jensen and J. P. Camden, *J. Am. Chem. Soc.*, 2011, **133**, 14590–14592.
- C. B. Milojevich, D. W. Silverstein, L. Jensen and J. P. Camden, *J. Phys. Chem. C*, 2013, **117**, 3046–3054.
- H. Wang, *J. Phys. Chem. A*, 2015, **119**, 7951–7965.
- M. H. Beck, A. Jäckle, G. A. Worth and H.-D. Meyer, *Phys. Rep.*, 2000, **324**, 1–105.
- G. A. Worth, M. H. Beck, A. Jäckle and H.-D. Meyer, *MCTDH Package, Version 8.5.5*, Heidelberg University, 2016, <http://www.mctdh.uni-hd.de>.
- M. J. Frisch, G. W. Trucks, H. B. Schlegel, G. E. Scuseria, M. A. Robb, J. R. Cheeseman, G. Scalmani, V. Barone, G. A. Petersson, H. Nakatsuji, X. Li, M. Caricato, A. V. Marenich, J. Bloino, B. G. Janesko, R. Gomperts, B. Mennucci, H. P. Hratchian, J. V. Ortiz, A. F. Izmaylov, J. L. Sonnenberg, D. Williams-Young, F. Ding, F. Lipparini, F. Egidi, J. Goings, B. Peng, A. Petrone, T. Henderson, D. Ranasinghe, V. G. Zakrzewski, J. Gao, N. Rega, G. Zheng, W. Liang, M. Hada, M. Ehara, K. Toyota, R. Fukuda, J. Hasegawa, M. Ishida, T. Nakajima, Y. Honda, O. Kitao, H. Nakai, T. Vreven, K. Throssell, J. A. Montgomery Jr., J. E. Peralta, F. Ogliaro, M. J. Bearpark, J. J. Heyd, E. N. Brothers, K. N. Kudin, V. N. Staroverov, T. A. Keith, R. Kobayashi, J. Normand, K. Raghavachari, A. P. Rendell, J. C. Burant, S. S. Iyengar, J. Tomasi, M. Cossi, J. M. Millam, M. Klene, C. Adamo, R. Cammi, J. W. Ochterski, R. L. Martin, K. Morokuma, O. Farkas, J. B. Foresman and D. J. Fox, *Gaussian, Inc.*, Wallingford CT, 2016.
- A. D. Becke, *J. Chem. Phys.*, 1993, **98**, 5648.
- P. J. Stephens, F. J. Devlin, C. F. Chabalowski and M. J. Frisch, *J. Phys. Chem.*, 1994, **98**, 11623–11627.

- 44 W. J. Hehre, R. Ditchfield and J. A. Pople, *J. Chem. Phys.*, 1972, **56**, 2257–2261.
- 45 S. Miertuš, E. Scrocco and J. Tomasi, *Chem. Phys.*, 1981, **55**, 117–129.
- 46 S. Miertus and J. Tomasi, *Chem. Phys.*, 1982, **65**, 239–245.
- 47 T. Yanai, D. P. Tew and N. C. Handy, *Chem. Phys. Lett.*, 2004, **393**, 51–57.
- 48 K. Aidas, C. Angeli, K. L. Bak, V. Bakken, R. Bast, L. Boman, O. Christiansen, R. Cimraglia, S. Coriani, P. Dahle, E. K. Dalskov, U. Ekström, T. Enevoldsen, J. J. Eriksen, P. Ettenhuber, B. Fernández, L. Ferrighi, H. Fliegl, L. Frediani, K. Hald, A. Halkier, C. Hättig, H. Heiberg, T. Helgaker, A. C. Hennum, H. Hettema, E. Hjertenæs, S. Høst, I.-M. Høyvik, M. F. Iozzi, B. Jansík, H. J. A. Jensen, D. Jonsson, P. Jørgensen, J. Kauczor, S. Kirpekar, T. Kjærgaard, W. Klopper, S. Knecht, R. Kobayashi, H. Koch, J. Kongsted, A. Krapp, K. Kristensen, A. Ligabue, O. B. Lutnæs, J. I. Melo, K. V. Mikkelsen, R. H. Myhre, C. Neiss, C. B. Nielsen, P. Norman, J. Olsen, J. M. H. Olsen, A. Osted, M. J. Packer, F. Pawłowski, T. B. Pedersen, P. F. Provasi, S. Reine, Z. Rinkevicius, T. A. Ruden, K. Ruud, V. V. Rybkin, P. Salek, C. C. M. Samson, A. S. de Merás, T. Saue, S. P. A. Sauer, B. Schimmelpfennig, K. Snegov, A. H. Steindal, K. O. Sylvester-Hvid, P. R. Taylor, A. M. Teale, E. I. Tellgren, D. P. Tew, A. J. Thorvaldsen, L. Thøgersen, O. Vahtras, M. A. Watson, D. J. D. Wilson, M. Ziolkowski and H. Ågren, *WIREs Comput. Mol. Sci.*, 2014, **4**, 269–284.
- 49 R. Di Remigio, T. Giovannini, M. Ambrosetti, C. Cappelli and L. Frediani, *J. Chem. Theory Comput.*, 2019, **15**, 4056–4068.
- 50 B. P. Krueger, G. D. Scholes and G. R. Fleming, *J. Phys. Chem. B*, 1998, **102**, 5378–5386.
- 51 H. Tamura, J.-M. Mallet, M. Oheim and I. Burghardt, *J. Phys. Chem. C*, 2009, **113**, 7548–7552.
- 52 J. A. Peterson, C. Wijesooriya, E. J. Gehrman, K. M. Mahoney, P. P. Goswami, T. R. Albright, A. Syed, A. S. Dutton, E. A. Smith and A. H. Winter, *J. Am. Chem. Soc.*, 2018, **140**, 7343–7346.

6.4 Asido *et al.*, J. Phys. Chem. Lett., 2021

**Transient near-UV Absorption of the Light-Driven Sodium Pump *Krokinobacter eikastus* Rhodopsin 2: A Spectroscopic Marker for Retinal Configuration**

M. Asido<sup>†</sup>, R. K. Kar<sup>†</sup>, C.N. Kriebel, M. Braun, C. Glaubitz, I. Schapiro and J. Wachtveitl,  
J. Phys. Chem. Lett., **2021**, 12, 6284-6291.

Reprinted with permission from J. Phys. Chem. Lett., 2021, 12, 6284-6291.

doi: <https://doi.org/10.1021/acs.jpcllett.1c01436>

Copyright 2021 American Chemical Society.



# Transient Near-UV Absorption of the Light-Driven Sodium Pump *Krokinobacter eikastus* Rhodopsin 2: A Spectroscopic Marker for Retinal Configuration

Marvin Asido,<sup>1</sup> Rajiv K. Kar,<sup>1</sup> Clara Nassrin Kriebel, Markus Braun, Clemens Glaubitz, Igor Schapiro, and Josef Wachtveitl\*



Cite This: *J. Phys. Chem. Lett.* 2021, 12, 6284–6291



Read Online

ACCESS |



Metrics & More

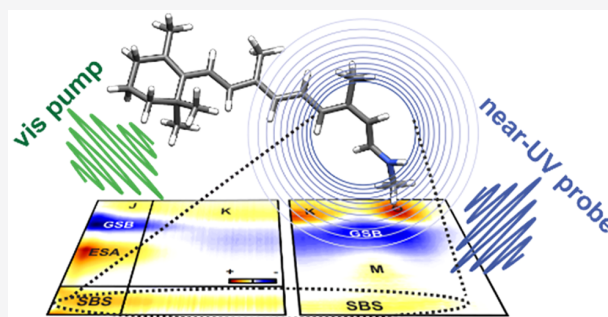


Article Recommendations



Supporting Information

**ABSTRACT:** We report a transient signature in the near-UV absorption of *Krokinobacter eikastus* rhodopsin 2 (KR2), which spans from the femtosecond up to the millisecond time scale. The signature rises with the all-*trans* to 13-*cis* isomerization of retinal and decays with the reversion to all-*trans* in the late photocycle, making it a promising marker band for retinal configuration. Hybrid quantum mechanics/molecular mechanics simulations show that the near-UV absorption signal corresponds to an  $S_0 \rightarrow S_3$  and/or an  $S_0 \rightarrow S_5$  transition, which is present in all photointermediates. These transitions exhibit a negligible spectral shift by the altering protein environment, in contrast to the main absorption band. This is rationalized by the extension of the transition densities that omits the Schiff base nitrogen. Further characterization and first steps into possible optogenetic applications were performed with near-UV quenching experiments of an induced photostationary state, yielding an ultrafast regeneration of the parent state of KR2.



Rhodopsins constitute a large family of photoreceptors which can be found throughout all domains of life. Their functions range from sensing such as vision in eukaryotic organisms, over signal transduction processes across individual cells, up to energy conversion in bacteria and archaea.<sup>1,2</sup> Even though many structural features are well-studied in various types of rhodopsins, some functional as well as mechanistic details are still not fully understood. Research efforts on these proteins have been intensified with new advances in technologies pushing possible applications in biotechnology and medicine, which ultimately culminated in the fast growing field of optogenetics.<sup>3–5</sup> The subclass of microbial rhodopsins that act as ion-channels (ChR1 and ChR2), proton pumps (BR, PR, and XeR), and ion transporters (HR and KR2) are now widely used tools for spatially and temporally precise manipulation of cells.<sup>6–12</sup> The discovery of the light-driven sodium pump KR2 has sparked new interest in the field.<sup>13</sup> Its ability to transport a positive (nonproton) charge across biological membranes is not just seen as a valuable addition to the optogenetic toolbox, but it also raises new questions toward a yet unknown mechanism.

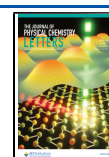
Expanding our knowledge of KR2, and light-driven cation transporters in general, might as well be a key to understand ion translocation processes as a whole. In this work we applied time-resolved UV/vis spectroscopy combined with hybrid quantum mechanics/molecular mechanics (QM/MM) simu-

lations, which are based on structural data reported by Skopintsev et al., Kato et al. (Figure 1), and Kovalev et al. (Figure S4),<sup>14–16</sup> to investigate the photophysics of the KR2 wild type and its D116N mutant ranging from their primary photoreaction (femtosecond–nanosecond) up to the photocycle (microsecond–second). A special focus was put in the near-UV region, which is barely characterized in studies on microbial rhodopsins. We observe a yet unreported spectral signature, which spans the whole time range from photoproduct formation up to the end of the photocycle. Our findings also reveal an extended absorption of the M intermediate, which ranges up to the near-UV. We investigated this further by applying near-UV quenching, which offers a way to exploit these properties for photocontrol experiments and optogenetic applications.<sup>17–20</sup> We restrict our report to wild type at pH 9 (WT9), wild type at pH 5.5 (WT5.5), and to the mutant at pH 9 (D116N), respectively (see the Supporting Information for sample preparation).

Received: May 4, 2021

Accepted: June 29, 2021

Published: July 2, 2021



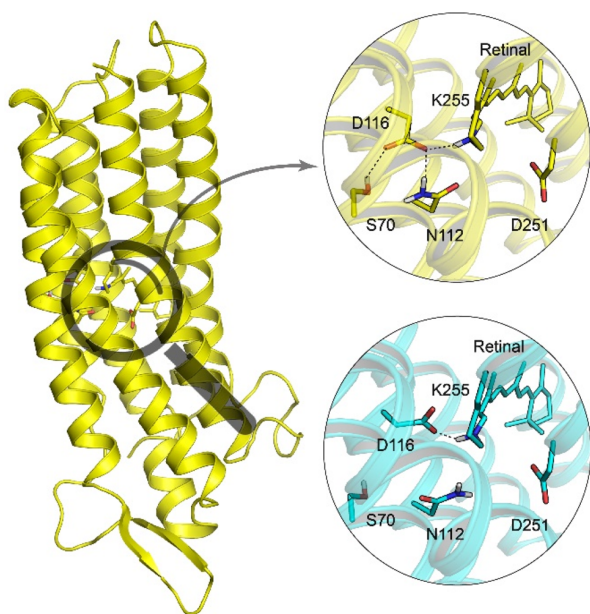


**Figure 1.** Structure of KR2 from Skopintsev et al. (PDB code: 6TK6).<sup>14</sup> The inset (yellow) shows the QM/MM optimized geometry of retinal PSB with key residues of the counterion complex. The QM/MM optimized structure from Kato et al. (PDB code: 3X3C)<sup>15</sup> is shown in cyan for comparison.

The primary photoreaction of the KR2 WT and the D116N mutant was studied with ultrafast UV/vis transient absorption (TA) spectroscopy, which covers the time scale from femtoseconds to nanoseconds (Figure 2). Photoexcitation of the retinal protonated Schiff base (PSB) leads to a depopulation of the ground state seen as ground-state bleach (GSB) around 560 nm and an associated population in the excited state seen as excited-state absorption (ESA) at 460 nm. The rise of these signals occurs on a time scale that is faster than the experimental resolution. The lifetime distribution of these signals stretches over several decades, suggesting a multiphasic decay. However, the amplitude distribution differs significantly from sample to sample (Figure 2a–c, right panel). Whereas for WT9 the biggest contribution lies in the femtosecond-range, the main component shifts toward later times (20–80 ps) for WT5.5 and D116N. This signature is accompanied by an additional positive signal at the red end of the spectral window (most evident for WT9). This induced absorption rises on the sub-300 fs time scale, which reflects the all-*trans* to 13-*cis* isomerization of retinal, forming the vibrationally hot J intermediate.<sup>14,21–24</sup> Because of vibrational cooling, the absorption then shifts to shorter wavelengths in the course of 1–3 ps, leading to the first ground-state photoproduct of KR2 (K intermediate).<sup>14,22–24</sup>

A similar behavior can be observed at pH 5.5, but with a weaker amplitude due to a stronger overlap with the GSB. The photoproduct absorption becomes dominant at 8–10 ps. In the case of D116N, a formation and decay of the J intermediate is not observed. The absorption of the K intermediate, however, becomes more pronounced on the 70–80 ps time scale. These differences can be rationalized in two ways: First, the spectrum of the ground state is strongly dependent on the protonation state of the counterion D116, which dictates its interaction with the retinal Schiff base (RSB) and therefore results in an absorption shift from 525 nm

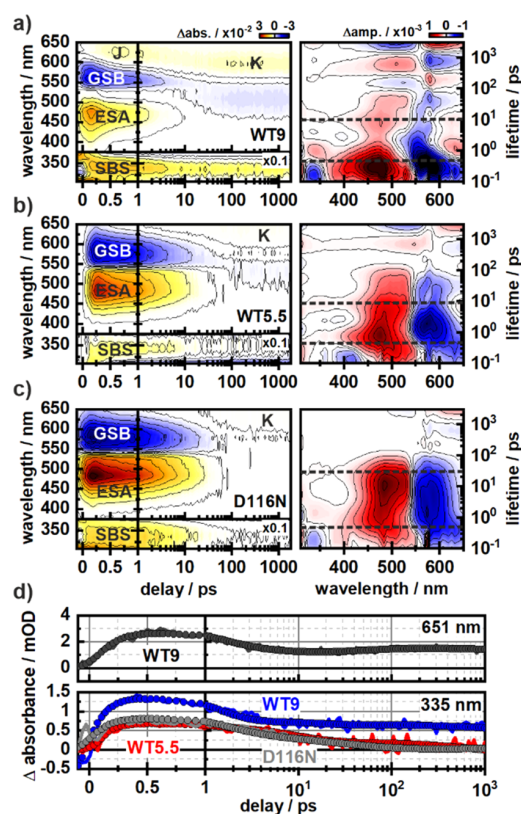


**Figure 2.** 2D-contour plots of the ultrafast TA measurements (left) and their corresponding lifetime density maps (right) for WT9 (a), WT5.5 (b), and D116N (c). The dashed lines in the LDMs indicate the time constants of retinal isomerization and the excited-state lifetime. The formation of the J-intermediate and its relaxation to the primary photoproduct shown exemplarily at 651 nm for the WT9 case (d, top). A similar temporal behavior is seen for the transients at 335 nm (d, bottom). However, only WT9 shows a significant residual amplitude on the longer time scale. Note that the amplitude range of the near-UV window is 10-fold smaller.

(strong interaction) up to 560 nm (weak/no interaction).<sup>15</sup> Consequently, the overlap of the GSB with the J signature is larger for WT5.5 and D116N. Second, the same interaction seems to influence the isomerization quantum yield itself, leading to a decreased photoproduct formation for WT5.5 and D116N. A possible reason for such a lowered quantum yield could be the change from a strongly pretwisted chromophore in WT9 to a more relaxed chromophore in WT5.5 or the D116N mutant due to a missing hydrogen bond.<sup>16,25</sup>

In the study of Tahara et al. it was reported that the excited state in KR2 shows a multiphasic decay with a fast and a slow component.<sup>24</sup> They attributed the fast component to the reactive pathway, which results in photoproduct formation, and the slower component to a nonreactive decay back to the ground state. By determining the pH-dependent ratios of these reactive/nonreactive lifetime amplitudes, they proposed a ground-state heterogeneity of hydrogen-bonded and non-hydrogen-bonded RSB species. This heterogeneity is easily visualized in the LDMs of our ultrafast TA measurements (Figure 2a–c, right panel). Upon extension of the probed wavelength, an additional and unreported absorption, here termed second bright state (SBS), can be observed for all samples around 335 nm (Figure 2a–c). The lifetime

distribution of this signal indicates that it has approximately the same lifetime components as the photoproduct formation. This becomes even more evident by comparing the transients at 335 nm (Figure 2d, lower panel) with the transient at 651 nm, which is representative for the J-K-formation in WT9 (Figure 2d, upper panel). Besides the kinetic similarity of these transients, another trend can be observed. For WT9 the signal reaches a plateau which persists up to the nanosecond time scale, whereas for WT5.5 the residual amplitude is less pronounced; for D116N, it is completely absent.

To learn more about the near-UV band response during the entire photocycle, we expanded our investigations to the microsecond–second time scale by utilizing UV/vis flash photolysis. Numerous spectroscopic studies of retinal proteins on this time scale are available; however, investigations in the spectral window below 350 nm are scarce. To simplify a kinetic description of the new findings, a brief review of the already known photocycle characteristics in KR2 shall be given with the data at hand.<sup>14,26–30</sup> At pH 9 the early photocycle dynamics is dominated by the decay of the K intermediate on the microsecond time scale (Figure 3a). This is followed by a

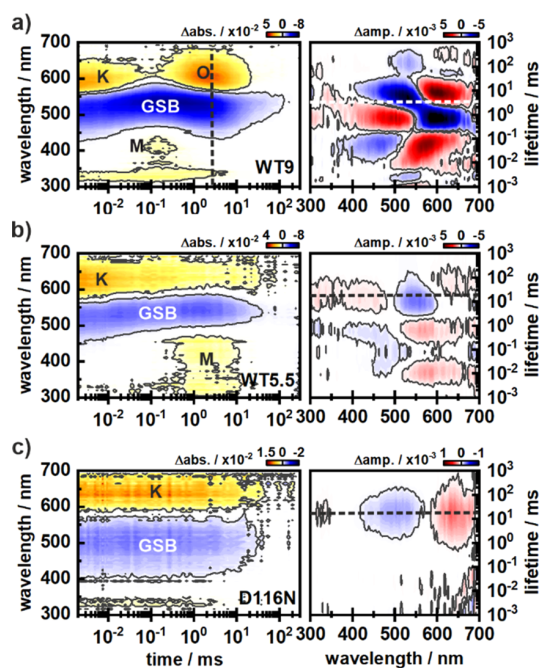


**Figure 3.** 2D-contour plots of the flash photolysis measurements (left) and their corresponding lifetime density maps (right) for WT9 (a), WT5.5 (b), and D116N (c). The dashed lines indicate the lifetime of the near-UV absorption decay. In contrast to WT5.5 and D116N, the decay of the near-UV absorption in WT9 shows an additional component, which correlates with the rise of the O-state.

spectral blue shift of the signal due to deprotonation of the RSB at 0.1 ms, which indicates the transition to the M intermediate. This blue shift is then reversed by reprotonation of the RSB during the M-to-O transition at around 1 ms. The photocycle is completed within 7–10 ms. At pH 5.5 the photocycle is altered. Acidic pH values lead to the protonation of the D116 residue, which then coordinates with S70 and N112 instead of the RSB (Figure 1).<sup>15,31</sup> This is reflected in the elongated, biphasic decay of the K intermediate (Figure

3b). The actual deprotonation step of the RSB, and therefore the K-to-M transition, occurs within 3–4 ms.

In contrast to WT9, the M-to-O transition in WT5.5 is almost completely missing. This is most likely due to the increased proton concentration which now competes with the sodium ions for actual charge transport.<sup>32</sup> In the case of D116N, both M and O are not observed. This is explained by the loss of pumping activity of KR2 caused by the lack of the essential acid group at position 116.<sup>27</sup> Instead, one can just observe the slow decay of the K photoproduct, which is well-described by a single lifetime (Figure 3c, right). Besides the common photocycle intermediates, an interesting signature can be found below 350 nm, which is most pronounced for WT9. The large amplitude at the beginning of the temporal window indicates a rise time, which precedes the temporal resolution of the flash photolysis experiments. The transients of this signal (Figure S2) show a clear additional rise in amplitude at 0.1 ms (WT9) and 3 ms (WT5.5). For D116N, where the M-intermediate is missing, no such behavior is observed. This is also reflected in the LDM of D116N (Figure 3c), which stresses the monoexponential nature of the recovery to the parent state. The kinetic analysis of WT9 and WT5.5 is more complicated. The lifetime distribution suggests a temporal correlation of this signal rise with the formation and decay of the M intermediate. For WT9, however, an additional but slightly delayed lifetime component is found in the spectral range of 330–360 nm. This component, in turn, correlates well with the lifetime found for the formation of the O intermediate, being indicative for the reisomerization process from 13-*cis* to all-*trans*, as shown in Jaktetchai et al. and Kovalev et al.<sup>16,33</sup> These findings suggest that the near-UV signature is in fact a composition of two overlapping features. The first contribution is centered around 335 nm and spans from the femtosecond time scale up to the late steps of the photocycle and can therefore be considered as a marker band for the 13-*cis* isomer of retinal. The second one is characterized by the additional rise component, which shows a strong correlation with the M intermediate and is consequently missing in D116N. In this context it is noteworthy that there are other well-established techniques to probe the retinal configuration, such as Raman spectroscopy of the fingerprint region from 1100 to 1400  $\text{cm}^{-1}$ , which was first established for BR by Braiman and Mathies<sup>34</sup> and has also been applied to KR2.<sup>23,35</sup> Even though the sensitivity of this technique is outstanding, it comes with a few challenges such as the complicated data analysis due to overlapping signals, small signal amplitudes, and the necessity of prior knowledge of the photocycle dynamics in order to correlate the Raman and UV/vis spectra.

So far, we discussed the near-UV signatures from the femtosecond time scale up to the final decay on the millisecond time scale. The long time range as well as the constant spectral position of this absorption band are surprising, considering the changes of the retinal chromophore over the duration of the photocycle. To elucidate this observation, we employed hybrid QM/MM simulations. The excitation energy was calculated for the structure of four different photocycle intermediates from the time-resolved serial femtosecond crystallography (TR-SFX) study by Skopintsev et al.<sup>14</sup> The computed vertical excitation energies for the parent state are summarized in Figure 4a and Table 1.

The  $S_1$  excitation energy is 2.54 eV (488 nm), which is 0.18 eV higher compared to the experimental absorption band

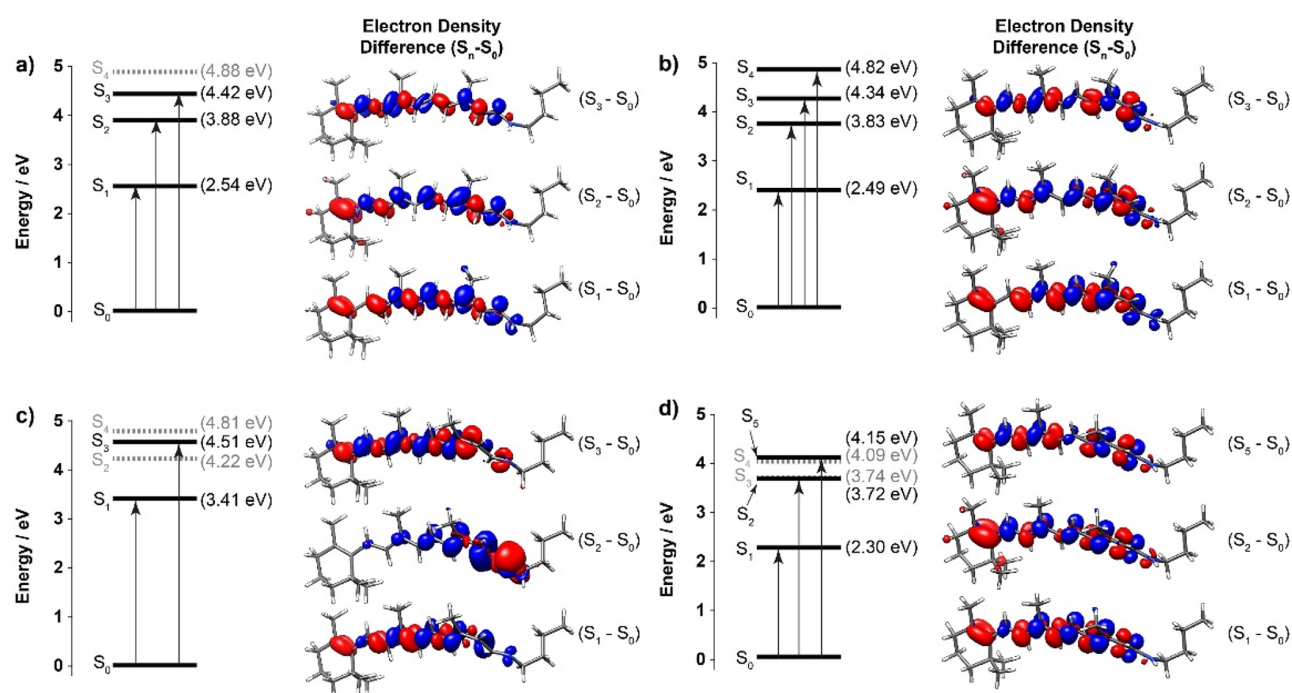


**Figure 4.** Excitation energies for (a) parent state, (b) K intermediate, (c) M intermediate, and (d) O intermediate of KR2. The electron density differences are given for each  $S_0 \rightarrow S_n$  excitation. The colors red and blue highlight negative and positive differences, respectively. Black lines connected by an arrow indicate bright states, while the gray dotted lines indicate dark states (oscillator strength  $\leq 0.100$ ).

**Table 1. QM/MM Excitation Energies and Oscillator Strength**

excited state	WT <sup>a</sup>		WT <sup>b</sup>		K intermediate <sup>a</sup>		M intermediate <sup>a</sup>		O intermediate <sup>a</sup>	
	wavelength eV (nm)	osc. str. (f)	wavelength eV (nm)	osc. str. (f)	wavelength eV (nm)	osc. str. (f)	wavelength eV (nm)	osc. str. (f)	wavelength eV (nm)	osc. str. (f)
S <sub>1</sub>	2.54 (488)	1.738	2.78 (446)	1.746	2.49 (498)	1.683	3.41 (364)	2.083	2.30 (539)	1.546
S <sub>2</sub>	3.88 (319)	0.196	4.06 (305)	0.219	3.83 (324)	0.155	4.22 (294)	0.002	3.72 (333)	0.164
S <sub>3</sub>	4.42 (280)	0.322	4.44 (279)	0.407	4.33 (286)	0.269	4.51 (275)	0.158	3.74 (332)	0.004
S <sub>4</sub>	4.88 (254)	0.058	5.02 (247)	0.048	4.82 (257)	0.112	4.81 (258)	0.029	4.09 (302)	0.005
S <sub>5</sub>	5.43 (228)	0.004	5.57 (222)	0.023	5.36 (231)	0.021	5.33 (233)	0.021	4.15 (299)	0.421

<sup>a</sup>Calculations based on Skopintsev et al. structures. <sup>b</sup>Calculations based on Kato et al. structure.

maximum of 2.36 eV (525 nm). We also performed the simulation based on the X-ray diffraction (XRD) structure reported by Kato et al. (Figure S6).<sup>15</sup> It also resulted in S<sub>1</sub> excitation energy higher than the experimental value, namely, 2.78 eV (446 nm) (Table 1). The relative difference in the computed excitation energy between the two structures could be attributed to rearrangement of the counterion complex involving D116 and N112.

This difference might originate from the different pH values in the crystallographic studies. Among the higher excited states based on the Skopintsev et al. structure, S<sub>2</sub> is found at 3.88 eV (319 nm) and S<sub>3</sub> at 4.42 eV (280 nm). These excitations have oscillator strengths (*f*) of 0.196 and 0.322, respectively. A similar trend was found in the Kato et al. structure, where S<sub>2</sub> at 4.06 eV (305 nm, *f* = 0.219) is less bright compared to S<sub>3</sub> at 4.44 eV (279 nm, *f* = 0.407). The energy difference  $\Delta E_{S_2-S_1}$  is 1.35 and 1.28 eV for both structures, while  $\Delta E_{S_3-S_1}$  is 1.88 and 1.67 eV, respectively. On the basis of the relative energy, S<sub>2</sub> is a better candidate to explain the experimental signal at 335 nm ( $\Delta E = 1.34$  eV). However, considering the higher intensity of

the S<sub>0</sub>–S<sub>3</sub> transition and an error of ca. 0.22 eV in the ADC(2) method, the S<sub>3</sub> state seems to be favored.<sup>36</sup>

In both structures, S<sub>2</sub> and S<sub>3</sub> have a similar pattern in the electron density difference (EDD) (Figures 4a and S6). The EDD indicates a significantly reduced contribution of the  $\pi$ -density from the Schiff base nitrogen compared the EDD from S<sub>1</sub>. The nitrogen carries the formal positive charge and is known to play a key role in the spectral tuning mechanism of retinal proteins. Therefore, a smaller extent of the EDD on this atom means that S<sub>2</sub> and S<sub>3</sub> will be less sensitive to changes in the protein environment. Indeed, the S<sub>0</sub>–S<sub>3</sub> excitation energy is nearly identical for the structures by Skopintsev et al. and Kato et al. (Table 1) despite the alternation in the counterion complex. For the K intermediate, the calculated S<sub>1</sub> was found at 2.49 eV (498 nm) compared to the experimental value of 2.45 eV (505 nm). Also, in this case S<sub>2</sub> is a better candidate than S<sub>3</sub> to explain the near-UV band in terms of energy.

The energy differences for  $\Delta E_{S_2-S_1}$  and  $\Delta E_{S_3-S_1}$  are 1.34 and 1.84 eV, respectively (Table 1). The exclusion of the nitrogen from EDDs of the higher excited states is analogous to the parent state described above (Figure 4b). The deprotonation of the retinal Schiff base in the M intermediate changes the

excited-state energies and the electronic structure (Figure 4c). It induces a strong blue shift on the main absorption band compared to the parent state, i.e. by 0.87 eV in the QM/MM simulation and by 0.73 eV in the TA-measurement. The  $S_2$  state has now an  $n-\pi^*$  instead of  $\pi-\pi^*$  character, which stems from the lone pair on the SB nitrogen. Therefore, it has a negligible oscillator strength and should not be experimentally observable. However, the  $S_0-S_3$  transition is bright and has an excitation energy of 4.51 eV (275 nm) which can explain the measured near-UV signal. For the O intermediate (Figure 4d), the  $S_1$  appears at 2.3 eV (539 nm) which is red-shifted by  $-0.24$  eV with respect to the parent state. This result is in good agreement with the experimental red shift of  $-0.27$  eV. We attributed this red shift to the presence of a positive point charge from the  $\text{Na}^+$  ion in the putative binding site described by Skopintsev et al. The presence of this charge also required extending the QM region (see methodology in the Supporting Information) to avoid overpolarization. The next two bright states were found to be  $S_2$  at 3.72 eV (333 nm) and  $S_5$  at 4.15 eV (299 nm) with oscillator strengths of 0.164 and 0.421, respectively. However, despite the close agreement it should be noted that experimental maxima from TA spectra can in some cases not be determined unambiguously because of the transient overlap of multiple intermediates.

Following the observation of a positive SBS signal in the transition from the parent state to the K and M intermediates (Figure 2), a corresponding trend is also expected for the oscillator strength of the  $S_3$  state. Instead, we noticed a lower oscillator strength for the K and M intermediates compared to the parent state that should lead to a negative signal. By inspecting higher lying states, we found  $S_4$  to be energetically close to  $S_3$  (Table 1). The  $S_4$  state is found to have an oscillator strength which is larger in the K intermediate than in the parent form. Therefore, the contribution from  $S_4$  could explain the positive signal. For the M intermediate, the  $\Delta E_{S_4-S_3}$  is smaller but the oscillator strength for both states is reduced compared to the other two structures. This discrepancy might be due to the change of the total charge in the QM region from +1 to 0 in the calculation of the M intermediate. Therefore, the oscillator strength might not be directly comparable between the parent form and the K intermediate on the one hand and the M intermediate on the other hand.

Additional calculations were also performed for O intermediate structures from Kovalev et al., which in contrast to the aforementioned structure has an all-*trans* retinal.<sup>16</sup> Two structures corresponding to the O-intermediate at 100 K temperature (PDB code: 6XYT) and at room temperature (PDB code: 6YC0) were calculated. The  $S_1$  excitation energy is 1.95 eV (635 nm) and 2.04 eV (607 nm), showing a red shift of  $-0.59$  and  $-0.5$  eV compared to the parent state (Table S2 and Figure S7). The  $S_2$  excited state is at 3.26 and 3.35 eV, respectively.

This is ca. 0.4 eV lower than the value from the 13-*cis* based structure. Given the fact that the calculated excitation energies are systematically higher than the experimental values, this would correspond to an absorption band at  $>400$  nm. However, Figure 3a shows a negative GSB signal in this region which together with the low oscillator strength of  $S_2$  makes it hard to detect. In contrast to the O intermediate with 13-*cis* retinal, the  $S_5$  state has a greatly reduced oscillator strength of 0.069 and 0.068, respectively. This explains the lack of the near-UV signal after 2 ms (Figure 3a). One also needs to consider that the discussed structures represent different

oligomeric states of KR2. Whereas the structures by Skopintsev et al. and Kato et al. were reported to be monomers, the structure of Kovalev et al. was reported as a pentamer. In contrast to the compact monomer, the more expanded conformation in the KR2 pentamer contains a large water cluster in the retinal binding pocket.<sup>33,37,38</sup> This could affect the spectral properties of retinal itself and in turn partly account for the deviations of the calculated energies with respect to the experiment.

To gain additional insight into the nature of the aforementioned UV-signature around 335 nm, we performed quenching experiments in the near-UV on WT9 and WT5.5. This has to be distinguished from the commonly known blue-light quenching (BLQ) effect, which was initially described for BR and has ever since been applied to several other retinal proteins.<sup>17–19</sup> Here, ultrafast TA measurements on PR could demonstrate that illumination of the blue-shifted photo-intermediate (M state) with blue light leads to a fast reprotonation of the RSB and a reisomerization of the chromophore, which subsequently leads to the fast regeneration of the parent state.<sup>20</sup>

We utilized a similar reasoning in order to investigate the near-UV deactivation dynamics and its possible applicability to optical control schemes. Because the near-UV signature itself is transient, several experimental limitations had to be considered. The sample was kept in a photostationary state (PSS) during the TA-measurements to ensure a significant accumulation of the photocycle intermediates. This was achieved by using a high-power LED with a central wavelength of 565 nm. The difference spectra (Figure 5a) show a similar signature for WT9 and WT5.5. In both cases, a blue-shifted band at 330 nm and a red-shifted band at 610 nm are observed. Interestingly, the blue-shifted band does not occur in D116N, even though a

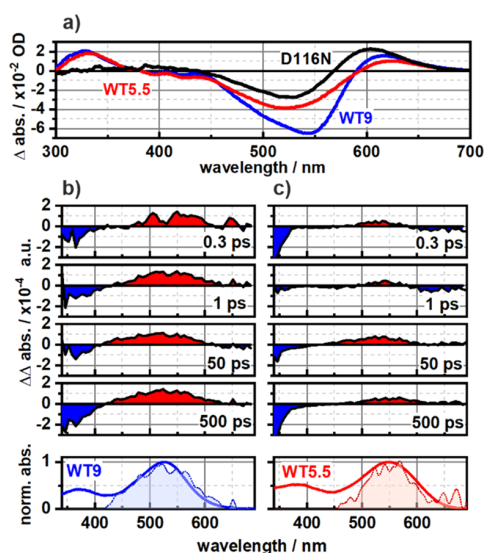


**Figure 5.** Steady-state difference spectra ( $A_{\text{illuminated}} - A_{\text{parent}}$ ) of WT9, WT5.5, and D116N (a). The PSS spectrum is a mixture of bleached ground-state absorption at 520–550 nm, UV-absorption at 335 nm, and a red-shifted absorption at around 600 nm. The UV-band is missing for the D116N mutant. Double-difference spectra of the near-UV quenching experiments for WT9 (b) and WT5.5 (c). The bottom panel shows an overlay of the respective normalized absorption spectra with the  $\Delta\Delta$  abs. spectra at 500 ps.

near-UV absorption was observed in the time-resolved flash photolysis experiments. It is also noteworthy that a signature for M around 400 nm is seemingly missing in WT9 and WT5.5. This is probably due to the dominant bleaching band, which spans from around 400 to 600 nm. The small shoulder at 390–450 nm may stem from a spectral contribution from M. The presence of several bands in the PSS, and therefore the implication of a mixture of states, underlines the complexity of the time-resolved quenching experiments.

To minimize error from mixed dynamics, the TA-experiments with excitation pulses of 330 nm were performed with and without constant illumination, respectively, to determine the dynamics primarily originating from the quenching process itself. The corresponding double-difference spectra (Figure 5b,c) show two dominant features for each sample: a negative (bleached) band, which is centered at a wavelength below 350 nm, and a broader positive band. The positive band seems to be fully developed on the 0.3–1 ps time scale for WT9, whereas for WT5.5 it takes significantly longer. The good spectral match of the resulting  $\Delta\Delta$  abs. spectra with the absorption spectra of the respective samples is a clear indication for the quenching process.

Because the PSS contains a mixture of intermediates, it is not possible to determine the deactivation pathway unambiguously. However, in addition to the main band from the bleached SBS, there are additional negative contributions, which might actually be indicative for the predominantly quenched state. The negative band is broader in WT9 and extends up to 420 nm, whereas in WT5.5 there is a small negative component at the red end of the spectral range. These signatures are in line with the spectral positions of the M intermediate for WT9 and the long-lived K intermediate for WT5.5. Thereby, one needs to consider that the recovery of the parent state from either K or M are to be distinguished. Whereas in both cases a 13-*cis* to all-*trans* isomerization is required, M additionally needs to undergo a reprotonation of the RSB. In the case of PR, this was considered to be the rate-limiting step of the quenching process.<sup>20</sup> It is therefore surprising that the deactivation dynamics is still seemingly faster in WT9. This would imply a closely connected network of amino acid residues and internal water molecules, which in turn respond very fast toward changes of the retinal configuration. Because the mechanistic details of proton translocation are still not fully understood, we cannot rule out the possibility of an alternative reprotonation pathway of the RSB. The slower transition from K to the parent state in the WT5.5 case could be the result of changes in the retinal binding pocket during the early stages of the photocycle as reported recently.<sup>33</sup> It was found that the retinal chromophore becomes significantly more twisted in K and L because of a more direct interaction with D116, which could in turn hamper the near-UV-induced reisomerization.

In conclusion, our integrated near-UV study on KR2, employing time-resolved optical spectroscopy together with QM/MM calculations, closes the gap between spectroscopic characterizations in the UV and in the visible ranges. The underrepresented near-UV region provides valuable information about the chromophore configuration and opens a new avenue for optogenetic applications. We could show that the rise of the induced absorption in the near-UV strongly correlates with the all-*trans* to 13-*cis* isomerization and the formation of the primary photoproduct.

A closer look at the electronic structures of retinal during the photocycle suggests an  $S_0 \rightarrow S_3$  (GS, K, and M) or an  $S_0 \rightarrow S_2$  (O) transition, which are energetically only weakly affected by electronic changes of the chromophore. The weaker spectral tuning of this excited state was explained based on the electron density difference, which showed no contribution to the  $\pi$ -electron density from the SB-nitrogen. The decay of this second bright state of 13-*cis* retinal implies a reisomerization back to all-*trans* during the formation of the O-intermediate and thus confirms recent findings by DNP-enhanced solid-state NMR.<sup>33</sup> We furthermore determined an additional contribution to this band for the WT samples on the millisecond time scale, which is exactly synchronized with the M-state and is completely missing in the D116N mutant. This correlation was further substantiated in experiments in the photostationary state. The results of the near-UV quenching experiments show a surprisingly fast regeneration of the parent state, which is faster in WT9 compared to WT5.5. We rationalize this by a predominant quenching of M (WT9) or K (WT5.5), which lead to differing deactivation pathways. In terms of applicability, we suggest that the near-UV region is not just a useful diagnostic spectral area but also interesting for optical control scenarios. Ranging from femtoseconds up to milliseconds, this spectral signature might be used to terminate the photocycle dynamics at different time points by applying a temporally delayed near-UV pulse.

## ■ ASSOCIATED CONTENT

### Supporting Information

The Supporting Information is available free of charge at <https://pubs.acs.org/doi/10.1021/acs.jpcllett.1c01436>.

Experimental details: expression of the KR2 WT and D116N mutant, sample preparation, steady-state absorption, flash photolysis experiments, fs-UV/vis-pump-probe experiments, kinetic analysis of spectroscopic data, computational methods; supplementary data: absorption spectra, flash photolysis transients, global lifetime analysis, hybrid QM/MM simulations, calculations of the O-intermediate (in all-*trans* configuration) (PDF)

## ■ AUTHOR INFORMATION

### Corresponding Author

Josef Wachtveitl – Institute of Physical and Theoretical Chemistry, Goethe University Frankfurt, 60438 Frankfurt am Main, Germany; [orcid.org/0000-0002-8496-8240](https://orcid.org/0000-0002-8496-8240); Email: [wveitl@theochem.uni-frankfurt.de](mailto:wveitl@theochem.uni-frankfurt.de)

### Authors

Marvin Asido – Institute of Physical and Theoretical Chemistry, Goethe University Frankfurt, 60438 Frankfurt am Main, Germany

Rajiv K. Kar – Fritz Haber Center for Molecular Dynamics Research at the Institute of Chemistry, The Hebrew University of Jerusalem, 9190401 Jerusalem, Israel; [orcid.org/0000-0003-4629-5863](https://orcid.org/0000-0003-4629-5863)

Clara Nassrin Kriebel – Institute for Biophysical Chemistry and Center for Biomolecular Magnetic Resonance (BMRZ), Goethe University Frankfurt, 60438 Frankfurt am Main, Germany

**Markus Braun** – Institute of Physical and Theoretical Chemistry, Goethe University Frankfurt, 60438 Frankfurt am Main, Germany

**Clemens Glaubitz** – Institute for Biophysical Chemistry and Center for Biomolecular Magnetic Resonance (BMRZ), Goethe University Frankfurt, 60438 Frankfurt am Main, Germany; [orcid.org/0000-0002-3554-6586](https://orcid.org/0000-0002-3554-6586)

**Igor Schapiro** – Fritz Haber Center for Molecular Dynamics Research at the Institute of Chemistry, The Hebrew University of Jerusalem, 9190401 Jerusalem, Israel; [orcid.org/0000-0001-8536-6869](https://orcid.org/0000-0001-8536-6869)

Complete contact information is available at:  
<https://pubs.acs.org/10.1021/acs.jpcllett.1c01436>

### Author Contributions

<sup>1</sup>M.A. and R.K.K. contributed equally.

### Notes

The authors declare no competing financial interest.

### ACKNOWLEDGMENTS

M.A., M.B., C.G., and J.W. greatly appreciate funding by the Deutsche Forschungsgemeinschaft (DFG) via the research training group CLiC (GRK 1986) and the SFB 807 (Transport and Communication across Biological Membranes). C.G. thanks DFG for support via GL 307-12-1, I.S. via the SFB 1078 within the Mercator program. I.S. gratefully acknowledges funding by the European Research Council (ERC) under the European Union's Horizon 2020 research and innovation program (Grant No. 678169, "PhotoMutant"). R.K.K. acknowledges support from the Lady Davis Trust for the Arskin postdoctoral fellowship. We also thank Torben Saßmannshausen and Gerrit Lamm for their assistance with the flash photolysis experiments.

### REFERENCES

- (1) Ernst, O. P.; Lodowski, D. T.; Elstner, M.; Hegemann, P.; Brown, L. S.; Kandori, H. Microbial and Animal Rhodopsins: Structures, Functions and Molecular Mechanisms. *Chem. Rev.* **2014**, *114*, 126–163.
- (2) Kouyama, T.; Murakami, M. Structural Divergence and Functional Versatility of the Rhodopsin Superfamily. *Photochem. Photobiol. Sci.* **2010**, *9* (11), 1458–1465.
- (3) Boyden, E. S.; Zhang, F.; Bamberg, E.; Nagel, G.; Deisseroth, K. Millisecond-Timescale, Genetically Targeted Optical Control of Neural Activity. *Nat. Neurosci.* **2005**, *8* (9), 1263–1268.
- (4) Deisseroth, K. Optogenetics. *Nat. Methods* **2011**, *8* (1), 26–29.
- (5) Deisseroth, K. Optogenetics: 10 Years of Microbial Opsins in Neuroscience. *Nat. Neurosci.* **2015**, *18* (9), 1213–1225.
- (6) Oesterhelt, D.; Stoekenius, W. Rhodopsin-like Protein from the Purple Membrane of Halobacterium Halobium. *Nat. New Biol.* **1971**, *233* (39), 149–152.
- (7) Schobert, B.; Lanyi, J. K. Halorhodopsin Is a Light-Driven Chloride Pump. *J. Biol. Chem.* **1982**, *257* (17), 10306–10313.
- (8) Beja, O.; Aravind, L.; Koonin, E. V.; Suzuki, M. T.; Hadd, A.; Nguyen, L. P.; Jovanovich, S. B.; Gates, C. M.; Feldman, R. A.; Spudich, J. L.; Spudich, E. N.; DeLong, E. F. Bacterial Rhodopsin: Evidence for a New Type of Phototrophy in the Sea. *Science (Washington, DC, U. S.)* **2000**, *289* (5486), 1902–1906.
- (9) Nagel, G.; Ollig, D.; Fuhrmann, M.; Kateriya, S.; Musti, A. M.; Bamberg, E.; Hegemann, P. Channelrhodopsin-1: A Light-Gated Proton Channel in Green Algae. *Science (Washington, DC, U. S.)* **2002**, *296* (5577), 2395–2398.
- (10) Nagel, G.; Szell, S.; Huhn, W.; Kateriya, S.; Adeishvili, N.; Berthold, P.; Ollig, D.; Hegemann, P.; Bamberg, E. Channelrhodop-

sin-2, a Directly Light-Gated Cation-Selective Membrane Channel. *Proc. Natl. Acad. Sci. U. S. A.* **2003**, *100*, 13940–13945.

(11) Bamann, C.; Bamberg, E.; Wachtveitl, J.; Glaubitz, C. Proteorhodopsin. *Biochim. Biophys. Acta, Bioenerg.* **2014**, *1837* (5), 614–625.

(12) Shevchenko, V.; Mager, T.; Kovalev, K.; Polovinkin, V.; Alekseev, A.; Juettner, J.; Chizhov, I.; Bamann, C.; Vavourakis, C.; Ghai, R.; Gushchin, I.; Borshchevskiy, V.; Rogachev, A.; Melnikov, I.; Popov, A.; Balandin, T.; Rodriguez-Valera, F.; Manstein, D. J.; Bueldt, G.; Bamberg, E.; Gordeliy, V. Inward H<sup>+</sup> Pump Xenorhodopsin: Mechanism and Alternative Optogenetic Approach. *Sci. Adv.* **2017**, *3* (9), e1603187.

(13) Inoue, K.; Ono, H.; Abe-Yoshizumi, R.; Yoshizawa, S.; Ito, H.; Kogure, K.; Kandori, H. A Light-Driven Sodium Ion Pump in Marine Bacteria. *Nat. Commun.* **2013**, *4*, 1678.

(14) Skopintsev, P.; Ehrenberg, D.; Weinert, T.; James, D.; Kar, R. K.; Johnson, P. J. M.; Ozerov, D.; Furrer, A.; Martiel, I.; Dworkowski, F.; Nass, K.; Knopp, G.; Cirelli, C.; Arrell, C.; Gashi, D.; Mous, S.; Wranik, M.; Gruhl, T.; Kekilli, D.; Brünle, S.; Deupi, X.; Schertler, G. F. X.; Benoit, R. M.; Panneels, V.; Nogly, P.; Schapiro, I.; Milne, C.; Heberle, J.; Standfuss, J. Femtosecond-to-Millisecond Structural Changes in a Light-Driven Sodium Pump. *Nature* **2020**, *583* (7815), 314–318.

(15) Kato, H. E.; Inoue, K.; Abe-Yoshizumi, R.; Kato, Y.; Ono, H.; Konno, M.; Hososhima, S.; Ishizuka, T.; Hoque, M. R.; Kunitomo, H.; Ito, J.; Yoshizawa, S.; Yamashita, K.; Takemoto, M.; Nishizawa, T.; Taniguchi, R.; Kogure, K.; Maturana, A. D.; Iino, Y.; Yawo, H.; Ishitani, R.; Kandori, H.; Nureki, O. Structural Basis for Na<sup>+</sup> Transport Mechanism by a Light-Driven Na<sup>+</sup> Pump. *Nature* **2015**, *521* (7550), 48–53.

(16) Kovalev, K.; Astashkin, R.; Gushchin, I.; Orekhov, P.; Volkov, D.; Zinovev, E.; Marin, E.; Rulev, M.; Alekseev, A.; Royant, A.; Carpentier, P.; Vaganova, S.; Zabelskii, D.; Baeken, C.; Sergeev, I.; Balandin, T.; Bourenkov, G.; Carpena, X.; Boer, R.; Maliar, N.; Borshchevskiy, V.; Büldt, G.; Bamberg, E.; Gordeliy, V. Molecular Mechanism of Light-Driven Sodium Pumping. *Nat. Commun.* **2020**, *11* (1), 2137.

(17) Karvaly, B.; Dancsházy, Z. Bacteriorhodopsin: A Molecular Photoelectric Regulator Quenching of Photovoltaic Effect of Bimolecular Lipid Membranes Containing Bacteriorhodopsin by Blue Light. *FEBS Lett.* **1977**, *76* (1), 36–40.

(18) Hegemann, P.; Oesterhelt, D.; Bamberg, E. The Transport Activity of the Light-Driven Chloride Pump Halorhodopsin Is Regulated by Green and Blue Light. *Biochim. Biophys. Acta, Biomembr.* **1985**, *819* (2), 195–205.

(19) Bamann, C.; Gueta, R.; Kleinlogel, S.; Nagel, G.; Bamberg, E. Structural Guidance of the Photocycle of Channelrhodopsin-2 by an Interhelical Hydrogen Bond. *Biochemistry* **2010**, *49* (2), 267–278.

(20) Eckert, C. E.; Kaur, J.; Glaubitz, C.; Wachtveitl, J. Ultrafast Photoinduced Deactivation Dynamics of Proteorhodopsin. *J. Phys. Chem. Lett.* **2017**, *8* (2), 512–517.

(21) Dobler, J.; Zinth, W.; Kaiser, W.; Oesterhelt, D. Excited-State Reaction Dynamics of Bacteriorhodopsin Studied by Femtosecond Spectroscopy. *Chem. Phys. Lett.* **1988**, *144* (2), 215–220.

(22) Tahara, S.; Takeuchi, S.; Abe-Yoshizumi, R.; Inoue, K.; Ohtani, H.; Kandori, H.; Tahara, T. Ultrafast Photoreaction Dynamics of a Light-Driven Sodium-Ion-Pumping Retinal Protein from Krokobacter Eikastus Revealed by Femtosecond Time-Resolved Absorption Spectroscopy. *J. Phys. Chem. Lett.* **2015**, *6* (22), 4481–4486.

(23) Hontani, Y.; Inoue, K.; Kloz, M.; Kato, Y.; Kandori, H.; Kennis, J. T. M. The Photochemistry of Sodium Ion Pump Rhodopsin Observed by Watermarked Femto- to Submillisecond Stimulated Raman Spectroscopy. *Phys. Chem. Chem. Phys.* **2016**, *18* (35), 24729–24736.

(24) Tahara, S.; Takeuchi, S.; Abe-Yoshizumi, R.; Inoue, K.; Ohtani, H.; Kandori, H.; Tahara, T. Origin of the Reactive and Nonreactive Excited States in the Primary Reaction of Rhodopsins: PH Dependence of Femtosecond Absorption of Light-Driven Sodium

Ion Pump Rhodopsin KR2. *J. Phys. Chem. B* **2018**, *122* (18), 4784–4792.

(25) Matsuo, J.; Kikukawa, T.; Fujisawa, T.; Hoff, W. D.; Unno, M. Watching a Molecular Twist in a Protein by Raman Optical Activity. *J. Phys. Chem. Lett.* **2020**, *11* (20), 8579–8584.

(26) Balashov, S. P.; Imasheva, E. S.; Dioumaev, A. K.; Wang, J. M.; Jung, K. H.; Lanyi, J. K. Light-Driven Na<sup>+</sup> Pump from *Gillisia limnaea*: A High-Affinity Na<sup>+</sup> Binding Site Is Formed Transiently in the Photocycle. *Biochemistry* **2014**, *53* (48), 7549–7561.

(27) Inoue, K.; Konno, M.; Abe-Yoshizumi, R.; Kandori, H. The Role of the NDQ Motif in Sodium-Pumping Rhodopsins. *Angew. Chem., Int. Ed.* **2015**, *54* (39), 11536–11539.

(28) Henrich, E.; Sörmann, J.; Eberhardt, P.; Peetz, O.; Mezhyrova, J.; Morgner, N.; Fendler, K.; Dötsch, V.; Wachtveitl, J.; Bernhard, F.; Bamann, C. From Gene to Function: Cell-Free Electrophysiological and Optical Analysis of Ion Pumps in Nanodiscs. *Biophys. J.* **2017**, *113*, 1331.

(29) Chen, H.-F.; Inoue, K.; Ono, H.; Abe-Yoshizumi, R.; Wada, A.; Kandori, H. Time-Resolved FTIR Study of Light-Driven Sodium Pump Rhodopsins. *Phys. Chem. Chem. Phys.* **2018**, *20*, 17694–17704.

(30) Asido, M.; Eberhardt, P.; Kriebel, C. N.; Braun, M.; Glaubitz, C.; Wachtveitl, J. Time-Resolved IR Spectroscopy Reveals Mechanistic Details of Ion Transport in the Sodium Pump *Krokinobacter eikastus* Rhodopsin 2. *Phys. Chem. Chem. Phys.* **2019**, *21*, 4461–4471.

(31) Gushchin, I.; Shevchenko, V.; Polovinkin, V.; Kovalev, K.; Alekseev, A.; Round, E.; Borshchevskiy, V.; Balandin, T.; Popov, A.; Gensch, T.; Fahlke, C.; Bamann, C.; Willbold, D.; Büldt, G.; Bamberg, E.; Gordeliy, V. Crystal Structure of a Light-Driven Sodium Pump. *Nat. Struct. Mol. Biol.* **2015**, *22* (5), 390–396.

(32) Kato, Y.; Inoue, K.; Kandori, H. Kinetic Analysis of H<sup>+</sup>-Na<sup>+</sup> Selectivity in a Light-Driven Na<sup>+</sup>-Pumping Rhodopsin. *J. Phys. Chem. Lett.* **2015**, *6* (24), 5111–5115.

(33) Jakdetchai, O.; Eberhardt, P.; Asido, M.; Kaur, J.; Kriebel, C. N.; Mao, J.; Leeder, A. J.; Brown, L. J.; Brown, R. C. D.; Becker-Baldus, J.; Bamann, C.; Wachtveitl, J.; Glaubitz, C. Probing the Photointermediates of Light-Driven Sodium Ion Pump KR2 by DNP-Enhanced Solid-State NMR. *Sci. Adv.* **2021**, *7* (11), eabf4213.

(34) Braiman, M.; Mathies, R. Resonance Raman Evidence for an All-Trans to 13-Cis Isomerization in the Proton-Pumping Cycle of Bacteriorhodopsin. *Biochemistry* **1980**, *19* (23), 5421–5428.

(35) Nishimura, N.; Mizuno, M.; Kandori, H.; Mizutani, Y. Distortion and a Strong Hydrogen Bond in the Retinal Chromophore Enable Sodium-Ion Transport by the Sodium-Ion Pump KR2. *J. Phys. Chem. B* **2019**, *123* (16), 3430–3440.

(36) Harbach, P. H. P.; Wormit, M.; Dreuw, A. The Third-Order Algebraic Diagrammatic Construction Method (ADC(3)) for the Polarization Propagator for Closed-Shell Molecules: Efficient Implementation and Benchmarking. *J. Chem. Phys.* **2014**, *141* (6), 064113.

(37) Gushchin, I.; Shevchenko, V.; Polovinkin, V.; Borshchevskiy, V.; Buslaev, P.; Bamberg, E.; Gordeliy, V. Structure of the Light-Driven Sodium Pump KR2 and Its Implications for Optogenetics. *FEBS J.* **2016**, *283* (7), 1232–1238.

(38) Shibata, M.; Inoue, K.; Ikeda, K.; Konno, M.; Singh, M.; Kataoka, C.; Abe-Yoshizumi, R.; Kandori, H.; Uchihashi, T. Oligomeric States of Microbial Rhodopsins Determined by High-Speed Atomic Force Microscopy and Circular Dichroic Spectroscopy. *Sci. Rep.* **2018**, *8* (1), 8262.



## 6.5 Asido *et al.*, *Phys. Chem. Chem. Phys.*, 2019

**Time-resolved IR spectroscopy reveals mechanistic details of ion transport in the sodium pump *Krokinobacter eikastus* Rhodopsin 2**

M. Asido, P. Eberhardt, C. N. Kriebel, M. Braun, C. Glaubitz and J. Wachtveitl,  
*Phys. Chem. Chem. Phys.*, 2019, 21, 4461-4471.



Cite this: *Phys. Chem. Chem. Phys.*,  
2019, 21, 4461

# Time-resolved IR spectroscopy reveals mechanistic details of ion transport in the sodium pump *Krokinobacter eikastus* rhodopsin 2†

Marvin Asido,<sup>a</sup> Peter Eberhardt,<sup>a</sup> Clara Nassrin Kriebel,<sup>b</sup> Markus Braun,<sup>a</sup> Clemens Glaubitz <sup>b</sup> and Josef Wachtveitl <sup>\*a</sup>

We report a comparative study on the structural dynamics of the light-driven sodium pump *Krokinobacter eikastus* rhodopsin 2 wild type under sodium and proton pumping conditions by means of time-resolved IR spectroscopy. The kinetics of KR2 under sodium pumping conditions exhibits a sequential character, whereas the kinetics of KR2 under proton pumping conditions involves several equilibrium states. The sodium translocation itself is characterized by major conformational changes of the protein backbone, such as distortions of the  $\alpha$ -helices and probably of the ECL1 domain, indicated by distinct marker bands in the amide I region. Carbonyl stretch modes of specific amino acid residues helped to elucidate structural changes in the retinal Schiff base moiety, including the protonation and deprotonation of D116, which is crucial for a deeper understanding of the mechanistic features in the photocycle of KR2.

Received 3rd December 2018,  
Accepted 1st February 2019

DOI: 10.1039/c8cp07418f

rsc.li/pccp

## Introduction

A basic and widely conserved principle in nature is the conversion of light energy into chemical energy by means of electrochemical potentials across cell membranes. In most archaea and bacteria this is achieved by membrane-embedded proteins, which contain a retinal chromophore.<sup>1,2</sup> Over many decades, several microbial rhodopsins, such as bacteriorhodopsin (BR), halorhodopsin (HR) and proteorhodopsin (PR), were discovered and thoroughly investigated.<sup>3–7</sup> These light-driven ion pumps all have in common that they are able to translocate charges in the form of protons or chloride ions across a biological membrane. The discovery of channelrhodopsins (ChRs) and the rise of optogenetics as a promising new field of research boosted interest in light-driven rhodopsins.<sup>8–11</sup> Since then, a lot of effort was put into a further characterization and functional analysis of modified and novel types of rhodopsins, which could be used to manipulate the physiological environment of cells by irradiation with light. Even though ChR and its variants enabled the light-gated conduction of various cations through a biomembrane, its

major disadvantage lies in the non-selectivity towards these cations and the desensitization in the course of a constant illumination.<sup>11</sup> This gap seems to be filled by the light-driven sodium pump *Krokinobacter eikastus* rhodopsin 2 (KR2), a novel member of the new class of non-proton cation pumps first described by the Kandori group.<sup>12,13</sup> Like all microbial rhodopsins, KR2 consists of seven tightly packed transmembrane  $\alpha$ -helices, of which one is linked covalently to the retinal chromophore through a Schiff base linkage with a lysine residue. Absorption of light induces the isomerization of the all-*trans* retinal to the 13-*cis* conformation, leading to a sequence of four distinct photo-intermediates.<sup>12</sup> New features of KR2 include the extracellular N-terminal helix, the ECL1-domain [Fig. 1a] and the NDQ-motif.<sup>14,15</sup> The latter one comprises the amino acid side chains of Asn112, Asp116 and Gln123 [Fig. 1b and c], which differs significantly from the conserved DTD- (BR) or DTE-motifs (PR) of well-known proton pumps.<sup>7</sup> In the absence of sodium, KR2 is able to pump H<sup>+</sup>, Li<sup>+</sup> and even K<sup>+</sup> after the exchange of specific amino acids.<sup>12,14,16</sup> Even though there have been a lot of advances since the discovery of KR2, its cation and proton transport mechanisms are still far from being understood. Therefore, a deeper understanding of its structure and mechanism is necessary to expand the toolbox for optogenetic research and applications. In this work, we focused on a comparative study of the proton and sodium pumping dynamics of the KR2 wild type by means of time-resolved UV/vis and infrared spectroscopy. Especially IR spectroscopy has proven to be a powerful tool to determine global as well as site-specific changes of a wide-range of retinal proteins during the course of a photocycle.

<sup>a</sup> Institute of Physical and Theoretical Chemistry, Goethe University Frankfurt, Max-von-Laue Straße 7, 60438 Frankfurt am Main, Germany.  
E-mail: wweitl@theochem.uni-frankfurt.de

<sup>b</sup> Institute for Biophysical Chemistry and Center for Biomolecular Magnetic Resonance (BMRZ), Goethe University Frankfurt, Max-von-Laue Straße 9, 60438 Frankfurt am Main, Germany

† Electronic supplementary information (ESI) available: Absorption spectra, life-time density analysis and the relationship of the absorption maxima/C=C stretch modes of retinal are presented. See DOI: 10.1039/c8cp07418f

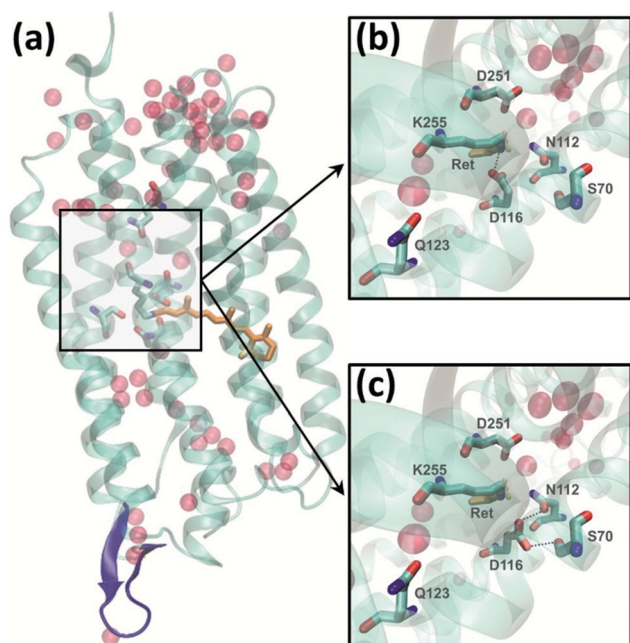


Fig. 1 (a) Crystal structure of the KR2 wildtype (PDB: 3 × 3C). The highlighted features are: retinal (orange), ECL1-domain (blue), water molecules (red spheres) and the amino acid side chains Q123, D116, S70, N112, D251 and K255. A closeup (with a different perspective) of the retinal moiety is given for (b) deprotonated D116 and (c) protonated D116 based on the results reported by Kato *et al.*<sup>14</sup>

The study of KR2 in proton and sodium pumping conditions did not just allow us to characterize common mechanistic features, but more importantly to also elucidate significant differences in the structural changes of the protein, which are still under-represented in to date literature.

## Experimental methods

### Expression of the KR2 wild type

Expression of KR2 WT was essentially carried out as described previously.<sup>17</sup> KR2 pET 26b DNA was transformed in *E. coli* C43 (DE3). Transformed cells were grown in LB media containing 100  $\mu\text{g ml}^{-1}$  of kanamycin at 37 °C. For protein production, cells were transferred to minimal media containing glucose and ammonium chloride (1:100 dilution). At an  $\text{OD}_{600}$  of  $\sim 0.6$ , protein expression was induced with 0.5 mM isopropyl  $\beta$ -D-1-thiogalactopyranoside (IPTG), and 7  $\mu\text{M}$  of all-*trans* retinal was added. After an incubation for 16 h at 27 °C cells were harvested and passed through Constant systems cell disruptor at 1.85 MPa. The collected membranes were suspended and solubilized in buffer containing 1.5% (w/v) dodecyl- $\beta$ -D-maltoside (DDM) overnight. The solubilized protein was purified by Ni-NTA affinity chromatography. Purity and homogeneity of the sample was verified by SDS PAGE and optical absorption spectroscopy. The protein yield was 22  $\text{mg L}^{-1}$ .

### Sample preparation

For our measurements under salt and salt-free conditions, we prepared a 50 mM Hepes/Tris (pD 8.3, 100 mM NaCl) and

a 50 mM MES (pD 6, salt-free) buffer, respectively, which were diluted in  $\text{D}_2\text{O}$ . The pH-values of the buffers were adjusted to the desired pD-value by using the relationship proposed by Glasoe *et al.*<sup>18</sup> Both buffers contained 0.05% DDM detergent. For each sample, 150  $\mu\text{l}$  of the KR2 wild type solution was washed with the respective buffer in a centrifuge (5415 R, Eppendorf, Germany) at a speed of  $10^5$  rpm (3 times total  $\times$  15 minutes). Consequently, 15  $\mu\text{l}$  of the obtained KR2 concentrate was placed and evenly spread on the center of a  $\text{CaF}_2$  window. The cuvette was then closed with a teflon spacer of 50  $\mu\text{m}$  thickness and a second  $\text{CaF}_2$  window.

### Absorption measurements

Steady state spectra of both samples [ESI,† Fig. S1] were recorded with a spectrometer (Specord 100, Analytik Jena, Germany), yielding an absorbance of 0.16 OD for KR2 in sodium pumping conditions ( $\text{KR2}_{\text{Na}}$ ) and an absorbance of 0.11 OD for KR2 in proton pumping conditions ( $\text{KR2}_{\text{H}}$ ). Furthermore, all measurements in the UV/vis and the IR were performed with the same sample to allow a proper correlation of the data.

### UV/vis and IR flash photolysis

The two samples for the UV/vis and IR experiments were excited by a Nd:YAG laser (Spitlight 600, Innolas Laser, Germany) pumping an optical parametric oscillator (preciScan, GWU-Lasertechnik, Germany). The OPO was set to generate pulses with a central wavelength of 525 nm for the sodium pump and 535 nm for the proton pump to account for the red shift of the retinal absorption at lower pD-values. The average pulse energy was set to  $\sim 1.7$   $\text{mJ cm}^{-2}$ . Continuous wave probe light for the UV/vis was generated by a mercury-xenon lamp (LC-08, Hamamatsu, Japan) and guided through two monochromators (Photon Technology International, USA) to select specific probing wavelengths (420 nm, 520/530 nm and 620 nm). The transient signals were detected with a photomultiplier tube (H6780-02, Hamamatsu, Japan) and recorded with an oscilloscope (DPO5204-10RL, Tektronix, USA). The oscilloscope recorded time traces at a sampling rate of 10 megasamples per second, resulting in a 100 ns resolution for an overall record length of one second. Each time trace was averaged 100 times. Continuous wave probe light for the IR was generated by a quantum cascade laser (MIRcat 1100-U2-5086, Daylight Solutions, USA), which is tunable in the range from 1508  $\text{cm}^{-1}$  to 1748  $\text{cm}^{-1}$ . The monochromatic emission of the QCL was recorded by a MCT detector (KV104 MCT, Kolmar Tech., USA), which is connected to the same oscilloscope mentioned above. Transients were recorded and averaged 50 times with a spectral resolution of 4  $\text{cm}^{-1}$  and the same oscilloscope settings as in the UV/vis experiments.

### Data processing

The transients obtained by the UV/vis and IR measurements were averaged and reduced to 50 linear and 50 exponential timepoints. The IR dataset was subjected to singular value decomposition (SVD) using five components in Matlab. More detailed information about SVD and its use in spectral analysis can be found in ref. 19. Both, the UV/vis and the IR datasets,

were analyzed and fitted by lifetime density analysis (LDA) [ESI,† Fig. S2a and b] and global lifetime analysis (GLA). The GLA allows the description of the data in terms of a sum of exponentials and their corresponding lifetimes. The Matlab-based program “Optimus Fit”, which we used for the LDA and GLA, is explained in detail in ref. 20.

## Results

### UV/vis flash photolysis

The first set of measurements was performed in the UV/vis flash photolysis, which monitors the retinal chromophore. To account for the different intermediate steps of the photocycle, we have chosen probing wavelengths at 420 nm, 520/530 nm and 620 nm, respectively, as shown in Fig. 2a (bottom). In  $\text{KR2}_{\text{Na}}$  [Fig. 2a, bottom], at around 80  $\mu\text{s}$  after the photo-excitation, a signal at 620 nm decays and a signal at 420 nm rises, representing the transition from the K to the L/M state. A subsequent transition from this equilibrium state<sup>12</sup> to the O intermediate takes place at 0.6 ms, indicated by the rise of the transient signal at 620 nm. After 9 ms, both, the transient at 620 nm and the transient at 520 nm, which represents the bleach of the ground state, approach zero. We therefore conclude that the photocycle is finished on that timescale. In  $\text{KR2}_{\text{H}}$ , the K/L equilibrium is prolonged up to the millisecond range. With a time constant of 26 ms, a positive signal at 420 nm is observable, whereas the transient signal at 620 nm approaches zero. This marks the transition from the K/L to the L/M state of the photocycle. Compared to  $\text{KR2}_{\text{Na}}$ , the M intermediate is more pronounced in H<sup>+</sup>

pumping conditions, whereas the spectroscopic signature of the O intermediate is completely missing. This was also observed in several flash photolysis studies before, leading to the conclusion that the O intermediate is indicative for sodium pumping.<sup>12,13</sup> A dominant part of the ground state bleach at 530 nm recovers fast up to the millisecond range and a residual signal remains, which reaches zero after approximately 70 ms. An overview of the time constants can be found in Tables 1 and 2.

### Infrared flash photolysis

The data obtained in the IR, ranging from 1508  $\text{cm}^{-1}$  to 1748  $\text{cm}^{-1}$  [Fig. 2a and b], can be sub-divided into three major groups of structural changes in the protein. They include the conformational changes of the retinal chromophore, structural changes in the protein backbone and site specific changes of amino acid residues. For a better overview they will be presented and discussed in different segments.

### Distortions in the $\pi$ -electron system of retinal

The first major set of changes originates from the distortion of the retinal chromophore itself, which can be seen in the range of 1508  $\text{cm}^{-1}$  to 1560  $\text{cm}^{-1}$  [Fig. 3a]. At first glance, a broad negative signal centered at around 1540  $\text{cm}^{-1}$  is observable in  $\text{KR2}_{\text{Na}}$ . This broad bleaching signal can be associated with the C=C stretch modes of all-*trans* retinal.<sup>21</sup> Correspondingly, a narrow positive band at around 1516  $\text{cm}^{-1}$  occurs in the microsecond to the tenth of a millisecond time scale, which then becomes more intense and broader at around one millisecond [see also Fig. 2a, top].

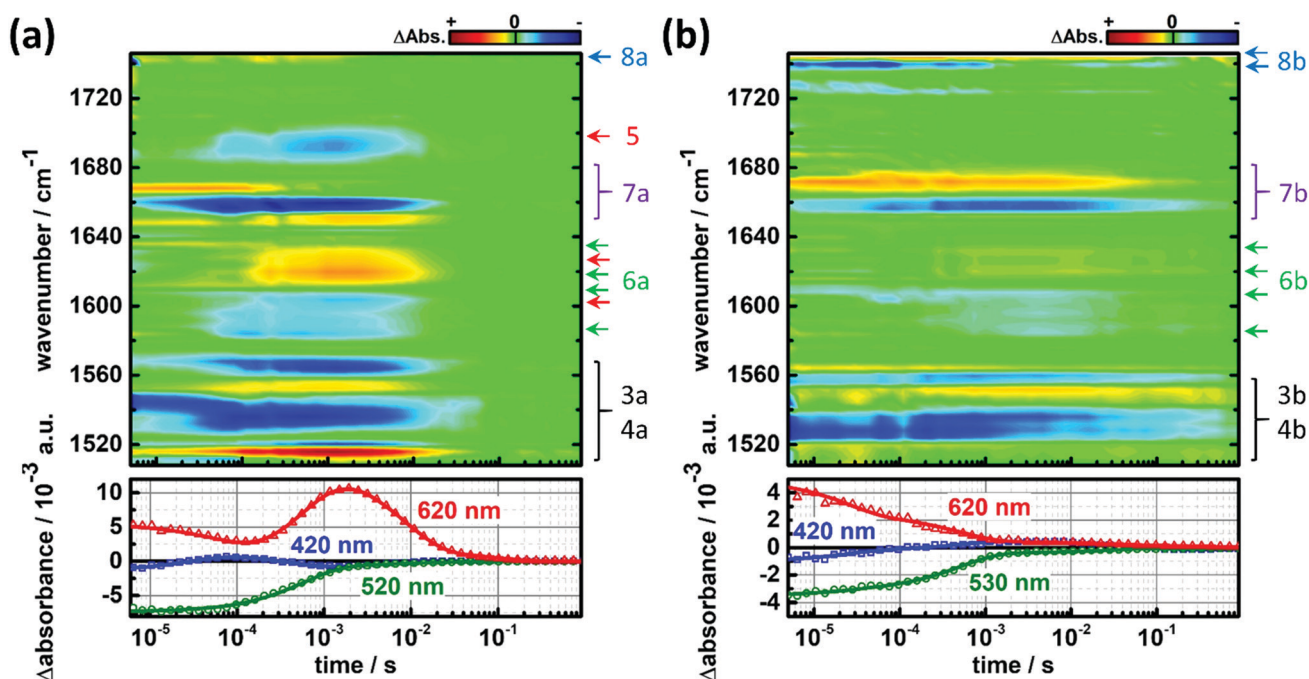


Fig. 2 Overview of the UV/vis and IR measurements for (a)  $\text{KR2}_{\text{Na}}$  and (b)  $\text{KR2}_{\text{H}}$ . IR data are color coded, so that negative signals are depicted by blue colors and positive signals by yellow/red colors. The corresponding raw data of the transients in the UV/vis flash photolysis and their fits are shown in the bottom panel. To account for the shifted absorption spectrum, the GSB signals of  $\text{KR2}_{\text{Na}}$  and  $\text{KR2}_{\text{H}}$  were probed at 10 nm shifted wavelengths (520 nm and 530 nm, respectively). The colored markings and numbers on the right hand side indicate the discussed transients and their corresponding figures in this report.

Table 1 GLA derived time constants of KR2<sub>Na</sub> in the IR and the UV/vis

	$\tau_1$ /ms	$\tau_2$ /ms	$\tau_3$ /ms	$\tau_4$ /ms	$\tau_5$ /ms
UV/vis	0.08	0.6	9	—	—
IR	0.03	0.4	9	—	—

Table 2 GLA derived time constants of KR2<sub>H</sub> in the IR and the UV/vis

	$\tau_1$ /ms	$\tau_2$ /ms	$\tau_3$ /ms	$\tau_4$ /ms	$\tau_5$ /ms
UV/vis	0.02	0.5	26	73	—
IR	0.01	0.5	19	200	Inf.

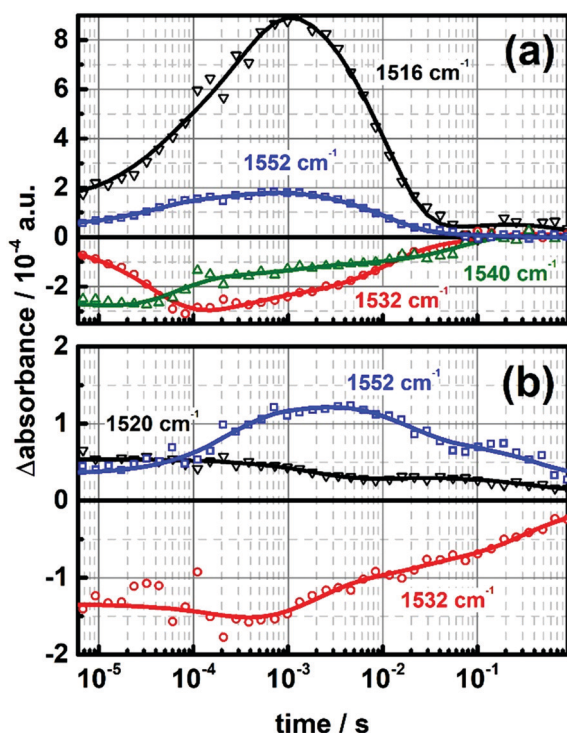


Fig. 3 Infrared transients of the retinal C=C stretch modes of (a) KR2<sub>Na</sub> and (b) KR2<sub>H</sub>. The individual data points of the SVD processed data are shown as symbols, whereas the fits are depicted as solid lines.

Similarly, the bleaching signal of the all-*trans* retinal C=C stretch mode at around 1532 cm<sup>-1</sup> exhibits weaker amplitudes between 10 μs and 100 μs. This signature suggests that there might be an overlap of positive and negative contributions in the spectral range between 1520 cm<sup>-1</sup> to 1532 cm<sup>-1</sup> [Fig. 2a, top], which could be a spectral indicator for the decay of the K intermediate. Following the time line, the next positive signal emerging lies around 1552 cm<sup>-1</sup> with a build-up time of approximately 80 μs. By taking a closer look at the transient at 1556 cm<sup>-1</sup>, one can see a slightly delayed dynamics in comparison to the transient at 1552 cm<sup>-1</sup> [Fig. 4a]. The additional shoulder in the sub-millisecond time range at 1552 cm<sup>-1</sup> might hint at spectroscopically distinguishable L and M intermediates in the photocycle, with the M intermediate being slightly more blue-shifted. After approximately half a millisecond the transient at 1516 cm<sup>-1</sup> shows an intense positive change in absorbance, which coincides with the transition

from the M to the O state. All transient signals in this spectral region decay in the time range of 9 milliseconds, which is in good agreement with the time constants found in the UV/vis measurements and therefore being indicative for the duration of the photocycle of the sodium pump. By taking a closer look at our measurements in salt-free conditions [Fig. 2b], one can clearly see that the dynamics is prolonged by at least one order of magnitude. Moreover, the spectral signature of the IR bands is slightly different compared to KR2<sub>Na</sub>. The bleaching signal of the C=C stretch mode of all-*trans* retinal can be found at around 1532 cm<sup>-1</sup>, which accounts for the red shift in the absorption spectrum at low pH. This negative signal is accompanied by three positive bands at around 1520 cm<sup>-1</sup>, 1548 cm<sup>-1</sup> and 1552 cm<sup>-1</sup>, which are already present from the beginning of the measurement [Fig. 3b and 4b]. The positive signal at 1520 cm<sup>-1</sup> shows a stable amplitude in the microsecond range and then starts to decay after approximately a few milliseconds, which correlates with the transition from the K to the L/M state. The transients at 1548 cm<sup>-1</sup> and 1552 cm<sup>-1</sup> start with a similar amplitude but follow different dynamics after 80 μs. While the transient at 1548 cm<sup>-1</sup> shows a small drop and then a subsequent increase of ΔA in a time window of a few hundred microseconds, the transient at 1552 cm<sup>-1</sup> steadily increases in amplitude. While the signal at 1552 cm<sup>-1</sup> reaches its maximum after a few milliseconds, the transient at 1548 cm<sup>-1</sup> starts to plateau over a time scale of several decades. In analogy to KR2<sub>Na</sub>, one can assign these two bands to the L and M intermediate, respectively, with the M intermediate being more blue-shifted. The co-existence of the transients at 1520 cm<sup>-1</sup>, 1548 cm<sup>-1</sup> and 1552 cm<sup>-1</sup> indicates that the K, L and M states might be in equilibrium, however, at later times the equilibrium shifts towards the M state. This state then decays very slowly in the millisecond to second time range ( $\tau_3$ - $\tau_5$ ), leaving a residual signal by the end of the experimental time window.

### Structural changes in the protein backbone

The spectral region from 1560 cm<sup>-1</sup> to 1700 cm<sup>-1</sup> is primarily representative for the amide vibrations of the protein backbone, with the exception of the C=N stretch mode of the retinal and a few contributions from amino acid side chains.<sup>22</sup> Hence, strong signals in this spectral window are usually due to major changes in the protein conformation during the photocycle. For KR2<sub>Na</sub> we could observe ten distinct bands in this region, which we sub-divided into three groups. The first set of signals are the transients at (-) 1604 cm<sup>-1</sup>, (+) 1620 cm<sup>-1</sup> and (-) 1692 cm<sup>-1</sup> as they show similar dynamics. The negative band centered around 1604 cm<sup>-1</sup> shows a strong increase of signal amplitude with a time constant  $\tau_2 = 0.4$  ms, which correlates with the decay of the K intermediate. Simultaneously with this bleaching signal, a broad positive band at around 1620 cm<sup>-1</sup>, which can be assigned to the L/M state, emerges, albeit it reaches its maximum later in the millisecond time range. By comparison of the signal amplitudes of these two bands, which differ by a factor of three, it is highly suggestive that the band at 1620 cm<sup>-1</sup> is not just the result of an up-shift of the 1604 cm<sup>-1</sup> transient. A closer look at the transient at 1692 cm<sup>-1</sup> reveals a similar temporal signature, which reaches its minimum after approximately one millisecond [Fig. 5].

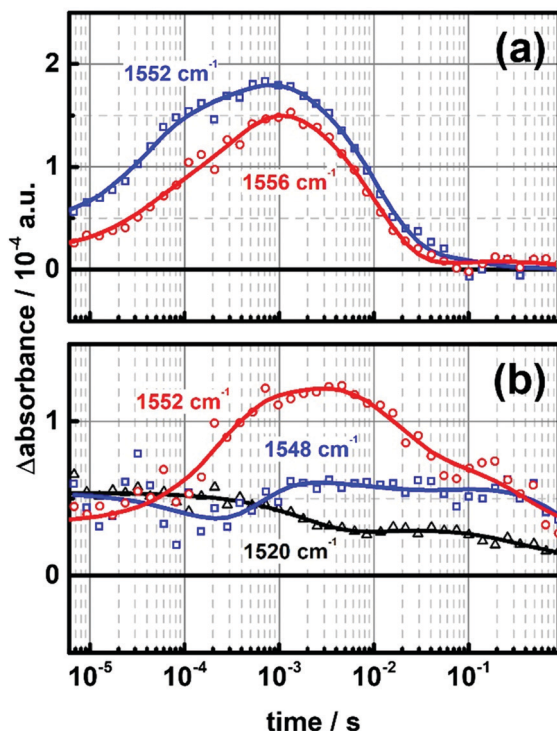


Fig. 4 (a) Comparison of the IR signals of  $\text{KR2}_{\text{Na}}$  at  $1552\text{ cm}^{-1}$  and  $1556\text{ cm}^{-1}$ . An additional shoulder around  $100\text{ }\mu\text{s}$  can be seen at  $1552\text{ cm}^{-1}$ . (b) Transient signals of  $\text{KR2}_{\text{H}}$  at  $1520\text{ cm}^{-1}$ ,  $1548\text{ cm}^{-1}$  and  $1552\text{ cm}^{-1}$ . The individual data points of the SVD processed data are shown as symbols, whereas the fits are depicted as solid lines.

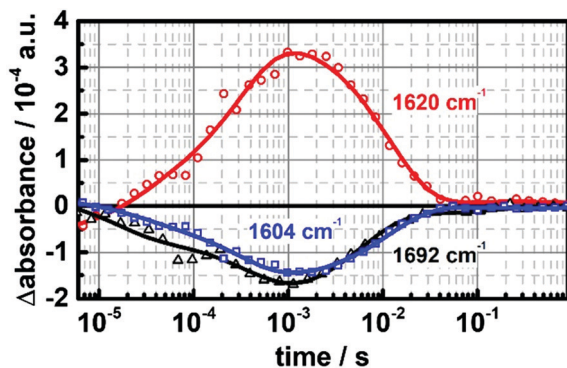


Fig. 5 IR transients of  $\text{KR2}_{\text{Na}}$  at  $1604\text{ cm}^{-1}$ ,  $1620\text{ cm}^{-1}$  and  $1692\text{ cm}^{-1}$ . The positive signal at  $1620\text{ cm}^{-1}$  might be an overlap of shifts from both bleaching signals at  $1604\text{ cm}^{-1}$  and  $1692\text{ cm}^{-1}$ . The individual data points of the SVD processed data are shown as symbols, whereas the fits are depicted as solid lines.

This can not be seen in salt-free conditions, where the band at  $1692\text{ cm}^{-1}$  is completely missing, and thus, making this a possible marker for sodium transport. In contrast to that,  $\text{KR2}_{\text{Na}}$  and  $\text{KR2}_{\text{H}}$  show spectral similarities in the region from  $1590\text{ cm}^{-1}$  to  $1640\text{ cm}^{-1}$ . In both cases, a set of two positive and two negative signals can be found [Fig. 6]. Except for the transient at  $1592\text{ cm}^{-1}$  in sodium pumping conditions, all other signals already have a significant amplitude at the earliest recorded times, which suggests that there are some major changes prior to the experimental time window. The transients at  $(-)\text{ }1608\text{ cm}^{-1}/(+)\text{ }1612\text{ cm}^{-1}$  in

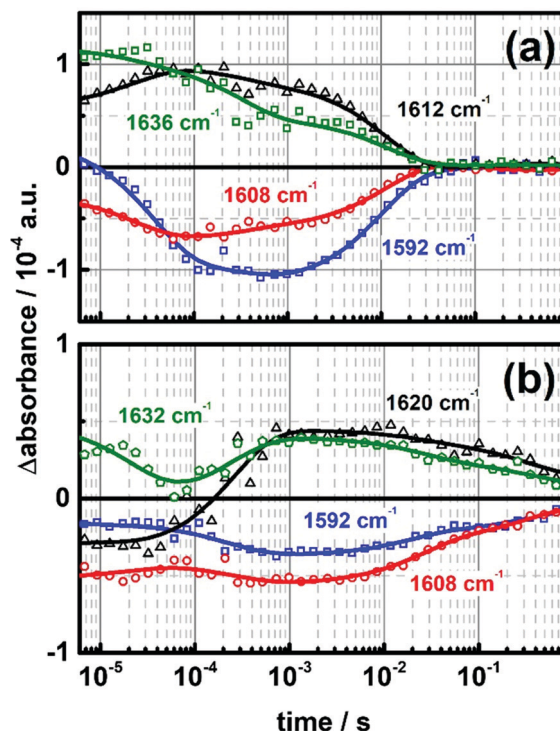


Fig. 6 IR transients of (a)  $\text{KR2}_{\text{Na}}$  and (b)  $\text{KR2}_{\text{H}}$  in the region from  $1592\text{--}1640\text{ cm}^{-1}$ . The individual data points of the SVD processed data are shown as symbols, whereas the fits are depicted as solid lines.

Fig. 6a show mirrored dynamics, which can be described with the same time constants. Both, the positive and the negative signal, rise mono-exponentially with a time constant of  $\tau_1 = 30\text{ }\mu\text{s}$  and then decay bi-exponentially with  $\tau_2 = 0.4\text{ ms}$  and  $\tau_3 = 9\text{ ms}$ . The remaining two transients at  $(-)\text{ }1592\text{ cm}^{-1}$  and  $(+)\text{ }1636\text{ cm}^{-1}$  [Fig. 6a] do not show such a similarity. Instead, the amplitude of the negative signal at  $1592\text{ cm}^{-1}$  increases bi-exponentially, peaking at approximately  $1\text{ ms}$ , and then decays mono-exponentially. At  $1636\text{ cm}^{-1}$ , the initial signal decays tri-exponentially with a small dip around  $1\text{ ms}$  suggesting some changes during the formation of the O intermediate. The corresponding transients of  $\text{KR2}_{\text{H}}$  [Fig. 6b] have a prolonged dynamics, which is in agreement with the extended duration of the photocycle in salt-free conditions. Even though the two negative transients at  $1592\text{ cm}^{-1}$  and  $1608\text{ cm}^{-1}$  are spectrally separated by  $16\text{ cm}^{-1}$ , they show a similar temporal profile, which can be characterized by two time constants  $\tau_1 = 10\text{ }\mu\text{s}$  and  $\tau_2 = 0.5\text{ ms}$  for the decay of K, as well as two time constants  $\tau_3 = 19\text{ ms}$  and  $\tau_4 = 200\text{ ms}$  for the regeneration of the ground state. In contrast to  $\text{KR2}_{\text{Na}}$ , the two positive transients at  $1620\text{ cm}^{-1}$  and  $1632\text{ cm}^{-1}$  have a more complex dynamics in the microsecond time range, which could be due to a superposition with bleaching signals on an earlier timescale. However, the decay of both transients can be described with the time constants  $\tau_3$  and  $\tau_4$ , which are identical to the ones found for the signals at  $1592\text{ cm}^{-1}$  and  $1608\text{ cm}^{-1}$ .

The next set of signals lies in the range of  $1650\text{ cm}^{-1}$  and  $1670\text{ cm}^{-1}$ , where three transients at  $(+)\text{ }1652\text{ cm}^{-1}$ ,  $(-)\text{ }1660\text{ cm}^{-1}$  and  $(+)\text{ }1668\text{ cm}^{-1}$  can be found [Fig. 7a]. The intense bleaching

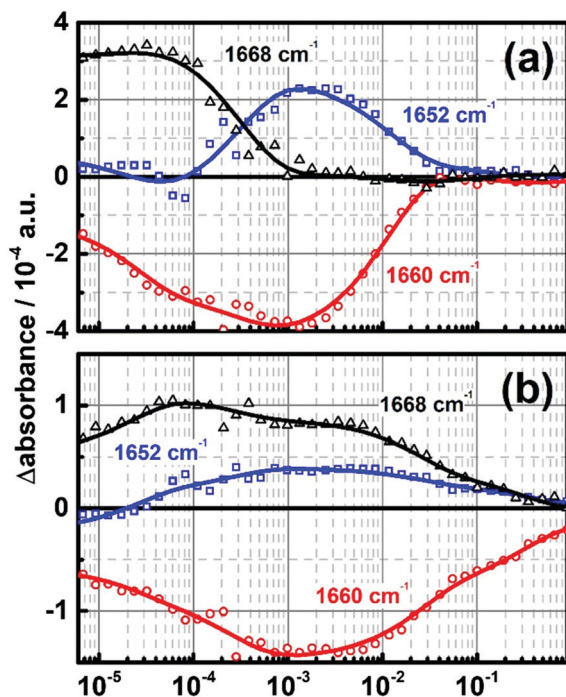


Fig. 7 IR transients of the amide I region of (a)  $\text{KR2}_{\text{Na}}$  and (b)  $\text{KR2}_{\text{H}}$ .  $\text{KR2}_{\text{Na}}$  exhibits a spectral shift from  $1668\text{ cm}^{-1}$  to  $1652\text{ cm}^{-1}$  in between  $100\ \mu\text{s}$  and  $1\text{ ms}$ , whereas this shift is not observed in  $\text{KR2}_{\text{H}}$ . The individual data points of the SVD processed data are shown as symbols, whereas the fits are depicted as solid lines.

signal at  $1660\text{ cm}^{-1}$  increases in amplitude in a time window of a few microseconds up to a millisecond and then quickly decays with a time constant of  $\tau_3 = 9\text{ ms}$ . By taking a closer look at the transient at  $1668\text{ cm}^{-1}$ , one can see a steady positive signal in the microsecond range, which starts to drop rapidly with a time constant of  $\tau_2 = 0.4\text{ ms}$ . At the same time, the weak positive signal of the transient at  $1652\text{ cm}^{-1}$  starts to increase. When it reaches its maximum after approximately one millisecond, the transient at  $1668\text{ cm}^{-1}$  becomes zero. This spectral shift is also reflected in the small shoulder of the bleaching signal at  $1660\text{ cm}^{-1}$ , which occurs in the time frame of  $100\ \mu\text{s}$  to  $1\text{ ms}$ . Considering the photocycle of  $\text{KR2}_{\text{Na}}$ , one can assign the band at  $1668\text{ cm}^{-1}$  mainly to the K intermediate. The spectral down shift from  $1668\text{ cm}^{-1}$  to  $1652\text{ cm}^{-1}$  occurs in the subsequent steps leading to the rise of the O intermediate. Such a behavior does not occur in the case of  $\text{KR2}_{\text{H}}$ . Here one can see an intense bleaching band at  $(-)\ 1660\text{ cm}^{-1}$  and an intense and broad positive band at  $1668\text{ cm}^{-1}$  [Fig. 7b]. Both signals span the microsecond to second time scale, reflecting the prolonged duration of the  $\text{KR2}_{\text{H}}$  photocycle. For a better comparison with  $\text{KR2}_{\text{Na}}$ , we also extracted the transient at  $1652\text{ cm}^{-1}$ . In fact, one can see a small positive amplitude between  $50\ \mu\text{s}$  and  $1\text{ s}$ . However, a spectral shift, as it is seen in salt conditions, can not be observed. This again stresses the major sodium-related changes in the protein backbone, which can be tracked with the signal pair at  $1668\text{ cm}^{-1}$  and  $1652\text{ cm}^{-1}$ .

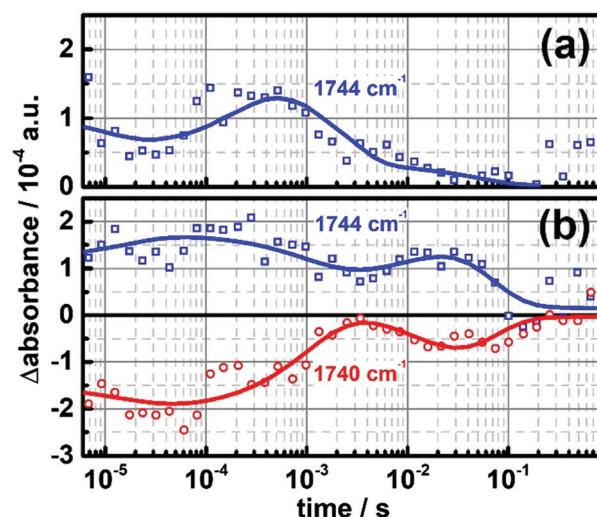


Fig. 8 IR transients of the carbonyl vibrations for (a)  $\text{KR2}_{\text{Na}}$  and (b)  $\text{KR2}_{\text{H}}$ . The individual data points of the SVD processed data are shown as symbols, whereas the fits are depicted as solid lines.

#### Amino acid side chains

In addition to the chromophore distortions and the movement of the protein backbone, one also has to consider the dynamics of the individual amino acid side chains, which are involved in the mechanism of sodium or proton transport. Such signals are expected in the range of  $1700\text{ cm}^{-1}$  to  $1800\text{ cm}^{-1}$ , in which one can find the carbonyl stretch modes of Asp, Glu, Asn or Gln.<sup>23</sup> For  $\text{KR2}_{\text{Na}}$ , we can observe a positive band at  $1744\text{ cm}^{-1}$ , which already has significant amplitude at the earliest times recorded in our measurement [Fig. 8a]. From there the signal decays with a lifetime of  $\tau_1 = 30\ \mu\text{s}$ , before it eventually rises again with  $\tau_2 = 0.4\text{ ms}$ . The final decay can be described with a lifetime  $\tau_3 = 9\text{ ms}$ . This general characteristic seems to be conserved in  $\text{KR2}_{\text{H}}$ , however, it is prolonged by two orders of magnitude [Fig. 8b]. In this case, one can see a stronger initial signal, which rises with a lifetime of  $\tau_1 = 10\ \mu\text{s}$  followed by a slow decrease of signal amplitude with  $\tau_2 = 0.5\text{ ms}$ . Another rise occurs within  $\tau_3 = 19\text{ ms}$ , followed by a relaxation to zero. In contrast to  $\text{KR2}_{\text{Na}}$ , an additional bleaching signal can be found at  $1740\text{ cm}^{-1}$ . Comparing the transients at  $1740\text{ cm}^{-1}$  and  $1744\text{ cm}^{-1}$ , the astonishing similarity of their temporal profiles has to be pointed out. In fact, their changes in absorption can be described with similar time constants, suggesting a spectral up shift from  $1740\text{ cm}^{-1}$  to  $1744\text{ cm}^{-1}$  after photo-isomerization. By comparison of these transients with the UV/vis data, one can deduce that the second rise of the signals occurs simultaneously with the decay of the M intermediate in both, the sodium and the proton pump.

## Discussion

#### Retinal distortions and characterization of photointermediates

The time-resolved measurements presented in this work span a wide range of dynamics, which are involved in the photocycle of KR2. In order to disentangle and assign the complex IR data,

the first step is a proper determination of the photo-intermediates occurring during the photocycle of **KR2<sub>Na</sub>** and **KR2<sub>H</sub>**, respectively. For this it is helpful to compare the data obtained in UV/vis measurements at 420 nm, 520/530 nm and 620 nm with the IR bands of the C=C stretch modes of the retinal chromophore. A commonly accepted rule of thumb is the inverse relationship between the absorption maximum in the visible and the resonance frequency of the C=C stretch mode. This is rooted in the assumption, that the level of  $\pi$ -delocalization, which is reflected in the absorption maximum, correlates with the strength of the C=C bonds along the chromophore.<sup>24–28</sup> Following the signals in the spectral window of 1500  $\text{cm}^{-1}$  to 1560  $\text{cm}^{-1}$  in **KR2<sub>Na</sub>** [Fig. 3a], one can see that there is an initial down shift from around 1540  $\text{cm}^{-1}$  in the ground state to the spectral area around 1520  $\text{cm}^{-1}$ . As stated above, the signals around 1520  $\text{cm}^{-1}$  are most likely a superposition of the ground state bleach and an additional positive contribution from the K intermediate. From there the signal shifts up to 1552  $\text{cm}^{-1}$  and 1556  $\text{cm}^{-1}$ , respectively. This correlates clearly with the rise of the M state, however, the additional shoulder at 1552  $\text{cm}^{-1}$  could be a contribution from L [Fig. 4a]. In the last step, a down shift to 1516  $\text{cm}^{-1}$  is observed, which occurs simultaneously with the rise of the O intermediate. The signal then decays with a lifetime of 9 ms, marking the recovery of the ground state. The temporal trace of the IR bands strongly correlates with the spectral shifts observed in the UV/vis, being in agreement with the empirical rule stated above [ESI,† Fig. S3]. In the case of **KR2<sub>H</sub>**, the time trace of the signals is not as clear. In addition to an initial downshift from 1532  $\text{cm}^{-1}$  to 1520  $\text{cm}^{-1}$  one can also observe transients at 1548  $\text{cm}^{-1}$  and 1552  $\text{cm}^{-1}$ , which show distinct kinetic features [Fig. 4b]. Following the assignments of the bands at 1532  $\text{cm}^{-1}$ , 1520  $\text{cm}^{-1}$ , 1548  $\text{cm}^{-1}$  and 1552  $\text{cm}^{-1}$  as the dark state, K state, L state and M state, respectively, one has to come to the conclusion that K/L/M form an equilibrium in **KR2<sub>H</sub>**. A major signal at 1516  $\text{cm}^{-1}$  is missing, stressing the correlation of the O state with this spectral feature in the **KR2<sub>Na</sub>**. The observations made here are in agreement with Raman spectroscopy and step-scan FTIR data previously published by the groups of Kennis and Kandori, in which the bands at 1519  $\text{cm}^{-1}$  and 1516  $\text{cm}^{-1}$  have been suggested to be markers for the K- and O-intermediates, respectively.<sup>29,30</sup> However, a definite IR assignment of the K, L and M intermediates and a quantitative analysis of possible equilibrium states is still subject to further investigation. The signals of the C=C stretch modes of the chromophore decay bi-exponentially with a remaining amplitude at the end of the measurement, even though an O intermediate is not formed in  $\text{H}^+$  pumping conditions. This is not observed in the UV/vis, which might suggest an additional, but spectrally silent, state after M. Such an intermediate has been found and discussed for other microbial rhodopsins like HR and PR.<sup>6,31–33</sup>

### Structural changes of the protein backbone during sodium uptake and translocation

Besides the dynamics of the retinal chromophore itself, a further characterization of the protein distortions is of great interest. With KR2 being able to transport protons and cations

of different sizes ( $\text{Li}^+$  and  $\text{Na}^+$ ), one expects charge and/or size induced changes in the protein backbone and its surroundings during the ion uptake and translocation. One way to detect such changes is to take a look at the amide I and II vibrations, which are spectrally located in the range of 1560  $\text{cm}^{-1}$  to 1700  $\text{cm}^{-1}$ . These bands include the C=O stretch mode (amide I), the C–N stretch mode (amide I + II), the N–H bending mode (amide I + II) and the C=O bending mode (amide II), of which most are sensitive to hydrogen bonding.<sup>22</sup> In the case of **KR2<sub>Na</sub>**, the signature found at (+) 1652  $\text{cm}^{-1}$ , (–) 1660  $\text{cm}^{-1}$  and (+) 1668  $\text{cm}^{-1}$  is certainly interesting. Whereas the bleaching signal at 1660  $\text{cm}^{-1}$  remains over a time period of several decades, the temporal profile of the two positive bands is strongly indicative for an initial up shift to 1668  $\text{cm}^{-1}$  and a subsequent down shift to 1652  $\text{cm}^{-1}$ , which can be described with the lifetime  $\tau_2 = 0.4$  ms [Fig. 7a]. As pointed out earlier, this spectral shift correlates with the transition from the M state to the O state in the photocycle. Crystal structures of KR2 published by Kato *et al.* and Gushchin *et al.* revealed that several water molecules are embedded in the ion translocation pathway [Fig. 1a], especially in the ion-uptake and ion-release cavities.<sup>14,15</sup> Furthermore, it is deduced from the mere size of the hydration shells of sodium and potassium that sodium has to be stripped off its hydration shell in order to enter the protein.<sup>13</sup> Apart from conformational changes in the protein backbone, a reasonable origin of the aforementioned spectral signature would be an interaction of the sodium ion with the water molecules inside the protein. An up (down) shift in the frequency of the amide I band could be explained by weaker (stronger) hydrogen bonds with the carbonyl groups in the  $\alpha$ -helices.<sup>22</sup> This suggests a weakened hydrogen network in the early stages of the photocycle, which is reflected in the up shifted band at 1668  $\text{cm}^{-1}$  during the K state and its transition to L/M. The down shift, which follows the transition from M to O, could then be the result of water re-organization and a further stabilization in the ion-release cavity. In the case of **KR2<sub>H</sub>**, such a clear feature is not observed. The bleaching signal at 1660  $\text{cm}^{-1}$  is conserved, albeit prolonged by two orders of magnitude and weaker in amplitude compared to the signal seen for **KR2<sub>Na</sub>**. Instead of a pair of rising and disappearing positive signals, one can see two co-existing positive signals at 1652  $\text{cm}^{-1}$  and 1668  $\text{cm}^{-1}$ . The spectral positions of the transients suggest, again, an initial decrease and subsequent increase of the hydrogen bond interaction with the  $\alpha$ -helices, which could be induced by rotation and flipping of several amino acid side chains. However, the camel-like shape of the 1668  $\text{cm}^{-1}$  band and its extended temporal profile might be the result of several orientation and re-orientation steps, due to the lacking stabilization from a sodium ion.

Another outstanding feature of **KR2<sub>Na</sub>** is the strong signal pair at (–) 1692  $\text{cm}^{-1}$ /(+) 1620  $\text{cm}^{-1}$  [Fig. 5]. The spectral width of these bands suggests a superposition of several vibrational modes, which makes a proper assignment difficult. Since this pair can not be observed in **KR2<sub>H</sub>**, it is very likely that a sodium related interaction might be the cause of the intense absorption changes. One contribution of the band around 1692  $\text{cm}^{-1}$  could



originate from the C=O stretch mode of asparagine, which was observed in the range of 1648–1704  $\text{cm}^{-1}$  in several proteins. In fact, a similar spectral shift was reported by Cao *et al.* for the D96N mutant in BR.<sup>34</sup> In the case of KR2 the most obvious candidate is N112. It was suggested that the two key roles of N112 are the stabilization of the D116 residue during the M state of the photocycle and the coordination of the sodium ion along with D251 in the O intermediate.<sup>14,15,35–37</sup> The initial down shift from 1692  $\text{cm}^{-1}$  to 1620  $\text{cm}^{-1}$  could therefore be due to strong hydrogen bonds, which are build up between the protonated D116 and N112 in the course of the M state. A further stabilization of the amino acid side chains through additional water molecules in close proximity, as it was seen in the crystal structures, is also possible.<sup>14,15</sup> The following transition from M to O is characterized by the transient binding of the sodium ion in between D251 and N112 leading to another change of the hydrogen bond network. These two steps could explain the bi-exponential rise of the band at 1620  $\text{cm}^{-1}$  with  $\tau_1 = 30 \mu\text{s}$  and  $\tau_2 = 0.4 \text{ ms}$ . Still, signals of this amplitude and spectral width do not very likely originate from a single amino acid. Considering the spectral width of the whole amide I band with its edges at around 1620  $\text{cm}^{-1}$  and 1700  $\text{cm}^{-1}$ , another explanation for the negative signal around 1692  $\text{cm}^{-1}$  and the positive signal around 1620  $\text{cm}^{-1}$  could be a change of several amide I modes in the course of sodium translocation.<sup>38,39</sup> This could be explained by size and charge induced changes in the protein conformation during the sodium transport, resulting in a shift of the whole amide I band. Signals in the range of 1670–1690  $\text{cm}^{-1}$  are often assigned to  $\beta$ -loop or  $\beta$ -sheet structures and they are usually accompanied by stronger main bands at around 1620–1640  $\text{cm}^{-1}$  due to band splitting.<sup>40–42</sup> Therefore it is also possible that the band pair of (–) 1692  $\text{cm}^{-1}$ /(+) 1620  $\text{cm}^{-1}$  is not the result of an actual down shift of the whole amide I band, but a result of either a shift of the  $\beta$ -sheet resonance or a perturbation in band coupling of  $\beta$ -sheet contributions. This would stress the involvement of the ECL1 domain [Fig. 1a] in the ion translocation, since this is the only known  $\beta$ -sheet structure in KR2.<sup>14,15</sup> As mentioned above, the 1620  $\text{cm}^{-1}$  transient seems to be a superposition of the just mentioned amide I signal and the blue shifted vibrational mode from 1604  $\text{cm}^{-1}$ . There are two additional side bands at 1612  $\text{cm}^{-1}$  and 1636  $\text{cm}^{-1}$  with a differing dynamics compared to the 1620  $\text{cm}^{-1}$  transient [Fig. 6a]. Such a double band also occurs in KR2<sub>H</sub> with a slightly different frequency [Fig. 6b]. They could be the result of an up shift from the signals observed at 1592  $\text{cm}^{-1}$  and 1608  $\text{cm}^{-1}$ , which we found for KR2<sub>H</sub> as well as KR2<sub>Na</sub>. This is a strong indication for a more or less sodium independent structural change. One possibility would be a change of the retinal Schiff base moiety, since the region from 1600  $\text{cm}^{-1}$  to 1650  $\text{cm}^{-1}$  can also contain major contributions of the C=N–H group as seen in several other retinal proteins.<sup>24</sup> Due to the strong overlap with the amide and amino acid side chain signals, it is necessary to perform H/D exchange, isotope labeling and mutational studies to discriminate the contributions of the individual functional groups.

### Protonation state of the D116 residue

Intense signals above 1700  $\text{cm}^{-1}$ , such as those we observe in both, the proton and sodium pump [Fig. 8], are usually indicative for changes in the C=O stretch modes of glutamic or aspartic acids.<sup>23,43</sup> This reduces the list of possible amino acid side chains to D116 and D251, which both play a key role in the photocycle of KR2. The two positive bands of KR2<sub>Na</sub> and KR2<sub>H</sub> at 1744  $\text{cm}^{-1}$ , exhibit similar but temporally shifted features. However, under the assumption that D251 is directly involved in the coordination of sodium one would expect major differences under sodium and salt free conditions.<sup>14,15</sup> Therefore we assign the bands in this spectral region to the C=O stretch mode of the D116 side chain. Since our measurements were performed at pD 6 (KR2<sub>H</sub>) and pD 8.3 (KR2<sub>Na</sub>), it is obvious that the resting conditions are not the same. At pD 6.0 it is very likely that the D116 is already protonated and the water network inside the protein is slightly altered.<sup>14,15</sup> Moreover, D116 seems to be in an M-like conformation [Fig. 1c] in the resting state of KR2 at acidic pH values.<sup>14</sup> This might be an explanation for the comparatively low frequency of the C=O stretch mode of D116 in the resting state of KR2<sub>H</sub>, as D116 might already be hydrogen bonded with N112.<sup>14,15,36,38</sup> Such a hydrogen bond is probably not formed initially at pD 8.3 [Fig. 1b] resulting in a higher frequency of the C=O stretch mode, which is not in the spectral window of our experiment.<sup>38</sup> In this context, the band pair at (–) 1740  $\text{cm}^{-1}$ /(+) 1744  $\text{cm}^{-1}$  found for KR2<sub>H</sub>, also reflects the strength of hydrogen bonds with the carbonyl oxygen of D116. Since D116 needs to be deprotonated before the retinal Schiff base can transfer its proton in the course of the photocycle, the D116 residue has to release its proton first. This could be reflected in the upshift from 1740  $\text{cm}^{-1}$  in the ground state to 1744  $\text{cm}^{-1}$  and the delayed rise of the L/M intermediate in KR2<sub>H</sub>. The transition from the K to the L/M state is marked by the local minimum of (+) 1744  $\text{cm}^{-1}$  and the local maximum of (–) 1740  $\text{cm}^{-1}$ , which indicates reprotonation of D116 and a subsequent hydrogen bonding with N112. The second deprotonation of D116 can then be observed during the decay of M, which is shown in the second local maximum of (+) 1744  $\text{cm}^{-1}$  and the second local minimum of (–) 1740  $\text{cm}^{-1}$ , respectively. In KR2<sub>Na</sub> at pD 8.3 the D116 side chain is probably rotated more towards the retinal Schiff base.<sup>14</sup> After photoisomerization, the Schiff base proton turns towards the D116, which increases hydrogen bond strength.<sup>44</sup> This would cause a downshift of the C=O stretch mode from initially > 1750  $\text{cm}^{-1}$ , which we could not resolve, to 1744  $\text{cm}^{-1}$ . The first local minimum of 1744  $\text{cm}^{-1}$  after approximately 30  $\mu\text{s}$  coincides with the transition from the K state to the L/M state, representing the protonation of D116. The decay of M and the rise of the O state, respectively, is in good agreement with the local maximum of the transient, which occurs with  $\tau_2 = 0.4 \text{ ms}$ .

### Kinetic model for sodium and proton transport

Based on the results found in this comparative study we are able to formulate a minimalistic model for the photocycles of proton and sodium pumping [Fig. 9]. In the case of KR2<sub>Na</sub>, we

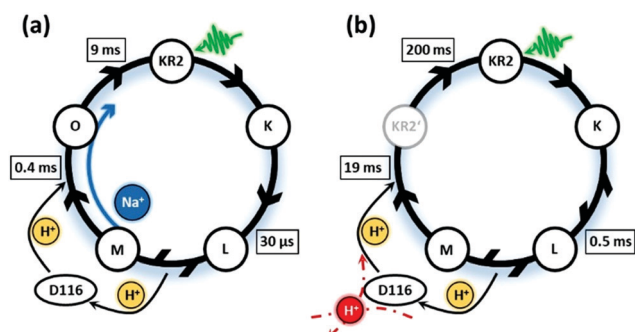


Fig. 9 Schematic models of the photocycle for (a)  $\text{KR2}_{\text{Na}}$  and (b)  $\text{KR2}_{\text{H}}$  based on the lifetimes derived from the analysis of the IR data.

observed a sequential rise and decay of most photointermediates with the exception of the L/M states, which seem to be in equilibrium. Schiff base deprotonation, and therefore protonation of the D116 residue, leads to the rise of the M state. At the same time the uptake of a sodium ion takes place. This is reflected in major changes of the protein backbone and the hydrogen bond network during the M to O transition. Besides the changes in the  $\alpha$ -helix conformation, we found strong indications for an involvement of the ECL1 domain, which is not seen in  $\text{KR2}_{\text{H}}$ . Synchronously with this transition, the D116 residue is deprotonated again, leading to the protonation of the Schiff base and therefore a recovery of the initial KR2 ground state. In contrast to that,  $\text{KR2}_{\text{H}}$  shows a prolonged K/L state, which is in equilibrium with the L/M state. The limiting factor for the transition to the M intermediate seems to be the protonation state of the D116 residue. This residue has to be deprotonated prior to the transfer from the Schiff base proton to D116. The proton transport pathway is still unknown and cannot be derived from the presented data alone. However, a major involvement of the hydrogen network and individual amino acid side chains in KR2 is very likely (depicted as the red proton pathway in Fig. 9b). The regeneration of the ground state seems to be biphasic, suggesting an additional intermediate  $\text{KR2}'$ , which is spectrally silent in the UV/vis.

## Conclusions

We were able to elucidate important mechanistic differences of the KR2 wild type in proton and sodium pumping mode by means of time-resolved UV/vis and infrared spectroscopy. By using an identical sample for both techniques, it was possible to correlate the data in both spectral windows directly and without the uncertainties stemming from different sample preparations. We found that the photocycle of  $\text{KR2}_{\text{Na}}$  shows a sequential character, whereas the photocycle of  $\text{KR2}_{\text{H}}$  involves several equilibria, which are reflected in intermediate specific vibrational changes of the retinal chromophore. Moreover,  $\text{KR2}_{\text{Na}}$  exhibits major conformational changes of the protein backbone, involving distortions of the  $\alpha$ -helices and probably of the ECL1 domain, which are not observed in  $\text{KR2}_{\text{H}}$ . The hereby identified marker bands of such protein distortions can help to

map the sodium ion uptake and transport. Besides larger structural changes inside the protein, we could also identify amino acid specific changes, including protonation and deprotonation of D116, which helped to monitor structural changes in close proximity to the retinal Schiff base. Based on these findings we could expand the kinetic model for the sodium pumping of KR2 and furthermore formulate a new kinetic model for KR2 in proton pumping conditions.

## Conflicts of interest

There are no conflicts to declare.

## Acknowledgements

This work was supported by the Deutsche Forschungsgemeinschaft (DFG) by means of the research training group CLiC (GRK 1986, Complex scenarios of light-control) and the SFB 807 (Transport and Communication across Biological Membranes). We also thank Dr Chavdar Slavov for help with the data evaluation.

## Notes and references

- O. P. Ernst, D. T. Lodowski, M. Elstner, P. Hegemann, S. Leonid and H. Kandori, Microbial and Animal Rhodopsins: Structures, Functions and Molecular Mechanisms, *Chem. Rev.*, 2014, **114**, 126–163.
- T. Kouyama and M. Murakami, Structural divergence and functional versatility of the rhodopsin superfamily, *Photochem. Photobiol. Sci.*, 2010, **9**, 1458–1465.
- D. Oesterhelt and W. Stoerkenius, Rhodopsin-like protein from the purple membrane of Halobacterium halobium, *Nature (London), New Biol.*, 1971, **233**, 149–152.
- B. Schobert and J. K. Lanyi, Halorhodopsin is a light-driven chloride pump, *J. Biol. Chem.*, 1982, **257**, 10306–10313.
- O. Beja, L. Aravind, E. V. Koonin, M. T. Suzuki, A. Hadd, L. P. Nguyen, S. B. Jovanovich, C. M. Gates, R. A. Feldman, J. L. Spudich, E. N. Spudich and E. F. DeLong, Bacterial Rhodopsin: Evidence for a New Type of Phototrophy in the Sea, *Science*, 2000, **289**, 1902–1906.
- C. Bamann, E. Bamberg, J. Wachtveitl and C. Glaubitz, Proteorhodopsin, *Biochim. Biophys. Acta, Bioenerg.*, 2014, **1837**, 614–625.
- H. Kandori, Ion-pumping microbial rhodopsins, *Front. Mol. Biosci.*, 2015, **2**, 52.
- G. Nagel, D. Ollig, M. Fuhrmann, S. Kateriya, A. M. Musti, E. Bamberg and P. Hegemann, Channelrhodopsin-1: A Light-Gated Proton Channel in Green Algae, *Science*, 2002, **296**, 2395–2398.
- G. Nagel, T. Szellas, W. Huhn, S. Kateriya, N. Adeishvili, P. Berthold, D. Ollig, P. Hegemann and E. Bamberg, Channelrhodopsin-2, a directly light-gated cation-selective membrane channel, *Proc. Natl. Acad. Sci. U. S. A.*, 2003, **100**, 13940–13945.

- 10 E. S. Boyden, F. Zhang, E. Bamberg, G. Nagel and K. Deisseroth, Millisecond-timescale, genetically targeted optical control of neural activity, *Nat. Neurosci.*, 2005, **8**, 1263–1268.
- 11 J. Y. Lin, A User's Guide to Channelrhodopsin Variants: Features, Limitations and Future Developments, *Exp. Physiol.*, 2012, **96**, 19–25.
- 12 K. Inoue, H. Ono, R. Abe-Yoshizumi, S. Yoshizawa, H. Ito, K. Kogure and H. Kandori, A light-driven sodium ion pump in marine bacteria, *Nat. Commun.*, 2013, **4**, 1678.
- 13 H. Kandori, K. Inoue and S. P. Tsunoda, Light-Driven Sodium-Pumping Rhodopsin: A New Concept of Active Transport, *Chem. Rev.*, 2018, **118**, 10646–10658.
- 14 H. E. Kato, K. Inoue, R. Abe-Yoshizumi, Y. Kato, H. Ono, M. Konno, S. Hososhima, T. Ishizuka, M. R. Hoque, H. Kunitomo, J. Ito, S. Yoshizawa, K. Yamashita, M. Takemoto, T. Nishizawa, R. Taniguchi, K. Kogure, A. D. Maturana, Y. Iino, H. Yawo, R. Ishitani, H. Kandori and O. Nureki, Structural basis for Na<sup>+</sup> transport mechanism by a light-driven Na<sup>+</sup> pump, *Nature*, 2015, **521**, 48–53.
- 15 I. Gushchin, V. Shevchenko, V. Polovinkin, K. Kovalev, A. Alekseev, E. Round, V. Borshchevskiy, T. Balandin, A. Popov, T. Gensch, C. Fahlke, C. Bamann, D. Willbold, G. Büldt, E. Bamberg and V. Gordeliy, Crystal structure of a light-driven sodium pump, *Nat. Struct. Mol. Biol.*, 2015, **22**, 390–396.
- 16 G. F. Z. da Silva, B. R. Goblirsch, A.-L. Tsai and J. L. Spudich, Cation-Specific Conformations in a Dual-Function Ion-Pumping Microbial Rhodopsin, *Biochemistry*, 2015, **54**, 3950–3959.
- 17 J. Kaur, C. N. Kriebel, P. Eberhardt, O. Jakdetchai, A. J. Leeder, I. Weber, L. J. Brown, R. C. D. Brown, J. Becker-Baldus, C. Bamann, J. Wachtveitl and C. Glaubitz, Solid-state NMR analysis of the sodium pump *Krokinobacter rhodopsin 2* and its H30A mutant, *J. Struct. Biol.*, 2018, DOI: 10.1016/j.jsb.2018.06.001, [Epub ahead of print].
- 18 P. K. Glasoe and F. A. Long, Use of Glass Electrodes to measure Acidities in Deuterium Oxide, *J. Phys. Chem.*, 1960, **64**, 188–190.
- 19 R. W. Hendler and R. I. Shrager, Deconvolutions based on singular value decomposition and the pseudoinverse: a guide for beginners, *J. Biochem. Biophys. Methods*, 1994, **28**, 1–33.
- 20 C. Slavov, H. Hartmann and J. Wachtveitl, Implementation and evaluation of data analysis strategies for time-resolved optical spectroscopy, *Anal. Chem.*, 2015, **87**, 2328–2336.
- 21 H. Ono, K. Inoue, R. Abe-Yoshizumi and H. Kandori, FTIR spectroscopy of a light-driven compatible sodium ion-proton pumping rhodopsin at 77 K, *J. Phys. Chem. B*, 2014, **118**, 4784–4792.
- 22 S. Krimm and J. Bandekar, *Advances in Protein Chemistry*, 1986, vol. 38, pp. 181–364.
- 23 Y. N. Chirgadze, O. V. Fedorov and N. P. Trushina, Estimation of amino acid residue side-chain absorption in the infrared spectra of protein solutions in heavy water, *Biopolymers*, 1975, **14**, 679–694.
- 24 M. E. Heyde, D. Gill, R. G. Kilponen and L. Rimai, Raman Spectra of Schiff Bases of Retinal (Models of Visual Photo-receptors), *J. Am. Chem. Soc.*, 1971, **93**, 6776–6780.
- 25 H. Kakitani, T. Kakitani, H. Rodman, B. Honlg and R. Callender, Correlation of Vibrational Frequencies with Absorption Maxima in Polyenes, Rhodopsin, Bacteriorhodopsin, and Retinal Analogues A number of important molecular properties have, *J. Phys. Chem.*, 1983, **87**, 3620–3628.
- 26 M. K. Verhoeven, K. Neumann, I. Weber, C. Glaubitz and J. Wachtveitl, Initial Reaction Dynamics of Proteorhodopsin Observed by Femtosecond Infrared and Visible Spectroscopy, *Biophys. J.*, 2008, **94**, 4796–4807.
- 27 M. K. Neumann-Verhoeven, K. Neumann, C. Bamann, I. Radu, J. Heberle, E. Bamberg and J. Wachtveitl, Ultrafast infrared spectroscopy on channelrhodopsin-2 reveals efficient energy transfer from the retinal chromophore to the protein, *J. Am. Chem. Soc.*, 2013, **135**, 6968–6976.
- 28 C. E. Eckert, J. Kaur, C. Glaubitz and J. Wachtveitl, Ultrafast Photoinduced Deactivation Dynamics of Proteorhodopsin, *J. Phys. Chem. Lett.*, 2017, **8**, 512–517.
- 29 Y. Hontani, K. Inoue, M. Kloz, Y. Kato, H. Kandori and J. T. M. Kennis, The photochemistry of sodium ion pump rhodopsin observed by watermarked femto- to submillisecond stimulated Raman spectroscopy, *Phys. Chem. Chem. Phys.*, 2016, **18**, 24729–24736.
- 30 H.-F. Chen, K. Inoue, H. Ono, R. Abe-Yoshizumi, A. Wada and H. Kandori, Time-resolved FTIR study of light-driven sodium pump rhodopsins, *Phys. Chem. Chem. Phys.*, 2018, **20**, 17694–17704.
- 31 G. Váró, L. S. Brown, J. Sasaki, H. Kandori, A. Maeda, R. Needleman and J. K. Lanyi, Light-Driven Chloride Ion Transport by Halorhodopsin from *Natronobacterium pharaonis*. 1. The Photochemical Cycle, *Biochemistry*, 1995, **34**, 14490–14499.
- 32 G. Váró, L. S. Brown, M. Lakatos and J. K. Lanyi, Characterization of the Photochemical Reaction Cycle of Proteorhodopsin, *Biophys. J.*, 2003, **84**, 1202–1207.
- 33 T. Köhler, I. Weber, C. Glaubitz and J. Wachtveitl, Proteorhodopsin Photocycle Kinetics Between pH 5 and pH 9, *Photochem. Photobiol.*, 2017, **93**, 762–771.
- 34 Y. Cao, G. Váró, A. L. Klinger, D. M. Czajkowsky, M. S. Braiman, R. Needleman and J. K. Lanyi, Proton transfer from Asp-96 to the bacteriorhodopsin Schiff base is caused by a decrease of the pKa of Asp-96 which follows a protein backbone conformational change, *Biochemistry*, 1993, **32**, 1981–1990.
- 35 R. Abe-Yoshizumi, K. Inoue, H. E. Kato, O. Nureki and H. Kandori, Role of Asn112 in a Light-Driven Sodium Ion-Pumping Rhodopsin, *Biochemistry*, 2016, **55**, 5790–5797.
- 36 S. P. Balashov, E. S. Imasheva, A. K. Dioumaev, J. M. Wang, K. H. Jung and J. K. Lanyi, Light-Driven Na<sup>+</sup> Pump from *Gillisia iimnaea*: A High-Affinity Na<sup>+</sup> Binding Site Is Formed Transiently in the Photocycle, *Biochemistry*, 2014, **53**, 7549–7561.
- 37 K. Inoue, M. Konno, R. Abe-Yoshizumi and H. Kandori, The Role of the NDQ Motif in Sodium-Pumping Rhodopsins, *Angew. Chem., Int. Ed.*, 2015, **54**, 11536–11539.

- 38 D. M. Byler and H. Susi, Examination of the Secondary Structure of Proteins by Deconvoluted FTIR, *Biopolymers*, 1986, **25**, 469–487.
- 39 A. Barth and C. Zscherp, What vibrations tell us about proteins, *Q. Rev. Biophys.*, 2002, **35**, 369–430.
- 40 H. Susi and D. M. Byler, Resolution-enhanced Fourier transform infrared spectroscopy of enzymes, *Methods Enzymol.*, 1986, **130**, 290–311.
- 41 Y. Abe and S. Krimm, Normal vibrations of crystalline polyglycine I, *Biopolymers*, 1972, **11**, 1817–1839.
- 42 A. Barth, The infrared absorption of amino acid side chains, *Prog. Biophys. Mol. Biol.*, 2000, **74**, 141–173.
- 43 K. Fahmy, O. Weidlich, M. Engelhard, H. Sigrist and F. Siebert, Aspartic Acid-212 of Bacteriorhodopsin Is Ionized in the M and N Photocycle Intermediates: An FTIR Study on Specifically <sup>13</sup>C-Labeled Reconstituted Purple Membranes, *Biochemistry*, 1993, **32**, 5862–5869.
- 44 C.-M. Suomivuori, A. P. Gamiz-Hernandez, D. Sundholm and V. R. I. Kaila, Energetics and dynamics of a light-driven sodium-pumping rhodopsin, *Proc. Natl. Acad. Sci. U. S. A.*, 2017, **114**, 7043–7048.

## 6.6 Jakdetchai *et al.*, *Sci. Adv.*, 2021

**Time-resolved IR spectroscopy reveals mechanistic details of ion transport in the sodium pump *Krokinobacter eikastus* Rhodopsin 2**

M. Asido, P. Eberhardt, C. N. Kriebel, M. Braun, C. Glaubitz and J. Wachtveitl,  
*Phys. Chem. Chem. Phys.*, **2019**, 21, 4461-4471.

## BIOPHYSICS

## Probing the photointermediates of light-driven sodium ion pump KR2 by DNP-enhanced solid-state NMR

Orawan Jakdetchai<sup>1</sup>, Peter Eberhardt<sup>2</sup>, Marvin Asido<sup>2</sup>, Jagdeep Kaur<sup>1</sup>, Clara Nassrin Kriebel<sup>1</sup>, Jiafei Mao<sup>1</sup>, Alexander J. Leeder<sup>3</sup>, Lynda J. Brown<sup>3</sup>, Richard C. D. Brown<sup>3</sup>, Johanna Becker-Baldus<sup>1</sup>, Christian Bamann<sup>4</sup>, Josef Wachtveitl<sup>2\*</sup>, Clemens Glaubitz<sup>1\*</sup>

The functional mechanism of the light-driven sodium pump *Krokinobacter eikastus* rhodopsin 2 (KR2) raises fundamental questions since the transfer of cations must differ from the better-known principles of rhodopsin-based proton pumps. Addressing these questions must involve a better understanding of its photointermediates. Here, dynamic nuclear polarization-enhanced solid-state nuclear magnetic resonance spectroscopy on cryo-trapped photointermediates shows that the K-state with 13-*cis* retinal directly interconverts into the subsequent L-state with distinct retinal carbon chemical shift differences and an increased out-of-plane twist around the C14-C15 bond. The retinal converts back into an all-*trans* conformation in the O-intermediate, which is the key state for sodium transport. However, retinal carbon and Schiff base nitrogen chemical shifts differ from those observed in the KR2 dark state all-*trans* conformation, indicating a perturbation through the nearby bound sodium ion. Our findings are supplemented by optical and infrared spectroscopy and are discussed in the context of known three-dimensional structures.

## INTRODUCTION

KR2 (*Krokinobacter eikastus* rhodopsin 2) is a light-driven sodium pump found in the marine bacteria *K. eikastus* (1, 2). It belongs to the family of microbial rhodopsins, characterized by seven transmembrane helices and a retinal cofactor linked via a Schiff base (SB) to a lysine (K255) in helix 7. If the sodium concentration is low, KR2 has been found to be able to translocate protons and lithium ions as well (1, 3). Engineering of the protein structure in the uptake cavity region leads to an expanded ion selectivity including potassium or cesium (4–6). As for other microbial rhodopsins, light-driven ion translocation by KR2 creates an electrochemical gradient and a membrane potential. KR2 has therefore attracted considerable interest because it is the first microbial rhodopsin that shows a cation pumping activity other than proton pumping, making it a promising tool for optogenetics. The potential application of KR2 as an effective optogenetic silencer would have the advantage that it could hyperpolarize the membrane potential without having an influence on the pH balance of cells (7).

Sodium pumps contain a signature NDQ motif (N112, D116, and Q123) in transmembrane helix 3 (1), which differs from the DTD [bacteriorhodopsin (BR) (8)] or DTE [proteorhodopsin (PR) (9)] motif found in proton pumps. In KR2, D116 is the retinal SB (RSB) counterion forming an H-bond with the protonated SB (pSB). The highly conserved proton donor and acceptor residues found in outward proton pumps are replaced by glutamine (Q123) and asparagine (N112) residues, which do not have such a functionality.

The discovery of KR2 was unexpected because the translocation of a cation such as Na<sup>+</sup> across the positively charged RSB appeared

energetically unfavorable due to the expected repulsion from the SB proton. Furthermore, sodium transport and its link to the photocycle raise many questions because mechanisms derived from well-studied proton pumps involving, for example, Grotthuss transfer steps do not apply.

Extensive efforts have been undertaken to resolve the structure and functional mechanism of KR2, making it the most intensively studied sodium pumping rhodopsin. Methods applied include femtosecond optical, ultrafast infrared, Raman, and solid-state nuclear magnetic resonance (NMR) spectroscopy (10–15) as well as molecular dynamics simulations (16). They were often combined with site-directed mutagenesis and transport assays to resolve the importance of key residues such as the NDQ motif as well as those affecting sodium binding, ion selectivity, or the ion transport pathway (e.g., H30, S70, D102, R109, R243, D251, N61, G263, E11, and E160) (1, 2, 4–6, 17).

Optical flash photolysis experiments revealed four distinct photointermediates named K, L, M, and O (Fig. 1A) (1, 18). After light activation, the retinal isomerizes from all-*trans* to 13-*cis*, resulting in the red-shifted K-state as known from BR and other microbial rhodopsins (10, 19). Subsequently, a blue-shifted L-state is formed, during which the pSB is prepared to transfer a proton to D116 in the even further blue-shifted M-state (1, 20). Uptake of sodium is believed to take place between the M-state and the red-shifted O-state (1, 3). The population of the O-state has been found to depend strongly on the sodium concentration (5, 21). The retinal conformation has been discussed controversially as 13-*cis* (20, 22) or all-*trans* (23, 24). The protein then relaxes back to the dark state to complete the photocycle.

Monomeric (5, 6) and pentameric (17) KR2 dark state crystal structures have been reported. In contrast to proton or chloride pumping microbial rhodopsins, no bound ion substrate has been found inside dark state KR2. The only bound sodium ion found in the resting state is at the extracellular side of the protomer interface in the pentameric crystal structure, but its binding site seems to be not directly related to the function of KR2 (6). The crystal structures

Copyright © 2021  
The Authors, some  
rights reserved;  
exclusive licensee  
American Association  
for the Advancement  
of Science. No claim to  
original U.S. Government  
Works. Distributed  
under a Creative  
Commons Attribution  
NonCommercial  
License 4.0 (CC BY-NC).

<sup>1</sup>Institute for Biophysical Chemistry and Center for Biomolecular Magnetic Resonance (BMRZ), Goethe University Frankfurt, Max von Laue Strasse 9, 60438 Frankfurt am Main, Germany. <sup>2</sup>Institute of Physical and Theoretical Chemistry, Goethe University Frankfurt, Max von Laue Strasse 7, 60438 Frankfurt am Main, Germany. <sup>3</sup>Department of Chemistry, University of Southampton, Southampton SO17 1BJ, Great Britain. <sup>4</sup>Max Planck Institute of Biophysics, Max von Laue Strasse 3, 60438 Frankfurt am Main, Germany.

\*Corresponding author. Email: wveitl@theochem.uni-frankfurt.de (J.W.); glaubitz@em.uni-frankfurt.de (C.G.)

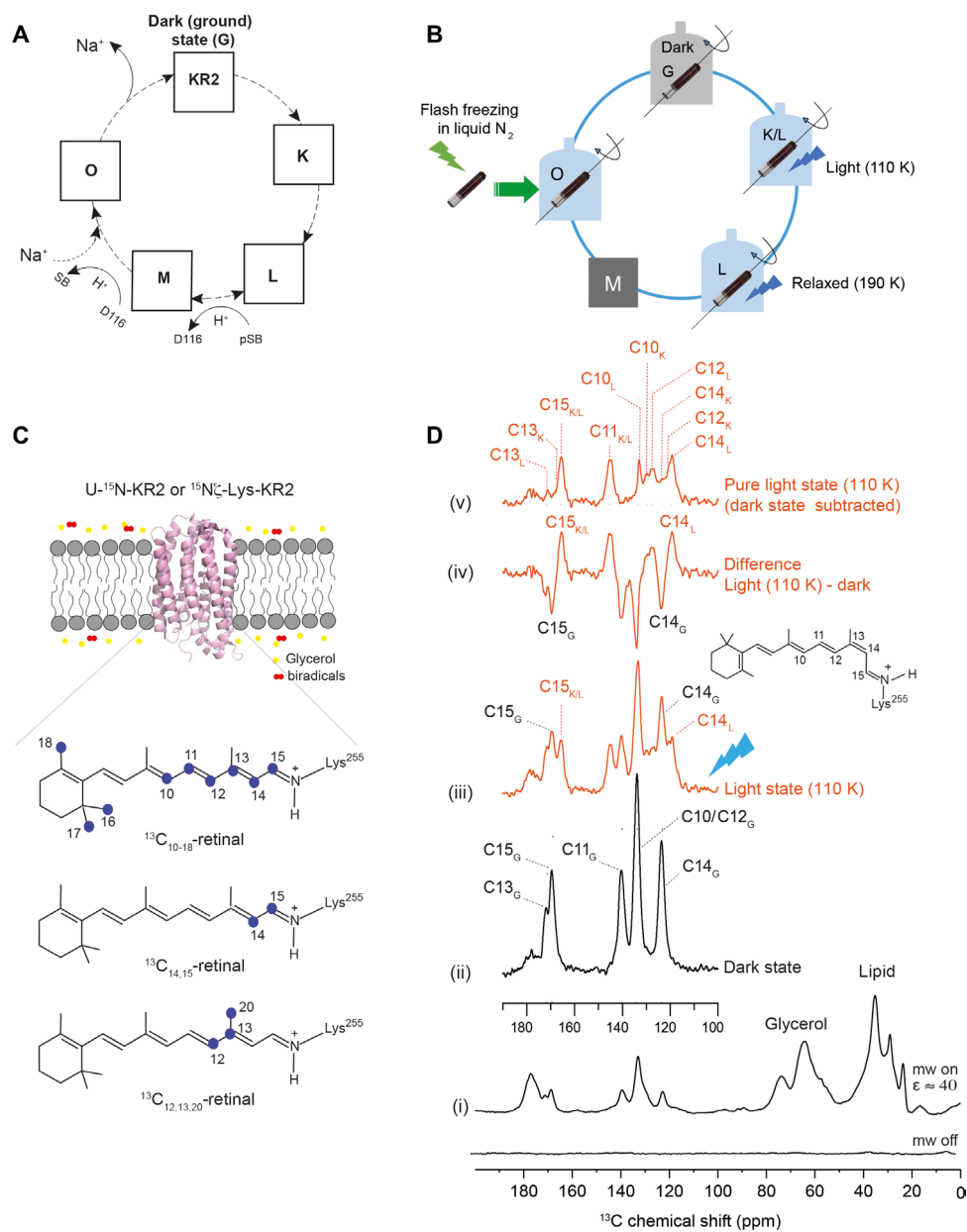


**Fig. 1. Experimental approach.** (A) Schematic photocycle of KR2. (B) Light-induced cryo-trapping for dynamic nuclear polarization (DNP)-enhanced magic angle spinning (MAS) NMR. (C) Retinal and KR2 isotope-labeling schemes. KR2 proteoliposomes were incubated with AMUPol in D<sub>2</sub>O/H<sub>2</sub>O/glycerol (see Materials and Methods). (D) DNP-enhanced <sup>13</sup>C spectra of <sup>13</sup>C<sub>10–18</sub>-KR2. (i) <sup>13</sup>C CP spectra reveal a DNP signal enhancement of 40. (ii) <sup>13</sup>C DQF spectra in the dark state and (iii) after illumination at 110 K. (iv) Difference spectrum (light dark). (v) Pure light-induced spectrum obtained by subtracting the remaining dark state contribution (see fig. S1). Retinal peak assignment is based on data in Fig. 2. mw, microwave.

of monomeric KR2 adopt a more “compact” conformation in which the large water-filled cavity close to the RSB found in the “expanded” pentameric state is missing (7).

Very recently, a serial crystallography study using an x-ray free-electron laser on monomeric KR2 has been reported (25). Two sodium-binding events have been observed, one near N112 and D251 (“O1 state”), followed by a second binding between E11, N106, and E160 (“O2 state”). In contrast, the crystal structure of the O-intermediate of pentameric KR2 (23) reveals a bound sodium ion near the RSB coordinated by N112 and D116 (23). These studies represent excellent progress in resolving structures of resting and

relevant photointermediate states. However, the resolution is still limited, and fine electrostatic details may not be observable.

To link three-dimensional (3D) structures with optical properties and functional data, NMR parameters such as chemical shifts, internuclear distances, or torsion angles within the chromophore can be extremely useful, especially in the context of model building assisted by quantum chemical approaches. In particular, solid-state NMR (ssNMR) has been very strong in the field as it offers unique possibilities to obtain structural details at atomic resolution for membrane proteins directly in lipid bilayer environments (26). It has been intensively used for the study of the retinal chromophore

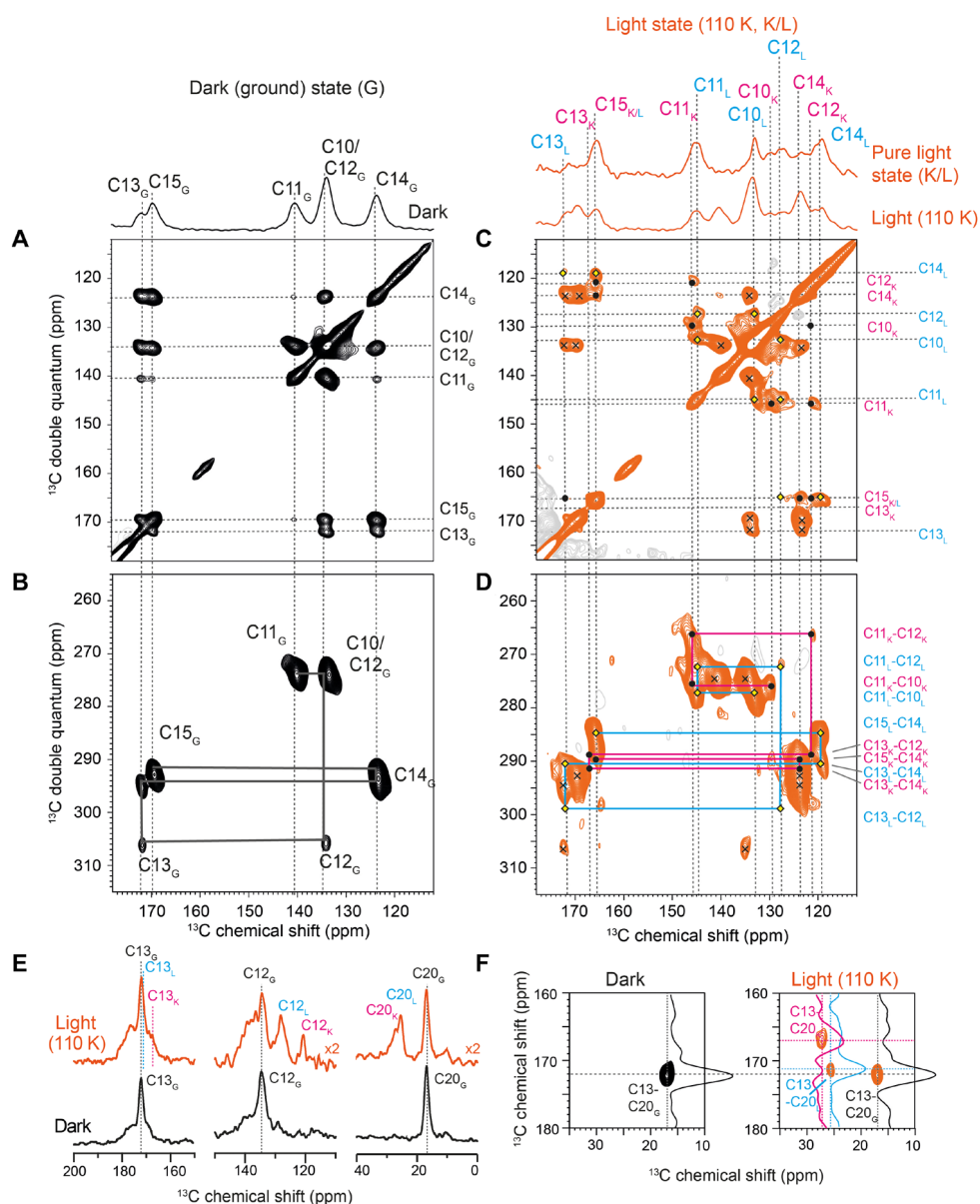


**Fig. 2. Retinal resonance assignment.**  $^{13}\text{C}$ - $^{13}\text{C}$  PDSD and DQSQ spectra of  $^{13}\text{C}_{10-18}$ -KR2 in the dark state (G) (A and B) and after illumination at 110 K (C and D). In the light state, two separate spin systems corresponding to the K-state ( $\bullet$ ) and L-state ( $\circ$ ) and the residual dark state ( $\times$ ) population are detected. Cross peaks belonging to the same spin system are connected in the DQSQ spectra (B and D). (E)  $^{13}\text{C}$  DQF spectra of  $^{13}\text{C}_{12,13,20}$ -KR2 in the dark state (G) and after illumination at 110 K (G, K, and L) show resonances for C13, C12, and C20. (F) PDSD spectra of  $^{13}\text{C}_{12,13,20}$ -KR2 reveal a C13-C20 cross peak in the dark, which splits into two additional signals assigned to C13<sub>K/L</sub> and C20<sub>K/L</sub> upon illumination.

(27–32). The sensitivity of NMR can be markedly improved by dynamic nuclear polarization (DNP), where polarization is transferred from paramagnetic dopants to nuclear spins (33). DNP, therefore, offers an excellent way to probe light-induced, cryo-trapped photointermediate states. The method was applied previously to the microbial rhodopsins BR (28, 34, 35), channelrhodopsin-2 (ChR2) (36), and PR (32, 37, 38) but has not been used for sodium pumps such as KR2.

Here, we applied DNP-enhanced ssNMR to monitor chemical shifts of retinal carbons and SB nitrogen in the dark state and K-, L-, and O-states of KR2 in its physiological pentameric form reconstituted into lipid bilayers. The light-induced photointermediates

were stabilized by various cryo-trapping protocols such as illumination at 110 K, thermal relaxation, or flash freezing (Fig. 1B). Cryo-trapping is highly compatible with the low-temperature requirements of DNP (39). The applied procedures were validated by recording time-resolved as well as cryo-trapped ultraviolet/visible (UV/Vis) absorption spectra of photointermediates. Our data reveal an equilibrium between the early K- and L-states with distinct  $^{13}\text{C}$  chemical shift differences. The  $^{15}\text{N}$  chemical shift of the SB nitrogen gradually increases from the dark state via K to L, indicating a stronger H-bond to D116. Furthermore, an increased out-of-plane twist at the end of the polyene chain in the L-state is observed. In the O-state, where sodium is bound inside KR2, the chromophore



adopts an all-trans conformation that, however, differs from the dark state. All-trans retinal has been suggested to aid sodium release (16), and the observed  $^{13}\text{C}$  and  $^{15}\text{N}$  chemical shift differences reflect slight structural rearrangement within the retinal binding pocket and altered SB interactions. The obtained data are complemented by time-resolved IR measurements, compared with those reported for proton pumping microbial rhodopsins, and discussed in the context of known x-ray data.

## RESULTS

To monitor the retinal conformation and SB-counterion interaction by ssNMR, we used three different isotope-labeling schemes (see Fig. 1C):  $10\text{-}18\text{-}^{13}\text{C}_9$  or  $14,15\text{-}^{13}\text{C}_2$  all-trans retinal was incorporated into U- $^{15}\text{N}$ -KR2. In addition,  $12,13,20\text{-}^{13}\text{C}_3$  all-trans retinal was reconstituted into  $^{15}\text{N}\zeta$ -Lys-KR2. We refer in the following to these samples as  $^{13}\text{C}_{10-18}$ -KR2,  $^{13}\text{C}_{14,15}$ -KR2, and  $^{13}\text{C}_{12,13,20}$ -KR2, respectively.

KR2 was reconstituted into lipid bilayers. All experiments were carried out in the presence of NaCl (30 to 100 mM) and with AMUPol as polarizing agent (see Materials and Methods for further details). Typically, a 40-fold signal enhancement (microwave on/off) was achieved by DNP in  $^1\text{H}$ - $^{13}\text{C}$  cross-polarization (CP) experiments as shown for  $^{13}\text{C}_{10-18}$ -KR2 [spectrum (i) in Fig. 1D]. Such an enhancement has been shown to be essential for in situ illumination and cryo-trapping experiments of photoreceptors (36, 37, 39). For  $^{13}\text{C}_{10-18}$  retinal, six of nine signals could be directly detected in

double-quantum filtered (DQF) spectra (40) in which the natural abundance  $^{13}\text{C}$  background has been suppressed [spectrum (ii) in Fig. 1D]. Four of these signals were well resolved and two overlapped (C10 and C12). The  $\beta$ -ionone ring methyl resonances C16, C17, and C18 were not considered here as they could not be detected under our DNP conditions (15, 32, 41). The assignment of all other carbons was derived from double-quantum single-quantum ( $^{13}\text{C}$ - $^{13}\text{C}$  DQSQ) (42) and carbon-carbon proton-driven spin diffusion (PDS) spectra (43) (Fig. 2, A and B). The obtained chemical shifts (table S1) in the dark state were identical to those reported by us before for KR2 in the proton-pumping mode in the absence of sodium (15). The C20 resonance was determined from a  $^{13}\text{C}$  DQF spectrum of  $^{13}\text{C}_{12,13,20}$ -KR2, which also confirmed the C12 and C13 assignments (Fig. 2E). The C14 and C15 resonance assignments were confirmed by a  $^{13}\text{C}$  DQF spectrum of  $^{13}\text{C}_{14,15}$ -KR2 (Fig. 3B).

## Cryo-trapping and assignment of the K- and L-intermediates

Sample illumination and cryo-trapping were carried out as described previously for green PR (GPR) (37). A high-power light-emitting diode (LED) was used for in situ illumination directly within the NMR spectrometer at 110 K for 60 min. As a result, new resonances occur in the  $^{13}\text{C}$  DQF spectrum [spectrum (iii) in Fig. 1D]. The light-dark difference spectrum [spectrum (iv) in Fig. 1D] demonstrates the depletion of the dark state and the creation of light-induced states. A conversion of approximately 45% can be achieved as estimated from the C11 resonance (fig. S1). A pure

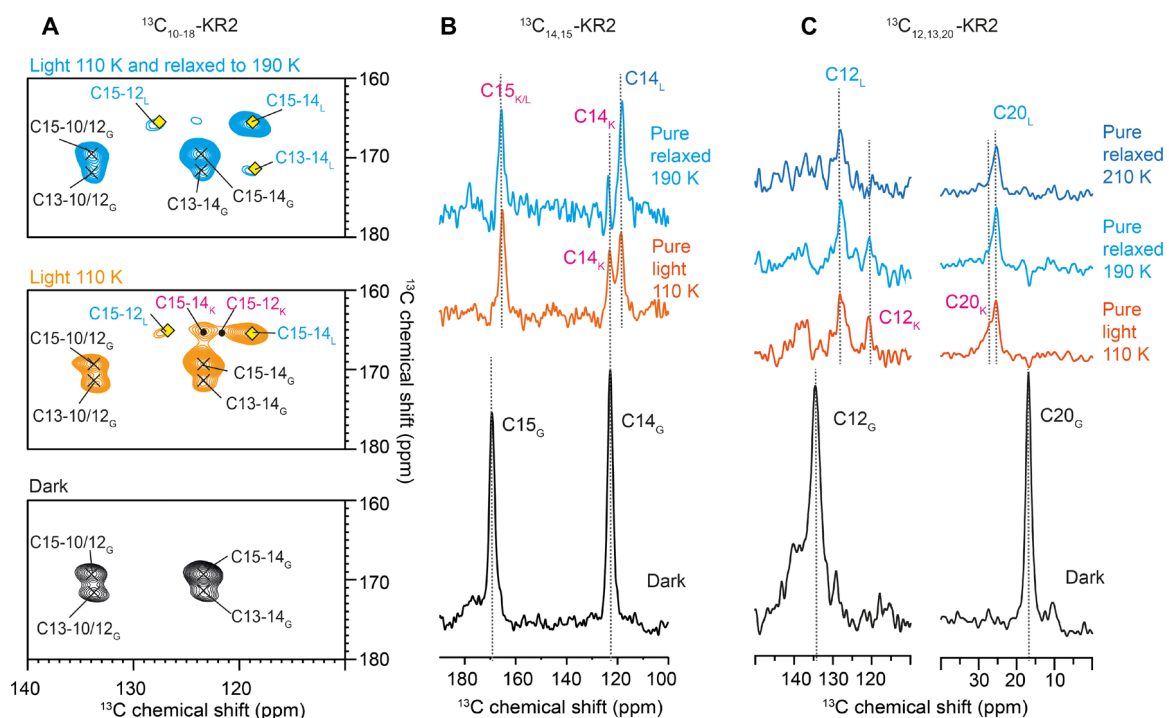


**Fig. 3. Thermal relaxation experiments for the identification of the K- and L-state spin system.** (A)  $^{13}\text{C}$ - $^{13}\text{C}$  PDS spectrum of  $^{13}\text{C}_{10-18}$ -KR2 in the dark (bottom). Upon illumination at 110 K (middle), two sets of C15-14 and C14-12 cross peaks occur in addition to the residual dark state resonances (x). Under thermal relaxation (top), only one set of these cross peaks remains and is assigned to the L-state (o). The disappearing resonances belong to the K-state (\*). (B)  $^{13}\text{C}$  DQF spectra of  $^{13}\text{C}_{14,15}$ -KR2. Upon illumination at 110 K, C15 shifts, while C14 splits into two resonances. The latter disappears upon thermal relaxation, which confirms the assignment of both resonances to K and L. The residual dark state contribution has been subtracted from the pure light-induced spectra. (C) Same experiment as in (B) but on  $^{13}\text{C}_{12,13,20}$ -KR2. Here, C20 shifts, and C12 shows a pronounced splitting, which reduces to just one peak after thermal relaxation, confirming here the resonance assignments to K- and L-states as well. See table S1 for chemical shift. An extensive temperature scan is shown in fig. S2.

light-induced spectrum is obtained by subtracting the remaining dark state population [spectrum ( $\nu$ ) in Fig. 1D].

To resolve and assign all new resonances, we recorded  $^{13}\text{C}$ - $^{13}\text{C}$  PDS and DQSQ spectra (Fig. 2, C and D). In these spectra, all signals from the residual dark state population could be identified. The newly appearing cross peaks correlate with each other and describe two separate retinal signal sets, which can be assigned by combining the DQSQ assignment walk with the correlations observed in the PDS spectrum. Unfortunately, the coexistence of dark and apparently two photointermediate states in our cryo-illuminated samples causes severe peak overlap in the 2D spectra of  $^{13}\text{C}_{10-18}$ -KR2. To unambiguously assign these new cross peaks, we also cryo-trapped  $^{13}\text{C}_{12,13,20}$ - and  $^{13}\text{C}_{14,15}$ -KR2 by illumination at 110 K. The C12 signal splits into two resonances (Fig. 2E). Furthermore, two additional C13-C20 cross peaks occur (Fig. 2F). Likewise, the C15 resonance shifts, and C14 splits into two signals (Fig. 3B). Using these spectra, two separate spin systems can be assigned, and it is therefore concluded that two early intermediates, tentatively assigned as K and L, have been trapped (table S1).

To identify which of the signals belongs to K and which belongs to L, we illuminated the sample at 110 K followed by thermal relaxation at various higher temperatures and subsequent detection by DNP-magic angle spinning (MAS) NMR after cooling down again to 110 K (36). Illumination under cryogenic conditions traps the protein in the earliest photointermediate state. By raising the temperature, subsequent photointermediates can be thermally reached before the system returns to the dark state. Upon illumination of  $^{13}\text{C}_{10-18}$ -KR2 at 110 K, two sets of C15-C14 and C15-C12 cross peaks occur in addition to the remaining dark state signals as described above (Fig. 3A). After thermal relaxation, two of the light-induced cross peaks disappear. They are therefore assigned to the K-intermediate, while the remaining peaks belong to the L-state. Additional support is provided by  $^{13}\text{C}$  DQF spectra of  $^{13}\text{C}_{14,15}$ -KR2, which show for C14 that under thermal relaxation at 190 K, the K-state decreases and the L-state increases (Fig. 3B). Similarly, we observe for  $^{13}\text{C}_{12,13,20}$ -KR2 that one of the C12 resonances increases, which allows us to assign the K- and L-state signals (Fig. 3C). The same effects are observed for C13 (fig. S2B) and C20 (Fig. 3C). Thermal relaxation experiments over a wider temperature range are shown in fig. S2A.

The assignments to K and L have been further validated by comparing UV/Vis absorbance spectra of photointermediates extracted from time-resolved flash photolysis experiments with those obtained under cryo-trapping conditions as used for DNP ssNMR (Fig. S4). Such an approach has been used before successfully to validate cryo-trapping of ChR2 (36) and PR (37). The difference spectra recorded at 110 and 160 K correspond well with the spectral signatures of the K- and L-state. The observation of both K- and L-photointermediates at temperatures as low as 100 K is unexpected as usually only the K-state can be produced in other microbial rhodopsins at such low temperatures (28, 34, 37).

### Characterization of the K- and L-intermediates

Chemical shift differences between dark and K/L-states are plotted in Fig. 4A. The 13-cis retinal isomer in the K-state causes largest effects for C12 with a shielding of 12.8 parts per million (ppm) and for C20 with a deshielding of 10.3 ppm. These values reduce in the L-state to 6.4 and 8.5 ppm for C12 and C20, respectively (table S2). The chemical shift changes are compared to those

observed for the trans-cis isomerization in model compounds (gray bars in Fig. 4A) (44, 45). For the K-state, they deviate by more than 4 ppm for C10 to C13 and C20 between KR2 and model compounds, which therefore suggests a protein-induced chromophore distortion around these carbons in the K-state. For the L-state, these differences are less pronounced. The chemical shift differences between K and L are shown in Fig. 4B. C12 (6.4 ppm) and C13 (4.1 ppm) are less shielded, while C14 displays an additional shielding (4.6 ppm), suggesting a slight movement toward a 15-syn conformation (46).

These observations suggest a fine adjustment of the chromophore upon illumination and a distortion at least near the SB region in early photointermediates as also indicated by previous time-resolved IR studies (10, 20). Such a distortion could be, for example, an out-of-plane twist of the polyene chain. This was further studied by time-resolved IR measurements, which span the spectral range of such hydrogen out-of-plane (HOOP) modes (Fig. 5A). The highlighted transients at 960, 980, and 992  $\text{cm}^{-1}$  show a biphasic decay, which correlates with the K/L-to-M transition and the decay of M, indicating a strong change of retinal distortion during the early intermediates in the photocycle. We therefore measured the HCCH torsion angle around the C14-C15 bond in  $^{13}\text{C}_{14,15}$ -KR2 by double-quantum heteronuclear local field experiments (47). Unfortunately, the K-intermediate could not be analyzed unambiguously because the C14 resonances of the dark and K-state as well as the C15 peaks of K- and L-states fully overlap (Fig. 3B and fig. S3A). However, for the L-state, dephasing curves could be obtained by deconvoluting the C14<sub>L</sub> peak from the C14<sub>G,K</sub> resonance. A comparison with the dark state is shown in Fig. 5B. The curves display a substantial deviation from planarity in the dark state ( $150^\circ \pm 2^\circ$ ), which becomes larger in the L-state ( $136^\circ \pm 6^\circ$ ; see also table S1). For comparison, we also performed light-induced cryo-trapping experiments in the absence of sodium. The chemical shifts of C14 and C15 do not change in K and L and also the same HCCH torsion angle is obtained (fig. S3).

The SB nitrogen  $^{15}\text{N}$  chemical shift is affected by its protonation state, H-bond formation and characteristics, its electrostatic environment, and the torsion around the C15=N bond. This NMR parameter has been extensively used for monitoring interactions between the SB and the counterion/proton acceptor during the photocycle (28, 34). The dark state signal for the pSB shifts and broadens upon illumination and cryo-trapping (fig. S2C). To resolve the K- and L-state contributions to the observed line shapes,  $^{15}\text{N}$ - $^{13}\text{C}$  transferred echo double resonance (TEDOR) (48, 49) spectra of  $^{13}\text{C}_{10-18}$ -KR2 were recorded. In these spectra, cross peaks between the SB nitrogen and retinal carbons C14 and C15 are observed (Fig. 6). In the dark state, the pSB nitrogen chemical shift at 173.3 ppm is as reported before (Fig. 6A) (13, 15). Upon illumination at 110 K (Fig. 6B), cross peaks for the K- and L-state subpopulations occur. After thermal relaxation at 190 K, only the L-state cross peaks remain (Fig. 6C). These spectra reveal the pSB nitrogen chemical shift for the K-state at 176.1 ppm and for the L-state at 181.3 ppm. The SB nitrogen becomes deshielded in the K- and L-states compared to the dark state, which indicates a stronger H-bond caused by stronger interactions with the counterion (D116) (50, 51). This effect is more pronounced in the L-state, which prepares the protein for the subsequent proton transfer step in the M-state. We also tried to trap the M-state by a further thermal relaxation step. However, the de-pSB signal, which is expected at around 320 ppm, could not be detected.

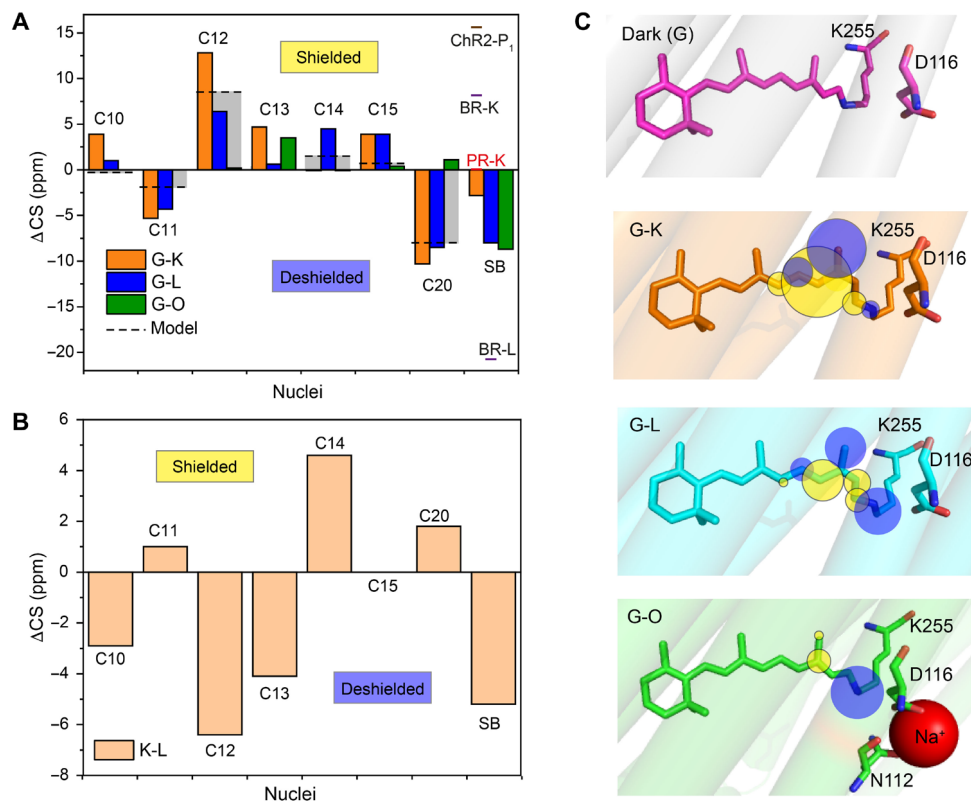


**Fig. 4. Light-induced  $^{13}\text{C}$  retinal carbon and SB chemical shift changes.** (A) Chemical shift differences between dark state (G) and photointermediates K, L, and O are plotted for carbon atoms C10 to C15, C20, and SB. The gray bars illustrate the effect of the all-trans 13-cis isomerization as observed for the model compounds *N*-retinylidenebutylamine (C10 to C15) and retinal (C20) (44, 45). The  $^{15}\text{N}$  chemical shift of KR2 in the dark and intermediate states is compared to GPR (37), BR (28), and Chr2 (36). (B) Chemical shift difference between the K- and L-state. (C) Illustration of chemical shift changes observed at retinal carbons and SB nitrogen in the dark state [Protein Data Bank (PDB): 6REW], K-state (PDB: 6TK5), L-state (PDB: 6TK4), and O-state (PDB: 6XYT). The yellow and blue spheres indicate shielding and deshielding at the nuclei, respectively.

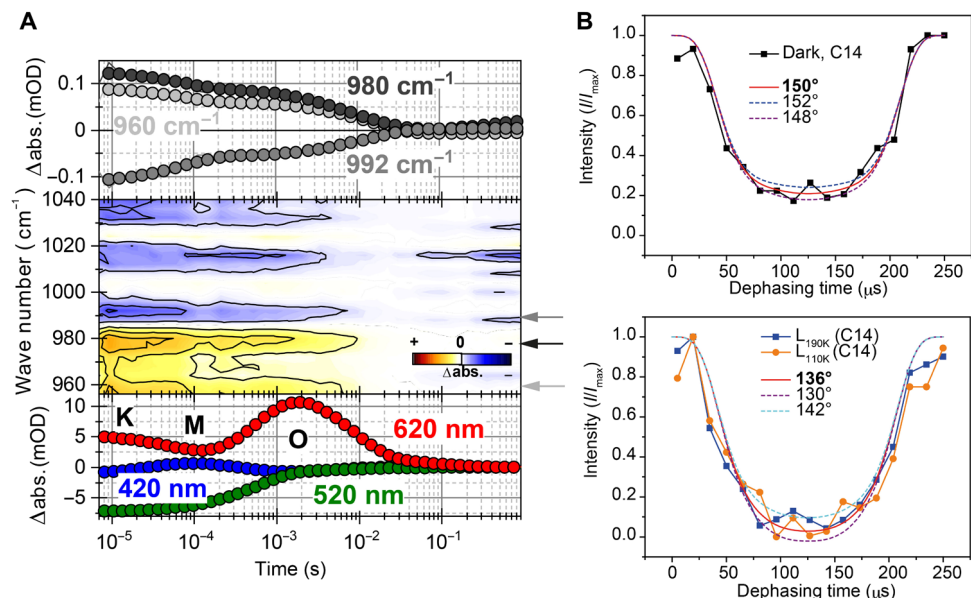


**Fig. 5. Twist of the retinal polyene chain.** (A) Transients of the UV/Vis measurements representing the intermediates of the photocycle (bottom), contour plot of the HOOP region (middle), and picked IR transients (top). The HOOP modes at 960, 980, and 992  $\text{cm}^{-1}$  show a biphasic decay, with the strongest amplitudes during the K/L-to-M transition and the decay of M. This biphasic behavior underlines the strongly twisted character of the retinal chromophore in the early photocycle of KR2, which relaxes back to a ground state-like conformation during the formation of O. (B) HCCH dephasing curves of the C14-C15 spin system in  $^{13}\text{C}_{14,15}$ -KR2 reporting on the H-C14-C15-H dihedral angle. (i) Dark state and (ii) L-intermediate were obtained by illumination at 110 K and followed by thermal relaxation at 190 K. Curves were obtained by analyzing the C14 signal intensity (see fig. S3 for further details). abs, absorbance; mOD, optical density/1000.

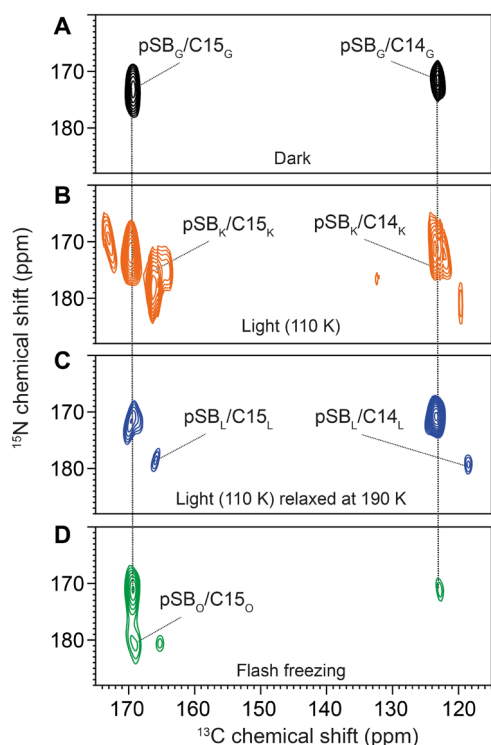


**Fig. 6.** DNP-enhanced  $^{15}\text{N}$ - $^{13}\text{C}$  TEDOR spectra of  $^{13}\text{C}_{10-18}$ -KR2 recorded under different trapping conditions. (A) In the dark state, cross peaks between the pSB nitrogen (173.3 ppm) and C14/C15 occur. (B) Upon illumination at 110 K, a mixture of new cross peaks and residual dark state populations arises. The main new population stems from the K-state. (C) A subsequent thermal relaxation step at 190 K depopulates the K-state and increases the L-state. The K- and L-state  $^{13}\text{C}$  chemical shifts agree with those described above (Fig. 3B). They correlate with pSB signals at 176.1 ppm (K-state) and 181.3 ppm (L-state). (D) Trapping the O-state by illumination at room temperature followed by flash freezing does not alter the C14/C15 chemical shifts significantly, but an additional cross peak between C15 and a new pSB nitrogen resonance at 182 ppm is observed. The signal at 181/175 ppm could be from a remaining L-state population but is not considered further because of its low signal-to-noise ratio. Spectra were recorded with a TEDOR mixing time of 6 ms.

One reason might be a very short lifetime/low population of the M-state (1).

### Cryo-trapping and analyzing the O-intermediate

The O-state is the last photointermediate in the KR2 photocycle (1). It becomes only populated in the presence of sodium ions and has the longest lifetime of all intermediates (18). Trapping is therefore based on continuous illumination outside the NMR spectrometer, followed by rapid flash freezing in liquid nitrogen and subsequent transfer into the DNP probe. This trapping procedure was first validated by cryo-UV/Vis spectroscopy, which demonstrated the feasibility of this method (fig. S4).

The O-state trapping procedure was then applied to  $^{13}\text{C}_{12,13,20}$ -KR2. A comparison of 1D  $^{13}\text{C}$  DQF spectra obtained after flash freezing with those recorded in the dark, after illumination at 110 K and after thermal relaxation, is shown in fig. S2B. No obvious chemical shift difference is detected between the ground and the O-state. To improve resolution, a  $^{13}\text{C}$ - $^{13}\text{C}$  PDS spectrum was recorded after flash freezing. Here, an additional correlation between C13 and C20 due to small chemical shift differences for both resonances

is observed (Fig. 7A). C13 and C20 are slightly more shielded with respect to the dark state by around 3 and 1 ppm, respectively. Similarly, an additional C13-C12 cross peak occurs. The C12 resonance is especially sensitive to the retinal isomerization. It is almost identical in the dark state and the O-state, suggesting a recovery of the all-trans retinal conformation.

To obtain O-state chemical shifts for the other retinal carbons and the SB nitrogen, we recorded  $^{15}\text{N}$ - $^{13}\text{C}$  TEDOR spectra on flash-frozen samples of  $^{13}\text{C}_{10-18}$ -KR2 (Fig. 6D). A new  $^{15}\text{N}$ -pSB- $^{13}\text{C}_{15}$  cross peak could be detected in addition to the signals from the remaining dark state population. The retinal  $^{13}\text{C}_{15}$  chemical shift of the O-state is the same as that of the all-trans retinal in the dark state. However, the  $^{15}\text{N}$  chemical shift of the pSB nitrogen occurs at 182.0 ppm and is therefore deshielded with respect to the dark state (173.3 ppm). To improve the magnetization transfer along the polyene chain, we performed an N(C)CX-type experiment with an initial CP step from the SB nitrogen to C15, followed by proton-driven carbon-carbon spin diffusion (52). This N(C15) CX spectrum of  $^{13}\text{C}_{10-18}$ -KR2 in the dark state shows  $^{15}\text{N}$ -pSB correlations at 173.3 ppm with all retinal carbons C10 to C15 (Fig. 7B). The  $^{13}\text{C}$  chemical shifts match those assigned by the PDS and DQSQ spectra (Fig. 2, A and B, and table S1). Upon trapping the O-state, new cross peaks between the  $^{15}\text{N}$ -pSB at 182 ppm and C12, C14, and C15 occur (Fig. 7C). The C12 chemical shift in the O-state is confirmed by the experiment on  $^{13}\text{C}_{12,13,20}$ -KR2 described above (Fig. 7A). The O-state C12, C14, and C15  $^{13}\text{C}$  chemical shifts are similar to the dark state. C13 overlaps with the C15 peak. The C10 and C11 resonances could not be observed because of their low peak intensities. The C12 and C20 O-state chemical shifts unambiguously show an all-trans conformation of the retinal chromophore similar to the dark state but with altered SB interactions since its nitrogen is deshielded by almost 9 ppm.

### DISCUSSION

The KR2 retinal and SB have been probed by DNP-enhanced ssNMR after light-induced cryo-trapping in early (K and L) and late (O) photointermediate states (Fig. 1B).

### Early photointermediate states

Our cryo-trapping experiments at 110 K revealed a mixture of K- and L-state populations. Very similar experimental conditions applied to BR, GPR, and ChR2 resulted just in a single trapped K-state, which hints toward differences in the energy landscape of early photointermediates between different rhodopsins. This view is also supported by the observed chemical shift changes in the K-state that are overall dominated by the retinal trans-cis isomerization in agreement with model compounds (Fig. 4). However, remarkable deviations from model compound behavior are observed for almost all labeled carbon positions, which therefore cannot solely be explained by isomerization but must partially be caused by specific interactions within the KR2 retinal binding pocket. These additional shielding/deshielding effects are protein specific as illustrated by comparing the K-state chemical shift changes of KR2 obtained with those from the same labeling scheme in the K-state of GPR (table S2). In PR, they also deviate from model compounds, but these changes are less pronounced: The overall root mean square deviation (RMSD) of the chemical shift differences (dark-K) in KR2 is larger than that in GPR (7.1 ppm versus 5.4 ppm; see table S2).

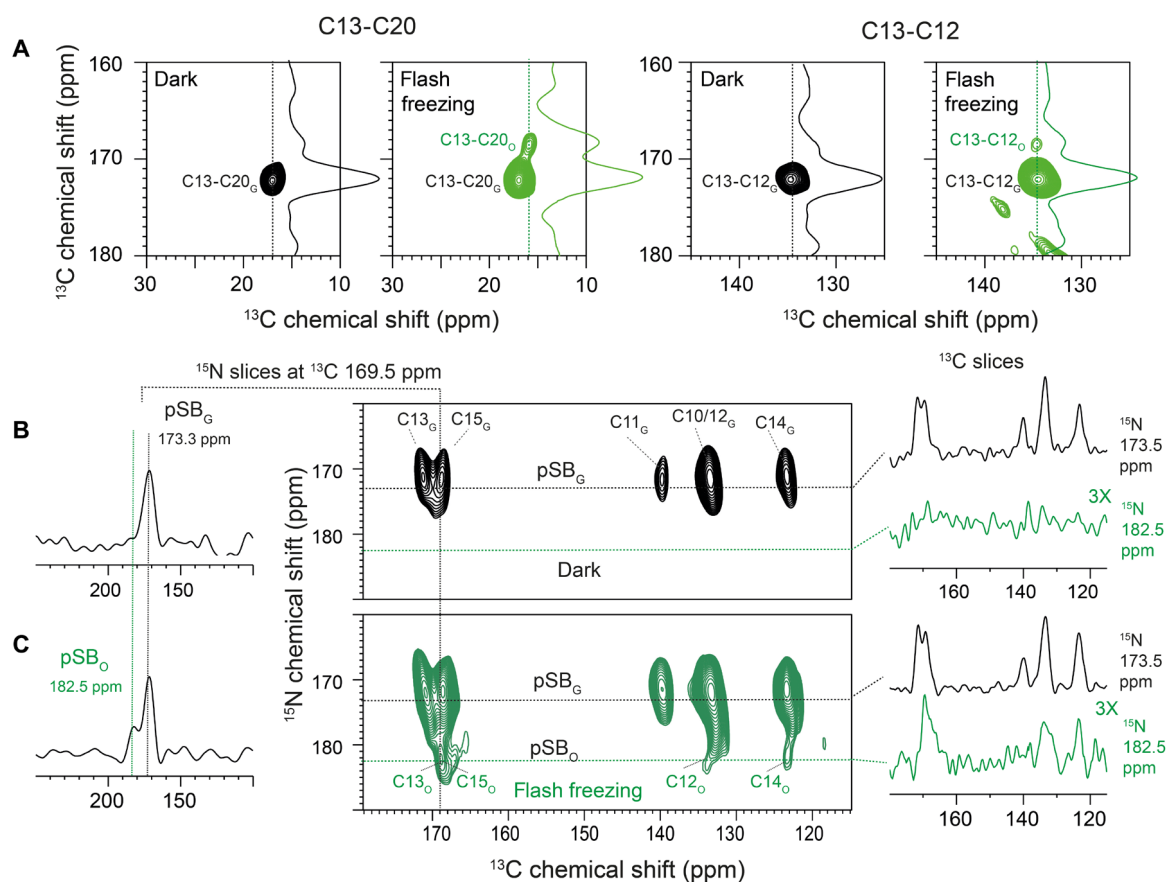


**Fig. 7. Analyzing the retinal chromophore in the KR2 O-state trapped by illumination and flash freezing.** (A)  $^{13}\text{C}$ - $^{13}\text{C}$  PDSD spectra of  $^{13}\text{C}_{12,13,20}$ -KR2 reveal a C13-C20 (left) and a C13-C12 cross peak (right) in the dark state. Upon flash freezing, an additional, small cross peak for C13-C20 and C13-C12 is detected. They arise from the O-state. C13 and C20 change by 3.5 and 1.1 ppm, respectively. (B)  $^{15}\text{N}$ - $^{13}\text{C}$  DCP (double cross polarization) correlation spectrum of  $^{13}\text{C}_{10-18}$ -KR2 (100 mM NaCl) with an N(C15)CX polarization transfer step in the dark state and (C) upon flash freezing. The trapped O-state population is characterized by a deshielding of the SB nitrogen by 9 ppm, while the C12, C14, and C15 resonances are similar to the dark state.

Similarly, distinct protein-induced effects have also been observed for BR and other rhodopsins using a range of different labeling schemes (28). Not only the retinal  $^{13}\text{C}$  but also the SB  $^{15}\text{N}$  chemical shift shows strong photocycle-dependent changes. Factors contributing to the chemical shift are primarily the protonation state, H-bonds, and the electrostatic environment. The latter two factors are often subsumed as a measure for the SB-counterion interactions since an empirical relationship between  $^{15}\text{N}$  chemical shift and  $\lambda_{\text{max}}$  for RSB model compounds has been found (50). In addition, the torsion around the SB bond C15=N will contribute to the observed chemical shift. Here, a deshielding in the K-state with respect to the dark state by 2.8 ppm is observed. Very different trends occur in other rhodopsin K-states although they are all red-shifted, underlining the role of the protein environment: While GPR shows no  $^{15}\text{N}$  chemical shift change (37), a large shielding is observed for light-adapted BR (BR568) (28) and Chr2 (36) (see Fig. 4A).

In the KR2 L-state, the overall  $^{13}\text{C}$  chemical shift changes with respect to the dark state are smaller compared to the K-state ( $^{13}\text{C}$  RMSD reduces from 7.1 to 4.9 ppm; table S2). In addition, the SB nitrogen is strongly deshielded by  $-8$  ppm and the torsion around the C14-C15 bond changes from  $150^\circ$  to  $136^\circ$ . The SB is already stronger drilled around the C15=N bond in the dark state compared to microbial proton pumps because the different position of

the proton acceptor D116 in KR2 requires another orientation of the SB N-H bond vector for a hydrogen bond formation (see fig. S3) (1, 5, 6, 17, 20). This is also reflected in the C14-C15 torsion. The larger out-of-plane twist brings the SB proton into an even more favorable position with respect to D116, which would be needed for the subsequent proton transfer step during the M-state. Such a twist in the polyene chain near the SB moiety might be necessary for the inhibition of the delocalization of the positive charge along the  $\pi$ -conjugated system, leading to the decrease of the  $\text{pK}_a$  value (where  $K_a$  is the acid dissociation constant) at the SB. This is also supported by the observed nitrogen deshielding, which is indicative of a stronger H-bond to D116. The C14 chemical shift has been found to be a sensitive marker for a 15-syn/anti conformation. In BR, the 15-anti-C14 resonance is found at 124 ppm and that for 15-syn is found at 111 ppm (28). Here, C14 shifts from 123.8 ppm in the dark and K-state to 119.2 ppm in the L-state. This means that the retinal is slightly turning toward a more compact 15-syn conformation in the L-state.

A twist along the retinal polyene chain is also supported by the HOOP modes in the range of  $950$  to  $1000\text{ cm}^{-1}$  (Fig. 5A). The band at  $992\text{ cm}^{-1}$  either stems from an in-plane bending vibration of the SB or stems from the C15-HOOP mode (53, 54). The positive signals at  $960$  and  $980\text{ cm}^{-1}$ , respectively, were also found for BR and were

attributed to the coupled C<sub>15</sub>-HOOP and N-HOOP mode of the SB (53, 55). All three transients show a biphasic decay, with their strongest contributions during the K/L-to-M transition and the decay of M (fig. S5). This implies a rather strong twisting of retinal in the early photocycle compared to the ground state.

Recently published serial crystallographic x-ray data of monomeric KR2 provide structural snapshots throughout the KR2 photocycle (25). We added our chemical shift changes to an overlay plot of the dark state [Protein Data Bank (PDB): 6TK6] and K-state (PDB: 6TK5;  $\Delta t = 800$  fs) structures (Fig. 8A). The largest changes stem from the isomerization. Additional protein-specific contributions to the observed chemical shift differences could be caused by altered ring-current effects due to small rearrangements of aromatic residues W113, W215, and Y218 by which the C10-C15 segment of the retinal polyene chain is surrounded. C20 tilts increasingly toward helix C in the L-state, which could also explain the C12, C13, and C14 chemical shift differences between K and L (PDB: 6TK5,  $\Delta t = 1$  ns; Fig. 8B). The distance between the SB nitrogen and O $\delta$ 2 of D116 changes from 3.0 Å in the dark state via 2.9 Å in the K-state to 2.4 Å in the L-state in these x-ray structures, which would agree with a <sup>15</sup>N deshielding due to an increasing H-bond strength.

BR is the only other rhodopsin for which chemical shift data for the L-state have also been obtained. As mentioned above, the <sup>15</sup>N SB nitrogen chemical shift becomes more shielded in the K-state but is significantly deshielded in the L-state (28). In light-adapted BR<sub>568</sub>, the SB forms an indirect H-bond with the proton acceptor D85 through the structural water molecule W402. In the K-state, this interaction is disturbed because of disordering of W402, followed by the formation of a new H-bond in the L-state (28, 35). The different trend in KR2 most likely hints toward a more direct interaction between SB and D116 throughout the photocycle. Note that T89 in BR, which is at the same position as D116 in KR2, has been found to be involved in proton transfer (35). The torsion and the K- and L-state chemical shifts are sodium independent (fig. S3), which supports the view that bound sodium near the RSB only occurs in later states.

### The late O-intermediate state

Structural data of microbial rhodopsin O-states are still rare. Fortunately, the KR2 O-state has a long lifetime and could be therefore trapped in proteoliposomes for ssNMR as reported here or in crystals for x-ray diffraction (23). The key difference between the KR2 O and dark states is the presence of an internally bound Na<sup>+</sup> ion. Sodium must pass the SB region during translocation, and the O-state has been shown to be directly connected with sodium binding and transport (3, 18, 24). This additional positive charge will alter the interaction network in the retinal binding pocket and will have an effect on the chemical shifts of nearby nuclei. Our <sup>13</sup>C chemical shift data show that the retinal in the O-state has switched back from 13-cis to all-trans but differences for the C13, C20, and of the SB nitrogen chemical shifts occur. Note that the retinal in the O-state x-ray structure is also in all-trans conformation, but the C14-C15 bond has been reported to be out of plane compared to the dark state (23). Furthermore, previous computational studies suggested that an all-trans retinal would facilitate exergonic Na<sup>+</sup> release to the extracellular side (16). The same study also suggested an electrostatic attraction of Na<sup>+</sup> to the negatively charged D116 resulting in a shielded interaction between D116 and the RSB with a subsequent red shift. This argument is in line with the coordination of bound

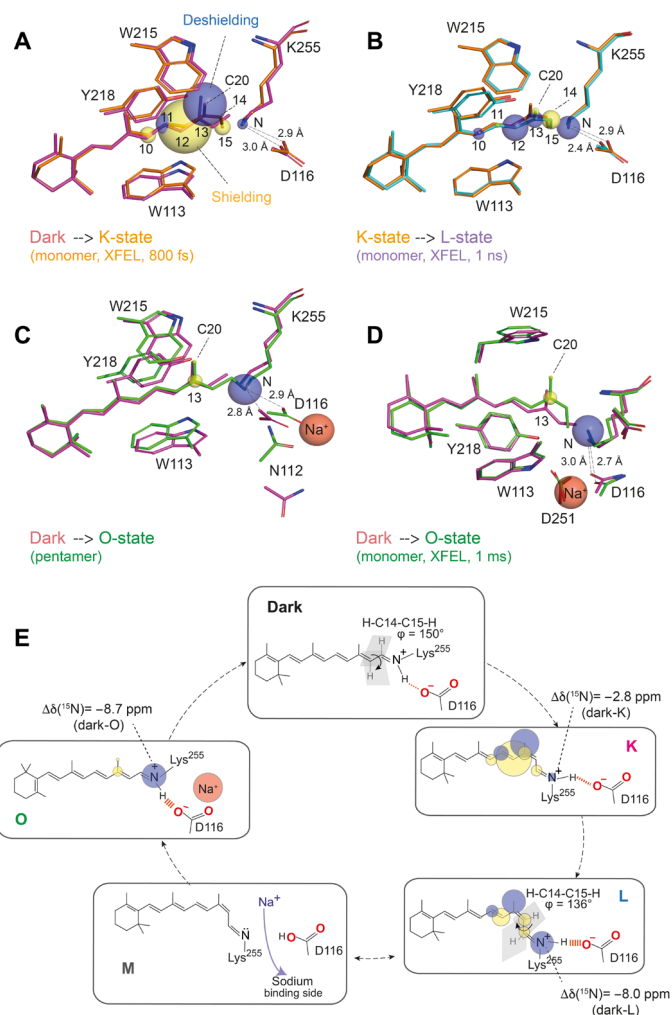


**Fig. 8. KR2 retinal binding pocket during the photocycle, structures, and chemical shifts.** (A) Comparison between dark- and K-state serial crystallography x-ray structures (6TK6 and 6TK5) (25) with <sup>13</sup>C and <sup>15</sup>N chemical shift changes (see tables S1 and S2). (B) As in (A) but comparison between the K-state (6TK5) and the L-state (6TK4). Plotted chemical shift changes are with respect to the K-state. (C) The dark state and O-state of pentameric KR2 x-ray structures (6REW and 6XYT) (23) and chemical shift changes with respect to the dark state. (D) The dark state and O-state of monomeric KR2 time-resolved structures (6TK6 and 6TK2) (23) and chemical shift changes with respect to the dark state. (E) Photocycle of KR2 and illustration of retinal conformation and electrostatic changes in K, L, and O as observed by ssNMR. The chromophore is highly twisted near the SB in the L-state, and the H-bond between SB nitrogen and D116 becomes stronger in L- and O-intermediates.

Na<sup>+</sup> by D116, N112, S70, and V67 revealed in the O-state x-ray structure (23) in which the ion is 5.4 Å away from the SB nitrogen (Fig. 8C).

For the SB nitrogen, a large deshielding by 9 ppm was observed in the O-state. As discussed before, factors contributing to the chemical shift are primarily the strength of the H-bond in which the SB nitrogen is involved, as well as electric charge effects and torsion around the C15=N bond.

An altered torsion appears less likely since the C14 chemical shift, a sensitive indicator for a 15-syn/anti isomerization, remains unchanged between the dark state and the O-state. This observation agrees with the KR2 dark state and O-state x-ray structures in

which the C14-C15-N-C $\epsilon$  dihedral angle does not significantly change (6REW, 135°; 6XYT, 132°) and which is also supported by our IR measurements. All three HOOP modes relax back to a ground state-like conformation with the formation of O (Fig. 5A).

The observed deshielding could, however, indicate a stretched N–H bond and, hence, a stronger O...H–N hydrogen bond between D116 and the SB nitrogen in the O-state. This seems plausible when considering that the SB becomes reprotonated with a proton being transferred from D116 during the M $\rightarrow$ O transition. This process is faster in the presence of Na<sup>+</sup>. It would require a favorable orientation of the aspartate carboxyl group and the SB with respect to each other and could result in a shorter O...H distance, which then relaxes and becomes longer again in the dark state (3, 24). On the other hand, this observation seems counterintuitive in comparison to RSB model compounds (50) for which a correlation between H-bond strength and  $\lambda_{\text{max}}$  was found and which would predict a blue shift with <sup>15</sup>N deshielding. This is usually discussed in terms of stronger counterion interactions and fits generally the observations on many rhodopsins in their dark states (13). Here, in the KR2 O-state, a red shift occurs, and it has been argued, as mentioned above, that this could be caused by a shielded counterion–SB interaction due to the bound Na<sup>+</sup>. However, the situation appears more complicated as Na<sup>+</sup> is coordinated by D116 and three other residues (23), which will alter the polarity/electric field within the SB vicinity in a complex manner. In addition, water molecules within the proximity of the SB will contribute to the polarity since the SB cavity contains four water molecules with one of them H-bonded to D116 (17).

In the O-state x-ray structure (PDB: 6XYT) (23), KR2 adopts a structure similar to the previously mentioned compact conformation with the SB cavity disappearing. These alterations will contribute to the H-bond character. It is also important to point out that substantial alterations in the H-bond geometry could be below the usual resolution of x-ray crystallography but will cause notable chemical shift changes (56). According to the dark state and O-state x-ray structures, the distance between OD2 of D116 and the SB nitrogen is, within the resolution limits, approximately the same (2.8 Å versus 2.9 Å). The observed chemical shift change, altered H-bond character, and red shift must, therefore, be caused by synergistic interplay of factors triggered by bound Na<sup>+</sup>. If one simply considers the bound Na<sup>+</sup> as a charge that shields D116<sup>−</sup>, then it would be interesting to know which effect a simple charge removal at the proton acceptor site would have. In both BR and GPR, upfield shifts/shieldings have been observed when replacing the proton acceptor Asp with Asn (50, 51, 57–60), which is consistent with a weaker counterion interaction. Unexpectedly, the corresponding KR2 mutant D116N shows the opposite trend with a small but notable downfield shift/deshielding of the SB nitrogen (13), which emphasizes that data interpretation in terms of a direct relationship between color/counterion interaction and SB chemical shift is in many cases too simplistic. Dissecting all contributing factors will ideally require quantum chemical computational approaches combining NMR and optical data with 3D structures.

The observed 4-ppm shielding for C13 most likely reflects an increased partial delocalization of the positive charge of the SB to C13. Furthermore, the C20 methyl group is a sensitive indicator for steric contacts between retinal chromophore and residues in the binding pocket (32, 61). Although the observed chemical shift difference is small (1 ppm), it could be caused, for example, by altered

contacts with residues such as W215 within the binding pocket. An overlay of the pentameric dark state structure (PDB: 6REW) with the trapped O-state (PDB: 6XYT) and our observed chemical shift changes is shown in Fig. 8C. The x-ray structures suggest small rearrangement of the aromatic residues within the binding pocket.

So far, the O-state has been discussed solely on the basis of the x-ray structure of the cryo-trapped KR2 pentamer. However, time-resolved x-ray structures derived from serial crystallography not only cover the K- and L-states but also have been extended via the M- into two O-states (25). After 1 ms, a Na<sup>+</sup> ion is found close to the retinal binding pocket but at a different position compared to the pentameric state. An overlay of this state with the dark state structure (Fig. 8D) shows that the structural differences should correspond to larger chemical shift changes than actually observed. One reason could be that our sample with KR2 pentamers in proteoliposomes is closer to the pentameric x-ray structure than to the monomeric preparation used for serial crystallography, a difference that has also been addressed by the authors as relevant to the O-state (25). On the other hand, the distance between SB and D116 in the serial crystallography study becomes shorter compared to the dark state (2.7 Å versus 3.0 Å), which could fit with our chemical shift changes on the SB nitrogen.

Note that the flash-freezing procedure used here for trapping the O-state has been used before successfully for long-lived states in PR and Chr2 (36, 37), but its trapping yield is limited when the lifetimes becomes shorter. A potential improvement is offered by novel fast freeze-quenching methods as recently demonstrated for DNP-enhanced ssNMR (62).

FTIR studies of trapped KR2 intermediates (22) and time-resolved Raman spectroscopy data (20) recently reported a 13-cis conformation for the retinal in the O-state. This is in contrast to our data and the pentameric O-state structure of KR2 (PDB: 6REW) (23). Data interpretation in these studies relied on spectra from all-trans and 13-cis retinal bound to BR. The C<sub>12</sub>D + C<sub>14</sub>D rocking vibrations in the IR HOOP region exhibits a band that is similar to the 13-cis conformation in BR. It might also be possible that the intermediate trapped at 240 K resembles an N-like state. The time-resolved Raman data of the C–C vibration peaks also suggested the 13-cis conformation. However, the signature interpretation was based only on the BR signature pattern, which might be divergent from KR2, and the all-trans conformation of O-intermediate might not be detected as it is very similar to the dark state.

Understanding how KR2 selects and pumps sodium ions requires a deep understanding of its photocycle intermediates at a level that allows one to link 3D structures with spectroscopic and functional data. ssNMR offers here a valuable insight since the relevant readout parameters are site-resolved and report not only on structural but also on electronic properties. Here, the retinal and SB-counterion interaction in the dark state and in K-, L-, and O-states of KR2 were characterized using DNP-enhanced ssNMR complemented by cryo-UV/Vis, flash photolysis, and time-resolved IR measurements. Our findings are summarized in Fig. 8E. The light-induced formation of the K-state is associated with <sup>13</sup>C chemical shift changes due to the retinal isomerization, which also reveal strong interactions between protein and chromophore. Such a “K-state signature” of chemical shift changes is specific to individual microbial rhodopsins and reflects the energy landscape of the early photocycle steps. The chemical shift perturbations slightly relax after formation of the subsequent L-state. However, the observed large twist at the end

of the retinal polyene chain further increases to prepare KR2 for the proton transfer step, which is also in line with an increased strength of the counterion interaction. These observations do not depend on the presence of sodium, which supports the view that the ion passes the protein during a later stage of the photocycle during the O-state formation. In the O-state, the chromophore relaxes back to all-trans, but in particular, the retinal C13 and SB nitrogen chemical shifts differ from the dark state and highlight a complex interaction pattern in the SB vicinity in the presence of a bound sodium ion. An all-trans retinal conformation has been suggested to be energetically favorable for sodium binding and release (16) and has also been observed by x-ray crystallography (23). Our NMR data offer an opportunity to reconcile a wealth of spectroscopic data with 3D structures if combined with future quantum mechanics/molecular mechanics calculations, by which increasingly larger systems can be addressed (63). In addition,  $^{23}\text{Na}$ -MAS NMR could offer a possibility to target the bound sodium ion directly.

## MATERIALS AND METHODS

### Sample preparation

[U- $^{15}\text{N}$ ]-KR2 was overexpressed and purified as described previously (15).  $^{14,15}\text{-}^{13}\text{C}_2$  all-trans retinal and  $^{10,18}\text{-}^{13}\text{C}_9$  all-trans retinal were synthesized as described by Leeder *et al.* (64).  $^{12,13,20}\text{-}^{13}\text{C}_3$  all-trans retinal was prepared in a similar way as published previously (32). The labeled retinals were incorporated into the membrane before the solubilization step. For  $^{15}\text{N}\zeta$ -Lys-KR2, the preparation protocol was similar to that of the uniformly labeled sample U- $^{15}\text{N}$ -KR2, but  $\text{NH}_4\text{Cl}$ , instead of  $^{15}\text{NH}_4\text{Cl}$ , was used in the medium together with other unlabeled amino acids. An amount of 116 mg of  $^{15}\text{N}\zeta$ -lysine was added to 0.5 liters of culture at the point where the optical density at 600 nm ( $\text{OD}_{600}$ ) reached a level of 0.2 and before induction with isopropyl- $\beta$ -D-thiogalactopyranoside at an  $\text{OD}_{600}$  of 0.6. The purified protein was reconstituted into liposomes containing 1,2-dimyristoyl-*sn*-glycero-3-phosphocholine [90 mole percent (mol %)]/1,2-dimyristoyl-*sn*-glycero-3-phosphate (10 mol %) liposomes. The lipid-to-protein ratio was 0.5 w/w. The proteoliposome samples were pelleted and washed with NMR buffer containing 25 mM tris, 5 mM  $\text{MgCl}_2$ , and 30 mM NaCl for  $^{13}\text{C}_{10,18}$ - and  $^{13}\text{C}_{14,15}$ -KR2 samples and 100 mM NaCl for  $^{13}\text{C}_{12,13,20}$ -KR2. These concentrations represent a good compromise between NMR buffer requirements and a sufficient O-state formation (25). For DNP-enhanced MAS ssNMR measurements, the samples were incubated for 20 hours at 4°C with a  $\text{d}^8$ -glycerol: $\text{H}_2\text{O}$ : $\text{D}_2\text{O}$  (6:3:1) solution containing 20 mM AMUPol (65), 25 mM tris (pH 8.5), 5 mM  $\text{MgCl}_2$ , and 30 or 100 mM NaCl. The supernatant was removed, and samples were packed into 3.2-mm sapphire rotors. They were uniformly distributed over the rotor wall by prespinning the rotors at room temperature.

### Trapping of photocycle intermediates

A high-power LED from Mightex was used to generate KR2 photocycle intermediates. The K- and L-intermediates were generated by directly illuminating KR2 inside the DNP probe within the magnet at 110 K with blue light (470 nm, 3.3 W) for 60 min as described before (37). Thermal relaxation experiments were performed by sample illumination at 110 K for 60 min, warming up to the desired temperature, followed by 2-min relaxation and subsequent cooling again to 110 K for DNP detection. The L-intermediate was best observed

by relaxation at 190 or 210 K for 2 min. The O-intermediate was generated by illuminating the sample with green light (525 nm) outside the magnet for 10 s, followed by fast freezing in liquid nitrogen (flash freezing) and subsequent transfer into the precooled DNP probe (110 K) within the NMR magnet.

### DNP-enhanced ssNMR experiments

All experiments were performed on a Bruker 400 DNP system consisting of a 400-MHz WB Advance II NMR spectrometer with a 3.2-mm DNP MAS probe head connected via a waveguide to a 263-GHz gyrotron. The probe head was modified with a fiber bundle for delivering light from a high-power LED directly into the MAS rotor. A MAS rate of 8 kHz was applied in all experiments, except for the spectra in Figs. 2 (E and F), 3C, and 8A, for which 10 kHz was used. The  $^{13}\text{C}$  and  $^{15}\text{N}$  chemical shifts were referenced indirectly to 2,2-dimethyl-2-silapentane-5-sulphonic acid using the  $^{13}\text{C}$  signal of CO-alanine at 179.85 ppm. Experimental details for CP, DQF, PDS, DQSQ correlation, double-quantum heteronuclear local field, TEDOR, and N(C)CX experiments are summarized in table S3.

### IR and UV/Vis flash photolysis

A Nd:YAG laser (SpitLight 600, InnoLas Laser GmbH) pumping an optical parametric oscillator (PreciScan, GWU-Lasertechnik) was used to generate single nanosecond pulses with a central wavelength of  $\lambda_{\text{max}} = 525$  nm to excite the sample. The power was set to  $1.7 \text{ mJ cm}^{-2}$  at 525-nm excitation wavelength. The IR probe light was generated by a quantum cascade laser (MIRcat 1100-U2-5086, Daylight Solutions, USA), which is tunable in the range of 950 to 1150  $\text{cm}^{-1}$ . The shown transients in the range from 956 to 1040  $\text{cm}^{-1}$  were recorded with a spectral resolution of 4  $\text{cm}^{-1}$ . For a better data correlation, we also measured UV/Vis transients at 420, 520, and 620 nm of the same sample, which was achieved using a mercury-xenon lamp (LC-08, Hamamatsu, Japan) and a set of two monochromators (Photon Technology International, USA). The KR2 wild-type sample was washed three times with a buffer containing 50 mM Hepes/tris, 100 mM NaCl, and 0.05% dodecyl- $\beta$ -D-maltosid detergent, which was diluted in  $\text{D}_2\text{O}$  and set to pD 8.1. A concentrated pellet was then evenly spread on the center of a  $\text{CaF}_2$  window and sandwiched with a Teflon spacer of 50- $\mu\text{m}$  thickness and an additional  $\text{CaF}_2$  window.

### SUPPLEMENTARY MATERIALS

Supplementary material for this article is available at <http://advances.sciencemag.org/cgi/content/full/7/11/eabf4213/DC1>

[View/request a protocol for this paper from Bio-protocol.](#)

### REFERENCES AND NOTES

1. K. Inoue, H. Ono, R. Abe-Yoshizumi, S. Yoshizawa, H. Ito, K. Kogure, H. Kandori, A light-driven sodium ion pump in marine bacteria. *Nat. Commun.* **4**, 1678 (2013).
2. H. Kandori, Ion-pumping microbial rhodopsins. *Front. Mol. Biosci.* **2**, 52 (2015).
3. Y. Kato, K. Inoue, H. Kandori, Kinetic analysis of  $\text{H}^+$ - $\text{Na}^+$  selectivity in a light-driven  $\text{Na}^+$ -pumping rhodopsin. *J. Phys. Chem. Lett.* **6**, 5111–5115 (2015).
4. M. Konno, Y. Kato, H. E. Kato, K. Inoue, O. Nureki, H. Kandori, Mutant of a light-driven sodium ion pump can transport cesium ions. *J. Phys. Chem. Lett.* **7**, 51–55 (2016).
5. H. E. Kato, K. Inoue, R. Abe-Yoshizumi, Y. Kato, H. Ono, M. Konno, S. Hososhima, T. Ishizuka, M. R. Hoque, H. Kunitomo, J. Ito, S. Yoshizawa, K. Yamashita, M. Takemoto, T. Nishizawa, R. Taniguchi, K. Kogure, A. D. Maturana, Y. Iino, H. Yawo, R. Ishitani, H. Kandori, O. Nureki, Structural basis for  $\text{Na}^+$  transport mechanism by a light-driven  $\text{Na}^+$  pump. *Nature* **521**, 48–53 (2015).
6. I. Gushchin, V. Shevchenko, V. Polovinkin, K. Kovalev, A. Alekseev, E. Round, V. Borshchevskiy, T. Balandin, A. Popov, T. Gensch, C. Fahlke, C. Bamann, D. Willbold,



- G. Büldt, E. Bamberg, V. Gordeliy, Crystal structure of a light-driven sodium pump. *Nat. Struct. Mol. Biol.* **22**, 390–395 (2015).
7. I. Gushchin, V. Shevchenko, V. Polovinkin, V. Borshchevskiy, P. Buslaev, E. Bamberg, V. Gordeliy, Structure of the light-driven sodium pump KR2 and its implications for optogenetics. *FEBS J.* **283**, 1232–1238 (2016).
  8. D. Oesterhelt, W. Stoekenius, Rhodopsin-like protein from the purple membrane of *Halobacterium halobium*. *Nat. New Biol.* **233**, 149–152 (1971).
  9. O. Bějík, L. Aravind, E. V. Koonin, M. T. Suzuki, A. Hadd, L. P. Nguyen, S. B. Jovanovich, C. M. Gates, R. A. Feldman, J. L. Spudich, E. N. Spudich, E. F. De Long, Bacterial rhodopsin: Evidence for a new type of phototrophy in the sea. *Science* **289**, 1902–1906 (2000).
  10. H. Ono, K. Inoue, R. Abe-Yoshizumi, H. Kandori, FTIR spectroscopy of a light-driven compatible sodium ion-proton pumping rhodopsin at 77 K. *J. Phys. Chem. B* **118**, 4784–4792 (2014).
  11. S. Tomida, S. Ito, K. Inoue, H. Kandori, Hydrogen-bonding network at the cytoplasmic region of a light-driven sodium pump rhodopsin KR2. *Biochim. Biophys. Acta Bioenerg.* **1859**, 684–691 (2018).
  12. Y. Hontani, K. Inoue, M. Klotz, Y. Kato, H. Kandori, J. T. M. Kennis, The photochemistry of sodium ion pump rhodopsin observed by watermarked femto- to submillisecond stimulated Raman spectroscopy. *Phys. Chem. Chem. Phys.* **18**, 24729–24736 (2016).
  13. A. Shigetani, S. Ito, K. Inoue, T. Okitsu, A. Wada, H. Kandori, I. Kawamura, Solid-state nuclear magnetic resonance structural study of the retinal-binding pocket in sodium ion pump rhodopsin. *Biochemistry* **56**, 543–550 (2017).
  14. A. Shigetani, S. Ito, R. Kaneko, S. Tomida, K. Inoue, H. Kandori, I. Kawamura, Long-distance perturbation on Schiff base-counterion interactions by His30 and the extracellular Na<sup>+</sup>-binding site in *Krokinobacter* rhodopsin 2. *Phys. Chem. Chem. Phys.* **20**, 8450–8455 (2018).
  15. J. Kaur, C. N. Kriebel, P. Eberhardt, O. Jakdetchai, A. J. Leeder, I. Weber, L. J. Brown, R. C. D. Brown, J. Becker-Baldus, C. Bamann, J. Wachtveitl, C. Glaubitz, Solid-state NMR analysis of the sodium pump *Krokinobacter* rhodopsin 2 and its H30A mutant. *J. Struct. Biol.* **206**, 55–65 (2019).
  16. C.-M. Suomivuori, A. P. Gamiz-Hernandez, D. Sundholm, V. R. I. Kaila, Energetics and dynamics of a light-driven sodium-pumping rhodopsin. *Proc. Natl. Acad. Sci. U.S.A.* **114**, 7043–7048 (2017).
  17. K. Kovalev, V. Polovinkin, I. Gushchin, A. Alekseev, V. Shevchenko, V. Borshchevskiy, R. Astashkin, T. Balandin, D. Bratanov, S. Vaganova, A. Popov, V. Chupin, G. Büldt, E. Bamberg, V. Gordeliy, Structure and mechanisms of sodium-pumping KR2 rhodopsin. *Sci. Adv.* **5**, eaav2671 (2019).
  18. M. Asido, P. Eberhardt, C. N. Kriebel, M. Braun, C. Glaubitz, J. Wachtveitl, Time-resolved IR spectroscopy reveals mechanistic details of ion transport in the sodium pump *Krokinobacter eikastus* rhodopsin 2. *Phys. Chem. Chem. Phys.* **21**, 4461–4471 (2019).
  19. S. Tahara, S. Takeuchi, R. Abe-Yoshizumi, K. Inoue, H. Ohtani, H. Kandori, T. Tahara, Ultrafast photochemical dynamics of a light-driven sodium-ion-pumping retinal protein from *Krokinobacter eikastus* revealed by femtosecond time-resolved absorption spectroscopy. *J. Phys. Chem. Lett.* **6**, 4481–4486 (2015).
  20. N. Nishimura, M. Mizuno, H. Kandori, Y. Mizutani, Distortion and a strong hydrogen bond in the retinal chromophore enable sodium-ion transport by the sodium-ion pump KR2. *J. Phys. Chem. B* **123**, 3430–3440 (2019).
  21. A. V. Bogachev, Y. V. Bertsova, M. L. Verkhovskaya, M. D. Mamedov, V. P. Skulachev, Real-time kinetics of electrogenic Na<sup>+</sup> transport by rhodopsin from the marine flavobacterium *Dokdonia* sp. PRO95. *Sci. Rep.* **6**, 21397 (2016).
  22. H.-F. Chen, K. Inoue, H. Ono, R. Abe-Yoshizumi, A. Wada, H. Kandori, Time-resolved FTIR study of light-driven sodium pump rhodopsins. *Phys. Chem. Chem. Phys.* **20**, 17694–17704 (2018).
  23. K. Kovalev, R. Astashkin, I. Gushchin, P. Orekhov, D. Volkov, E. Zinovev, E. Marin, M. Rulev, A. Alekseev, A. Royant, P. Carpentier, S. Vaganova, D. Zabelskii, C. Baeken, I. Sergeev, T. Balandin, G. Bourenkov, X. Carpena, R. Boer, N. Maliar, V. Borshchevskiy, G. Büldt, E. Bamberg, V. Gordeliy, Molecular mechanism of light-driven sodium pumping. *Nat. Commun.* **11**, 2137 (2020).
  24. S. P. Balashov, E. S. Imasheva, A. K. Dioumaev, J. M. Wang, K. H. Jung, J. K. Lanyi, Light-driven Na<sup>+</sup> pump from *Gillisia limnaea*: A high-affinity Na<sup>+</sup> binding site is formed transiently in the photocycle. *Biochemistry* **53**, 7549–7561 (2014).
  25. P. Skopintsev, D. Ehrenberg, T. Weinert, D. James, R. K. Kar, P. J. M. Johnson, D. Ozerov, A. Furrer, I. Martiel, F. Dworkowski, K. Nass, G. Knopp, C. Cirelli, C. Arrell, D. Gashi, S. Mous, M. Wraniak, T. Gruhl, D. Kekilli, S. Brünle, X. Deupi, G. F. X. Schertler, R. M. Benoit, V. Pannels, P. Nogly, I. Schapiro, C. Milne, J. Heberle, J. Standfuss, Femtosecond-to-millisecond structural changes in a light-driven sodium pump. *Nature* **583**, 314–318 (2020).
  26. V. S. Mandala, J. K. Williams, M. Hong, Structure and dynamics of membrane proteins from solid-state NMR. *Annu. Rev. Biophys.* **47**, 201–222 (2018).
  27. J. C. Lansing, M. Hohwy, C. P. Jaronec, A. F. Creemers, J. Lugtenburg, J. Herzfeld, R. G. Griffin, Chromophore distortions in the bacteriorhodopsin photocycle: Evolution of the H–C14–C15–H dihedral angle measured by solid-state NMR. *Biochemistry* **41**, 431–438 (2002).
  28. V. S. Bajaj, M. L. Mak-Jurkauskas, M. Belenky, J. Herzfeld, R. G. Griffin, Functional and shunt states of bacteriorhodopsin resolved by 250 GHz dynamic nuclear polarization-enhanced solid-state NMR. *Proc. Natl. Acad. Sci. U.S.A.* **106**, 9244–9249 (2009).
  29. N. Kimata, A. Pope, M. Eilers, C. A. Opefi, M. Ziliox, A. Hirshfeld, E. Zaitseva, R. Vogel, M. Sheves, P. J. Reeves, S. O. Smith, Retinal orientation and interactions in rhodopsin reveal a two-stage trigger mechanism for activation. *Nat. Commun.* **7**, 12683 (2016).
  30. D. B. Good, S. Wang, M. E. Ward, J. Struppe, L. S. Brown, J. R. Lewandowski, V. Ladizhansky, Conformational dynamics of a seven transmembrane helical protein Anabaena sensory rhodopsin probed by solid-state NMR. *J. Am. Chem. Soc.* **136**, 2833–2842 (2014).
  31. S. Ahuja, M. Eilers, A. Hirshfeld, E. C. Yan, M. Ziliox, T. P. Sakmar, M. Sheves, S. O. Smith, 6-*s-cis* Conformation and polar binding pocket of the retinal chromophore in the photoactivated state of rhodopsin. *J. Am. Chem. Soc.* **131**, 15160–15169 (2009).
  32. J. Mao, V. Aladin, X. Jin, A. J. Leeder, L. J. Brown, R. C. D. Brown, X. He, B. Corzilius, C. Glaubitz, Exploring protein structures by DNP-enhanced methyl solid-state NMR spectroscopy. *J. Am. Chem. Soc.* **141**, 19888–19901 (2019).
  33. Q. Z. Ni, E. Daviso, T. V. Can, E. Markhasin, S. K. Jawa, T. M. Swager, R. J. Temkin, J. Herzfeld, R. G. Griffin, High frequency dynamic nuclear polarization. *Acc. Chem. Res.* **46**, 1933–1941 (2013).
  34. M. L. Mak-Jurkauskas, V. S. Bajaj, M. K. Hornstein, M. Belenky, R. G. Griffin, J. Herzfeld, Energy transformations early in the bacteriorhodopsin photocycle revealed by DNP-enhanced solid-state NMR. *Proc. Natl. Acad. Sci. U.S.A.* **105**, 883–888 (2008).
  35. Q. Z. Ni, T. V. Can, E. Daviso, M. Belenky, R. G. Griffin, J. Herzfeld, Primary transfer step in the light-driven ion pump bacteriorhodopsin: An irreversible U-turn revealed by dynamic nuclear polarization-enhanced magic angle spinning NMR. *J. Am. Chem. Soc.* **140**, 4085–4091 (2018).
  36. J. Becker-Baldus, C. Bamann, K. Saxena, H. Gustmann, L. J. Brown, R. C. D. Brown, C. Reiter, E. Bamberg, J. Wachtveitl, H. Schwalbe, C. Glaubitz, Enlightening the photoactive site of channelrhodopsin-2 by DNP-enhanced solid-state NMR spectroscopy. *Proc. Natl. Acad. Sci. U.S.A.* **112**, 9896–9901 (2015).
  37. M. Mehler, C. E. Eckert, A. J. Leeder, J. Kaur, T. Fischer, N. Kubatova, L. J. Brown, R. C. D. Brown, J. Becker-Baldus, J. Wachtveitl, C. Glaubitz, Chromophore distortions in photointermediates of proteorhodopsin visualized by dynamic nuclear polarization-enhanced solid-state NMR. *J. Am. Chem. Soc.* **139**, 16143–16153 (2017).
  38. J. Maciejko, J. Kaur, J. Becker-Baldus, C. Glaubitz, Photocycle-dependent conformational changes in the proteorhodopsin cross-protoner Asp-His-Trp triad revealed by DNP-enhanced MAS-NMR. *Proc. Natl. Acad. Sci. U.S.A.* **116**, 8342–8349 (2019).
  39. J. Becker-Baldus, C. Glaubitz, Cryo-trapped intermediates of retinal proteins studied by DNP-enhanced MAS NMR spectroscopy. *Emagres* **7**, 79–91 (2018).
  40. M. Hohwy, H. J. Jakobsen, M. Edén, M. H. Levitt, N. C. Nielsen, Broadband dipolar recoupling in the nuclear magnetic resonance of rotating solids: A compensated C7 pulse sequence. *J. Chem. Phys.* **108**, 2686–2694 (1998).
  41. Q. Z. Ni, E. Markhasin, T. V. Can, B. Corzilius, K. O. Tan, A. B. Barnes, E. Daviso, Y. Su, J. Herzfeld, R. G. Griffin, Peptide and protein dynamics and low-temperature/DNP magic angle spinning NMR. *J. Phys. Chem. B* **121**, 4997–5006 (2017).
  42. M. Hong, Solid-state dipolar INADEQUATE NMR spectroscopy with a large double-quantum spectral width. *J. Magn. Reson.* **136**, 86–91 (1999).
  43. N. M. Szeverenyi, M. J. Sullivan, G. E. Maciel, Observation of spin exchange by two-dimensional fourier-transform <sup>13</sup>C cross polarization-magic-angle spinning. *J. Magn. Reson.* **47**, 462–475 (1982).
  44. Y. Inoue, Y. Tokito, S. Tomonoh, R. Chujo, Carbon-13 chemical-shifts of retinal isomers and their Schiff-bases as models of visual chromophores. *B. Chem. Soc. Jpn.* **52**, 265–266 (1979).
  45. K.-W. Wang, S.-W. Wang, Q.-Z. Du, Complete NMR assignment of retinal and its related compounds. *Magn. Reson. Chem.* **51**, 435–438 (2013).
  46. G. S. Harbison, S. O. Smith, J. A. Pardo, C. Winkel, J. Lugtenburg, J. Herzfeld, R. Mathies, R. G. Griffin, Dark-adapted bacteriorhodopsin contains 13-*cis*, 15-*syn* and all-*trans*, 15-*anti* retinal Schiff bases. *Proc. Natl. Acad. Sci. U.S.A.* **81**, 1706–1709 (1984).
  47. M. Concistre, O. G. Johannessen, N. McLean, P. H. Bovee-Geurts, R. C. Brown, W. J. Degrip, M. H. Levitt, A large geometric distortion in the first photointermediate of rhodopsin, determined by double-quantum solid-state NMR. *J. Biomol. NMR* **53**, 247–256 (2012).
  48. C. P. Jaronec, C. Filip, R. G. Griffin, 3D TEDOR NMR experiments for the simultaneous measurement of multiple carbon-nitrogen distances in uniformly <sup>13</sup>C, <sup>15</sup>N-labeled solids. *J. Am. Chem. Soc.* **124**, 10728–10742 (2002).
  49. V. S. Bajaj, M. L. Mak-Jurkauskas, M. Belenky, J. Herzfeld, R. G. Griffin, DNP enhanced frequency-selective TEDOR experiments in bacteriorhodopsin. *J. Magn. Reson.* **202**, 9–13 (2010).
  50. J. Hu, R. G. Griffin, J. Herzfeld, Synergy in the spectral tuning of retinal pigments: Complete accounting of the opsin shift in bacteriorhodopsin. *Proc. Natl. Acad. Sci. U.S.A.* **91**, 8880–8884 (1994).

51. J. G. Hu, R. G. Griffin, J. Herzfeld, Interactions between the protonated Schiff base and its counterion in the photointermediates of bacteriorhodopsin. *J. Am. Chem. Soc.* **119**, 9495–9498 (1997).
52. J. Pauli, M. Baldus, B. van Rossum, H. de Groot, H. Oschkinat, Backbone and side-chain <sup>13</sup>C and <sup>15</sup>N signal assignments of the  $\alpha$ -spectrin SH3 domain by magic angle spinning solid-state NMR at 17.6 tesla. *ChemBiochem* **2**, 272–281 (2001).
53. A. Maeda, S. P. Balashov, J. Lugtenburg, M. A. Verhoeven, J. Herzfeld, M. Belenky, R. B. Gennis, F. L. Tomson, T. G. Ebrey, Interaction of internal water molecules with the schiff base in the L intermediate of the bacteriorhodopsin photocycle. *Biochemistry* **41**, 3803–3809 (2002).
54. N. Mizuide, M. Shibata, N. Friedman, M. Sheves, M. Belenky, J. Herzfeld, H. Kandori, Structural changes in bacteriorhodopsin following retinal photoisomerization from the 13-cis form. *Biochemistry* **45**, 10674–10681 (2006).
55. Y. Furutani, Y. Sudo, A. Wada, M. Ito, K. Shimono, N. Kamo, H. Kandori, Assignment of the hydrogen-out-of-plane and -in-plane vibrations of the retinal chromophore in the K intermediate of *pharaonis* phoborhodopsin. *Biochemistry* **45**, 11836–11843 (2006).
56. S. Sharif, G. S. Denisov, M. D. Toney, H.-H. Limbach, NMR studies of coupled low- and high-barrier hydrogen bonds in pyridoxal-5'-phosphate model systems in polar solution. *J. Am. Chem. Soc.* **129**, 6313–6327 (2007).
57. G. S. Harbison, J. Herzfeld, R. G. Griffin, Solid-state nitrogen-15 nuclear magnetic resonance study of the Schiff base in bacteriorhodopsin. *Biochemistry* **22**, 1–5 (1983).
58. H. J. de Groot, G. S. Harbison, J. Herzfeld, R. G. Griffin, Nuclear magnetic resonance study of the Schiff base in bacteriorhodopsin: Counterion effects on the <sup>15</sup>N shift anisotropy. *Biochemistry* **28**, 3346–3353 (1989).
59. M. E. Hatcher, J. G. Hu, M. Belenky, P. Verdegem, J. Lugtenburg, R. G. Griffin, J. Herzfeld, Control of the pump cycle in bacteriorhodopsin: Mechanisms elucidated by solid-state NMR of the D85N mutant. *Biophys. J.* **82**, 1017–1029 (2002).
60. N. Pfeleger, A. C. Wörner, J. Yang, S. Shastri, U. A. Hellmich, L. Aslimovska, M. S. M. Maier, C. Glaubitz, Solid-state NMR and functional studies on proteorhodopsin. *Biochim. Biophys. Acta* **1787**, 697–705 (2009).
61. H. Yomoda, Y. Makino, Y. Tomonaga, T. Hidaka, I. Kawamura, T. Okitsu, A. Wada, Y. Sudo, A. Naito, Color-discriminating retinal configurations of sensory rhodopsin I by photo-irradiation solid-state NMR spectroscopy. *Angew. Chem. Int. Ed.* **53**, 6960–6964 (2014).
62. J. Jeon, W.-M. Yau, R. Tycko, Millisecond time-resolved solid-state NMR reveals a two-stage molecular mechanism for formation of complexes between calmodulin and a target peptide from myosin light chain kinase. *J. Am. Chem. Soc.* **142**, 21220–21232 (2020).
63. X. He, B. Wang, K. M. Merz Jr., Protein NMR chemical shift calculations based on the automated fragmentation QM/MM approach. *J. Phys. Chem. B* **113**, 10380–10388 (2009).
64. A. J. Leeder, L. J. Brown, J. Becker-Baldus, M. Mehler, C. Glaubitz, R. C. D. Brown, Synthesis of isotopically labeled all-trans retinals for DNP-enhanced solid-state NMR studies of retinylidene proteins. *J. Labelled Comp. Radiopharm.* **61**, 922–933 (2018).
65. C. Sauvée, M. Rosay, G. Casano, F. Aussenac, R. T. Weber, O. Ouari, P. Tordo, Highly efficient, water-soluble polarizing agents for dynamic nuclear polarization at high frequency. *Angew. Chem. Int. Ed.* **52**, 10858–10861 (2013).
66. J. Mao, N.-N. Do, F. Scholz, L. Reggie, M. Mehler, A. Lakatos, Y.-S. Ong, S. J. Ullrich, L. J. Brown, R. C. D. Brown, J. Becker-Baldus, J. Wachtveitl, C. Glaubitz, Structural basis of the green-blue color switching in proteorhodopsin as determined by NMR spectroscopy. *J. Am. Chem. Soc.* **136**, 17578–17590 (2014).
67. M. Bak, J. T. Rasmussen, N. C. Nielsen, SIMPSON: A general simulation program for solid-state NMR spectroscopy. *J. Magn. Reson.* **147**, 296–330 (2000).
68. F. A. Carey, R. J. Sundberg, *Advanced Organic Chemistry* (Springer, 5th ed, 2007), p. 2.
69. E. Henrich, J. Sörmann, P. Eberhardt, O. Peetz, J. Mezhyrova, N. Morgner, K. Fendler, V. Dötsch, J. Wachtveitl, F. Bernhard, C. Bamann, From gene to function: Cell-free electrophysiological and optical analysis of ion pumps in nanodiscs. *Biophys. J.* **113**, 1331–1341 (2017).
70. E. Vinogradov, P. K. Madhu, S. Vega, High-resolution proton solid-state NMR spectroscopy by phase-modulated Lee-Goldburg experiment. *Chem. Phys. Lett.* **314**, 443–450 (1999).

#### Acknowledgments

**Funding:** This work was funded by DFG/SFB807 “Transport and communications across membranes.” DNP experiments were enabled through an equipment grant provided by DFG (GL307/4-1) and Cluster of Excellence Macromolecular Complexes Frankfurt. **Author contributions:** O.J. prepared samples, performed all NMR experiments, carried out data analysis, prepared figures, and wrote the paper. P.E. performed optical spectroscopy, analyzed data, and contributed to discussion and interpretation. M.A. performed IR spectroscopy, analyzed data, and contributed to discussion and interpretation. J.K. and C.N.K. contributed to sample preparation and data interpretation. J.M. contributed to retinal synthesis and data interpretation. A.J.L., L.J.B., and R.C.D.B. synthesized retinal. J.B.-B. contributed to NMR spectroscopy and data interpretation. C.B. contributed to sample preparation and discussions. J.W. designed and supervised optical and IR experiments and contributed to data interpretation, discussion, and paper writing. C.G. designed and supervised the study, carried out data interpretation, prepared figures, and wrote the paper. **Competing interests:** The authors declare that they have no competing interests. **Data and materials availability:** All data needed to evaluate the conclusions in the paper are present in the paper and/or the Supplementary Materials. Additional data related to this paper may be requested from the authors.

Submitted 27 October 2020

Accepted 29 January 2021

Published 12 March 2021

10.1126/sciadv.abf4213

**Citation:** O. Jakdetchai, P. Eberhardt, M. Asido, J. Kaur, C. N. Kriebel, J. Mao, A. J. Leeder, L. J. Brown, R. C. D. Brown, J. Becker-Baldus, C. Bamann, J. Wachtveitl, C. Glaubitz, Probing the photointermediates of light-driven sodium ion pump KR2 by DNP-enhanced solid-state NMR. *Sci. Adv.* **7**, eabf4213 (2021).

## Probing the photointermediates of light-driven sodium ion pump KR2 by DNP-enhanced solid-state NMR

Orawan JakdetchaiPeter EberhardtMarvin AsidoJagdeep KaurClara Nassrin KriebelJiafei MaoAlexander J. LeederLynda J. BrownRichard C. D. BrownJohanna Becker-BaldusChristian BamannJosef WachtveitlClemens Glaubitz

*Sci. Adv.*, 7 (11), eabf4213. • DOI: 10.1126/sciadv.abf4213

### View the article online

<https://www.science.org/doi/10.1126/sciadv.abf4213>

### Permissions

<https://www.science.org/help/reprints-and-permissions>

Use of this article is subject to the [Terms of service](#)

---

*Science Advances* (ISSN 2375-2548) is published by the American Association for the Advancement of Science, 1200 New York Avenue NW, Washington, DC 20005. The title *Science Advances* is a registered trademark of AAAS. Copyright © 2021 The Authors, some rights reserved; exclusive licensee American Association for the Advancement of Science. No claim to original U.S. Government Works. Distributed under a Creative Commons Attribution NonCommercial License 4.0 (CC BY-NC).

Chapter 6 Publications

6.7 Krüger *et al.*, *Comm. Mat.*, 2022

**Sensitizer-enhanced two-photon patterning of biomolecules in photoinstructive hydrogels**

H. Krüger, M. Asido, J. Wachtveitl, R. Tampé and R. Wieneke,  
*Comm. Mat.*, 2022, 3.

## Sensitizer-enhanced two-photon patterning of biomolecules in photoinstructive hydrogels

Heike Krüger<sup>1</sup>, Marvin Asido <sup>2</sup>, Josef Wachtveitl <sup>2</sup>, Robert Tampé <sup>1</sup> & Ralph Wieneke <sup>1</sup>✉

Photoresponsive hydrogels can be employed to coordinate the organization of proteins in three dimensions (3D) and thus to spatiotemporally control their physiochemical properties by light. However, reversible and user-defined tethering of proteins and protein complexes to biomaterials pose a considerable challenge as this is a cumbersome process, which, in many cases, does not support the precise localization of biomolecules in the z direction. Here, we report on the 3D patterning of proteins with polyhistidine tags based on in-situ two-photon lithography. By exploiting a two-photon activatable multivalent chelator head, we established the protein mounting of hydrogels with micrometer precision. In the presence of photosensitizers, a substantially enhanced two-photon activation of the developed tool inside hydrogels was detected, enabling the user-defined 3D protein immobilization in hydrogels with high specificity, micrometer-scale precision, and under mild light doses. Our protein-binding strategy allows the patterning of a wide variety of proteins and offers the possibility to dynamically modify the biofunctional properties of materials at defined subvolumes in 3D.

<sup>1</sup>Institute of Biochemistry, Biocenter, Goethe University Frankfurt, Max-von-Laue-Str. 9, 60438 Frankfurt a.M., Germany. <sup>2</sup>Institute of Physical and Theoretical Chemistry, Goethe University Frankfurt, Max-von-Laue-Str. 7, 60438 Frankfurt a.M., Germany. ✉email: [wieneke@em.uni-frankfurt.de](mailto:wieneke@em.uni-frankfurt.de)

Photoresponsive materials benefit from the inherent spatiotemporal control of light to generate sophisticated microstructures<sup>1,2</sup>. Photoinstructive hydrogels are very promising scaffolds as they offer contact-free remote control of the (bio)physical or (bio)chemical properties by light actuation<sup>3–7</sup>. Photoresponsive gels have been developed based on photoisomerization<sup>8–10</sup>, photoclick chemistry<sup>11–17</sup>, or photolabile protecting groups<sup>18–22</sup> in order to modulate their microenvironment by light. Via a contactless mode of action, light allows minute spatial modifications in 2D and 3D as well as temporal control over material features. Applications of photoinstructive hydrogels range from site-specific therapeutic delivery and biosensors to synthetic cell culture platforms for tissue engineering<sup>2,23,24</sup>. An exciting perspective for protein organization is based on two-photon (2P) patterning techniques<sup>25,26</sup>. By utilizing femtosecond (fs) pulsed near-infrared (NIR) laser sources, photoreactions can be confined to the focal plane, improving the z resolution to 2–3  $\mu\text{m}$ . Currently, there is considerable interest in using protein-functionalized hydrogels in the context of 3D smart materials, biosensors, and drug delivery systems<sup>27–30</sup>. Natural and engineered proteins offer a diverse set of biochemical characteristics and properties. Their integration as biofunctional components into synthetic hydrogel networks is an attractive approach to modulate material features. For instance, hydrogels harboring proteins such as antibodies or enzymes were engineered to change hydrogel properties in response to specific triggers<sup>31–33</sup>. Here, protein arrangement via 2P-patterning of hydrogels facilitates a 3D control over the topography of a photoresponsive material, enabling the creation of hydrogels into more complex 3D devices. In addition, 3D protein immobilization permits a high (bio)specificity over subvolumes of the gel and hence a volumetric control of the response. However, the design and establishment of photoinstructive hydrogels that allow for in-situ protein immobilization are required to dynamically tune the material properties. Due to the lack of selectivity, reversibility, and uniform orientation of protein assembly, 3D protein grafting is far from reaching broad applicability. In particular, the orientation, homogeneity, and stability of proteins immobilized in photoresponsive matrices play a vital role in governing their biochemical properties. Efforts to pattern proteins by 2P-processes are frequently affected by the chemical cross-linking reactions for hydrogel formation, which often involves free radicals, or unspecific bioconjugation resulting in random protein orientation<sup>17,22,34</sup>. There are only few examples regarding a 3D organization of biomolecules, many of them restricted to synthetic peptides or small molecules<sup>15,18,21,22,35,36</sup>. Recently, the site-specific patterning of functional proteins by light was achieved via oxime ligation<sup>37</sup> and chemoenzymatic strategies<sup>38–40</sup>. Regarding high-precision structuring, advancements in the 2P-patterning specificity and sensitivity at very low laser power are crucial. To overcome these restrictions, generic procedures are required that take advantage of high-affinity protein binders amenable to 2P-patterning of functional proteins in hydrogels.

Here, we developed an optochemical tool based on autoinhibition and photoactivation of multivalent *N*-nitrilotriacetic acid (*tris*NTA)<sup>41,42</sup>. After UV illumination, the photoliberated *tris*NTA site-specifically binds His<sub>6–10</sub>-tagged proteins with (sub)nanomolar affinity ( $K_D = 0.1–10$  nM, PBS-TE buffer, pH 7.4, 25 °C)<sup>43</sup>. The ultra-small tag-size combined with the high-affinity binding of His-tagged proteins allow for the direct and oriented immobilization of functional proteins<sup>44</sup>. In addition, *tris*NTA offers kinetically stable binding ( $k_{\text{off}} = 0.18$  h<sup>-1</sup>, HBS buffer, pH 7.5, 25 °C) but remains fully reversible in the presence of imidazole, histidine, or EDTA<sup>45</sup>. Of note, this strategy relies on noncovalent protein

association that is less stable compared to covalent protein immobilization<sup>37–40</sup>. In live-cell applications, the long-term stability of the *tris*NTA/His-tag interaction can be affected by the utilized cell media, especially when high histidine concentrations (>200  $\mu\text{M}$ ) are present. Nevertheless, the high-affinity *tris*NTA/His-tag complex formation was successfully exploited in live-cell applications such as in-cell protein labeling, live-cell super-resolution microscopy, or 2D in-situ receptor confinement at single-cell level, demonstrating applicability and sufficient persistence of the interaction pair under cell culture conditions<sup>46–48</sup>.

To conceive a versatile strategy for 3D protein assembly by high-affinity tools, we engineered photoinstructive hydrogels, equipped with a two-photon-activatable *tris*NTA (TPA-*tris*NTA) for precise protein organization by 2P laser lithography. By facile addition of 2P-sensitizers, we significantly enhanced the 2P photocleavage of TPA-*tris*NTA regarding efficient protein alignment at low laser power. The improved photoactivation efficacy facilitated the user-defined and site-specific photopatterning of proteins in hydrogels with exquisite control over 3D localization, culminating in high-resolution volumetric structures in multiple z dimensions and 1  $\mu\text{m}$  thin features in x/y dimension. In addition, subcellular protein deposition in close proximity to single cells is demonstrated, providing basic cell applicability.

## Results and discussion

### Design of a two-photon activatable tool for photopatterning.

The design of TPA-*tris*NTA and its functional mechanism is based on the autoinhibition of the multivalent chelator head *tris*NTA, which is connected via a peptide linker to an intramolecular His<sub>5</sub>-tag (Fig. 1). In presence of Ni(II) ions, the *tris*NTA head group is self-inhibited by forming an intramolecular complex (OFF-state). By incorporating a photocleavable amino acid, the inactivating histidines were released upon illumination thereby liberating the *tris*NTA (ON-state). Due to the high affinity of the *tris*NTA for His<sub>6–10</sub>-tagged proteins, the cleaved-off His<sub>5</sub>-tag is competed out and a stable complex with the protein of interest (POI) is formed. As a result, TPA-*tris*NTA functionalized matrices are able to immobilize any His-tagged POI with defined orientation after illumination (TRAPPED-state).

For rapid assembly of TPA-*tris*NTA, we employed fluorenylmethoxycarbonyl (Fmoc) solid-phase peptide synthesis (SPPS). To achieve photoactivation of *tris*NTA by UV and NIR-light, the optochemical tool was strategically equipped with a 7-diethylaminocoumarin (DEAC)-based  $\beta$ -amino acid<sup>49</sup>. DEAC provides beneficial features e.g., small size, biocompatibility, a strong absorption maximum at 390–400 nm ( $\epsilon = 20,000$  M<sup>-1</sup> cm<sup>-1</sup>), a photolysis quantum yield of up to 0.3 as well as two-photon uncaging properties (Supplementary Fig. 1). A short ethylenediamine carbamate linker was installed, since carbamate protected photocages showed superior light responsiveness and resistance to hydrolysis within hydrogel microenvironments<sup>50</sup>. To allow hydrogel immobilization, a cysteine residue was included close to the *N*-terminus. After a six-step synthesis, the DEAC-based  $\beta$ -amino acid was integrated via SPPS into the backbone of TPA-*tris*NTA (Supplementary Methods 1.1, Supplementary Methods 1.2, Supplementary Fig. 2) and identified after RP-C<sub>18</sub>-HPLC purification by mass spectrometry (Supplementary Fig. 3, Supplementary Fig. 4).

**Photophysical properties of TPA-*tris*NTA.** First, we measured the one-photon absorption and fluorescence spectra of TPA-*tris*NTA as well as DEAC  $\beta$ -amino acid in HBS buffer/MeCN (1:1) (Fig. 2a, Supplementary Methods 1.4, Supplementary Fig. 5). Both compounds displayed an intense absorption band located around 390 nm and a strong fluorescence emission with a

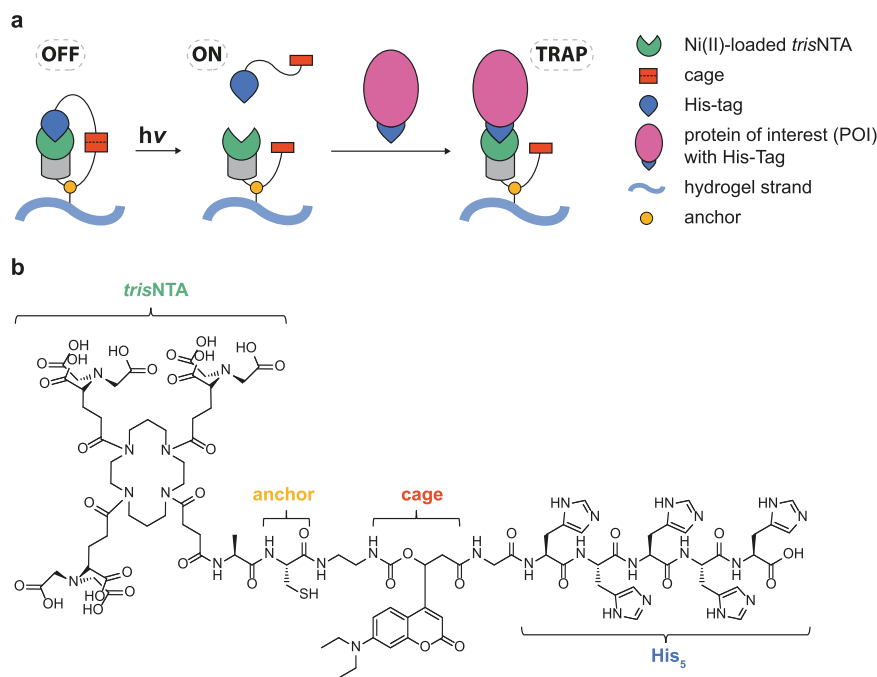


**Fig. 1** Concept and chemical structure of a two-photon activatable *tris*NTA interaction molecule. **a** Schematic illustration of the autoinhibition (OFF) and light-activation (ON) of TPA-*tris*NTA with subsequent trapping of His-tagged POIs. **b** Design of TPA-*tris*NTA. The interaction molecule consists of the *tris*NTA head group and an intramolecular His<sub>5</sub>-tag at the C-terminus. For 2P photocleavage, a DEAC-based  $\beta$ -amino acid is strategically incorporated within the linker. A single cysteine is used as an anchor for hydrogel immobilization.

maximum around 480 nm. The absorption profile of TPA-*tris*NTA compared to the spectrum of the DEAC  $\beta$ -amino acid shows that the light absorbing properties are unaffected.

Next, we verified the one-photon uncaging kinetics of the DEAC-based  $\beta$ -amino acid as a model system upon photolysis. Therefore, the model peptide was illuminated using a 405 nm LED lamp (185 mW/cm<sup>2</sup>) with increasing light doses (5–900 s) and analyzed by RP-C<sub>18</sub>-HPLC (Supplementary Fig. 6). The photocleavage of the  $\beta$ -amino acid followed a mono-exponential decay with simultaneous mono-exponential formation of the uncaged product, documenting a fast photoactivation ( $t_{1/2} = 12$  s) under one-photon photolysis conditions (Fig. 2b).

To evaluate the photophysical properties of TPA-*tris*NTA, the 2P absorption action cross sections ( $\varphi_F \sigma_2$ ) were determined by 2P-excited fluorescence (TPEF) and given in units of Goeppert-Mayer (GM). Within the excitation range from 770 to 860 nm, we determined  $\varphi_F \sigma_2$  values of 7.1 GM at 800 nm and 7.7 GM at 810 nm for TPA-*tris*NTA (Fig. 2c), which were consistent with reported values of DEAC-caged compounds<sup>51</sup>. The fluorescence quantum yield  $\varphi_F$  of TPA-*tris*NTA was determined to be 15% (Supplementary Methods 1.5, Supplementary Fig. 7). To examine the 2P-activation, we tested the power dependent 2P absorption of TPA-*tris*NTA at 800 nm by varying the excitation energies from 20 to 100 mW (Fig. 2d). The double-logarithmical dependence of excitation energy *versus* fluorescence intensity of  $1.93 \pm 0.02$  reflects an almost perfect quadratic power dependency (Fig. 2e) and confirms a 2P-activation process. These results demonstrate that TPA-*tris*NTA undergoes a fast one-photon photocleavage and can be activated by two-photon excitation.

**Photoinstructive matrices for 3D protein assembly.** To advance 3D protein assembly, we engineered 2P-photoinstructive hydrogels. TPA-*tris*NTA was coupled to a maleimide polyvinyl alcohol (PVA) precursor (Supplementary Fig. 8) and immediately

cross-linked with a dithiol polyethylene glycol (PEG). We investigated the global one-photon activation of TPA-*tris*NTA in hydrogels (Fig. 3a) using mask-patterning (405 nm LED lamp, 185 mW/cm<sup>2</sup>, 1 min). Visualization of the illuminated areas was realized by binding of GFP-His<sub>6</sub> (300 nM) followed by confocal laser-scanning microscopy (CLSM) (Fig. 3b). GFP-His<sub>6</sub> was exclusively assembled in photoactivated areas with excellent signal-to-noise ratio, highlighting the specificity of the *tris*NTA/His-tag interaction. Patterning occurred in 3D with a penetration depth of 100  $\mu$ m into the scaffold. Although mask lithography offers only limited spatial resolution, the rapid structuring of large areas with well-defined bulk hydrogel properties can be realized. In contrast, laser lithography allows to photostructure hydrogels with high spatial flexibility over protein assembly (Fig. 3c). We therefore exploited laser-scanning activation of TPA-*tris*NTA in a spatially defined region-of-interest (ROI: heart) using either UV light (405 nm) or focused NIR fs-laser pulses at 800 nm. ROI visualization was followed by binding of a fluorescent His<sub>6</sub>-peptide (His<sub>6</sub>-AF647). In both cases, a localized photoreaction proximal to the focal point in *x/y* direction was observed. In the focal plane, however, a well-defined photoactivation and thus protein assembly was received for 2P-patterning compared to UV activation. Analyzing the protein patterning in *z* direction illustrated the improved 3D resolution for the photoreaction. Via 2P-activation processes, a localized and precise activation of TPA-*tris*NTA and thus POI alignment in *z* direction was accomplished, which is proven by a sharp image in the focal plane and a *z* resolution of  $\sim 10$   $\mu$ m. In contrast, conventional laser-scanning lithography resulted in a conical shape of protein alignment and a *z* resolution  $> 40$   $\mu$ m. Owing to photoreactions initiated above and below the focal plane, partial protein assembly throughout the beam path is induced by 1P activation. This verifies that focused 2P-activation of TPA-*tris*NTA allows the accurate design of volumetric structures in hydrogels in 3D.

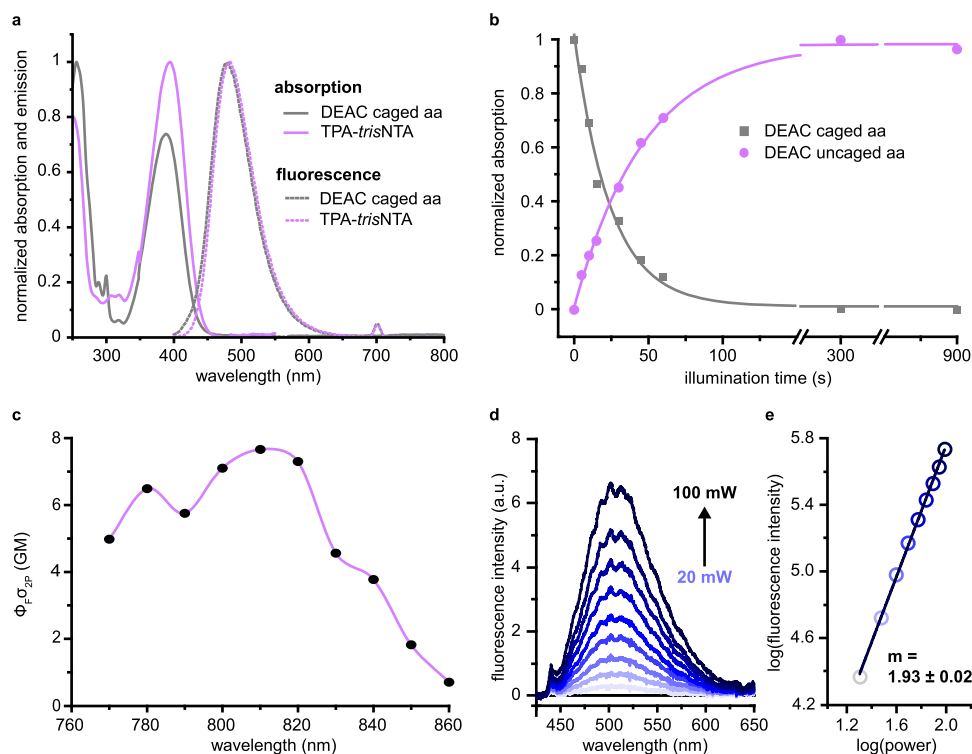


**Fig. 2 Photophysical properties of TPA-trisNTA.** **a** Normalized absorption and fluorescence spectra of DEAC  $\beta$ -amino acid and TPA-trisNTA in HBS buffer/MeCN (1:1, v/v). **b** Quantification of photocleavage showed the disappearance of DEAC  $\beta$ -amino acid and formation of the uncaged product as a function of illumination time at 405 nm. **c** Two-photon absorption cross section values of GM ( $\Phi_{T\sigma_{2P}}$ ) for TPA-trisNTA determined by two-photon excited fluorescence measurement and referenced to values of coumarin 307. **d** Power-dependent fluorescence spectra upon two-photon excitation of TPA-trisNTA at an excitation wavelength of 800 nm. **e** Intensities of the power dependent fluorescence spectra of TPA-trisNTA were logarithmically plotted against the logarithm of the power. The parameter for two-photon power dependency was found to be  $1.93 \pm 0.02$ , confirming a two-photon process for TPA-trisNTA activation at 800 nm.

**In-gel photoevolution of TPA-trisNTA.** The precise 2P-patterning of proteins within hydrogels and the very sensitive TPA-trisNTA photochemistry was further explored in terms of wavelength-selective activation and resolution in 3D. To examine the in-gel excitation profile of TPA-trisNTA, we tested activation wavelengths ranging from 720 to 800 nm with 20 nm increments and a constant laser power of 5 mW (Fig. 4a). After binding of His<sub>6</sub>-AF647, the fluorescence intensities of the activated ROIs were visualized by CLSM. Assessed by an intensity profile through the focal plane, the photocleavage of TPA-trisNTA increases gradually to the wavelength increment with the strongest TPA-trisNTA photoactivation at 800 nm. This result is in good agreement with the 2P absorption profile determined in solution (Fig. 2c).

The smallest scale of possible features in ROIs relies on the resolution of the scanning process. To determine the minimal patterning area in x/y dimension, we wrote six quadratic ROIs of decreasing size (50, 25, 12, 6, 3, and 2  $\mu$ m) by utilizing 800 nm for TPA-trisNTA photoactivation (Fig. 4b). Photopatterns were again visualized via immobilization of His<sub>6</sub>-AF647 followed by CLSM. Even the 2  $\mu$ m ROI could precisely be written into the hydrogel. However, the intensity profile of the ROIs revealed a diminished fluorescence intensity of the 2  $\mu$ m ROI compared to the 3  $\mu$ m or larger ROIs. Under these 2P-patterning conditions, the minimal ROI size is between 2 and 3  $\mu$ m and can be locally specified with single-digit micrometer precision in the hydrogel.

We next determined the x/y resolution of the writing process and thus the ability of our approach to discern individual diffraction-limited spots. Therefore, varying sets of four adjacent quadratic ROIs (5  $\mu$ m) were written into the hydrogel with

successively decreased spacing between the squares (Fig. 4c). Whereas photopatterns with an inter-ROI distance of 1  $\mu$ m or larger were clearly distinguishable, shorter ROI-spacing resulted in fuzzy and barely discriminable photopatterned areas. The shorter-spaced ROIs could no longer be spatially classified into individual patterns, indicating that an inter-ROI distance of 1  $\mu$ m or larger is required for accurate photopatterning.

The major advantage of 2P-excitation is the precise control of activation in z dimension. To demonstrate a defined 3D protein organization, circular ROIs at different z locations and 10  $\mu$ m distance to each other, were photostructured into the TPA-trisNTA-functionalized hydrogel (Fig. 4d). In x/y- as well as in z dimension a homogenous and spatially defined protein arrangement was detected by CLSM. The intensity profiles along the z axis showed distinct and clearly distinguishable photopatterned regions, further highlighting the 3D precision of the 2P-writing process. A z resolution of  $5 \pm 1 \mu$ m (FWHM) was determined for the 2P-activation process, which is in good agreement with typically observed z resolutions. A major difference of the trisNTA-His-tag system compared to other covalent 2P-patterning strategies is its reversibility<sup>42</sup>. For orthogonal detachment of the POI, the hydrogel was thus exposed to 500 mM imidazole. CLSM imaging before and after treatment revealed a rapid release of the immobilized His-tagged POI (Supplementary Methods 1.6, Supplementary Fig. 9). Pattern recovery was readily facilitated by immobilization of another His-tagged POI, permitting write-read-erase applications as well as enable repetitive cycles of protein patterning and release. We also assessed the long-term stability and persistence of the photopatterns. Remarkably, imaging the written ROIs ten days after 2P-structuring



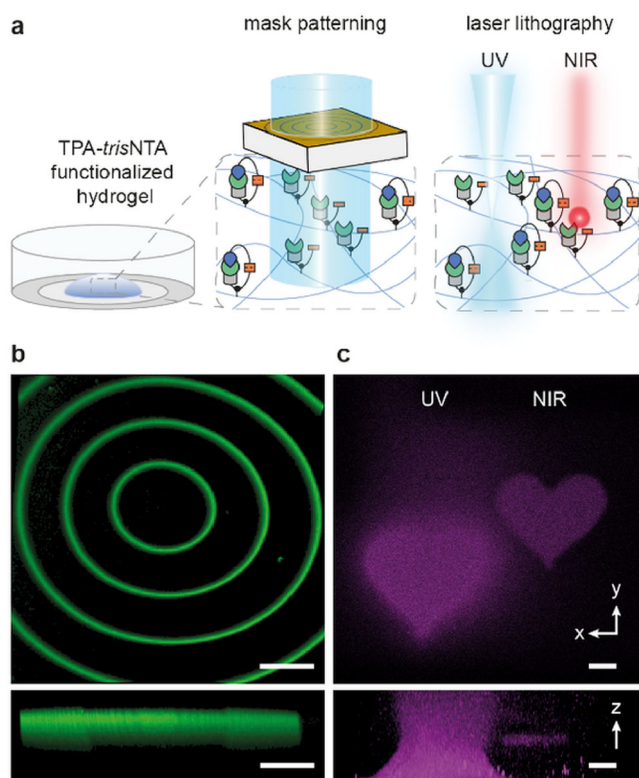


**Fig. 3 In-situ protein assembly in 3D by one- and two-photon excitation.**

**a** Schematic illustration of photoactivation in hydrogels by mask patterning or laser lithography using UV or NIR light. **b** Mask patterning of circular structures using a 405 nm UV/LED system ( $185 \text{ mW/cm}^2$  for 60 s) showed a very good contrast between illuminated and non-illuminated areas (top). Photopatterning occurred in three dimensions with a penetration depth of  $100 \mu\text{m}$  and uniform organization of GFP-His<sub>6</sub> (bottom). 3D structures were visualized by immobilization of GFP-His<sub>6</sub>, and images were reconstructed from a series of z stacks. Scale bars:  $100 \mu\text{m}$ . **c** In-situ laser lithography of TPA-trisNTA and assembly of AF647-labeled His-tagged POI within heart-shaped ROIs via one-photon excitation at 405 nm ( $4.5 \text{ mW}$ ) or two-photon excitation at 800 nm ( $5.5 \text{ mW}$ ). One-photon activation occurred primarily proximal to the focal plane with vicinal photoactivation of TPA-trisNTA above and below the focal plane, resulting in a conical shape of POI alignment in the gel. Two-photon excitation of TPA-trisNTA led to a sharp and precise POI assembly in x/y direction and localized activation in z dimension, accentuating the superior control over photoactivation and subsequently over protein organization. 3D images were reconstructed after collecting a series of z stacks by CLSM recording. Scale bars:  $20 \mu\text{m}$ .

showed that the gel was still decorated with the POI. After this prolonged time, a fivefold decreased fluorescence intensity was observed (Supplementary Methods 1.7, Supplementary Fig. 10). All images were taken in HBS buffer pH 7.2 at  $25^\circ\text{C}$ . On day 10, fresh HBS buffer pH 7.2 was added before imaging the ROI. Important to note, cell culture media may affect the kinetic complex stability and thus critically reduce the long-term stability of the trisNTA/His-tag interaction, particularly when histidine-rich buffers will be utilized. Overall, the modularity and reversibility of TPA-trisNTA offers iterative tethering and replacement of proteins as well as regeneration of hydrogels.

**Photosensitizers amplify the two-photon patterning.** Encouraged by these results, we aimed to improve the photoactivation efficacy and sensitivity of TPA-trisNTA under 2P-excitation. By

acting as auxiliary chromophore, 2P active fluorophores efficiently absorb NIR light and transfer the absorbed energy to acceptor photocages to enhance photolysis. Although a covalent tandem system for intramolecular energy transfer is more efficient and provides an acceptor-donor ratio of 1:1, we strived for a bimolecular sensitization through diffusive encounter<sup>52,53</sup>. Hence, we investigated the effect of the 2P active fluorophores ATTO390 and rhodamine B (RB) during the 2P-patterning process. Both fluorophores have large 2P absorption cross sections (ATTO390: 14 GM; RB: 150 GM) and are fully biocompatible, which is important for cell applications<sup>53,54</sup>. By writing a matrix of 20 quadratic ROIs in the hydrogel, we systematically modified the light dose of the 800 nm laser ( $0.5\text{--}5.5 \text{ mW}$  or  $0.3\text{--}2.2\%$  laser power *versus*  $6\text{--}30 \text{ s}$  illumination time) (Fig. 5a). For quantification, the fluorescence intensities emanating from the entire activated volume (voxel) of each ROI were analyzed. During writing, the TPA-trisNTA functionalized hydrogels were exposed to distinct concentrations of ATTO390 ( $50, 100, \text{ and } 500 \mu\text{M}$ ) or RB ( $50 \text{ and } 100 \mu\text{M}$ ) or buffer. In total, 120 conditions were screened to systematically optimize the 2P accessibility of our optochemical tool as well as to establish robust protocols for arbitrary 2P protein patterning (Supplementary Fig. 11, Supplementary Fig. 12). For hydrogels immersed to HBS buffer, POI patterns were faintly visible below  $3.1 \text{ mW}$  at 18 s or  $1.5 \text{ mW}$  at 24 s, indicating that the photolysis of TPA-trisNTA occurred only to a minor degree. In contrast, hydrogels exposed to  $100 \mu\text{M}$  ATTO390 or  $50 \mu\text{M}$  RB and subjected to 2P-patterning showed a globally enhanced POI recruitment and thus 2P-activation of the optochemical tool (Fig. 5a, Supplementary Fig. 13, Supplementary Fig. 14). In case of  $50 \mu\text{M}$  RB, the onset of visibly detectable POI tethering was already displayed at a laser power of  $0.5 \text{ mW}$  at 18 s, whereas  $1.5 \text{ mW}$  at 6 s were required for  $100 \mu\text{M}$  ATTO390. Generally, the presence of  $50 \mu\text{M}$  RB induced a more efficient photolysis of TPA-trisNTA and thus enhanced 3D protein binding, which was expressed by increased fluorescence intensities as well as improved signal-to-noise ratio. For RB, even the lowest applied laser power effectually fostered protein patterning. In contrast, photostucturing in presence of  $50 \mu\text{M}$  ATTO390 resulted in no significant increase in POI tethering and thus photoactivation of TPA-trisNTA. At higher ATTO390 or RB concentration, quenching effects of the auxiliary chromophore need to be considered and can thus stall an efficient energy transfer to TPA-trisNTA. Moreover, at high light doses ( $5.5 \text{ mW}$ ; 30 s), a halo-effect exceeding the ROI boundary was observed, concomitant with a diminished fluorescence intensity within the spot compared to surrounding ROIs. This observation is indicative for a destruction of the hydrogel in the focal plane. Indeed, a dumbbell-shaped pattern was visible in the z stack of the CLSM image with depleted POI tethering in the focal plane (Fig. 5b). Depending on the photoactivation conditions, extended photopatterned areas in z direction were visible with out of focus and diffuse protein tethering. The deteriorated POI recruitment is most likely a result of plasma-mediated ablation in combination with enhanced light scattering, also corroborated by the intensity profiles along the z axis (Supplementary Methods 1.8, Supplementary Fig. 15)<sup>55,56</sup>. Destructive effects were further promoted in 2P-patterned hydrogels immersed to higher 2P fluorophore concentrations. Overall, hydrogels photostructured in the presence of  $100 \mu\text{M}$  ATTO390 and  $50 \mu\text{M}$  RB under  $3.1 \text{ mW}$  at 12 s showed boosted TPA-trisNTA photoactivation without significant photodestruction. Compared to untreated gels, TPA-trisNTA activation was enhanced 3.8-fold for ATTO390 and 15.6-fold for RB (Fig. 5c) with these settings. As a corollary, the laser power can be reduced up to tenfold ( $5.5\text{--}0.5 \text{ mW}$ ) during protein alignment to obtain efficient protein densities. In our endeavor to improve the photoactivation efficacy, the 2P

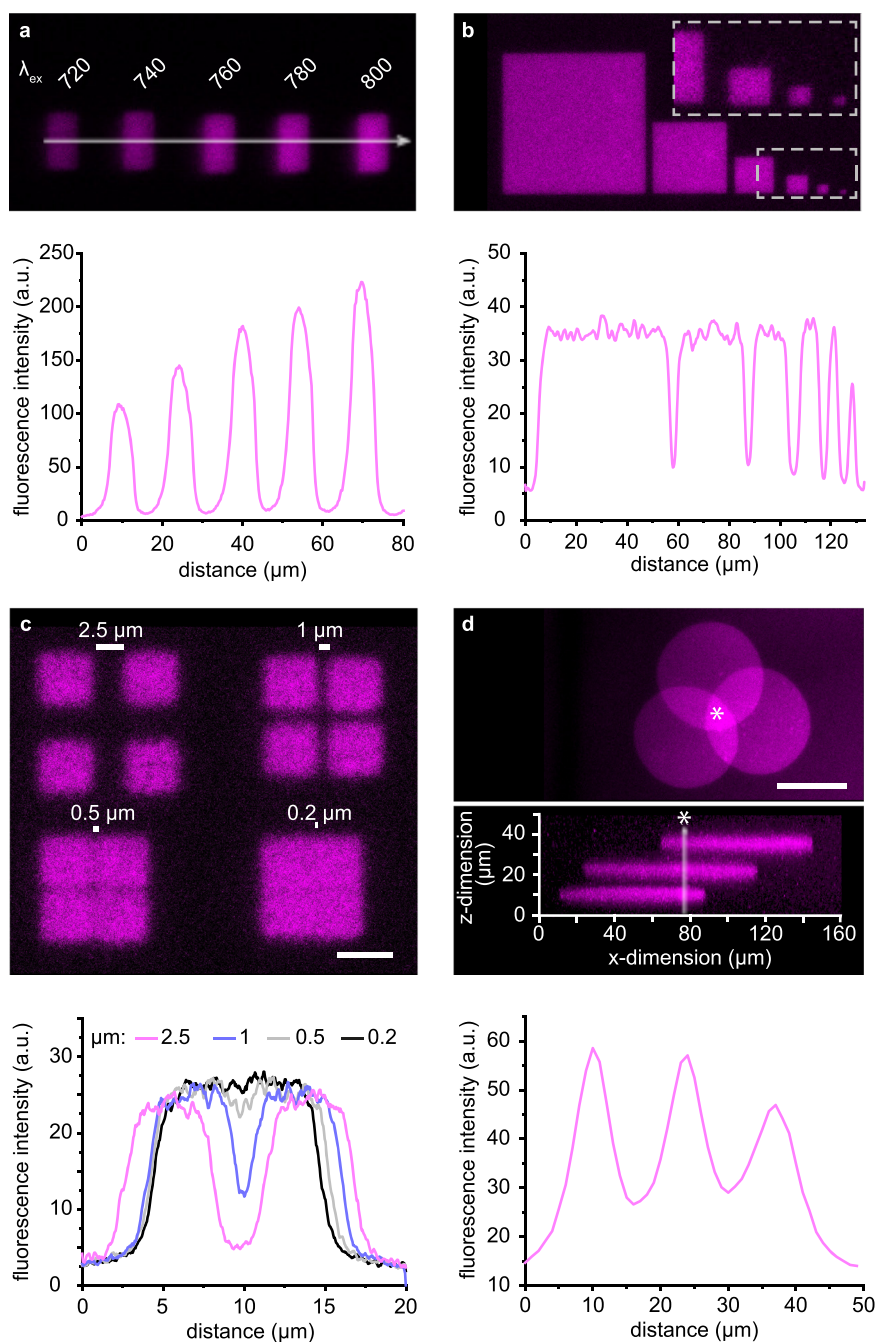


**Fig. 4 In-gel photoevolution of TPA-trisNTA under two-photon excitation.** **a** TPA-trisNTA functionalized hydrogel was activated with wavelengths from  $\lambda_{\text{ex}} = 720\text{--}800$  nm at 5 mW. Intensity profiles through the sum of  $z$  slices of immobilized AF647-POI showed the best photoactivation at 800 nm. For technical reasons, wavelengths higher than 800 nm are not applicable. **b** Assignment of the size limit for photostructuring in  $x/y$  dimension by writing six quadratic ROIs of decreasing size (50, 25, 12, 6, 3, and 2  $\mu\text{m}$ ) into the gel. Intensity profiles of the ROIs demonstrated constant fluorescence intensities heights in all ROIs except for the 2  $\mu\text{m}$ -ROI. **c** Determination of the resolution limit via two-photon structuring of four individual diffraction-limited squares in  $x/y$  direction. Spots separated by 1  $\mu\text{m}$  or more can be clearly distinguished by CLSM imaging, which is also reflected in the intensity profile. Scale bar: 5  $\mu\text{m}$ . **d** 3D POI network constructed by two-photon activation of TPA-trisNTA. Three circular spots were written in different  $z$  layers to investigate the  $z$  resolution. Intensity profiles of AF647-POI in  $z$  direction showed spatially localized photoactivation with clearly distinguishable edges of the three written ROIs. a.u. corresponds to arbitrary units. Scale bar: 50  $\mu\text{m}$ .

fluorophore sensitized photorelease of TPA-trisNTA simply advanced the 2P-writing process.

The high spatial positioning of biomolecules provided by light actuation constitutes photoinstructive hydrogels as powerful platforms for cellular applications. Hence, we tested the applicability of the TPA-trisNTA functionalized hydrogels for cell studies as well as the cytotoxicity of the 2P-sensitizers under

illumination conditions. To evaluate cell viability in gels, living HeLa cells were embedded within the TPA-trisNTA functionalized scaffold to form a cell-laden hydrogel. The encapsulated HeLa cells were assessed by annexin V staining to report on apoptotic cells (Supplementary Fig. 16). A very high cell viability ( $91 \pm 1\%$ ) was observed, confirming that cell embedding in the photoinstructive gel is non-toxic. Of note, Ni(II) ions complexed

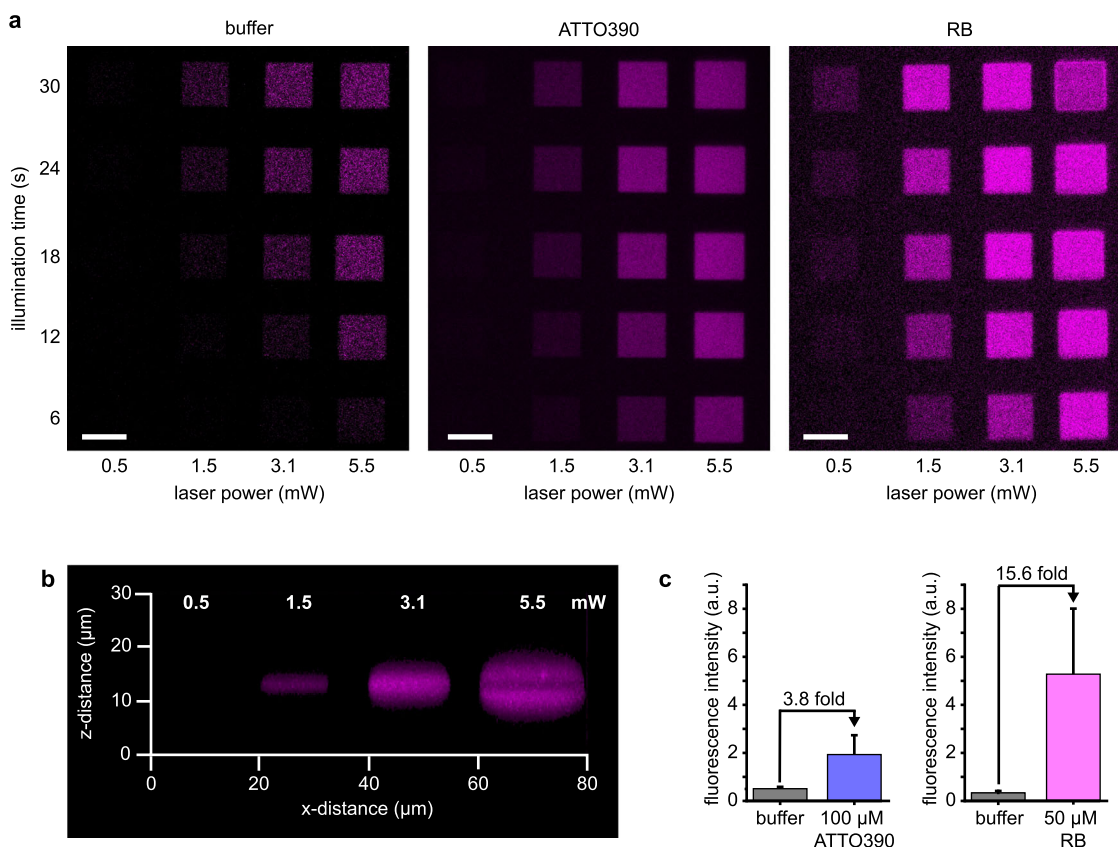


**Fig. 5 Sensitized two-photon laser lithography in photoinstructive matrices.** **a** TPA-*tris*NTA functionalized hydrogels were activated at 800 nm in the presence of HBS buffer, 100  $\mu$ M ATTO390 or 50  $\mu$ M RB with varying laser power and illumination time. With increased laser power or illumination time, an enhanced tethering of AF647-POI was observed, reporting on improved photoactivation of TPA-*tris*NTA. The presence of photosensitizers induced an intensified photoscission and consequently enriched POI binding. Scale bar: 15  $\mu$ m. **b** Orthogonal cross section (*x/z* direction) of ATTO390 soaked hydrogel and photoactivated with increasing laser power for 12 s. With elevated laser power, an expanded *z* depth of the activated area was observed, finally ending up in a dumbbell-shaped pattern due to plasma-mediated ablation. **c** Comparison the fluorescence intensity of ROIs illuminated with 3.1 mW and 12 s demonstrated enhanced photoactivation of the gels exposed to photosensitizers. For 100  $\mu$ M ATTO390, a 3.8-fold higher fluorescence intensity was detected compared to HBS buffer, and for a hydrogel photopatterned in presence of 50  $\mu$ M RB, a 15.6-fold increased fluorescence intensity was determined ( $n = 3$ ). a.u. corresponds to arbitrary units.

to *tris*NTA at concentrations up to 5  $\mu$ M exhibit no cytotoxic effects on cells<sup>46</sup>. To estimate the cytotoxicity of the 2P-sensitizers under illumination conditions, cells were exposed to increasing concentrations of either ATTO390 or RB and analyzed via a 3-(4,5-dimethylthiazol-2-yl)-2,5-diphenyltetrazolium bromide (MTT) assay (Supplementary Methods 1.12, Supplementary Fig. 17). Both enhancers showed no dark toxicity up to 100  $\mu$ M (ATTO390: >70% cell viability; RB: >90% cell viability). However, 500  $\mu$ M ATTO390 severely affected the cell viability, both in the non-illuminated and illuminated state. In contrast, 500  $\mu$ M RB hardly affected the cells at all (>70% cell viability). Hence, both sensitizers were cytocompatible at the optimized concentrations for laser lithography in the dark and particularly under light actuation. Even though these cell assays only partly demonstrate cell viability, we next aimed to prove general cell applicability of our photoinstructive matrices. First, mask patterning as well as in-situ lithography by one-photon illumination in presence of HeLa cells was performed. After mask patterning (405 nm LED lamp, 185 mW/cm<sup>2</sup>, 1 min) of a cell-laden hydrogel, tethering of His<sub>6</sub>-mCherry (300 nM) to distinct patterns and vicinity to living cells was realized. Visualization via CLSM showed the structuring of large areas with His<sub>6</sub>-POIs covering multiple cells (Supplementary Fig. 18). In addition, in-situ one-photon activation of a single cell stably expressing the G-protein coupled receptor Y2 equipped with an

external His<sub>6</sub>-tag as well as an autofluorescent protein (His<sub>6</sub>-Y<sub>2</sub>R<sup>mEGFP</sup>) was done after embedding in a photoinstructive matrix. A defined ROI (10  $\times$  20  $\mu$ m) covering a cell hemisphere was illuminated with 405 nm at 4.5 mW/cm<sup>2</sup> laser power and 200 s. The intensity profile of the GFP signal emanating from the Y2 receptor before and after illumination, illustrated the enrichment of the receptor to the light-exposed area and thus *tris*NTA mediated receptor assembly after photoactivation (Supplementary Fig. 19). Lastly, in-situ 2P-activation of a TPA-*tris*NTA functionalized hydrogel was performed in presence of live, intact HeLa cells. Various sized ROIs in vicinity to distinct single cells were simultaneously photo-patterned by 2P-scission of the optochemical tool at 800 nm (3.1 mW; 12 s) and subsequently decorated with His<sub>6</sub>-mCherry (300 nM). The precise, subcellular protein deposition at gel subvolumes in close proximity to living cells was accomplished, highlighting the applicability of the 2P-writing process via TPA-*tris*NTA in presence of live cells (Fig. 6, Supplementary Fig. 20). Here, we employed HeLa cells, which possess enhanced fitness and robustness toward external stimuli and are a widely used basic model for cell applications. Within the time frame of experiments (12 h), we did not observe any abnormal behavior of the cells after 2P-patterning, indicating basic cell compatibility. Since the studies were performed on single-cell level, they do not allow drawing conclusions of ensemble cell behavior yet. Although

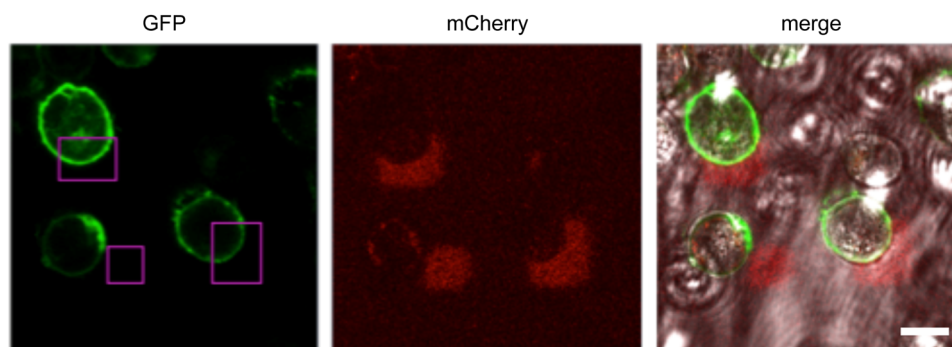


**Fig. 6 Subcellular protein patterning of a cell-laden, photoinstructive hydrogel by 2P laser lithography.** In close proximity to encapsulated HeLa cells stably expressing Y2R<sup>mEGFP</sup>, distinct ROIs (magenta boxes) were simultaneously photoactivated at 800 nm (3.1 mW, 18 s) and subsequently assembled with His<sub>6</sub>-mCherry (300 nM). Within the user-specified gel subvolumes, the 2P-activation of TPA-*tris*NTA created anchoring sites for the His<sub>6</sub>-POI in the photoinstructive hydrogel, demonstrating successful 2P-scission of TPA-*tris*NTA in presence of and close proximity to living cells. Scale bar: 10  $\mu$ m.

future studies are required to investigate long-term cell viability as well as to demonstrate the proof-of-principle with stem cells as model cell line, we believe that the results represent a valuable demonstration of the user-defined, spatially controlled protein patterning in cell-laden TPA-*tris*NTA functionalized hydrogels.

### 3D protein networks with single-digit micrometer precision.

Finally, we aimed to transfer the enhanced 2P-writing process to small-scale protein alignment at selected loci in hydrogels. Typically, 2P lithography is applied to write 3D patterns on the order of tens of microns (>100  $\mu$ m). While this scale is powerful for manipulating the behavior of larger cell networks or multicellular clusters, the ability of 2P-processes to in-situ modify hydrogels with micrometer-scale precision is underrepresented. To scrutinize TPA-*tris*NTA functionalized hydrogels on the order of a few microns in 3D, we created custom-made, spatially defined ROIs. Patterning was performed in the presence of 50  $\mu$ M RB at 800 nm (3.1 mW; 12 s). Upon locally defined photoactivation of the portrait of Maria Goeppert-Mayer in three distinct *z* planes, fluorescently labeled POI was site-selectively immobilized (Fig. 7). Remarkably, the enhanced 2P-activation facilitated the writing of complex 3D patterns, exhibiting feature sizes with micrometer precision (cheek of Maria Goeppert-Mayer: ~1  $\mu$ m) (Supplementary Fig. 21). The very good signal-to-background ratio between patterned and non-patterned areas is a result of the improved 2P lithography as well as high-affinity, site-selective binding of photoliberated *tris*NTA to His-tagged POI. With regard to fineness and precision of protein assembly in 3D, the TPA-*tris*NTA system extends the level of protein patterning as well as expands the repertoire of tools for protein immobilization. Noteworthy, the images were not background corrected and depict the genuine, current state. Important to mention, the apparent resolution of the imaging process is reduced compared to the precision of the writing process, since the observed resolution is a convolution of both processes. The microheterogeneity of the fluorescent signal in the different *x/y* planes depends on the efficiency of the 2P-uncaging process, which in turn is pre-determined by the density of tethered TPA-*tris*NTA. In *z* dimension, a continuous decrease of the POI density with increasing *z* depth to ~40–70  $\mu$ m was observed. Important to note, the penetration depth depends on both the laser intensity and the wavelength. Here, structuring was performed with a tenfold lower laser intensity compared to common 2P laser lithography approaches<sup>57</sup>. If required, additional depth can be achieved by increasing the laser power. Nevertheless, the 3D POI network of Maria Goeppert-Mayer clearly shows the power of 2P

lithography to pattern freely designed 3D structures at small-scale and with good *z* resolution.

### Conclusion

In summary, by incorporation of TPA-*tris*NTA into hydrogels, we engineered a photoinstructive matrix, which was successively photostructured by 2P laser lithography with various His-tagged POIs. NIR-light guided protein organization offered an exquisite control of protein alignment in 3D with submicron resolution, culminating in well-resolved structures particularly along the *z* coordinate. By facile addition of 2P-sensitizers (ATTO390 or RB) as diffuse encounter, we devised a proceeding to significantly improve the efficiency of 2P laser lithography. This approach contributed to considerably reduce the laser power for 2P lithography and was successfully applied to photopattern custom designed volumetric structures at small-scale in 3D. As the engineered photoinstructive matrix showed cell applicability, our approach will be extremely useful for the arrangement of more complex bioactive proteins into matrices by NIR-light. Since methods for hydrogel photopatterning of fragile full-length proteins are cumbersome and thus rare, the highly localized protein tethering via *tris*NTA/His-tag interaction opens up new perspectives for a reliable and flexible protein patterning within hydrogels. As an exciting application, we currently aim to confine membrane-associated receptors in 3D as well as to assemble signaling molecules at defined subvolumes around hydrogel-embedded cells, multicellular clusters or organoids.

### Methods

**Synthesis of TPA-*tris*NTA.** Fmoc-protected DEAC  $\beta$ -amino acid was synthesized in six steps and characterized by nuclear magnetic resonance (NMR) spectroscopy and high-resolution electrospray ionization mass spectrometry (HR ESI-MS). TPA-*tris*NTA (*tris*NTA-AC-DEAC-GHHHHH-OH) was synthesized through microwave-assisted Fmoc solid-phase methodology using the *Liberty Blue* microwave peptide synthesizer (CEM, Germany) and starting from a preloaded Fmoc-His(Trt)-Wang (Sigma Aldrich, Germany) resin. All reactions except for coupling of the Fmoc-protected DEAC  $\beta$ -amino acid (single coupling) were done twice with 0.2 M of Fmoc-protected amino acid, 0.5 M *N,N'*-diisopropylcarbodiimide, 0.5 M 1-hydroxybenzotriazole monohydrate in dimethylformamide (DMF). Fmoc-deprotection was performed with 20% (v/v) piperidine in DMF. *O*<sup>t</sup>Bu-protected carboxy-*tris*NTA was manually coupled on the N-terminal glycine using (1-cyano-2-ethoxy-2-oxoethylideneamino-oxo)dimethylamino-morpholino-carbenium-hexafluoro-phosphat (COMU) and *N,N*-diisopropylethylamine (DIPEA) in DMF. Peptide cleavage/deprotection was achieved using 95% trifluoroacetic acid (TFA), 2.5% H<sub>2</sub>O and 2.5% 1,2-ethanedithiol followed by two precipitation cycles (50 mL diethyl ether, 0 °C). The crude peptide was purified via preparative reverse-phase high-performance liquid chromatography (RP-C<sub>18</sub>-HPLC) using a 30 min gradient (5–70% of acetonitrile and 0.1% TFA in H<sub>2</sub>O) and lyophilized (Supplementary Methods 1.3, Supplementary Fig. 4). TPA-*tris*NTA purity was confirmed by HR ESI-MS. The complete synthetic details and characterization of TPA-*tris*NTA and Fmoc-

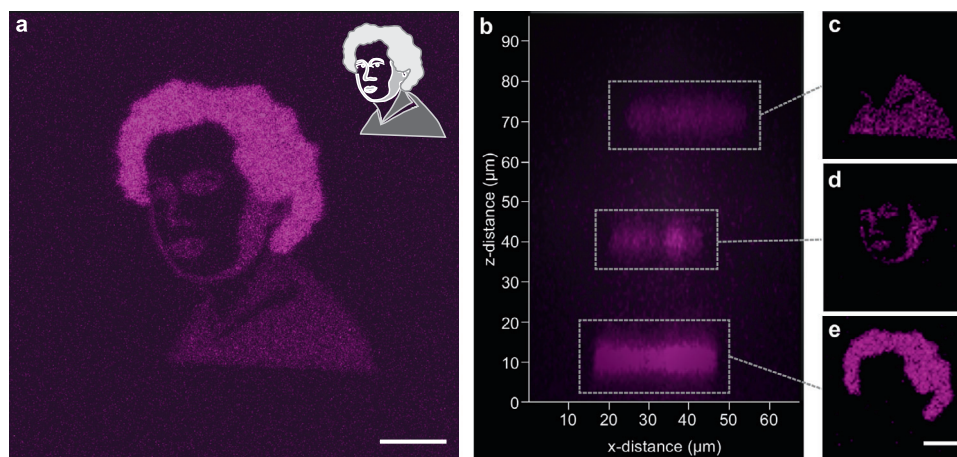


**Fig. 7 Two-photon induced 3D arbitrary patterns in a photoinactive TPA-trisNTA matrix.** **a** The portrait of Maria Goeppert-Mayer was printed by two-photon excitation (800 nm, 3.1 mW, 12 s; presence of 50  $\mu\text{M}$  RB) in three different z layers. Structures were visualized by assembly of AF647-POI followed by CLSM. The custom-made ROI design for laser activation is shown on the top right. **b** Orthogonal cross sections (x/z plane) of the two-photon patterned ROIs imaged by CLSM. Images displayed a sharp, spatially localized activation of TPA-trisNTA at  $\mu\text{m}$ -scale within multiple z layers and showed a confined immobilization of AF647-POI in z direction. **c–e** CLSM images show the respective focal plane (x,y) indicated by gray dashed lines. Scale bars: 10  $\mu\text{m}$ .

protected DEAC  $\beta$ -amino acid are given in the Supplementary Methods. For NMR and ESI spectra see Supplementary Figs. 22–36.

**Photolysis reaction of the DEAC  $\beta$ -amino acid in solution.** 50  $\mu\text{L}$  aliquots of a stock solution of Fmoc-protected DEAC  $\beta$ -amino acid in HBS buffer (20 mM HEPES/NaOH, 150 mM NaCl pH 7.2) were illuminated at 405 nm (185  $\text{mW}/\text{cm}^2$ , Thorlabs LED system). To study the kinetics of photolysis, samples were taken at different time points (0, 5, 10, 15, 30, 45, 60, 300, and 900 s). Photocleavage of Fmoc-protected DEAC  $\beta$ -amino acid was assessed by analytical RP-C<sub>18</sub>-HPLC (20 min gradient, 5–100% of acetonitrile and 0.1% TFA in H<sub>2</sub>O, Supplementary Methods 1.3, Supplementary Table 2), revealing conversion to uncaged DEAC  $\beta$ -amino acid with a different retention time (Supplementary Fig. 6). Photolysis efficiency was determined by evaluating the integral of the Fmoc-protected DEAC  $\beta$ -amino signal ( $t_{\text{R}} = 17.0$  min) as well as of the uncaged product ( $t_{\text{R}} = 12.0$  min). The photolysis kinetics were fitted with a mono-exponential function to determine the lifetime  $t_{1/2}$ , indicating a fast one-step photoconversion.

**Two-photon absorption spectrum of TPA-trisNTA.** Two-photon excitation fluorescence (TPEF) measurements were performed using a tunable Ti:Sa laser (Tsunami, Spectra-Physics, USA) with a pulse duration of 150 fs and a 80 MHz repetition rate. The TPEF-signal was coupled into a spectrograph (SpectraPro 300i, Acton Research Corp., USA), equipped with a CCD-camera (EEV 400\_1340F, Roper Scientific, USA). The excitation was adjusted to an average energy of 100 mW and the pulses were tightly focused on the sample compartment. The concentrations of the TPA-trisNTA and coumarin 307 were adjusted to 100  $\mu\text{M}$  in a final volume of 300  $\mu\text{L}$ . Coumarin 307 was used as reference, and values for calculation were taken from Xu et al.<sup>54</sup>. To obtain the two-photon absorption spectrum, the two-photon absorption action cross sections in the range of 770–870 nm were determined. After baseline and detector correction of the fluorescence spectra, the integrals were computed to obtain  $I_{\text{F}}(X)$  and  $I_{\text{F}}(R)$ . For calculations the following equation was used:

$$\phi_{\text{F}}(X)\sigma_2(X) = \sigma_2(R) \cdot \phi_{\text{F}}(R) \frac{I_{\text{F}}(X) \cdot c(R) \cdot \eta(R)}{I_{\text{F}}(R) \cdot c(X) \cdot \eta(X)}$$

with  $\sigma_2$  = two-photon absorption cross section,  $\phi_{\text{F}}$  = fluorescence quantum yield,  $X$  = TPA-trisNTA,  $R$  = coumarin 307,  $I_{\text{F}}$  = fluorescence intensity,  $c$  = concentration,  $\eta$  = refractive index of the solvent. The one-photon fluorescence quantum yield was assumed to equal the two-photon fluorescence quantum yield. The refractive indices of the samples (at 20  $^{\circ}\text{C}$ , Vis-NIR range) were determined to be  $\eta(R) = 1.33$  (in MeOH) and  $\eta(X) = 1.33$  (in H<sub>2</sub>O).

**Two-photon power dependency measurement of TPA-trisNTA.** To validate the two-photon absorption of TPA-trisNTA, a scan of the fluorescence intensity over a series of excitation energies (20–100 mW) was performed at a specific wavelength (800 nm). The count rate of the fluorescence response was logarithmically plotted against the logarithm of the excitation energy. A slope of  $1.93 \pm 0.02$  was obtained, implicating an almost quadratic power dependency of the two-photon response. According to Bradley et al. deviations from a strict quadratic power dependency can occur due to heating effects or competing non-linear processes<sup>58</sup>.

**Confocal imaging.** Imaging was performed using a confocal laser-scanning microscope (LSM 880 AxioObserver, Carl Zeiss Microscopy, Germany), and images were taken with the Plan-Apochromat 20x (NA 0.8) and/or the Plan-Apochromat 63x/Oil (NA 1.4) objective. The following laser lines were used for excitation: 405 nm (diode laser) for Hoechst33342; 488 nm (argon laser) for green fluorescent protein (GFP-His<sub>6</sub>); and 633 nm (helium-neon laser) for His<sub>6</sub>-AF647 and Annexin V-AF647. All probes were imaged in HBS buffer (20 mM HEPES/NaOH, 150 mM NaCl, pH 7.2, 25  $^{\circ}\text{C}$ ) or in case of live cells incorporated in the gel, the hydrogel was covered with Live Cell Imaging Solution (Invitrogen). The imaging process was controlled with the Zeiss Zen Black software. Image processing and evaluation was done with Fiji<sup>59</sup>.

**Formation of TPA-trisNTA functionalized hydrogels.** Gridded *ibidi* imaging dishes ( $\mu$ -Dish 35 mm, high Grid-500, *ibidi*, Germany) were used for hydrogel preparation. For protein photopatterning, hydrogels were prepared from a commercial slow gelling 3-D Life PVA-PEG Hydrogel Kit (Cellendes, Germany). Gel formation was performed by mixing 0.6  $\mu\text{L}$  HBS buffer pH 7.2 with 0.98  $\mu\text{L}$  H<sub>2</sub>O and 1.20  $\mu\text{L}$  maleimide-PVA (Supplementary Fig. 8). Then, 1.52  $\mu\text{L}$  of a 790  $\mu\text{M}$  TPA-trisNTA solution (aq.) was added and immediately mixed via pipetting and incubated for 5 min at RT in the dark. After a quick spin down, the reaction mixture was added to 1.74  $\mu\text{L}$  dithiol-linker placed in the middle of an *ibidi* imaging dish and quickly mixed by pipetting. The network formation was allowed to proceed for 10 min in the dark. The solidified hydrogel was equilibrated with 1 mL HBS buffer (20 mM HEPES/NaOH, 150 mM NaCl, pH 7.2, 25  $^{\circ}\text{C}$ ).

**Laser-assisted photopatterning in hydrogels.** For photostructuring by one- or two-photon excitation, a confocal laser-scanning microscope (LSM 880 AxioObserver, Carl Zeiss Microscopy, Germany) equipped with a Plan-Apochromat 63x/Oil (NA 1.4) objective, a 405 nm LED diode, and an ultrafast Ti:Sa Chameleon laser (Coherent Inc., Santa Clara, USA) with a pulse duration of 140 fs, a 80 MHz repetition rate and maximal output of 2.5 W tuned to 800 nm was employed for localized illumination. The user-defined ROI scanning mode and bleaching option were used to precisely control arbitrary patterns in 3D. The laser output power of the Ti:Sa Chameleon laser was precisely adjusted before each experiment to match 0.5, 1.5, 3.1 and 5.5 mW (corresponding to 0.3–0.7–1.2–2.2% of maximal laser power). The illumination time was 6, 12, 18, 24, or 30 s, equaling the sum of 500–2500 iterations. The scan speed was fixed at 1.54  $\mu\text{s}/\text{pixel}$ . Photoactivation of hydrogels was performed in HBS buffer (20 mM HEPES/NaOH, 150 mM NaCl, pH 7.2, 25  $^{\circ}\text{C}$ ). The illumination process was controlled with the Zeiss Zen Black software.

**TPA-trisNTA mediated POI immobilization to hydrogels in 3D.** Laser-treated hydrogels were washed five times with 2 mL HBS buffer (20 mM HEPES/NaOH, 150 mM NaCl, pH 7.2, 25  $^{\circ}\text{C}$ ) prior to His-tagged POI tethering. All steps were performed at room temperature and protected from light. For POI patterning, the gel was covered with 1 mL of 10 mM NiCl<sub>2</sub> in MQ water and incubated for 30 min followed by five times washing with HBS buffer (2 mL). Visualization of written structures was realized by incubation with 1 mL of 300 nM His<sub>6</sub>-GFP in HBS buffer or 300 nM His<sub>6</sub>-AF647 (HHHHHHSSGGGSGGGG-C<sup>AF647</sup>-A-NH<sub>2</sub>) in HBS buffer. After 30 min, the hydrogel was washed with HBS buffer (50 mL) by gently shaking

for 30 min. Finally, the hydrogel was covered with 1 mL HBS buffer and subsequently imaged via CLSM (LSM 880 AxioObserver, Carl Zeiss).

**Global photolithography of hydrogels.** For photopatterning of large areas, hydrogels were exposed to UV light ( $\lambda = 405$  nm LED lamp,  $185$  mW/cm<sup>2</sup>, 1 min) through a quartz mask with various sized chrome patterns on top of the gel. After illumination, the hydrogels were washed five times with HBS buffer (20 mM HEPES/NaOH, 150 mM NaCl, pH 7.2, 25 °C). POI binding and patterning was performed with His<sub>6</sub>-GFP after incubation with 10 mM NiCl<sub>2</sub> in MQ. POI assembly was visualized by CLSM (LSM 880 AxioObserver, Carl Zeiss).

**Cell viability assessed in cell-laden hydrogels.** To analyze cell viability throughout encapsulation in hydrogels, a live-cell annexin V staining was performed to report on apoptotic cells. HeLa Kyoto cells ( $1 \times 10^6$  cells/mL) were washed and suspended in 100  $\mu$ L annexin V binding buffer (Invitrogen). After adding 25  $\mu$ L of annexin V-AF647 conjugate (Invitrogen) and one drop of NucBlue Live Ready Probes (ThermoFisher), cells were incubated for 15 min at room temperature and then washed once again with annexin V binding buffer. For hydrogel encapsulation, 10  $\mu$ L of the HeLa cell suspension were mixed with 3.0  $\mu$ L HBS buffer (20 mM HEPES/NaOH, 150 mM NaCl, pH 7.2, 25 °C), 11.3  $\mu$ L H<sub>2</sub>O, 2.5  $\mu$ L maleimide-PVA, 0.8  $\mu$ L of a 20 mM TPA-*tris*NTA solution (aq.) and 3.0  $\mu$ L dithiol-linker (Supplementary Table 4). After mixing via pipetting, hydrogel network formation was allowed to proceed for 10 min, followed by covering with 1 mL Live Cell Imaging Solution (Invitrogen). Cell viability analysis was performed by CLSM (Supplementary Fig. 16). Hoechst33342 stained nuclei were excited with 405 nm diode laser and HeLa cells in an early apoptosis state were displayed via the AF647 signal of the annexin V-AF647 conjugate and excited with the 633 nm laser.  $708.5 \mu\text{m} \times 708.5 \mu\text{m}$  images were taken. The total amount of cells indicated by the Hoechst33342 signal and the number of AF647-stained cells were counted with *Fiji multipoint* tool<sup>59</sup>. Determining the ratio between Hoechst33342- and AF647-stained cells revealed that  $91 \pm 1\%$  of the encapsulated cells were vital. All experiments were performed in triplicates and error bars indicate the s.d. For general cell culture maintenance, see Supplementary Methods 1.10.

**Preparation of cell-laden hydrogels for photopatterning of proteins.** Y2R expressing HeLa cells were detached with 0.05% trypsin/0.02% EDTA/PBS (GE Healthcare) 16 h post receptor induction, centrifuged ( $300 \times g$  for 3 min) and solubilized in 200  $\mu$ L Life Cell Imaging Solution (Invitrogen). For hydrogel formation, 10  $\mu$ L of the HeLa cell suspension were mixed with 3.0  $\mu$ L HBS buffer (20 mM HEPES/NaOH, 150 mM NaCl, pH 7.2, 25 °C), 11.3  $\mu$ L H<sub>2</sub>O, 2.5  $\mu$ L maleimide-PVA, 0.8  $\mu$ L of a 20 mM TPA-*tris*NTA solution (aq.) and 3.0  $\mu$ L dithiol-linker. After mixing via pipetting, hydrogel network formation was allowed to proceed for 10 min. Subsequently, the hydrogel was covered with 1 mL Life Cell Imaging Solution. For mask lithography, hydrogels were exposed to UV light ( $\lambda = 405$  nm LED lamp,  $185$  mW/cm<sup>2</sup>, 1 min) through a quartz mask with lattice designed chrome patterns on top of the gel (Supplementary Fig. 18). Laser lithography by one- or two-photon excitation was conducted on a confocal laser-scanning microscope utilizing the 405 nm LED diode (maximum output of 4.5 mW) or the ultrafast Ti:Sa Chameleon laser (Coherent Inc., Santa Clara, USA) tuned to 800 nm and a Plan-Apochromat 63x/Oil (NA 1.4) objective in Life Cell Imaging Solution at 37 °C. The written ROIs were visualized by binding of His<sub>6</sub>-mCherry (300 nM) or via following His<sub>6</sub>-Y2R<sup>mEGFP</sup> assembly at the activated cell hemisphere (Supplementary Fig. 19, Supplementary Fig. 20).

**Photoenhancement effect of two-photon sensitizers in hydrogels.** Photopatterning by two-photon excitation was conducted on a confocal laser-scanning microscope utilizing the ultrafast Ti:Sa Chameleon laser (Coherent Inc., Santa Clara, USA) tuned to 800 nm and a Plan-Apochromat 63x/Oil (NA 1.4) objective. Before each experiment, the laser intensity of the Ti:Sa Chameleon laser was precisely adjusted to match the given laser powers. 20 rectangular ROIs (15  $\mu$ m width) were written into the gel with stepwise increased laser power (0.5, 1.5, 3.1, and 5.5 mW) or illumination time (6, 12, 18, 24, 30 s). The scan speed was fixed at 1.54  $\mu$ s/pixel. Precise control of the laser dosage assigned to each ROI allowed generating photopatterns of different densities. Photoactivation of hydrogels was performed in HBS buffer (20 mM HEPES/NaOH, 150 mM NaCl, pH 7.2, 25 °C), in presence of ATTO390 (50, 100, 500  $\mu$ M in HBS buffer) or of RB (50, 100  $\mu$ M in HBS buffer). After rinsing with HBS buffer, Ni(II)-loading (10 mM in MQ water) and washing with HBS buffer, His<sub>6</sub>-AF647 (300 nM) tethering was performed. Via CLSM, *z* stacks (35 slices, *z* step width 1  $\mu$ m) of the written ROIs were recorded. Imaging conditions (laser power, detector amplification and pinhole) were kept constant and applied to all photopatterned hydrogels. After background subtraction, *z* slices of each ROI were summed up and quantified by determining the total integrated fluorescence density of each voxel (Supplementary Fig. 11, Supplementary Fig. 12). For comparison, the total integrated fluorescence densities obtained under equal conditions were averaged (Supplementary Fig. 13, Supplementary Fig. 14). Each experiment was performed in triplicate or quadruplicate, and error bars indicate the s.d. Quantification was performed using *Zeiss Zen Black* and *Fiji* software<sup>59</sup>.

**Intensified 3D arbitrary protein organization at low laser power.** For locally precise two-photon excitation in hydrogels, the Ti:Sa Chameleon laser tuned to 800 nm and a Plan-Apochromat 63x/Oil (NA 1.4) objective on the confocal laser-scanning microscope were employed. Photostructuring was conducted in HBS buffer (20 mM HEPES/NaOH, 150 mM NaCl, pH 7.2, 25 °C) supplemented with 50  $\mu$ M rhodamine B. By the user-defined ROI scanning option in combination with the bleaching mode of the microscope software (*Zeiss Zen Black*), the diverse shapes and size regions of the portrait of Maria Goeppert-Mayer were precisely written in *x/y/z* direction. The different ROIs in each *z* plane were photoactivated for 12 s with an average energy of 3.1 mW (1.2%; max output 2.5 W), a scan speed of 1.54  $\mu$ s/pixel and a *z* stack thickness of 5  $\mu$ m separated by 30  $\mu$ m. The written structures were visualized by washing with HBS buffer followed by Ni(II)-loading (10 mM NiCl<sub>2</sub> in MQ) and subsequent POI binding via incubation with 300 nM His<sub>6</sub>-AF647 in HBS buffer at room temperature. The POI assembly was recorded by CLSM (118 slices *z* stacks, 96  $\mu$ m).

## Data availability

The data that support the findings of this study are available from the corresponding author upon reasonable request. The raw data underlying any graph is provided as a source data file.

Received: 5 February 2021; Accepted: 19 January 2022;

Published online: 14 February 2022

## References

- Lee, M., Rizzo, R., Surman, F. & Zenobi-Wong, M. Guiding lights: tissue bioprinting using photoactivated materials. *Chem. Rev.* **120**, 10670–10747 (2020).
- Ruskowitz, E. R. & DeForest, C. A. Photoresponsive biomaterials for targeted drug delivery and 4D cell culture. *Nat. Rev. Mater.* **3**, 17087 (2018).
- Unal, A. Z. & West, J. L. Synthetic ECM: Bioactive synthetic hydrogels for 3D tissue engineering. *Bioconjugate Chem.* **31**, 2253–2271 (2020).
- Tam, R. Y., Smith, L. J. & Shoichet, M. S. Engineering cellular microenvironments with photo- and enzymatically responsive hydrogels: Toward biomimetic 3D cell culture models. *Accounts Chem. Res.* **50**, 703–713 (2017).
- Zhang, Y. S. & Khademhosseini, A. Advances in engineering hydrogels. *Science (New York, N.Y.)* **356**, eaaf3627 (2017).
- Rosales, A. M. & Anseth, K. S. The design of reversible hydrogels to capture extracellular matrix dynamics. *Nat. Rev. Mater.* **1**, 15012 (2016).
- Burdick, J. A. & Murphy, W. L. Moving from static to dynamic complexity in hydrogel design. *Nat. Commun.* **3**, 1269 (2012).
- Matsumoto, S. et al. Photo-responsive gel droplet as a nano- or pico-litre container comprising a supramolecular hydrogel. *Chem. Commun.* **44**, 1545–1547 (2008).
- He, M. T., Li, J. B., Tan, S., Wang, R. Z. & Zhang, Y. Photodegradable supramolecular hydrogels with fluorescence turn-on reporter for photomodulation of cellular microenvironments. *J. Am. Chem. Soc.* **135**, 18718–18721 (2013).
- Li, X. M., Gao, Y., Kuang, Y. & Xu, B. Enzymatic formation of a photoresponsive supramolecular hydrogel. *Chem. Commun.* **46**, 5364–5366 (2010).
- McNitt, C. D., Cheng, H., Ullrich, S., Popik, V. V. & Bjerknes, M. Multiphoton activation of photo-strain-promoted azide alkyne cycloaddition “click” reagents enables in situ labeling with submicrometer resolution. *J. Am. Chem. Soc.* **139**, 14029–14032 (2017).
- Azagarsamy, M. A. & Anseth, K. S. Wavelength-controlled photocleavage for the orthogonal and sequential release of multiple proteins. *Angewandte Chemie-Int. Ed.* **52**, 13803–13807 (2013).
- DeForest, C. A., Sims, E. A. & Anseth, K. S. Peptide-functionalized click hydrogels with independently tunable mechanics and chemical functionality for 3D cell culture. *Chem. Mater.* **22**, 4783–4790 (2010).
- DeForest, C. A. & Anseth, K. S. Cytocompatible click-based hydrogels with dynamically tunable properties through orthogonal photoconjugation and photocleavage reactions. *Nat. Chem.* **3**, 925–931 (2011).
- Adzima, B. J. et al. Spatial and temporal control of the alkyne-azide cycloaddition by photoinitiated Cu(II) reduction. *Nat. Chem.* **3**, 256–259 (2011).
- DeForest, C. A. & Anseth, K. S. Photoreversible patterning of biomolecules within click-based hydrogels. *Angewandte Chemie-Int. Ed.* **51**, 1816–1819 (2012).
- DeForest, C. A., Polizzotti, B. D. & Anseth, K. S. Sequential click reactions for synthesizing and patterning three-dimensional cell microenvironments. *Nat. Mater.* **8**, 659–664 (2009).

18. Luo, Y. & Shoichet, M. S. A photolabile hydrogel for guided three-dimensional cell growth and migration. *Nat. Mater.* **3**, 249–253 (2004).
19. Griffin, D. R. & Kasko, A. M. Photodegradable macromers and hydrogels for live cell encapsulation and release. *J. Am. Chem. Soc.* **134**, 13103–13107 (2012).
20. Kloxin, A. M., Kasko, A. M., Salinas, C. N. & Anseth, K. S. Photodegradable hydrogels for dynamic tuning of physical and chemical properties. *Science (New York, N.Y.)* **324**, 59–63 (2009).
21. Wosnick, J. H. & Shoichet, M. S. Three-dimensional chemical patterning of transparent hydrogels. *Chem. Mater.* **20**, 55–60 (2008).
22. Wylie, R. G. et al. Spatially controlled simultaneous patterning of multiple growth factors in three-dimensional hydrogels. *Nat. Mater.* **10**, 799–806 (2011).
23. Seliktar, D. Designing cell-compatible hydrogels for biomedical applications. *Science (New York, N.Y.)* **336**, 1124–1128 (2012).
24. DeForest, C. A. & Anseth, K. S. Advances in bioactive hydrogels to probe and direct cell fate. *Ann. Rev. Chem. Biomol. Eng. Vol 3* **3**, 421–444 (2012).
25. LaFratta, C. N., Fourkas, J. T., Baldacchini, T. & Farrer, R. A. Multiphoton fabrication. *Angewandte Chemie-Int. Ed.* **46**, 6238–6258 (2007).
26. Tibbitt, M. W., Shadish, J. A. & DeForest, C. A. Photopolymers for Multiphoton Lithography in Biomaterials and Hydrogels. In *Multiphoton Lithography: Techniques, Materials, and Applications* 183–220 (Wiley Publishing, 2016).
27. Wang, L. & Huang, X. in *Artificial Protein and Peptide Nanofibers*. (eds. G. Wei & S. G. Kumar) 415–436 (Woodhead Publishing, 2020).
28. Gonçalves, A. et al. Trends in Protein-Based Biosensor Assemblies for Drug Screening and Pharmaceutical Kinetic Studies. *Molecules (Basel, Switzerland)* **19**, 12461–12485 (2014).
29. Yuan, Y. et al. Conjugated polymer and drug co-encapsulated nanoparticles for Chemo- and Photo-thermal Combination Therapy with two-photon regulated fast drug release. *Nanoscale* **7**, 3067–3076 (2015).
30. Mynar, J. L. et al. Two-photon degradable supramolecular assemblies of linear-dendritic copolymers. *Chem. Commun.* **43**, 2081–2082 (2007).
31. Miyata, T., Asami, N. & Urugami, T. A reversibly antigen-responsive hydrogel. *Nature* **399**, 766–769 (1999).
32. Ehrick, J. D. et al. Genetically engineered protein in hydrogels tailors stimuli-responsive characteristics. *Nat. Mater.* **4**, 298–302 (2005).
33. Murphy, W. L., Dillmore, W. S., Modica, J. & Mrksich, M. Dynamic hydrogels: Translating a protein conformational change into macroscopic motion. *Angewandte Chemie-Int. Ed.* **46**, 3066–3069 (2007).
34. Alge, D. L., Azagarsamy, M. A., Donohue, D. F. & Anseth, K. S. Synthetically tractable click hydrogels for three-dimensional cell culture formed using tetrazine-norbornene chemistry. *Biomacromolecules* **14**, 949–953 (2013).
35. Hahn, M. S., Miller, J. S. & West, J. L. Three-dimensional biochemical and biomechanical patterning of hydrogels for guiding cell behavior. *Adv. Mater.* **18**, 2679 (2006). +.
36. Fisher, S. A. et al. Photo-immobilized EGF chemical gradients differentially impact breast cancer cell invasion and drug response in defined 3D hydrogels. *Biomaterials* **178**, 751–766 (2018).
37. DeForest, C. A. & Tirrell, D. A. A photoreversible protein-patterning approach for guiding stem cell fate in three-dimensional gels. *Nat. Mater.* **14**, 523–531 (2015).
38. Mosiewicz, K. A. et al. In situ cell manipulation through enzymatic hydrogel photopatterning. *Nat. Mater.* **12**, 1071–1077 (2013).
39. Shadish, J. A., Benuska, G. M. & DeForest, C. A. Bioactive site-specifically modified proteins for 4D patterning of gel biomaterials. *Nat. Mater.* **18**, 1005–1014 (2019).
40. Broguiere, N. et al. Morphogenesis guided by 3D patterning of growth factors in biological matrices. *Adv. Mater.* **32**, 1908299 (2020).
41. Grunwald, C. et al. In situ assembly of macromolecular complexes triggered by light. *Proc. Natl Acad. Sci. USA* **107**, 6146–6151 (2010).
42. Labòria, N., Wieneke, R. & Tampé, R. Control of nanomolar interaction and in situ assembly of proteins in four dimensions by light. *Angewandte Chemie-Int. Ed.* **52**, 848–853 (2013).
43. Gatterdam, K., Joest, E. F., Gatterdam, V. & Tampé, R. The Scaffold Design of Trivalent Chelator Heads Dictates Affinity and Stability for Labeling His-tagged Proteins in vitro and in Cells. *Angewandte Chemie Int. Ed.* **57**, 12395–12399 (2018).
44. Wieneke, R. & Tampé, R. Multivalent chelators for in vivo protein labeling. *Angewandte Chemie Int. Ed.* **58**, 8278–8290 (2019).
45. Lata, S., Reichel, A., Brock, R., Tampé, R. & Piehler, J. High-affinity adaptors for switchable recognition of histidine-tagged proteins. *J. Am. Chem. Soc.* **127**, 10205–10215 (2005).
46. Wieneke, R. et al. Live-cell targeting of His-tagged proteins by multivalent N-nitritriacetic acid carrier complexes. *J. Am. Chem. Soc.* **136**, 13975–13978 (2014).
47. Kollmannsperger, A. et al. Live-cell protein labelling with nanometre precision by cell squeezing. *Nat. Commun.* **7**, 10372 (2016).
48. Sánchez, M. F., Els-Heindl, S., Beck-Sickinger, A. G., Wieneke, R. & Tampé, R. Photoinduced receptor confinement drives ligand-independent GPCR signaling. *Science (New York, N.Y.)* **371**, eabb7657 (2021).
49. Hagen, V. et al. Highly efficient and ultrafast phototriggers for cAMP and cGMP by using long-wavelength UV/Vis-activation. *Angewandte Chemie Int. Ed.* **40**, 1045–1048 (2001).
50. LeValley, P. J. et al. Photolabile linkers: exploiting labile bond chemistry to control mode and rate of hydrogel degradation and protein release. *J. Am. Chem. Soc.* **142**, 4671–4679 (2020).
51. Goegan, B., Terzi, F., Bolze, F., Cambridge, S. & Specht, A. Synthesis and characterization of photoactivatable doxycycline analogues bearing two-photon-sensitive photoremovable groups suitable for light-induced gene expression. *Chembiochem* **19**, 1341–1348 (2018).
52. Klausen, M., Dubois, V., Verlhac, J. B. & Blanchard-Desce, M. Tandem Systems for Two-Photon Uncaging of Bioactive Molecules. *Chempluschem* **84**, 589–598 (2019).
53. Hammer, C. A. et al. Sensitized Two-Photon Activation of Coumarin Photocages. *J. Phys. Chem. Lett.* **9**, 1448–1453 (2018).
54. Xu, C. & Webb, W. W. Measurement of two-photon excitation cross sections of molecular fluorophores with data from 690 to 1050 nm. *J. Opt. Soc. Am. B* **13**, 481–491 (1996).
55. Pradhan, S., Keller, K. A., Sperduto, J. L. & Slater, J. H. Fundamentals of laser-based hydrogel degradation and applications in cell and tissue engineering. *Adv. Healthcare Mater.* **6**, 1700681 (2017).
56. Tsai, P. S. et al. Plasma-mediated ablation: an optical tool for submicrometer surgery on neuronal and vascular systems. *Curr. Opin. Biotechnol.* **20**, 90–99 (2009).
57. Lunzer, M. et al. A modular approach to sensitized two-photon patterning of photodegradable hydrogels. *Angewandte Chemie Int. Ed.* **57**, 15122–15127 (2018).
58. Bradley, D. J. et al. Interactions of picosecond laser pulses with organic molecules I. Two-photon fluorescence quenching and singlet states excitation in Rhodamine dyes. *Proc. Royal Soc. London. A. Mathematical Phys. Sci.* **328**, 97–121 (1997).
59. Schindelin, J. et al. Fiji: An open-source platform for biological-image analysis. *Nat. Methods* **9**, 676–682 (2012).

## Acknowledgements

This research was supported by the German Research Foundation (GRK 1986 to R.W. and R.T.), the LOEWE program (DynaMem A03 to R.W. and R.T.), the Volkswagen Foundation (Az. 96 498 to R.W. and Az. 96 496 to R.T.) and the Reinhart Koselleck Project (TA 157/12–1 to R.T.). The authors thank all members of the Institute of Biochemistry (Goethe University Frankfurt) for helpful discussion and comments. We thank Christian Winter for his support with the peptide synthesizer and LC-MS and Yagmur Aydogan for assistance with the TPEF measurements.

## Author contributions

H.K. performed the synthesis, experiments, and analysis. M.A. carried out the two-photon absorption measurements, the fluorescence quantum yield measurements and power-dependency measurements of TPA-*tris*NTA. J.W. was involved in analysis and discussion. H.K., R.T., and R.W. designed the experiments and analyzed the data. H.K. and R.W. wrote the paper. R.W. conceived the study and supervised the project.

## Funding

Open Access funding enabled and organized by Projekt DEAL.

## Competing interests

The authors declare no competing interests.

## Additional information

**Supplementary information** The online version contains supplementary material available at <https://doi.org/10.1038/s43246-022-00230-w>.

**Correspondence** and requests for materials should be addressed to Ralph Wieneke.

**Peer review information** *Communications Materials* thanks the anonymous reviewers for their contribution to the peer review of this work. Primary Handling Editors: Steven Caliar and John Plummer.

**Reprints and permission information** is available at <http://www.nature.com/reprints>

**Publisher's note** Springer Nature remains neutral with regard to jurisdictional claims in published maps and institutional affiliations.



**Open Access** This article is licensed under a Creative Commons Attribution 4.0 International License, which permits use, sharing, adaptation, distribution and reproduction in any medium or format, as long as you give appropriate credit to the original author(s) and the source, provide a link to the Creative Commons license, and indicate if changes were made. The images or other third party material in this article are included in the article's Creative Commons license, unless indicated otherwise in a credit line to the material. If material is not included in the article's Creative Commons license and your intended use is not permitted by statutory regulation or exceeds the permitted use, you will need to obtain permission directly from the copyright holder. To view a copy of this license, visit <http://creativecommons.org/licenses/by/4.0/>.

© The Author(s) 2022



# Glossary of Terms and Abbreviations

## Symbols

**1PA** one-photon absorption  
**2PA** two-photon absorption  
**2PIF** two-photon induced fluorescence

## A

**AO** atomic orbital

## B

**BBO**  $\beta$ -barium-borate  
**BLQ** blue-light quenching  
**BO** Born-Oppenheimer  
**BODIPY** Boron-dipyromethene  
**BR** Bacteriorhodopsin

## C

**cAMP** adenosine cyclic 3',5'-phosphate  
**ChR2** Channelrhodopsin-2  
**CI** conical intersection  
**CLiC** Complex Light Control  
**CPA** chirped pulse amplification  
**CT** charge transfer  
**cw** continuous wave

## D

**DAS** decay-associated spectra  
**DEACM** (7-diethylaminocoumarin-4-yl)methyl  
**DFG** difference-frequency generation

**DFG** Deutsche Forschungsgemeinschaft  
**DNA** deoxyribonucleic acid  
**DNP** dynamic nuclear polarization  
**DS** dark state

## E

**e** extraordinary  
**ec** extracellular  
**EM** electromagnetic  
**EMW** electromagnetic wave  
**EPR** electron paramagnetic resonance  
**ES** excited state  
**ESA** excited state absorption  
**ESB** excited state branching  
**ET** energy transfer

## F

**FC** Franck-Condon  
**FP** flash photolysis  
**FRET** Förster-resonance energy transfer  
**fs-TA** ultrafast transient absorption  
**FT** Fourier-transform

## G

**GLA** global lifetime analysis  
**GS** ground state  
**GSB** ground state bleach  
**GSH** ground state heterogeneity  
**GVD** group velocity dispersion

*Glossary of Terms and Abbreviations*

**GVM** group velocity mismatch

**H**

**HOOP** hydrogen out-of-plane

**HPLC** high-performance liquid chromatography

**HR** Halorhodopsin

**I**

**IC** internal conversion

**ic** intracellular

**ICCD** intensified charge-coupled device

**ICT** intramolecular charge transfer

**IR** infrared

**IRF** instrument response function

**ISC** intersystem crossing

**K**

**KR2** *Krokinobacter eikastus* rhodopsin 2

**L**

**LCAO** linear combination of atomic orbitals

**LDA** lifetime density analysis

**LDM** lifetime density map

**LE** locally excited state

**LED** light-emitting diode

**LG** leaving group

**M**

**MCM** (7-methoxycoumarin-4-yl)methyl

**MCT** mercury cadmium telluride

**ML-MCTDH** multi-layer multiconfiguration time-dependent Hartree

**MO** molecular orbital

**mRho** microbial rhodopsin

**N**

**Nd:YAG** Neodymium-doped-yttrium aluminium garnet

**Nd:YVO<sub>4</sub>** neodymium-doped-yttrium vanadate

**NLO** non-linear optical

**NMR** nuclear magnetic resonance

**NOPA** non-collinear optical parametric amplification

**NRP** non-reactive pathway

**O**

**o** ordinary

**oNB** *ortho*-nitrobenzyl

**OPA** optical parametric amplification

**OPO** optical parametric oscillator

**P**

**PA** proton acceptor

**PBS** phosphate-buffered saline

**PD** proton donor

**PG** protecting group

**PI** population inversion

**PMT** photomultiplier tube

**PNA** p-nitroaniline

**PPA** photoproduct absorption

**PPG** photolabile protecting group

**PR** Proteorhodopsin

**PSS** photostationary state

**Q**

**QCL** quantum cascade laser

**QD** quantum dynamics

*Glossary of Terms and Abbreviations*

<b>QM/MM</b> quantum mechanics/molecular mechanics	<b>SVEA</b> slowly varying envelope approximation
<b>QY</b> quantum yield	
<b>R</b>	<b>T</b>
<b>RBP</b> retinal binding pocket	<b>TCSPC</b> time-correlated single photon counting
<b>RNA</b> ribonucleic acid	<b>TD-DFT</b> time-dependent density functional theory
<b>ROID</b> readout integrated circuit	<b>THG</b> third harmonic generation
<b>RP</b> reactive pathway	<b>Ti:Sa</b> Ti <sup>3+</sup> -doped sapphire
<b>RSB</b> retinal Schiff base	<b>TICT</b> twisted intramolecular charge transfer
<b>S</b>	<b>TIP</b> tight ion pair
<b>SB</b> Schiff base	<b>TMH</b> $\alpha$ -transmembrane helix
<b>SBS</b> second bright state	
<b>SC</b> supercontinuum	<b>V</b>
<b>SCG</b> supercontinuum generation	<b>VR</b> vibrational relaxation
<b>SE</b> stimulated emission	
<b>SFG</b> sum-frequency generation	<b>W</b>
<b>SFM</b> self-phase modulation	<b>WT</b> wildtype
<b>SHG</b> second harmonic generation	



# List of Figures

2.1	The electromagnetic spectrum and a zoom-in of the UV/vis part. . . . .	6
2.2	Jablonski diagram of the photochemical relaxation pathways. Processes involving absorption or emission of a photon are depicted in color. Non-radiative processes are depicted with black arrows: VR(curled), IC (solid) and ISC (dashed). . . . .	12
2.3	The index ellipsoid of a birefringent crystal. The relative orientation between the direction of incidence and the optical axis determine the elliptic surface of the $n_e$ and $n_o$ components. . . . .	14
2.4	Schematic representation of cw- and stroboscopic probing in a pump-probe experiment. . . . .	17
2.5	Schematic overview of the flash photolysis setup including cw- and pulsed UV/vis probing, as well as cw-probing in the IR. All three setups are fed with pump-pulses from the Nd:YAG and OPO configuration. . . . .	19
2.6	Schematic overview of the ultrafast TA setup. In addition to a two-staged NOPA for pump-pulse generation, it is also possible to produce UV-pulses via SFG. . . . .	23
2.7	Origin of the $\Delta$ abs. spectra in a fs-TA experiment. . . . .	24
2.8	Energy diagram showcasing the generate and degenerate 2PA cases. Schematic overview of the 2PIF setup and a closed-in view on the focal volume. The remaining IR pump beam has to be filtered with a dichroic filter in order to get a clean fluorescence signal. . . . .	27
2.9	Schematic representation of time-resolved data evaluation. The dataset (middle) can either be evaluated by GLA or LDA. The former one yields DAS, whereas the latter one yields LDMs. Both strategies are implemented in the OPTIMUS package. <sup>[66]</sup> . . . . .	29
2.10	Schematic representation of the four MRh types: Proton pumps, cation or anion channels, chloride pumps and sodium pumps. . . . .	30
2.11	Reduced structure of BR from the side, top and bottom view. . . . .	31
2.12	Isomerization of <i>all-trans</i> into 13- <i>cis</i> retinal upon absorption of a photon. . . . .	32
2.13	Schematic representation of the ESB (a) and GSH (b) models. . . . .	33

## List of Figures

2.14	Generalized photocycle scheme with the crucial M-intermediate highlighted in blue. . . . .	34
2.15	The basic structure of coumarin (a) and its PPG-variants based on the 7-alkoxy- (b), 6,7-dialkoxy- (c), 6-bromo-7-alkoxy- (d) and 7-dialkyl-amino-substituted coumarins (e). . . . .	37
2.16	Reaction pathways pathways of DEACM after photoabsorption. The photochemical cleavage occurs via a TIP, which needs to be stabilized by the solvent. . . . .	39
2.17	Mesomeric structures of the BODIPY scaffold. . . . .	40
2.18	Uncaging mechanism of BODIPY-based PPGs. The mechanism involves the formation of a carbocation, which is stabilized by the solvent. Both, singlet and triplet, mechanisms have been reported. . . . .	41
4.1	Absorption spectra of KR2 at different conditions (a). Close-up view on the RBP at neutral (b) and acidic (c) pH conditions. . . . .	46
4.2	Overview of the IR dataset for KR2 <sub>Na</sub> and KR2 <sub>H</sub> . The UV/vis data is given in the lower panels to simplify the temporal correlation of the signals. . . . .	47
4.3	Transients representing the ethylenic stretch modes of the chromophore. . . . .	48
4.4	Transients representing changes of the amide I band. . . . .	49
4.5	Possible marker bands for changes in the ECL1-domain. . . . .	50
4.6	Transients representing changes of the D116 protonation state in KR2 <sub>H</sub> . . . . .	51
4.7	The HOOP-mode region in KR2 <sub>Na</sub> . . . . .	53
4.8	Complete representation of the transient absorption measurements ranging from fs to s. The near-UV region of the fs-measurements is scaled by a factor of 5 to account for the smaller signal amplitude in this spectral region. . . . .	54
4.9	Transients of the red-shifted absorption corresponding to J (upper panel) and the near-UV band (lower panel). . . . .	55
4.10	Electron density differences of the K-, M- and O-intermediate in KR2. The higher order transitions correspond to the SBS. In the case of the O-intermediate, calculations on structure A are shown. . . . .	56
4.11	Double difference spectra at different time delays for the KR2 WT at pH 9. The photoproduct band resembles the absorption of the parent state. . . . .	58
4.12	Overview of the ATTO-derived compounds without (7a-d) and with a serotonin LG (9a-d). . . . .	60
4.13	The corresponding absorption and fluorescence spectra (a) and 2P action cross sections (b) of compounds 7a-d in PBS. . . . .	61

4.14	Excited state dynamics of 7a in MeOH (a) and toluene (b). . . . .	62
4.15	Solvent dependent transients of $ESA_{ICT}$ in 7a. . . . .	63
4.16	Schematic representation of the ES pathways in ATTO-based compounds. . . . .	64
4.17	Chemical structures of Rho 1-4. . . . .	66
4.18	Chemical structure of the dyad system with and without LG and the corresponding absorption spectra. . . . .	67
4.19	Photodynamics of the first 600 fs after excitation of Rho-BPY-OH with 565 nm (a) or 660 nm (b) pulses and their respective lifetime densities (c) and (d). . . . .	68
4.20	$GSB_{Rho}$ and $GSB_{BPY}$ representing the ET process (a). Corresponding LE populations (b) and coherence lifetimes (c). . . . .	69
4.21	Energy diagram representing crucial pathways after 1PA or 2PA. . . . .	70
4.22	Spectral changes in the region of the PNA absorption after illumination of Rho-BPY-PNA with (a) 565 nm or (b) 660 nm. No shift is observed in Rho-BPY-OH after illumination with 565 nm light (c). . . . .	71





## List of Tables

2.1	Highlighted photocycle characteristics in BR. The prefixes d (deprotonated) and p (protonated) in the RSB, PD and PA columns indicate proton movements along the respective transitions. . . . .	35
4.1	Transition energies and oscillator strengths of the SBS transition for the individual photointermediates in KR2. The O-state was calculated with 13- <i>cis</i> and <i>all-trans</i> retinal. . . . .	57
4.2	Uncaging QYs of compounds 9a-9d and the DEACM-Ser reference in PBS/MeOH. . . . .	63
4.3	Photophysical properties of the tested antenna compounds Rho 1-4 in MeOH. . . . .	66



# Bibliography

- [1] C. R. Woese, *Proceedings of the National Academy of Sciences* **1965**, *54*, 1546–1552.
- [2] F. H. C. Crick, *Journal of Molecular Biology* **1968**, *38*, 367–379.
- [3] M. Neveu, H.-J. Kim, S. A. Benner, *Astrobiology* **2013**, *13*, 391–403.
- [4] A. Rich, *Horizons in biochemistry* **1962**, 103–126.
- [5] W. Gilbert, *Nature* **1986**, *319*, 618–618.
- [6] C. Woese, *Proceedings of the National Academy of Sciences of the United States of America* **1998**, *95*, 6854–6859.
- [7] D. A. Bryant, N.-U. Frigaard, *Trends in Microbiology* **2006**, *14*, 488–496.
- [8] T. Cardona, *Heliyon* **2018**, *4*, e00548.
- [9] A. Tomitani, A. H. Knoll, C. M. Cavanaugh, T. Ohno, *Proceedings of the National Academy of Sciences of the United States of America* **2006**, *103*, 5442–5447.
- [10] S. Schulz, R. Brankatschk, A. Dümig, I. Kögel-Knabner, M. Schloter, J. Zeyer, *Biogeosciences* **2013**, *10*, 3983–3996.
- [11] G. I. McFadden, G. G. van Dooren, *Current Biology* **2004**, *14*, R514–R516.
- [12] K. R. Moore, C. Magnabosco, L. Momper, D. A. Gold, T. Bosak, G. P. Fournier, *Frontiers in Microbiology* **2019**, *10*.
- [13] W. J. Gehring, *WIREs Developmental Biology* **2014**, *3*, 1–40.
- [14] C. Brieke, F. Rohrbach, A. Gottschalk, G. Mayer, A. Heckel, *Angewandte Chemie - International Edition* **2012**, *51*, 8446–8476.
- [15] E. S. Boyden, F. Zhang, E. Bamberg, G. Nagel, K. Deisseroth, *Nature Neuroscience* **2005**, *8*, 1263–1268.
- [16] L. Fenno, O. Yizhar, K. Deisseroth, *Annual Review of Neuroscience* **2011**, *34*, 389–412.
- [17] K. Deisseroth, *Nature Methods* **2011**, *8*, 26–29.
- [18] L. Rayleigh, *The London Edinburgh and Dublin Philosophical Magazine and Journal of Science* **1899**, *47*, 375–384.

## Bibliography

- [19] G. Mie, *Annalen der Physik* **1908**, 330, 377–445.
- [20] C. V. Raman, K. S. Krishnan, *Nature* **1928**, 122, 12–13.
- [21] J. E. Lennard-Jones, *Transactions of the Faraday Society* **1929**, 25, 668–686.
- [22] E. Hückel, *Transactions of the Faraday Society* **1934**, 30, 40–52.
- [23] R. S. Mulliken, *Science* **1967**, 157, 13–24.
- [24] G. Wentzel, *Zeitschrift für Physik* **1927**, 43, 524–530.
- [25] M. Born, R. Oppenheimer, *Annalen der Physik* **1927**, 389, 457–484.
- [26] J. Franck, E. G. Dymond, *Transactions of the Faraday Society* **1926**, 21, 536–542.
- [27] E. Condon, *Physical Review* **1926**, 28, 1182–1201.
- [28] Beer, *Annalen der Physik* **1852**, 162, 78–88.
- [29] T. G. Mayerhöfer, S. Pahlow, J. Popp, *ChemPhysChem* **2020**, 21, 2029–2046.
- [30] A. Jablonski, *Nature* **1933**, 131, 839–840.
- [31] L. H. Thomas, *Nature* **1926**, 117, 514–514.
- [32] M. Kasha, *Discussions of the Faraday Society* **1950**, 9, 14–19.
- [33] J. C. Maxwell, *Philosophical Transactions of the Royal Society of London* **1865**, 155, 459–512.
- [34] F. Arecchi, R. Bonifacio, *IEEE Journal of Quantum Electronics* **1965**, 1, 169–178.
- [35] S. Lochbrunner, T. Wilhelm, J. Piel, S. Sporlein, E. Riedle in *Advanced Solid State Lasers (1999)*, *Advanced Solid State Lasers*, Optica Publishing Group, **1999**, TuA4.
- [36] A. H. Zewail, *Science* **1988**, 242, 1645–1653.
- [37] G. Porter, *Science* **1968**, 160, 1299–1307.
- [38] W. S. Boyle, G. E. Smith, *The Bell System Technical Journal* **1970**, 49, 587–593.
- [39] G. F. Amelio, *Scientific American* **1974**, 230, 22–31.
- [40] J. L. Wiza, *Nuclear Instruments and Methods* **1979**, 162, 587–601.
- [41] V. Deckert, W. Kiefer, *Applied Spectroscopy* **1992**, 46, 322–328.
- [42] J. Connes, P. Connes, *Journal of the Optical Society of America* **1966**, 56, 896–910.
- [43] J. Chamberlain, J. E. Gibbs, H. A. Gebbie, *Infrared Physics* **1969**, 9, 185–209.
- [44] J. Faist, F. Capasso, D. Sivco, C. Sirtori, A. Hutchinson, A. Cho, *Science* **1994**, 264, 553–556.

- [45] R. N. Hall, G. E. Fenner, J. D. Kingsley, T. J. Soltys, R. O. Carlson, *Physical Review Letters* **1962**, 9, 366–368.
- [46] M. I. Nathan, W. P. Dumke, G. Burns, F. H. Dill, G. Lasher, *Applied Physics Letters* **1962**, 1, 62–64.
- [47] N. Holonyak, S. F. Bevacqua, *Applied Physics Letters* **1962**, 1, 82–83.
- [48] T. M. Quist, R. H. Rediker, R. J. Keyes, W. E. Krag, B. Lax, A. L. McWhorter, H. J. Zeigler, *Applied Physics Letters* **1962**, 1, 91–92.
- [49] H. Kroemer, *Proceedings of the IEEE* **1963**, 51, 1782–1783.
- [50] R. F. Kazarinov, R. Suris, *Soviet Physics - Semiconductors* **1971**, 5, 797–800.
- [51] P. Norton, *Opto-Electronics Review* **2002**, 10, 159–174.
- [52] G. L. Hansen, J. L. Schmit, T. N. Casselman, *Journal of Applied Physics* **1982**, 53, 7099–7101.
- [53] H. Nelson, *RCA review* **1963**, 24, 603–615.
- [54] O. P. Agnihotri, C. A. Musca, L. Faraone, *Semiconductor Science and Technology* **1998**, 13, 839–845.
- [55] D. Strickland, G. Mourou, *Optics Communications* **1985**, 56, 219–221.
- [56] J. Enderlein, R. Erdmann, *Optics Communications* **1997**, 134, 371–378.
- [57] M. Göppert-Mayer, *Annalen der Physik* **1931**, 401, 273–294.
- [58] M. Pawlicki, H. A. Collins, R. G. Denning, H. L. Anderson, *Angewandte Chemie - International Edition* **2009**, 48, 3244–3266.
- [59] M. Rumi, J. W. Perry, *Advances in Optics and Photonics* **2010**, 2, 451.
- [60] P. Sperber, A. Penzkofer, *Optical and Quantum Electronics* **1986**, 18, 381–401.
- [61] B. Gu, J. Wang, J. Chen, Y.-X. Fan, J. Ding, H.-T. Wang, *Optics Express* **2005**, 13, 9230–9234.
- [62] B. Gu, Y. X. Fan, J. Chen, H. T. Wang, J. He, W. Ji, *Journal of Applied Physics* **2007**, 102, DOI 10.1063/1.2795997.
- [63] C. Xu, R. M. Williams, W. Zipfel, W. W. Webb, *Bioimaging* **1996**, 4, 198–207.
- [64] M. A. Albota, C. Xu, W. W. Webb, *Applied Optics* **1998**, 37, 7352–7356.
- [65] I. H. Van Stokkum, D. S. Larsen, R. Van Grondelle, *Biochimica et Biophysica Acta - Bioenergetics* **2004**, 1657, 82–104.

## Bibliography

- [66] C. Slavov, H. Hartmann, J. Wachtveitl, *Analytical Chemistry* **2015**, *87*, 2328–2336.
- [67] D. R. James, W. R. Ware, *Chemical Physics Letters* **1986**, *126*, 7–11.
- [68] R. A. F. Dixon, B. K. Kobilka, D. J. Strader, J. L. Benovic, H. G. Dohlman, T. Frielle, M. A. Bolanowski, C. D. Bennett, E. Rands, R. E. Diehl, R. A. Mumford, E. E. Slater, I. S. Sigal, M. G. Caron, R. J. Lefkowitz, C. D. Strader, *Nature* **1986**, *321*, 75–79.
- [69] T. P. Sakmar, *Current Opinion in Cell Biology* **2002**, *14*, 189–195.
- [70] Y. Shichida, T. Yamashita, *Photochemical and Photobiological Sciences* **2003**, *2*, 1237–1246.
- [71] O. P. Ernst, D. T. Lodowski, M. Elstner, P. Hegemann, L. S. Brown, H. Kandori, S. Leonid, H. Kandori, *Chemical Reviews* **2014**, *114*, 126–163.
- [72] A. Rozenberg, K. Inoue, H. Kandori, O. Béjà, *Annual Review of Microbiology* **2021**, *75*, 427–447.
- [73] D. Oesterhelt, W. StoECKenius, *Nature: New biology* **1971**, *233*, 149–152.
- [74] O. Beja, L. Aravind, E. V. Koonin, M. T. Suzuki, A. Hadd, L. P. Nguyen, S. B. Jovanovich, C. M. Gates, R. A. Feldman, J. L. Spudich, E. N. Spudich, E. F. DeLong, *Science* **2000**, *289*, 1902–1906.
- [75] A. Matsuno-Yagi, Y. Mukohata, *Biochemical and Biophysical Research Communications* **1977**, *78*, 237–243.
- [76] B. Schobert, J. K. Lanyi, *Journal of Biological Chemistry* **1982**, *257*, 10306–10313.
- [77] K. Inoue, H. Ono, R. Abe-Yoshizumi, S. Yoshizawa, H. Ito, K. Kogure, H. Kandori, *Nature Communications* **2013**, *4*, 1–10.
- [78] G. Nagel, T. Szellas, W. Huhn, S. Kateriya, N. Adeishvili, P. Berthold, D. Ollig, P. Hegemann, E. Bamberg, *Proceedings of the National Academy of Sciences of the United States of America* **2003**, *100*, 13940–13945.
- [79] M. Akhtar, P. T. Blosse, P. B. Dewhurst, *Biochemical Journal* **1968**, *110*, 693–702.
- [80] J. von Lintig, K. Vogt, *Journal of Biological Chemistry* **2000**, *275*, 11915–11920.
- [81] G. DuEster, *Cell* **2008**, *134*, 921–931.
- [82] J. K. Lanyi, *Annual Review of Physiology* **2004**, *66*, 665–88.
- [83] H. Kandori, *Frontiers in Molecular Biosciences* **2015**, *2*, DOI 10.3389/fmolb.2015.00052.

- [84] C. Bamann, E. Bamberg, J. Wachtveitl, C. Glaubitz, *Biochimica et Biophysica Acta - Bioenergetics* **2014**, 1837, 614–625.
- [85] H. Luecke, B. Schobert, H.-T. Richter, J.-P. Cartailler, J. K. Lanyi, *Journal of Molecular Biology* **1999**, 291, 899–911.
- [86] J. K. Lanyi, H. Luecke, *Current Opinion in Structural Biology* **2001**, 11, 415–419.
- [87] H. Kandori, *Biochimica et Biophysica Acta - Bioenergetics* **2000**, 1460, 177–191.
- [88] D. Ikeda, Y. Furutani, H. Kandori, *Biochemistry* **2007**, 46, 5365–5373.
- [89] S. Schenkl, F. Van Mourik, G. Van Der Zwan, S. Haacke, M. Chergui, *Science* **2005**, 309, 917–920.
- [90] J. Lugtenburg, M. Muradin-Szweykowska, C. Heeremans, J. A. Pardoën, *Journal of the American Chemical Society* **1986**, 108, 3104–3105.
- [91] R. Rajamani, J. Gao, *Journal of Computational Chemistry* **2002**, 23, 96–105.
- [92] M. Wanko, M. Hoffmann, P. Strodel, A. Koslowski, W. Thiel, F. Neese, T. Frauenheim, M. Elstner, *Journal of Physical Chemistry B* **2005**, 109, 3606–3615.
- [93] G. Zgrablić, K. Voitchovsky, M. Kindermann, S. Haacke, M. Chergui, *Biophysical Journal* **2005**, 88, 2779–2788.
- [94] A. C. Florean, D. Cardoza, J. L. White, J. K. Lanyi, R. J. Sension, P. H. Bucksbaum, *Proceedings of the National Academy of Sciences of the United States of America* **2009**, 106, 10896–900.
- [95] P. Hamm, M. Zurek, T. Röschinger, H. Patzelt, D. Oesterhelt, W. Zinth, *Chemical Physics Letters* **1996**, 268, 180–186.
- [96] R. R. Birge, *Biochimica et Biophysica Acta (BBA) - Bioenergetics* **1990**, 1016, 293–327.
- [97] R. Gross, C. Schumann, M. M. N. Wolf, J. Herbst, R. Diller, N. Friedman, M. Sheves, *The Journal of Physical Chemistry B* **2009**, 113, 7851–7860.
- [98] J. Léonard, E. Portuondo-Campa, A. Cannizzo, F. Van Mourik, G. Van Der Zwan, J. Tittor, S. Haacke, M. Chergui, *Proceedings of the National Academy of Sciences of the United States of America* **2009**, 106, 7718–7723.
- [99] E. Bühl, P. Eberhardt, C. Bamann, E. Bamberg, M. Braun, J. Wachtveitl, *The Journal of Physical Chemistry Letters* **2018**, 9, 7180–7184.
- [100] S. Tahara, H. Kuramochi, S. Takeuchi, T. Tahara, *The Journal of Physical Chemistry Letters* **2019**, 10, 5422–5427.
- [101] K. Heyne, *The Journal of Physical Chemistry B* **2022**, 126, 581–587.

## Bibliography

- [102] S. Tahara, S. Takeuchi, R. Abe-Yoshizumi, K. Inoue, H. Ohtani, H. Kandori, T. Tahara, *Journal of Physical Chemistry B* **2018**, *122*, 4784–4792.
- [103] D. Oesterhelt, P. Hegemann, J. Tittor, *The EMBO journal* **1985**, *4*, 2351–2356.
- [104] Y. Hontani, M. Marazzi, K. Stehfest, T. Mathes, I. H. Van Stokkum, M. Elstner, P. Hegemann, J. T. Kennis, *Scientific Reports* **2017**, *7*, 1–12.
- [105] S. Tahara, S. Takeuchi, R. Abe-Yoshizumi, K. Inoue, H. Ohtani, H. Kandori, T. Tahara, *Journal of Physical Chemistry Letters* **2015**, *6*, 4481–4486.
- [106] H. Kandori, K. Yoshihara, H. Tomioka, H. Sasabe, *Journal of Physical Chemistry* **1992**, *96*, 6066–6071.
- [107] M. K. Verhoefen, C. Bamann, R. Blöcher, U. Förster, E. Bamberg, J. Wachtveitl, *ChemPhysChem* **2010**, *11*, 3113–3122.
- [108] R. Huber, T. Köhler, M. O. Lenz, E. Bamberg, R. Kalmbach, M. Engelhard, J. Wachtveitl, *Biochemistry* **2005**, *44*, 1800–1806.
- [109] F. Peters, J. Herbst, J. Tittor, D. Oesterhelt, R. Diller, *Chemical Physics* **2006**, *323*, 109–116.
- [110] M. O. Lenz, R. Huber, B. Schmidt, P. Gilch, R. Kalmbach, M. Engelhard, J. Wachtveitl, *Biophysical Journal* **2006**, *91*, 255–262.
- [111] Y. Sudo, M. Mizuno, Z. Wei, S. Takeuchi, T. Tahara, Y. Mizutani, *The Journal of Physical Chemistry B* **2014**, *118*, 1510–1518.
- [112] G. Zgrablić, A. M. Novello, F. Parmigiani, *Journal of the American Chemical Society* **2012**, *134*, 955–961.
- [113] C.-F. Chang, H. Kuramochi, M. Singh, R. Abe-Yoshizumi, T. Tsukuda, H. Kandori, T. Tahara, *Angewandte Chemie - International Edition* **2022**, *134*, DOI 10.1002/ange.202111930.
- [114] P. A. Kusochek, A. V. Scherbinin, A. V. Bochenkova, *Journal of Physical Chemistry Letters* **2021**, 8664–8671.
- [115] H. Abramczyk, *The Journal of Chemical Physics* **2004**, *120*, 11120–11132.
- [116] M. Olivucci, A. Lami, F. Santoro, *Angewandte Chemie - International Edition* **2005**, *117*, 5248–5251.
- [117] A. Cembran, F. Bernardi, M. Olivucci, M. Garavelli, *Proceedings of the National Academy of Sciences of the United States of America* **2005**, *102*, 6255–6260.



- [118] G. Zgrablić, S. Haacke, M. Chergui, *Journal of Physical Chemistry B* **2009**, *113*, 4384–4393.
- [119] T. Arlt, S. Schmidt, W. Zinth, U. Haupts, D. Oesterhelt, *Chemical Physics Letters* **1995**, *241*, 559–565.
- [120] I. Burghardt, L. S. Cederbaum, J. T. Hynes, *Faraday Discussions* **2004**, *127*, 395–411.
- [121] I. Burghardt, J. T. Hynes, *Journal of Physical Chemistry A* **2006**, *110*, 11411–11423.
- [122] K. A. Freedman, R. S. Becker, *Journal of the American Chemical Society* **1986**, *108*, 1245–1251.
- [123] C. F. Chang, H. Kuramochi, M. Singh, R. Abe-Yoshizumi, T. Tsukuda, H. Kandori, T. Tahara, *Physical Chemistry Chemical Physics* **2019**, *21*, 25728–25734.
- [124] R. R. Birge, T. M. Cooper, A. F. Lawrence, M. B. Masthay, C. Vasilakis, C. F. Zhang, R. Zidovetzki, *Journal of the American Chemical Society* **1989**, *111*, 4063–4074.
- [125] J. H. Hanamoto, P. Dupuis, M. A. El-Sayed, *Proceedings of the National Academy of Sciences of the United States of America* **1984**, *81*, 7083–7087.
- [126] M. Asido, R. K. Kar, C. N. Kriebel, M. Braun, C. Glaubitz, I. Schapiro, J. Wachtveitl, *The Journal of Physical Chemistry Letters* **2021**, *12*, 6284–6291.
- [127] E. Siva Subramaniam Iyer, R. Misra, A. Maity, O. Liubashevski, Y. Sudo, M. Sheves, S. Ruhman, *Journal of the American Chemical Society* **2016**, *138*, 12401–12407.
- [128] S. P. Balashov, T. G. Ebrey, *Photochemistry and Photobiology* **2001**, *73*, 453–462.
- [129] U. Haupts, J. Tittor, D. Oesterhelt, *Annual Review of Biophysics and Biomolecular Structure* **1999**, *28*, 367–399.
- [130] J. Herzfeld, J. C. Lansing, *Annual Review of Biophysics and Biomolecular Structure* **2002**, *31*, 73–95.
- [131] R. A. Mathies, S. W. Lin, J. B. Ames, W. T. Pollard, *Annual Review of Biophysics and Biophysical Chemistry* **1991**, *20*, 491–518.
- [132] J. Sasaki, T. Yuzawa, H. Kandori, A. Maeda, H. Hamaguchi, *Biophysical Journal* **1995**, *68*, 2073–2080.
- [133] L. A. Drachev, A. D. Kaulen, V. P. Skulachev, *FEBS Letters* **1984**, *178*, 331–335.
- [134] G. Váró, J. K. Lanyi, *Biochemistry* **1991**, *30*, 5016–5022.
- [135] S. Subramaniam, R. Henderson, *Nature* **2000**, *406*, 653–657.

## Bibliography

- [136] A. Maeda, *Israel Journal of Chemistry* **1995**, *35*, 387–400.
- [137] K. J. Rothschild, *Journal of Bioenergetics and Biomembranes* **1992**, *24*, 147–167.
- [138] K. Gerwert, *Biological chemistry* **1999**, *380*, 931–935.
- [139] J. Heberle, *Biochimica et biophysica acta* **2000**, *1458*, 135–147.
- [140] A. Isidro-Llobet, M. Álvarez, F. Albericio, *Chemical Reviews* **2009**, *109*, 2455–2504.
- [141] M. Schelhaas, H. Waldmann, *Angewandte Chemie International Edition in English* **1996**, *35*, 2056–2083.
- [142] K. Jarowicki, P. Kocienski, *Journal of the Chemical Society Perkin Transactions 1* **2000**, 2495–2527.
- [143] J. S. Debenham, R. Madsen, C. Roberts, B. Fraser-Reid, *Journal of the American Chemical Society* **1995**, *117*, 3302–3303.
- [144] A. Herrmann, *Photochemical & Photobiological Sciences* **2012**, *11*, 446–459.
- [145] H. Yu, J. Li, D. Wu, Z. Qiu, Y. Zhang, *Chemical Society Reviews* **2010**, *39*, 464–473.
- [146] C. G. Bochet, *Journal of the Chemical Society Perkin Transactions 1* **2002**, 125–142.
- [147] P. Wang, *Asian Journal of Organic Chemistry* **2013**, *2*, 452–464.
- [148] P. Klan, T. Solomek, C. G. Bochet, R. Givens, M. Rubina, V. Popik, A. Kostikov, J. Wirz, P. Klán, T. Šolomek, C. G. Bochet, A. Blanc, R. Givens, M. Rubina, V. Popik, A. Kostikov, J. Wirz, *Chemical Reviews* **2012**, *113*, 119–191.
- [149] J. A. Barltrop, P. Schofield, *Tetrahedron Letters* **1962**, *3*, 697–699.
- [150] J. Engels, E. J. Schlaeger, *Journal of Medicinal Chemistry* **1977**, *20*, 907–911.
- [151] S. Gug, S. Charon, A. Specht, K. Alarcon, D. Ogden, B. Zietz, J. Léonard, S. Haacke, F. Bolze, J.-F. Nicoud, M. Goeldner, *ChemBioChem* **2008**, *9*, 1303–1307.
- [152] J. Rautio, N. A. Meanwell, L. Di, M. J. Hageman, *Nature Reviews Drug Discovery* **2018**, *17*, 559–587.
- [153] I. Elamri, C. Abdellaoui, J. K. Bains, K. F. Hohmann, S. L. Gande, E. Stirnal, J. Wachtveitl, H. Schwalbe, *Journal of the American Chemical Society* **2021**, *143*, 10596–10603.
- [154] S. Bonnet, *Dalton Transactions* **2018**, *47*, 10330–10343.
- [155] G. Alachouzos, A. M. Schulte, A. Mondal, W. Szymanski, B. L. Feringa, *Angewandte Chemie* **2022**, *134*, e202201308.

- [156] C.-H. Yang, J. Denne, S. Reed, H. Wang, *Computational and Theoretical Chemistry* **2019**, *1151*, 1–11.
- [157] P. Wang, H. Hu, Y. Wang, *Organic Letters* **2007**, *9*, 2831–2833.
- [158] M. Abe, Y. Chitose, S. Jakkampudi, P. T. T. Thuy, Q. Lin, B. T. Van, A. Yamada, R. Oyama, M. Sasaki, C. Katan, *Synthesis (Germany)* **2017**, *49*, 3337–3346.
- [159] R. Klimek, M. Asido, V. Hermanns, S. Junek, J. Wachtveitl, A. Heckel, *Chemistry – A European Journal* **2022**, *28*, e202200647.
- [160] C. Morville, J. Chaud, F. Bolze, A. Specht, *Journal of Inclusion Phenomena and Macrocyclic Chemistry* **2021**, DOI 10.1007/s10847-021-01071-9.
- [161] C. G. Bochet, *Angewandte Chemie International Edition* **2001**, *40*, 2071–2073.
- [162] A. Blanc, C. G. Bochet, *Organic Letters* **2007**, *9*, 2649–2651.
- [163] Y. Becker, E. Unger, M. A. H. Fichte, D. A. Gacek, A. Dreuw, J. Wachtveitl, P. J. Walla, A. Heckel, *Chemical Science* **2018**, *9*, 2797–2802.
- [164] I. Aujard, C. Benbrahim, M. Gouget, O. Ruel, J. B. Baudin, P. Neveu, L. Jullien, *Chemistry - A European Journal* **2006**, *12*, 6865–6879.
- [165] C. A. Hammer, K. Falahati, A. Jakob, R. Klimek, I. Burghardt, A. Heckel, J. Wachtveitl, *Journal of Physical Chemistry Letters* **2018**, *9*, 1448–1453.
- [166] M. Asido, C. Hamerla, R. Weber, M. Horz, M. S. Niraghatam, A. Heckel, I. Burghardt, J. Wachtveitl, *Physical Chemistry Chemical Physics* **2022**, *24*, 1795–1802.
- [167] A. Dienes, C. V. Shank, A. M. Trozzolo, *Applied Physics Letters* **1970**, *17*, 189–191.
- [168] E. J. Schimitschek, J. A. Trias, P. R. Hammond, R. L. Atkins, *Optics Communications* **1974**, *11*, 352–355.
- [169] R. S. Givens, B. Matuszewski, *Journal of the American Chemical Society* **1984**, 6860–6861.
- [170] A. Z. Suzuki, T. Watanabe, M. Kawamoto, K. Nishiyama, H. Yamashita, M. Ishii, M. Iwamura, T. Furuta, *Organic Letters* **2003**, *5*, 4867–4870.
- [171] B. Schmidt, C. Sobotta, B. Heinz, S. Laimgruber, M. Braun, P. Gilch, *Biochimica et Biophysica Acta - Bioenergetics* **2005**, *1706*, 165–173.
- [172] M. Bojtár, A. Kormos, K. Kis-Petik, M. Kellermayer, P. Kele, *Organic Letters* **2019**, *21*, 9410–9414.

## Bibliography

- [173] C. Hamerla, C. Neumann, K. Falahati, J. von Cosel, L. J. G. W. van Wilderen, M. S. Niraghatam, D. Kern-Michler, N. Mielke, M. Reinfelds, A. Rodrigues-Correia, A. Heckel, J. Bredenbeck, I. Burghardt, *Physical Chemistry Chemical Physics* **2020**, *22*, 13418–13430.
- [174] L. J. G. W. van Wilderen, C. Neumann, A. Rodrigues-Correia, D. Kern-Michler, N. Mielke, M. Reinfelds, A. Heckel, J. Bredenbeck, *Physical Chemistry Chemical Physics* **2017**, *19*, 6487–6496.
- [175] R. S. Becker, S. Chakravorti, C. A. Gartner, M. d. G. Miguel, *Journal of the Chemical Society Faraday Transactions* **1993**, *89*, 1007–1019.
- [176] Z. R. Grabowski, K. Rotkiewicz, A. Siemiarczuk, *Journal of Luminescence* **1979**, *18–19*, 420–424.
- [177] A. Nag, T. Kundu, K. Bhattacharyya, *Chemical Physics Letters* **1989**, *160*, 257–260.
- [178] A. Nag, K. Bhattacharyya, *Chemical Physics Letters* **1990**, *169*, 12–16.
- [179] B. Schade, V. Hagen, R. Schmidt, R. Herbrich, E. Krause, T. Eckardt, J. Bendig, *The Journal of Organic Chemistry* **1999**, *64*, 9109–9117.
- [180] R. Schmidt, D. Geissler, V. Hagen, J. Bendig, *The Journal of Physical Chemistry A* **2007**, *111*, 5768–5774.
- [181] G. Jones, W. R. Jackson, C. Y. Choi, W. R. Bergmark, *The Journal of Physical Chemistry* **1985**, *89*, 294–300.
- [182] B. Cohen, D. Huppert, *The Journal of Physical Chemistry A* **2001**, *105*, 7157–7164.
- [183] A. Treibs, F.-H. Kreuzer, *Justus Liebigs Annalen der Chemie* **1968**, *718*, 208–223.
- [184] A. Schmitt, B. Hinkeldey, M. Wild, G. Jung, *Journal of Fluorescence* **2009**, *19*, 755–758.
- [185] K. Tram, H. Yan, H. A. Jenkins, S. Vassiliev, D. Bruce, *Dyes and Pigments* **2009**, *82*, 392–395.
- [186] I. J. Arroyo, R. Hu, G. Merino, B. Z. Tang, E. Peña-Cabrera, *The Journal of Organic Chemistry* **2009**, *74*, 5719–5722.
- [187] E. Bassan, A. Gualandi, P. Giorgio Cozzi, P. Ceroni, *Chemical Science* **2021**, *12*, 6607–6628.
- [188] A. C. Benniston, G. Copley, *Physical Chemistry Chemical Physics* **2009**, *11*, 4124–4131.

- [189] F. Schweighöfer, I. Yüce, L. Dworak, P. Guo, M. Zastrow, K. Mayer, C. Barta, D. Liebmann, N. Ziebart, K. Rück-Braun, J. Wachtveitl, *Journal of Physics: Condensed Matter* **2018**, *30*, 054001.
- [190] N. Boens, V. Leen, W. Dehaen, *Chemical Society Reviews* **2012**, *41*, 1130–1172.
- [191] T. Slanina, P. Shrestha, E. Palao, D. Kand, J. A. Peterson, A. S. Dutton, N. Rubinstein, R. Weinstain, A. H. Winter, P. Klán, *Journal of the American Chemical Society* **2017**, *139*, 15168–15175.
- [192] R. Weinstain, T. Slanina, D. Kand, P. Klán, *Chemical Reviews* **2020**, *120*, 13135–13272.
- [193] N. Umeda, H. Takahashi, M. Kamiya, T. Ueno, T. Komatsu, T. Terai, K. Hanaoka, T. Nagano, Y. Urano, *ACS Chemical Biology* **2014**, *9*, 2242–2246.
- [194] P. P. Goswami, A. Syed, C. L. Beck, T. R. Albright, K. M. Mahoney, R. Unash, E. A. Smith, A. H. Winter, *Journal of the American Chemical Society* **2015**, *137*, 3783–3786.
- [195] N. Rubinstein, P. Liu, E. W. Miller, R. Weinstain, *Chemical Communications* **2015**, *51*, 6369–6372.
- [196] P. K. Singh, P. Majumdar, S. P. Singh, *Coordination Chemistry Reviews* **2021**, *449*, 214193.
- [197] T. Šolomek, J. Wirz, P. Klán, *Accounts of Chemical Research* **2015**, *48*, 3064–3072.
- [198] H. E. Kato, K. Inoue, R. Abe-Yoshizumi, Y. Kato, H. Ono, M. Konno, S. Hososhima, T. Ishizuka, M. R. Hoque, H. Kunitomo, J. Ito, S. Yoshizawa, K. Yamashita, M. Takemoto, T. Nishizawa, R. Taniguchi, K. Kogure, A. D. Maturana, Y. Iino, H. Yawo, R. Ishitani, H. Kandori, O. Nureki, *Nature* **2015**, *521*, 48–53.
- [199] I. Gushchin, V. Shevchenko, V. Polovinkin, K. Kovalev, A. Alekseev, E. Round, V. Borshchevskiy, T. Balandin, A. Popov, T. Gensch, C. Fahlke, C. Bamann, D. Willbold, G. Büldt, E. Bamberg, V. Gordeliy, *Nature Structural and Molecular Biology* **2015**, *22*, 390–396.
- [200] K. Inoue, M. Konno, R. Abe-Yoshizumi, H. Kandori, *Angewandte Chemie - International Edition* **2015**, *54*, 11536–11539.
- [201] R. Abe-Yoshizumi, K. Inoue, H. E. Kato, O. Nureki, H. Kandori, *Biochemistry* **2016**, *55*, 5790–5797.

## Bibliography

- [202] K. Kovalev, R. Astashkin, I. Gushchin, P. Orekhov, D. Volkov, E. Zinovev, E. Marin, M. Rulev, A. Alekseev, A. Royant, P. Carpentier, S. Vaganova, D. Zabelskii, C. Baeken, I. Sergeev, T. Balandin, G. Bourenkov, X. Carpena, R. Boer, N. Maliar, V. Borshchevskiy, G. Büldt, E. Bamberg, V. Gordeliy, *Nature Communications* **2020**, *11*, 2137.
- [203] P. Skopintsev, D. Ehrenberg, T. Weinert, D. James, R. K. Kar, P. J. M. Johnson, D. Ozerov, A. Furrer, I. Martiel, F. Dworkowski, K. Nass, G. Knopp, C. Cirelli, C. Arrell, D. Gashi, S. Mous, M. Wranik, T. Gruhl, D. Kekilli, S. Brünle, X. Deupi, G. F. X. Schertler, R. M. Benoit, V. Panneels, P. Nogly, I. Schapiro, C. Milne, J. Heberle, J. Standfuss, *Nature* **2020**, *583*, 314–318.
- [204] S. P. Balashov, E. S. Imasheva, A. K. Dioumaev, J. M. Wang, K. H. Jung, J. K. Lanyi, *Biochemistry* **2014**, *53*, 7549–7561.
- [205] C.-M. Suomivuori, A. P. Gamiz-Hernandez, D. Sundholm, V. R. I. Kaila, *Proceedings of the National Academy of Sciences of the United States of America* **2017**, *114*, 7043–7048.
- [206] M. Konno, Y. Kato, H. E. Kato, K. Inoue, O. Nureki, H. Kandori, *Journal of Physical Chemistry Letters* **2016**, *7*, 51–55.
- [207] Y. Kato, K. Inoue, H. Kandori, *Journal of Physical Chemistry Letters* **2015**, *6*, 5111–5115.
- [208] Y. Hontani, K. Inoue, M. Kloz, Y. Kato, H. Kandori, J. T. Kennis, *Physical Chemistry Chemical Physics* **2016**, *18*, 24729–24736.
- [209] H. Ono, K. Inoue, R. Abe-Yoshizumi, H. Kandori, *Journal of Physical Chemistry B* **2014**, *118*, 4784–4792.
- [210] C. Zscherp, J. Heberle, *Journal of Physical Chemistry B* **1997**, *101*, 10542–10547.
- [211] A. Barth, *Progress in Biophysics and Molecular Biology* **2000**, *74*, 141–173.
- [212] M. Asido, P. Eberhardt, C. N. Kriebel, M. Braun, C. Glaubitz, J. Wachtveitl, *Physical Chemistry Chemical Physics* **2019**, *21*, 4461–4471.
- [213] H. Kakitani, T. Kakitani, H. Rodman, B. Honlg, R. Callender, *The Journal of Physical Chemistry* **1983**, *87*, 3620–3628.
- [214] M. E. Heyde, D. Gill, R. G. Kilponen, L. Rimai, *Journal of the American Chemical Society* **1971**, *93*, 6776–6780.
- [215] H. Kandori, K. Inoue, S. P. Tsunoda, *Chemical Reviews* **2018**, *118*, 10646–10658.

- [216] S. Tomida, S. Ito, T. Mato, Y. Furutani, K. Inoue, H. Kandori, *Biochimica et Biophysica Acta - Bioenergetics* **2020**, 1861, 148190.
- [217] N. Nishimura, M. Mizuno, H. Kandori, Y. Mizutani, *Journal of Physical Chemistry B* **2019**, 123, 3430–3440.
- [218] Y. Cao, G. Váró, A. L. Klinger, D. M. Czajkowsky, M. S. Braiman, R. Needleman, J. K. Lanyi, *Biochemistry* **1993**, 32, 1981–90.
- [219] D. M. Byler, H. Susi, *Biopolymers* **1986**, 25, 469–487.
- [220] A. Barth, C. Zscherp, *Quarterly reviews of biophysics* **2002**, 35, 369–430.
- [221] S. Krimm, J. Bandekar, *Advances in protein chemistry* **1986**, 38, 181–364.
- [222] H. Susi, D. M. Byler, *Methods in enzymology* **1986**, 130, 290–311.
- [223] Y. Abe, S. Krimm, *Biopolymers* **1972**, 11, 1817–1839.
- [224] J. Kubelka, T. A. Keiderling, *Journal of the American Chemical Society* **2001**, 123, 12048–12058.
- [225] S. Hahn, S.-S. Kim, C. Lee, M. Cho, *The Journal of Chemical Physics* **2005**, 123, 084905.
- [226] R. Diller, R. Jakober, C. Schumann, F. Peters, J. P. Klare, M. Engelhard, *Biopolymers* **2006**, 82, 358–362.
- [227] S. O. Smith, M. S. Braiman, A. B. Myers, J. A. Pardo, J. M. L. Courtin, C. Winkel, J. Lugtenburg, R. A. Mathies, *Journal of the American Chemical Society* **1987**, 109, 3108–3125.
- [228] C.-W. Wu, L. Stryer, *Proceedings of the National Academy of Sciences of the United States of America* **1972**, 69, 1104–1108.
- [229] M. Hoffmann, M. Wanko, P. Strodel, P. H. König, T. Frauenheim, K. Schulten, W. Thiel, E. Tajkhorshid, M. Elstner, *Journal of the American Chemical Society* **2006**, 128, 10808–10818.
- [230] R. Rajamani, Y.-L. Lin, J. Gao, *Journal of Computational Chemistry* **2011**, 32, 854–865.
- [231] S. Arnis, K. P. Hofmann, *Proceedings of the National Academy of Sciences of the United States of America* **1993**, 90, 7849–7853.
- [232] S. W. Lin, T. P. Sakmar, *Biochemistry* **1996**, 35, 11149–11159.
- [233] I. Gushchin, V. Shevchenko, V. Polovinkin, V. Borshchevskiy, P. Buslaev, E. Bamberg, V. Gordeliy, *The FEBS Journal* **2016**, 283, 1232–1238.

## Bibliography

- [234] B. Karvaly, Z. Dancsházy, *FEBS Letters* **1977**, 76, 36–40.
- [235] P. Hegemann, D. Oesterhelt, E. Bamberg, *BBA - Biomembranes* **1985**, 819, 195–205.
- [236] C. Bamann, R. Gueta, S. Kleinlogel, G. Nagel, E. Bamberg, *Biochemistry* **2010**, 49, 267–278.
- [237] C. E. Eckert, *Dissertation* **2017**, 2017, 1–200.
- [238] O. Jakdetchai, P. Eberhardt, M. Asido, J. Kaur, C. N. Kriebel, J. Mao, A. J. Leeder, L. J. Brown, R. C. D. Brown, J. Becker-Baldus, C. Bamann, J. Wachtveitl, C. Glaubitz, *Science Advances* **2021**, 7.
- [239] T. Lopez Arbeloa, F. Lopez Arbeloa, M. J. Tapia, I. Lopez Arbeloa, *The Journal of Physical Chemistry* **1993**, 97, 4704–4707.
- [240] J. Catalán, C. Díaz, F. García-Blanco, *The Journal of Organic Chemistry* **2001**, 66, 5846–5852.
- [241] F. Schweighöfer, L. Dworak, C. A. Hammer, H. Gustmann, M. Zastrow, K. Rück-Braun, J. Wachtveitl, *Scientific Reports* **2016**, 6, 28638.
- [242] M. Beija, C. A. Afonso, J. M. Martinho, *Chemical Society Reviews* **2009**, 38, 2410–2433.
- [243] L. Wang, W. Du, Z. Hu, K. Uvdal, L. Li, W. Huang, *Angewandte Chemie - International Edition* **2019**, 58, 14026–14043.
- [244] C. B. Milojević, D. W. Silverstein, L. Jensen, J. P. Camden, *Journal of Physical Chemistry C* **2013**, 117, 3046–3054.



# Acknowledgements

At this point it is time for the most important part of this written work: Thanking all the people who supported and guided me, the people who contributed to the scientific success of the projects, and people who were simply there for me. I apologize, but this section will be a long one.

First of all I would like to thank my supervisor, Josef Wachtveitl, for giving me the opportunity to work on a broad bandwidth of exciting projects. Thank you for your scientific and academic guidance and the "open-door" policy, despite of your very tight schedule. I deeply appreciate the trust you put in me, which allowed me to further develop a more critical and independent scientific thinking. Your emphasis on group harmony certainly is one of the main reasons that the overall work atmosphere is not just productive but also comfortable and welcoming.

I would also like to thank my mentors Jens Bredenbeck and Boris Fürtig for their perpetual feedback, their support and also for their encouragement over the years.

A special thanks goes to Alexander Heckel for agreeing upon to be the second reviewer of this work and more so his seemingly endless dedication in terms of CLiC. I am grateful for being part of this RTG, which did not just lead to fruitful collaborations but also many memorable experiences over the years.

In the same context I would also like to thank Heike Köhler and Christian Grünewald for their administrative work in CLiC without which a well-functioning of the whole program would not be possible. Of course this also applies to the steering board in its different compositions in the three phases of CLiC.

I would like to thank my collaborators for the productive work and the scientific goals we could achieve together. Thank you Rebekka Weber, Robin Klimek, Volker Hermanns (Heckel), Carsten Hamerla, Madhava N. Shyam, Maximiliane Horz (Burghardt), Clara N. Kriebel, Orawan Jakdetchai, Jagdeep Kaur (Glaubitz), Rajiv. K. Kar (Schapiro) and Heike Krüger (Wieneke / Tampé). Naturally, this goes also for the respective PIs, namely Alexander Heckel, Irene Burghardt, Clemens Glaubitz, Igor Schapiro, Ralph Wieneke and Robert Tampé.

Very important, but often forgotten, is the work done by interns, bachelor- and masterstudents. I would like to thank Nazmiye Cekir, Nagihan Aydin, Kerby Chok, Torben

## *Acknowledgements*

Saßmannshausen, Simon Wittemann, Yagmur Aydogan and Gerrit Lamm for their excellent work and their contribution to the respective projects. Especially, Yagmur, Torben and Gerrit I wish the very best for their own pursuit of a PhD in our group.

When it comes to technical problems we heavily rely on the expertise of the mechanics and electronics workshops. In this context I would like to thank Markus van Tankeren and his workshop team for perpetually delivering mechanical solutions, as well as Jochen Feldhaar for his incredible knowledge and support in all matters concerning our lab electronics.

Also I would like to thank Mark Thomson for his lectures, the many discussions and his advice in the course of my studies, which convinced me that lasers are the coolest invention besides lightsabers.

Now, there are many people in the Wachtveitl group I need to explicitly express my thanks to.

Thank you, Iso, for helping us finding a way through the administrative tangle of forms and declarations.

Thank you, Markus, for your helpful advice and discussions whenever a project got stuck. I am always amazed about your encyclopedic knowledge in laser spectroscopy.

Similarly, I would like to express my thanks to Chavdar for helping me out on many issues concerning data evaluation. Also thank you for teaching me the fundamentals of our ultrafast setups. I will never forget the characteristic "oops"- or "you can tweak it a little"-moments. You will be greatly missed!

On this occasion I would like to especially thank Peter Eberhardt for supervising my master thesis. Thank you for your support and advice, even beyond the time of the master project. Also thank you for introducing the most incredible beverage of all time to the group: Stranta!

Sina and Chahinez, it has been a long way from our masterthesis up to our PhD graduation. But it has also been a great pleasure to go this journey with you. I deeply appreciate that we could cheer us up to keep on going. Thank you for that!

Now a special thanks goes to the office 215 in its changing compositions. Thank you Lars, Peter, Chris and Chokri for taking me in as a fresh and inexperienced PhD candidate and helping me with the overwhelming struggles one has in the beginning of such a journey. Thank you Tobias, Kosta, Torben and Gerrit for keeping the atmosphere productive but not too serious. It's always a pleasure to start the working day with a good portion of laughter.

Thao, first of all thank you for proof reading this thesis. But an even bigger thank you for keeping the group dynamics going with your work "behind-the-scenes" and

for always finding a way to make even a tense situation funny. Also there is no better Stranta drinking-partner!

Likewise I would like to thank Gerrit for proof reading this thesis and more so for joining the rhodopsin crew. Keep up with that excellent work!

An honorable mention is dedicated to the former members Chris, Chokri and Dinh who still are available for the occasional beer and football match. Thank you for staying in touch. Nur die SGE!

Overall, I would like to thank the whole group for creating a productive, yet comfortable and joyful atmosphere. This has been especially important to me during times when things did not work. Being able to count on your help and your support was invaluable. It has been - and of course still is - a great pleasure to be part of this group. And please forgive me if I forgot to mention someone specifically here.

Certainly, there have been many more people I did not explicitly mention here but who contributed to the success of this work in one way or the other. I would like to express my gratitude to them as well.

Of course this work could not have been possible without the support of people in my personal life.

First of all I would like to thank my friends, who became to realize that I had much less time to hang out but still stood loyal to me. Thank you Tim, Max, Mario, David, Selcuk and Jamal for your support over the many years we have known each other.

I am deeply grateful for my family, my little sister Josephine, my mother Gudrun, and my father Arnold. Thank you for being there for me from ever since (and probably even before) I could think. Thank you mum and dad for all the sacrifices you made to make all this possible for me. There are no words to properly express my gratitude.

Last, but certainly not least, I would like to thank my partner-in-crime, Jae Eun. Thank you for bringing me laughter, bringing me joy and cheering me up after a stressful day. I am grateful for your support, your understanding and your encouragement. Thank you for going this journey with me.



# Appendix

## Declaration

I herewith declare that I have produced my doctoral dissertation on the topic of

**“Multiphoton Processes and Photocontrol of Biochemical Reaction Pathways“**

independently and using only the tools indicated therein. In particular, all references borrowed from external sources are clearly acknowledged and identified.

I confirm that I have respected the principles of good scientific practice and have not made any use of the services of any commercial agency in respect of my doctorate.

Frankfurt am Main,





# Marvin Phil Ronald Asido

---

## *Curriculum Vitae*

### Personal Information

Date of birth 25.07.1991  
Place of birth Frankfurt am Main  
Nationality German

### Education

2017–2022 **PhD (Chemistry)**, *Goethe University, Frankfurt, Germany.*  
2014–2017 **Master of Science (Biophysics)**, *Goethe University, Frankfurt, Germany.*  
2014–2015 **Year abroad**, *Seoul National University, Seoul, South Korea.*  
2011–2014 **Bachelor of Science (Biophysics)**, *Goethe University, Frankfurt, Germany.*  
2001–2010 **Allgemeine Hochschulreife (Abitur)**, *Helmholtzschule, Frankfurt, Germany.*

### Dissertation

Title *Multiphoton Processes and Photocontrol of Biochemical Reaction Pathways*  
Supervisor Prof. Dr. Josef Wachtveitl

### Master Thesis

Title *Time-Resolved Measurements on the Sodium Pump KR2 in the Infrared*  
Supervisor Prof. Dr. Josef Wachtveitl

### Bachelor Thesis

Title *Detektion von Glucose mittels THz-Strahlung*  
Supervisor Prof. Dr. Hartmut Roskos

